111-012-7C96
MOTC-IOT-110-H2CA001f

水波時尺或時頻分析法之比較與應用(4/4)

The Best Wavelet for Water Waves

交通部運輸研究所

中華民國 111 年 3 月

111-012-7C96
MOTC-IOT-110-H2CA001f

水波時尺或時頻分析法之比較與應用(4/4)

The Best Wavelet for Water Waves

著者：李勇榮

交通部運輸研究所

中華民國 111 年 3 月

水波時尺或時頻分析法之比較與應用(4/4)
The Best Wavelet for Water Waves

著　　者：李勇榮
出版機關：交通部運輸研究所
地　　址：105004 臺北市松山區敦化北路 240 號
網　　址：www.iot.gov.tw (中文版＞數位典藏＞本所出版品)
電　　話：(04)2658-7200
出版年月：中華民國 111 年 03 月
印 刷 者：
版(刷)次冊數：初版
書同時登載於交通部運輸研究所網站
定　　價：400 元
展 售 處：
交通部運輸研究所運輸資訊組・電話：(02)2349-6789
國家書店松江門市：104472 臺北市中山區松江路 209 號•電話：(02)2518-0207
五南文化廣場：400002 臺中市中區中山路 6 號•電話：(04)2226-0330

GPN：1011100167　　ISBN：978-986-531-384-5（平裝）

交通部運輸研究所自行研究計畫出版品摘要表

出版品名稱：水波時尺或時頻分析法之比較與應用(4/4)-The Best Wavelet for Water Waves

國際標準書號（或叢刊號）	政府出版品統一編號	運輸研究所出版品編號	計畫編號
ISBN 978-986-531-384-5(平裝)	1011100167	111-012-7C96	MOTC-IOT-110-H2CA001f

主辦單位：港灣技術研究中心
主管：
計畫主持人：李勇榮
研究人員：李勇榮
聯絡電話：04-26587183
傳真號碼：04-26571329

研究期間
自 107 年 01 月
至 110 年 12 月

關鍵詞：The best wavelet for water waves, Identification, Verification, Optimization, Application, Innovation, Wavelet coherences, Energy cascade model

摘要：

本研究探討水波分析之最佳仔波，並及於一個新型態的類仔波，其全文主要可以分為四大部分，即：鑑取、驗証、應用、創新。在鑑取上，研究所含蓋之離散仔波函基類屬相當廣泛，具有函基屬性上的全面性或完整性含蓋，其所得最佳仔波在離散領域是為半正交之樞點順適仔波，而其在連續領域的對應仔波則是為莫利仔波，此外我們亦將富立葉函基加入該鑑取比較考量。另其標準及鑑取手法係在統計方面取用多種熵值規範，多元性地比較熵值表現，並探討各種類型仔波轉換係數之累積機率密度函數，由這些統計比較，我們得出此一最佳仔波的表現除了遠較其它仔波突出，亦且明顯優於富立葉波譜函基者。在驗証上，我們由仔波等位解析方程式推得仔波共關頻振關係式，再進一步比較使用這一最佳仔波函基的共關頻振與使用富立葉函基之共關頻振表現。由仔波共關頻振之明確可判性與絕對優越性得以建構上述鑑取結果之立論性。在應用上，此處研究風、波、雨偶合下的波浪衰減現象，從而提出了一個能量遞轉機制，並藉由試驗，將前述最佳仔波函基及共關頻振結果應用於波流場互作用尺度演化行為，從而解說降雨對波浪衰減的物理現象。在創新上，提出一個在研究過程中意外發現的新型態類仔波，我們探討其學理特性，並用模擬訊號與試驗水槽訊號加以檢核驗証，此外並以之與莫利仔波進行各方面的比較，其結果顯現這一類仔波較之莫利仔波有多方面的突出表現，其時頻特徵無論在模值或相位分佈都可提供有義及明顯的訊息，另亦可提供一些水陂高階物理現象，如能量遞轉、側頻不穩、演化調變行為等。總而言之，吾人深信，此處所得水波模擬之最適離散暨最適連續仔波已是定論。

出版日期	頁數	定價	本出版品取得方式
111 年 3 月	313	400	凡屬機密性出版品均不對外公開。普通性出版品，公營、公益機關團體及學校可函洽本所免費贈閱；私人及私營機關團體可按定價價購。

備註：本研究之結論與建議不代表交通部之意見。

PUBLICATION ABSTRACTS OF RESEARCH PROJECTS
INSTITUTE OF TRANSPORTATION
MINISTRY OF TRANSPORTATION AND COMMUNICATIONS

TITLE: The Best Wavelet for Water Waves

ISBN(OR ISSN)	GOVERNMENT PUBLICATIONS NUMBER	IOT SERIAL NUMBER	PROJECT NUMBER
978-986-531-384-5(pbk)	1011100167	111-012-7C96	MOTC-IOT-110-H2CA001f

DIVISION: HARBOR & MARINE TECHNOLOGY CENTER
DIVISION DIRECTOR: Li-Hung Tsai
PRINCIPAL INVESTIGATOR: Yueon-Ron Lee
PROJECT STAFF: Yueon-Ron Lee
PHONE: 886-4-26587183
FAX: 886-4-26571329

PROJECT PERIOD
FROM Jan. 2018
TO Dec. 2021

KEY WORDS: The best wavelet for water waves, Identification, Verification, Optimization, Application, Innovation, Wavelet coherences, Energy cascade model

ABSTRACT:

Centering on the best wavelet for water waves, the study here can be divided into four main parts: identification, verification, application and innovation. It is believed that the best basis identified here is the last and ultimate word in wavelets concerning their applications to water waves.

In identification, the best wavelet for water wave simulations, either in the discrete or in the continuous domain, is named; to wit, the best basis in the discrete domain is the semi-orthogonal cardinal spline wavelet and the counterpart wavelet in the continuous domain is the Morlet wavelet. In the identifying process, broad and comprehensive basis categories of discrete wavelet groups are taken into account; and, inclusive and extensive entropy measures, as well as statistical probability distributions, are adopted.

In verification, as the further affirmation of the realization of the best basis, the formula for wavelet coherence is devised based upon the equation of wavelet resolution of identity; and, the performances of wavelet coherences are compared to those of the Fourier spectral coherences using data from measurements of wave and aqueous flow fields in a wind-wave tank. The wavelet's absolute superiority and its outstanding and informative outcomes fully vindicate the identification. Reasons that yield the superiority are also given.

In application, as a demonstration of the possible usefulness of the best basis and the contrived coherence approach, first, an energy cascade model is proposed for the damping of waves due to rain in the wind, wave and rain coupling system; afterwards, the wavelet coherences are used to explicate its physics and the interaction scales within the coupling system. Overall, they are able to reflect two categories of mechanisms involved. One emphasizes the local mechanism within the air and aqueous boundary layers, especially on the role played by a match layer due to rain of interfacial aqueous flows. Another emphasizes the stratification-induced mechanism governing a large water body, and it involves the following key elements: the vortical contribution to wave attenuation, the impact of rain and the catalysts of tuning and de-tuning processes, the forming of tetra-interactions of surface waves, and the further diversification of coupling scales mainly due to triad interactions of surface and internal waves.

In innovation, a wavelet variant is proposed and its characterizations and performances are analyzed and compared to those of the Morlet wavelet. Both numerical signals from simulation and water waves data from experiments are used to check their serviceability and to validate the comparisons. It is found that the wavelet variant is capable of furnishing distinguish features either from the modulus or the phase rendition of transform coefficients, as well as yielding a few intrinsic physical phenomena of water waves that are basically inaccessible to the Morlet wavelet.

DATE OF PUBLICATION	NUMBER OF PAGES	PRICE
Mar. 2022	313	400

The Best Wavelet for Water Waves

Yueon-Ron Lee (李勇榮)

交通部運輸研究所港灣技術研究中心

ronlee@ms4.hinet.net

Revision: January 3, 2022
Printed: January 3, 2022

LIST OF CONTENTS

LIST OF FIGURES

LIST OF TABLES

ABSTRACT

Centering on the best wavelet for water waves, the study here can be divided into four main parts: identification, verification, application and innovation. It is believed that the best basis identified here is the last and ultimate word in wavelets concerning their applications to water waves.

In identification, the best wavelet for water wave simulations, either in the discrete or in the continuous domain, is named; to wit, the best basis in the discrete domain is the semi-orthogonal cardinal spline wavelet and the counterpart wavelet in the continuous domain is the Morlet wavelet. In the identifying process, broad and comprehensive basis categories of discrete wavelet groups are taken into account; and, inclusive and extensive entropy measures, as well as statistical probability distributions, are adopted.

In verification, as the further affirmation of the realization of the best basis, the formula for wavelet coherence is devised based upon the equation of wavelet resolution of identity; and, the performances of wavelet coherences are compared to those of the Fourier spectral coherences using data from measurements of wave and aqueous flow fields in a wind-wave tank. The wavelet's absolute superiority and its outstanding and informative outcomes fully vindicate the identification. Reasons that yield the superiority are also given.

In application, as a demonstration of the possible usefulness of the best basis and the contrived coherence approach, first, an energy cascade model is proposed for the damping of waves due to rain in the wind, wave and rain coupling system; afterwards, the wavelet coherences are used to explicate its physics and the interaction scales within the coupling system. Overall, they are able to reflect two categories of mechanisms involved. One emphasizes the local mechanism within the air and aqueous boundary layers, especially on the role played by a match layer due to rain of interfacial aqueous flows. Another emphasizes the stratification-induced mechanism governing a large water body, and it involves the following key elements: the vortical contribution to wave attenuation, the impact of rain and the catalysts of tuning and de-tuning processes, the forming of tetra-interactions of surface waves, and the further diversification of coupling scales mainly due to triad interactions of surface and internal waves.

In innovation, a wavelet variant is proposed and its characterizations and performances are analyzed and compared to those of the Morlet wavelet. Both numerical signals from simulation and water waves data from experiments are used to check their serviceability and to validate the comparisons. It is found that the wavelet variant is capable of furnishing distinguish features either from the modulus or the phase rendition of transform coefficients, as well as yielding a few intrinsic physical phenomena of water waves that are basically inaccessible to the Morlet wavelet.

摘要

本研究探討水波分析之最佳仔波，並及於一個新型態的類仔波，其全文主要可以分爲四大部分，即：鑑取、驗証、應用、創新。在鑑取上，研究所含蓋之離散仔波函基類屬相當廣泛，具有函基屬性上的全面性或完整性含蓋，其所得最佳仔波在離散領域是爲半正交之樞點順適仔波，而其在連續領域的對應仔波則是爲莫利仔波，此外我們亦將富立葉函基加入該鑑取比較考量。另其標準及鑑取手法係在統計方面取用多種熵值規範，多元性地比較熵值表現，並探討各種類型仔波轉換係數之累積機率密度函數，由這些統計比較，我們得出此一最佳仔波的表現除了遠較其它仔波突出，亦且明顯優於富立葉波譜函基者。在驗証上，我們由仔波等位解析方程式推得仔波共關頻振關係式，再進一步比較使用這一最佳仔波函基的共關頻振與使用富立葉函基之共關頻振表現。由仔波共關頻振之明確可判性與絕對優越性得以建構上述鑑取結果之立論性。在應用上，此處研究風、波、雨偶合下的波浪衰減現象，從而提出了一個能量遞轉機制，並藉由試驗，將前述最佳仔波函基及共關頻振結果應用於波流場互作用尺度演化行爲，從而解說降雨對波浪衰減的物理現象。在創新上，提出一個在研究過程中意外發現的新型態類仔波，我們探討其學理特性，並用模擬訊號與試驗水槽訊號加以檢核驗証，此外並以之與莫利仔波進行各方面的比較，其結果顯現這一類仔波較之莫利仔波有多方面的突出表現，其時頻特徵無論在模值或相位分佈都可提供有義及明顯的訊息，另亦可提供一些水陂高階物理現象，如能量遞轉、側頻不穩、演化調變行爲等。總而言之，吾人深信，此處所得水波模擬之最適離散暨最適連續仔波已是定論。

Chapter 1

Introduction

1.1 Background

In wavelets' applications to physics of water waves, it is quite often seen that a specific function basis is adopted for no reason or with yet any slightest hint of rationality. The results thus yielded are fated to be equivocal and problematic, or even misleading and erroneous — mathematics does not need to be liable to physics. Mathematics provides the tools without any precondition while physics should be reasonedly and needs proper instrumentation. Moreover, the usefulness of a particular data analysis methodology is highly case dependent; there simply exists neither a full-fledged analyzing function basis nor an all-purpose numerical scheme for all sorts of signals and applications. Hence, to find a suitable, or yet the optimal, wavelet among the multitude of wavelet function bases is thereof the first priority for water wave related researches and applications.

Chronically, from the somewhat traditional and well established spectral perspective to the more recent wavelet viewpoints, we have the following instrumentations:

- Fourier transform;
- Short time Fourier transform or windowed Fourier transform;
- The Gabor's analytical signal procedure and the relevant Hilbert transform;
- Various time-frequency transforms associated with individual distribution kernels,

such as Wigner Distribution, Page distribution, Choi-Williams distribution, etc. [17];

- The continuous wavelet transform or the integral wavelet transform;
- The discrete wavelet transform.

It is noted that, unlike the discrete and continuous Fourier transforms, which are basically identical in both function bases and formulations, the discrete wavelet transform and the continuous wavelet transform are two essentially different categories with regard to the following two aspects. First, they generally use completely different function bases; Second, they involve relatively quite independent mathematical formulations.

In the following descriptions let assume the analytical target to be a one-dimensional time series signal and let outline the most basic attributes for individual analytical methodologies.

The Fourier transform yields another one-dimensional data in frequency domain. The transform correspondence is one to one. And the correspondence is a time domain variable to a frequency one.

For short time Fourier transform, it yields somewhat localized frequency contents by capping the signal with a window. And, when the capping window is shifted along the time line, it provides time-dependent spectral information. Through such multiple processes the transform correspondence is from the one dimensional time variable to the two dimensional time and frequency variables.

For Gabor's analytical signal procedure, it is based upon the Hilbert transform, which is basically the inverse Fourier transform of a one-sided spectrum that is formed through the chopping off the part of negative frequency. Here the independent variable in the two corresponding transform domains is both time. And the procedure yields instantaneous frequency distribution and amplitude envelop curve along the time line [17, 38]. Ideally, the instantaneous frequency and amplitude should be independent with each other (since they are of two completely different physical units), but in reality they are intertwined and

quite often twist in an unimaginable way. Moreover, the interaction is extremely serious when the relative rate of variation of amplitude is significant. And the symptoms brought out here manifest its relevance to the intrinsic properties of the Fourier transform. Thusly, insurmountable uncertainty involved is always a concern [38].

As for various time-frequency transforms associated with individual distributions (or kernels), they also provide time-varying frequency contents that are conceptually identical to the short time Fourier transform, except that the involved analyzing kernels are related to individual distribution kernels rather than the Fourier kernel of short time Fourier transform. For these transforms they always have their individual pros and cons; none is perfect.

For the discrete wavelet transforms, a one-dimensional time series yields directly another one-dimensional coefficient series that contains the information that covers both "time" and "scale". The correspondence is one independent variable to a variable that mixes two independent variables into one in one transform process. But here, for almost all of the discrete wavelets, the "scale" is generally quite different from the sinusoidal frequency and normally not even possible to be assigned to a "representative frequency". And this causes tremendous difficulties in physics apprehension. Besides, we rarely see a complex discrete wavelet in water wave applications. The dual-tree complex discrete wavelet transform may still provide a measure completely different from the general concept of "sinusoidal frequency".

As to the continuous wavelet transform, the one-dimensional time series yields two-dimensional coefficients that contain information varying both in time and in scale. But now, due to its loosen theoretical requirement and hence its flexibility in design, it is possible to bring in the physically meaningful "representative frequency" rather than just the "scale". The numerical implementation is a multi-process scheme conceptually similar to the short time Fourier transform, except the two core differences: its design of capping windows of varying sizes and its better localization under the fulfillment of the requirement of the wavelet "resolution of identity". Again, every time point has a component

scale distribution, and every scale may play a role at a specific time.

1.2 Local and transient effects

It is well known that Fourier transform is suitable for characterizing stationary signals and not quite satisfactory for analyzing transient local phenomena. The reasons can be illustrated by the following properties of the transform.

- Any Function cannot be both time- and band-limited. If a function is limited (finitely supported) in one domain, then the independent variable of its corresponding function in the other domain stretches the entire real line (**R**). In real world situations, however, signals are almost always limited in time and space; meanwhile, hardware's capability is generally band-limited. This simply implies that there is not going to be a function basis that perfectly matches theory to practice. A slight variation of the Fourier transform is the short time Fourier transform, which is just the Fourier transform of the windowed signal, i.e., the original signal capped with or multiplied by a window function. In short time Fourier transform this property of mutual exclusivity in time and frequency localizations is indicated by the Balian-Low theorem, which basically states that if the window function $g(t)$ of a Gabor type frame

$$g_{m,n}(t) = e^{-2\pi imt} g(t-n), \tag{1.1}$$

  in which $m, n \in \mathbf{Z}$, is well localized in time, then the associated Fourier transform window can not be well localized in frequency. The point here sounds a bit abstract, but, in reality, this is conceptually equivalent to the following points.

- The Gibbs phenomenon states that, if there is a jump in signal, then the overshoots, occurring at both sides of the discontinuity when the inverse Fourier transform is implemented, can never disappear and remain at constant. This amounts to say that it takes quite many a spectral component to make up a sharp transient feature

and that a local variation affects a broad range of the spectrum just as the Fourier transform of the delta function (more precisely, delta distribution) covers the whole frequency axis.

- Fourier basis functions are periodic and extend bi-infinitely; signals thus analyzed are better to be periodic and sampled infinitely. The unavoidable side effects for not fulfilling these requirements are many: frequency leakages, smoothing errors, edge effects due to data truncations, aliasing due to under-sampling or non-periodicity (figure 1.1 (TFW–WP BB) is actually a case of under-sampling, where a linear chirp is sampled at a rate half of the Nyquist frequency), and, uncontrollable spectral variance due to the finite resolution or histogram processing.

Overall, the syndromes associated with the above listed items can be referred to the non-stationary effects.

1.3 Windowed transforms

Except the Fourier transform all the transforms mentioned in the preceding section can be classified as a form of windowed transform (either in time or in frequency).

Both short-time Fourier transform and wavelet transform try to remedy Fourier basis's deficiencies in characterizing transient phenomena by analyzing the set of localized signals. For the short time Fourier transform this can easily be executed by varying m and n in equation 1.1. For the wavelet transform this can be illustrated through the use of the Morlet wavelet by varying its translation and dilation variables. Both transforms yield local spectral information – more precisely, local scale information, if the term "frequency", "Hz", or "spectrum" is strictly reserved for sinusoidal functions. However, due to the Balian-Low theorem mentioned above, the waveform associated with short time Fourier transform can never be truly local in time since in reality the frequency domain of discrete Fourier transform is always band-limited by obeying the Nyquist law. In this re-

gard, wavelets can be of exactly local; at least, they must have suitable or better decaying property such that they contain no zero-frequency component.

Let us further outline a few specific properties pertaining to individual transform:

- Both short time Fourier transform and wavelet transform are windowed transforms. In short time Fourier transform there exist two quite distinctive operations. The first operation is applying a suitable time-window to the signal; the second operation is performing the Fourier transform for the capped signal. The corresponding inverse transform (or reconstruction process) of the short time Fourier transform is naturally associated with a frequency-window and involves two similar distinctive operations too. However, in wavelet transform these two distinctive steps are not clearly observable — rather than using the very distinctive "window (either time- or frequency-window)" and "Fourier basis function (i.e., sine or cosine function)", the "window" and the "basis function" are synthesized in an inseparable specific form called "wavelet". In fact, one can clearly solidify this notion by comparing the Gabor type frame (equation 1.1) with the Morlet wavelet when the window function $g(t)$ of equation 1.1 is assumed to be a Gaussian bell. The intention for either the combined operation or synthesized operation is completely the same: to provide a mechanism (or kernel) for projecting a signal into modulated or oscillating wave constituents.

- The time-frequency windows in short time Fourier transform keep rigid for different scales since the window function $g(t)$ in Equation 1.1 does not depend on m, i.e., their widths (usually referring to time) and heights (usually referring to frequency) do not change for all frequencies. In wavelet transform, the windows are adjusted to different scales, but the sizes (or areas) of different windows are still fixed, i.e., each window's height and width are inversely proportional and the product remains constant (either for discrete wavelet transform or continuous wavelet transform). The concept of fixed size windows is illustrated by the fixed area of the gray blocks

in the phase planes shown in figures 1.1 (TFW–WP BB) and 1.2 (TFW–WP BL), where the discrete wavelet packet transforms are performed for a chirp signal using different bases originating from the same seeding mother wavelet. In the figures, since the bases are orthonormal, all time-frequency windows do not overlap. As for the continuous wavelet transform, various time-frequency windows severely tangle with each others. And we generally do not show the actual sizes and shapes of various windows — rather, each window is represented by a point (or a small area depicting the time-frequency resolution) having coordinates corresponding to its centroids in the time and frequency axes.

- The function basis of the short time Fourier transform is the unique orthonormal Fourier basis comprised of sine and cosine functions; whereas, for wavelet transform, apart from the very loose constrain that the basis function (or the mother wavelet) satisfies the admissibility condition (for continuous wavelet transform) or stability condition (for discrete wavelet transform), there is virtually no restriction on the choice of basis functions. The coefficients of short time Fourier transform, which represent local Fourier spectral information, still have the exact meaning of "frequency". In wavelet transform, wavelet coefficients refer to specific scales rather than "frequencies". Here, we generally suffer from their physical interpretability due to the following reasons: (1) No unique basis — the analyzing function or mother wavelet can be designed in a plenty of ways, and the basis functions related to the mother wavelet can be either dependent or independent (orthogonal or non-orthogonal); (2) Scale does not have unit — together with the first point, it severely hampers out ability to directly perceive the wavelet's size and physical shape; and, (3) No fixed algorithm to implement wavelet transform — many techniques and various adaptations exist, such as, the treatment using flexible time-frequency windows for continuous wavelet transform, multi-voice [20] or multi-wavelet [18, 19, 74] frames, and discrete wavelet transform using different dilation factors other than the most often seen value of 2 [6]. Generally speaking,

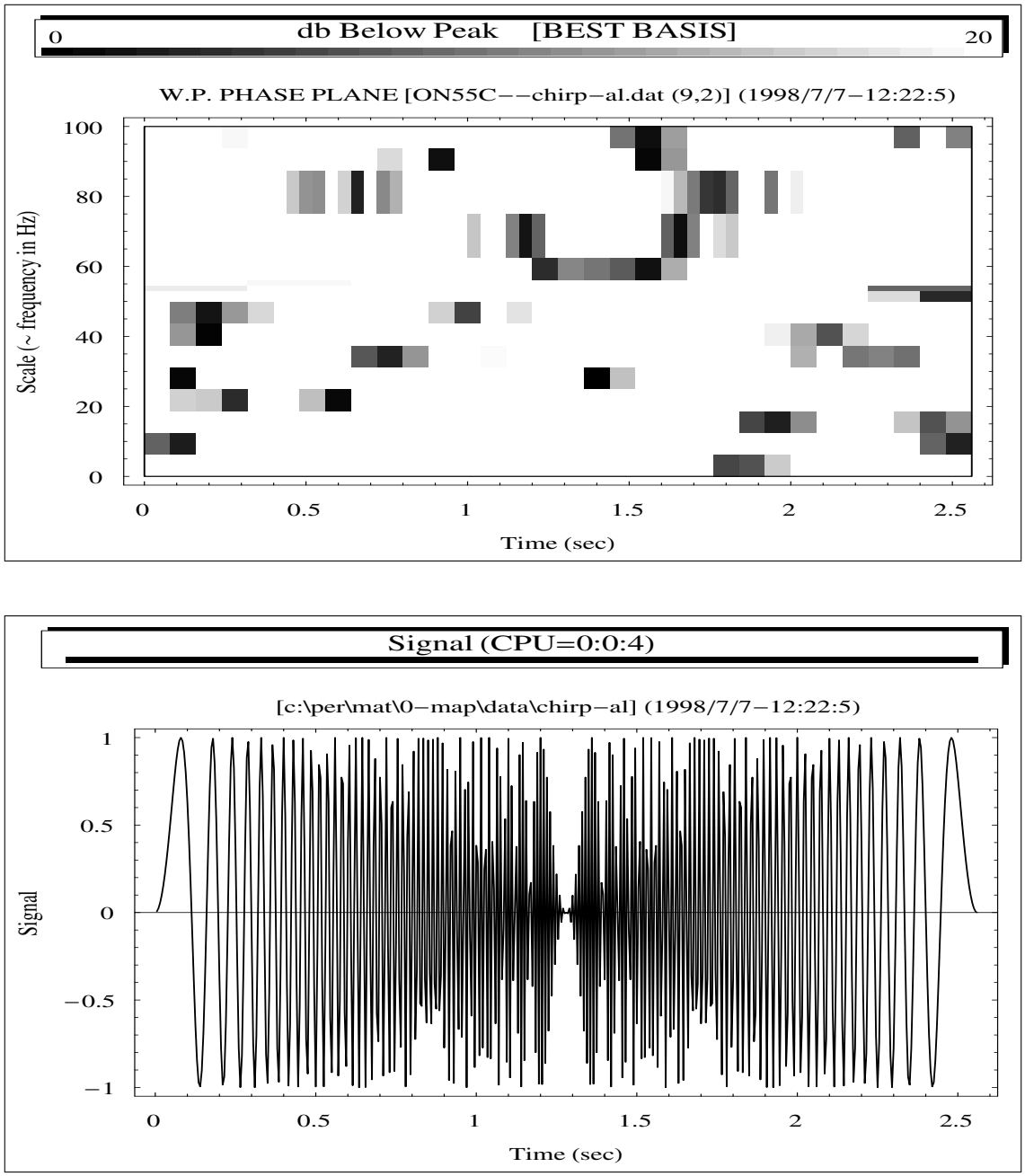

Fig 1.1 (TFW–WP BB) The time-frequency window distribution (or phase plane) of a wavelet packet's best basis (`top`) for a linear chirp signal that is sampled under an aliasing condition (thus the symmetric frequency distribution (`bottom`) is yielded). Here the wavelet packet is associated with a Coiflet of 30 convolution weights and the basis refers to the best basis rather than basis associated with the best level as to be shown in the next figure. The original signal, if not under-sampled, has linear instantaneous frequency distribution form 0 to 100 Hz in the full span of time. Note the non-symmetric distribution and and the scattering of windows. These phenomena reflect the composite frequency bands of a mother wavelet and inherent quarks that may arise, as well as the shift-non-invariant transform property.

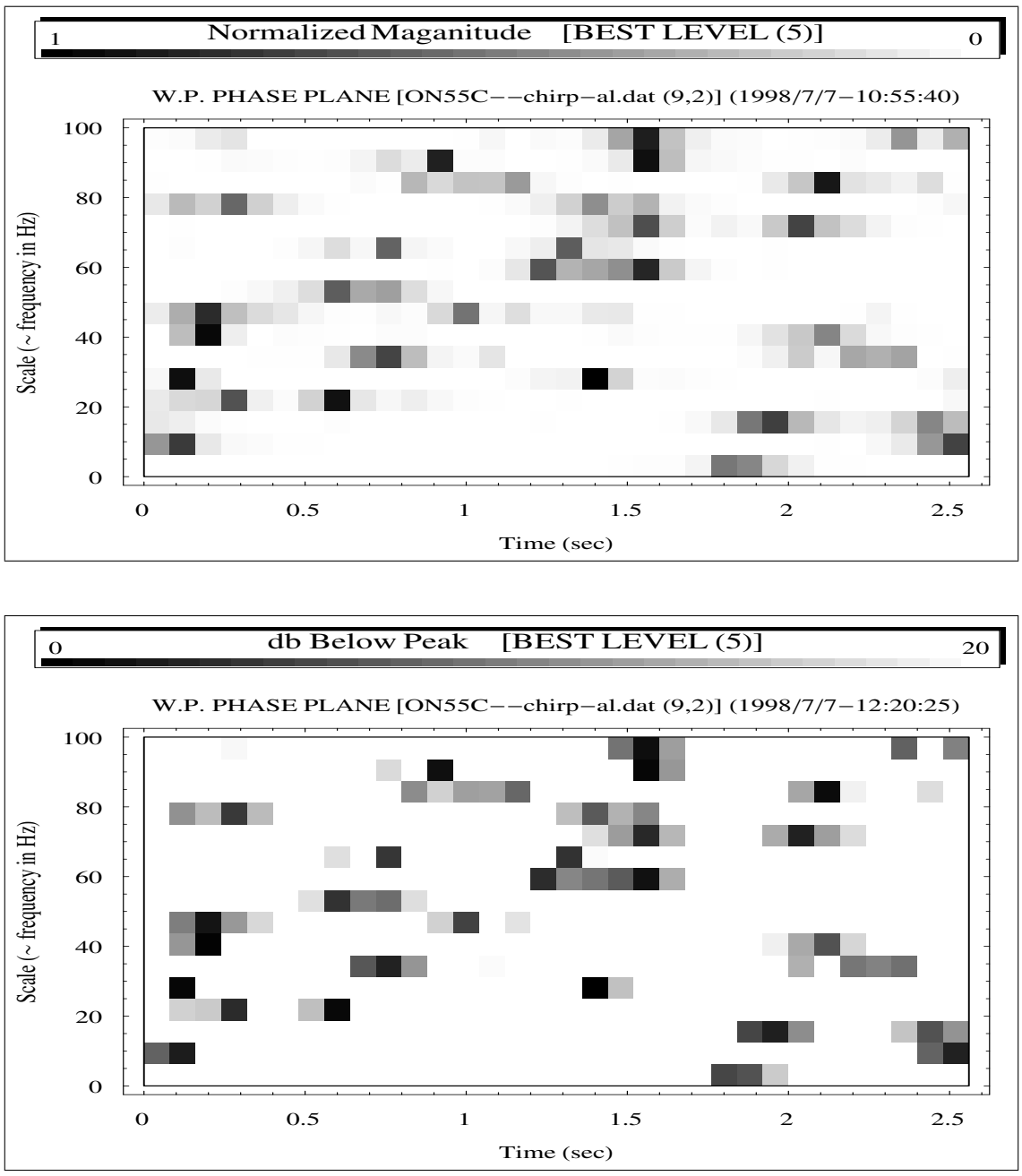

Fig 1.2 (TFW–WP BL) Choosing an appropriate wavelet basis is a dilemma to be resolved first; and the existence of the numerous quandaries of wavelet analyses shall be acknowledged foremost. Here are shown two different wavelet packet phase plane representations associated with the same Coiflet and the same aliasing signal as the preceding figure. The distributions are now based on wavelet packet's best level, which occurs at transform level 5 for such a signal. The top sub-figure is in logarithmic measure and the bottom is in linear measure. In view of the fact that a single orthonormal mother wavelet can yield many different wavelet representations, and the fact that there are basically infinitely many wavelet bases, as well as the fact that we may use different graphic renderings; we are easily trapped in the quandaries of wavelet analyses.

these varieties may not be as disturbing in certain application fields (such as data transmission or signal decomposition and reconstruction) as they are for our studies focusing on the water wave physics.

- We note that the present scope focuses on the $L^2(\mathbf{R})$ Banach space, i.e., the Hilbert space, since some of the statements here may not apply to other function spaces or classes [20, 55]. Nevertheless, most of the intricacies that differentiate different spaces are only of analytic interest up until now (e.g., on the existence of multiresolution analysis (MRA), on the regularity and differentiability of wavelets and its associated scaling functions). From the practical point of view, it is far enough to restrict to the Hilbert space, i.e., a space of functions with finite "energy" contents.

1.4 The scopes

There are basically infinitely many wavelet function bases to choose from for any data analysis and any application, whereas it is not uncommon to see that a particular wavelet is chosen while its usage specificity is not hinted at all. Thusly, the arising problems quite often exceed the problems they want to solve, and the provided results are shoddy and misleading in most cases or even erroneous in generalizations. Moreover, a mathematical existence does not always conciliate the nicety of reasonability and physicalness. And these are particularly true for wavelets' employment in our field focusing on physics of water waves.

The fundamental footing to use localized transforms in our water wave applications can be stated quite simply, as well as intuitively — if we perceive our signal as composed of waves which are limited both in life span and in spatial extent, i.e., constituent components are evolving with time and in space, then it is natural to adopt wavelet as our analyzing function basis. Furthermore, in addition to waves' modulation nature, if we also acknowledge, even for regular waves, that intrinsic instability due to nonliner effects may exist and that mutual interactions and boundary conditions are everywhere to

be observed, then it is still quite possible that, even for stationary signals, wavelet decomposition can provide better descriptions of physics than can the Fourier decomposition. Besides, another advantage of using wavelets is the possible flexibility in adapting their wave forms to our desires; this is related to the modifications of time-frequency windows for better physical implications.

In this study the subject matter can essentially be separated into a few independent, as well as intertwined, parts centering on the best wavelet for water waves; videlicet, the identification, the optimization, the vindication, the application, and an addendum of a wavelet extension, to wit a wavelet variant for refined ridge extraction and interesting physics. And their contents can basically further be divided sequentially into the following core constituents.

- First, we focus on the characterizations of various discrete wavelet basis categories. It is expected that the covered categories should be quite comprehensive — in the sense that they include all the extreme analytical properties in wavelet designs, as well as those in between. And it is the author's belief that if you ever find an individual wavelet you have great chance to assign it into one of these categories, and if not, you have great reason to say that its properties fall within (or between) the covered characterizations and thus its possible usefulness (or its fate) trammeled accordingly. The relevant characterizations and intrinsic properties for all the categories are extensively illustrated through the depictions of their mother and farther wavelets, the translations and dilations of wavelets, the zoom-ins or blowups of any kind of wavelets, and their the linear phase filtering features. Physical counterparts of analytical aspects are provided when possible.

- Second, we use entropy statistics to facilitate the identification of the optimal wavelet basis for water wave signals, and the signals are short wind waves from tank experiments. Herein broad and inclusive entropy criteria and probability distribution curves of transform coefficients are adopted for both the comprehensive wavelet

bases and the Fourier basis.

- Third, we investigate the mathematical factor of the wavelet bases that leads to the different statistical performances based on the entropy, in other words, what is the analytical essence of the wavelet function basis concerning its fitness in water wave simulation or its intimacy to the nature of water wave. And this is related to the study of the phase distribution of a wavelet characterizing function (the $m_0(\xi)$ to be described in a later chapter) for each individual basis.

- Fourth, we further identify the continuous counterpart wavelet of the optimum discrete basis, i.e., a continuous wavelet transform corresponding to the multiresolution analysis of the semi-orthogonal cardinal spline dual wavelet. Here we come up to why there is the need of a continuous transform both mathematically and physically; that is to say, what are the advantages and disadvantages of discrete and continuous wavelet transforms concerning their applications to water waves.

- Fifth, we address what can be done to improve the physical relevance between the basis functions in the continuous domain and the wave constituents of our signals. Here the topics include: the demand of better physics in modeling the energy phenomenon; the uncertainty relationship and the degrees of freedom for adaptivity; the physics of the "carrier frequency" and the time-frequency windows of flexible size and shape; and finally the proof of the existence of admissability condition under such an adaptation.

- Sixth, we make the comparisons between the wavelet coherences based upon the identified best wavelet and the spectral coherences based upon the Fourier basis. The absolute superiority of wavelet coherences is shown, and the reasons are delineated.

- Seventh, to serve as an example of possible applications of the best wavelet and its coherence approach, a model concerning the calming of waves due to rain will

be proposed first and explicated afterwards. The model concerns the interaction scales in the wind, wave and rain coupling system. It is an energy cascade model and involves two categories of mechanisms. One emphasizes the local mechanism within the air and aqueous boundary layers, especially on the role played by a match layer due to rain of interfacial aqueous flows. Another emphasizes the stratification-induced mechanism governing a large water body that shows the interactions among surface and internal waves and leads to rapid damping of waves.

- Eighth, we detail the experimentations, as well as the importance of the development of the real-time system for both experiment and analysis.

- Ninth, wave tank data, mainly of wave-current coherences, will be used to show the wavelet spectral trend of the coupling system concerning the interaction and evolution of scales in the wind, wave, and rain coupling system, hence, the physics of the energy cascade and the damping of surface waves.

- Tenth, a wavelet variant found by chance owing to a mistake in the coding process is investigated and its performances and characterizations are compared to those of the Morlet wavelet. Various simulation signals and experimentation water waves are used to check their serviceability and validate the comparisons. It is found that the wavelet variant is capable of furnishing distinguish features either from the modulus or the phase rendition of transform coefficients, as well as highlighting a few intrinsic physics of water wave, in particular, the modulation, the energy recurrence and the intrinsic instability nature.

1.5 Summary

In a compendious way, the study is to put forward an optimal wavelet basis that is both mathematically and physically right for water wave analyses and to prove it beyond doubt. Moreover, to serve as an example of possible applications of the identified best wavelet

basis and the relevant coherence approach, an energy cascade model is proposed. The model aims at the physics concerning the rapid damping of surface waves in the wind, wave and rain coupling system. Still, as an addendum of innovation by chance, a wavelet variant is proposed and shown to be with refined capability in ridge identification and in the extraction of certain physics. ❖

Chapter 2

The Wavelet Categories and Their Characterizations

2.1 Introduction

In almost all lab or model experiments various modeling or scaling laws can at best be partially satisfied, and the situation is further complicated for a multi-scale and multi-dimensional phenomenon in a multi-factor system.

In the introduction chapter we noted the problems of transient effects that attested to diversified scales. Moreover, for water wave experiments, it is acknowledgeable that there may exist significant distortions concerning the coupling mechanisms targeted. For example, a limitation in space and time in the tank, on the one hand, introduces the lack of scale diversification that may hinder the development of certain mechanisms and impose restrictions upon the evolutions of certain interactions; on the other hand, introduces serious boundary and initial conditions that may act as exploitations of factual considerations. With these understandings, as well as the cognizance regarding the inadequacy of the Fourier spectral approach in our applications as mentioned earlier, it is understandable that, if the modeling of the proposed physics is at all possible, the deployment of an optimized analyzing scheme using sensitive and appropriate basis functions is desired. Specifically speaking, we shall select among a broad array of functional bases the most appropriate one for our signals and describe the proper analyzing method. Akin to such

an attempt, it warrants to give more systematical descriptions of different properties of various categories of wavelet function bases.

Herein comprehensive categories of discrete wavelet are studied. Their comprehensiveness is essentially reflected by the inclusions of all the extreme and opposite analytical properties in wavelet designs. That is to say, the characterization of a particular wavelet not seen or not named here should fall between or within the basis properties covered here.

2.2 Program and workbench developments

The wavelet programming and all relevant numerical characterizations [79] were developed from the ground up using mainly the **Asyst** programming language. The programs not only cater comprehensive wavelet bases but also provide inclusive characterizations of their relevant functions and intrinsic properties. The code is written with the mind of being flexible, friendly, and versatile. Accuracy and error-free requisites are highly abided by. And it is espoused that keyboard strokes should be minimized and any manual input of original or intermediate data should not be allowed. In addition, several add-in programs and auxiliary applications are integrated. Overall, they mainly consist of the following.

- The Postfix language — The Postfix add-in to the **Asyst** core programming enables the real-time, as well as direct, generation of high quality Adobe Encapsulated Postscript figures. The process secures the proper labeling and correct legends. And it is confidently guaranteed that the statements or analyses deriving from the figures make no mistakes. Besides, the automation exceeds the condition that the generation of quality figures as many as one wishes is surely possible, and that the elimination of the painful task of plotting seemly countless figures when making parametric alterations or test cases is certainly true. Using a commercial graphical application software can never archive such functionalities, moreover, it is basically

error-prone.

- The on-screen real time display of PCX format figures — The Encapsulated Postscript figures are mainly for quality printing and created in the background. A real-time and interactive monitor display is desirable and essential. This should greatly enhance the debugging efficiency and make possible the writing of a huge and complex code that is user-friendly, easy to maintain, as well as flexible, interactive and accurate.

- The data spreadsheet interface — The output or input of data to or from the Excel or Lotus-123 compatible worksheets is integrated. In cases that articulated or complex figures are desired or post-processing and supplementary analysis are needed such an interface is readily convenient and trouble free.

- The **Mathematica** programming language — This coding is mainly for the streamlined generation of various high quality graphical renditions for the two-dimensional or three-dimensional time-scale data, such as the modulus and phase information derived from the **Asyst** programs. There is no manual intervention when commuting between the **Asyst** outputs and the **Mathematica** inputs.

- The LaTeXmacros and packages — In addition to the utilization of various existing LaTeXpackages, a vast amount of LaTeXcodes and macros were also written for the following purposes: the systematic displays and printouts of voluminous all sorts of figures for analyzing, reasoning, and comparing; the pleasant listings of codes for the comfort of eyes and the easy debugging; the nonchalant production of printouts, papers, reports, etc. for proof-reading and archiving; the facilitation for efficient management and pain-free integration among different case studies.

- The **WinEdt** macro programming language — The language is specifically used to develop a non-fallible workbench. Hundreds of these macros were written and integrated. The workbench provides a working platform or shell environment for

writing the codes of various programming languages, as well as provide various add-on operations, such as file management, various format operations, code compiling, cloud backups (these were developed in the `Windows 2000` or pre `XP` era when handsets and cloud concept were unfamiliar to the general public), etc. Lots of attention were paid to the accomplishment of an environment that is pleasant, efficient, easy and safe. With this workbench all the code pieces, subroutines, and component files are managed and displayed in a way of being scientific, organized and reflexive. Moreover, various tasks can be integrated and streamlined. Without such a workbench the editing and debugging, as well as the whole work, must be extremely painful and exhausting and the present study is surely inconceivable.

2.3 Wavelet basis categories

The Riesz wavelet bases tested here can basically be divided into four categories: orthonormal (ON), semi-orthogonal (SO), bi-orthogonal (BO), and orthonormal wavelet packets bases. For the orthonormal category it is divided into several different subgroups: Daubechies wavelets (both the most and least asymmetric), Coiflets, Meyer wavelet, and Battle-Lemarié wavelets.

No detail accounts of these wavelets will be given; only the main criteria and core features of each categories will be briefed. Let first state the related notations and conventions needed for the context that follows. Let a function or a signal be denoted by $f(t)$; the two-scale scaling function of a Riesz basis be $\phi(t)$; the associate mother wavelet be $\psi(t)$ and its dyadic wavelets be $\psi_{j,k}(t) = \sqrt{2^j}\,\psi(2^j t - k)$, where $j, k \in \mathbf{Z}$ and k stands for translation and j for dilation. The concept of translations and dilations are illustrated in figures 2.1 (Wavelet T&D-1) through 2.6 (Wavelet T&D-6).

The space V_j (formed by $\psi_{j,k}$, $k \in \mathbf{Z}$ for a given j) in the multiresolution ladder are nested in $\cdots \subset V_{-1} \subset V_0 \subset V_1 \cdots$, and the finest and the coarsest scale space, say, for a 1024-point signal, are V_{10} and V_0, respectively; the number of filter coefficients or

the number of convolution weights be N if the associated wavelet is finitely supported (support length equals to $N-1$); the dual wavelet and dual scaling function, if exist, be $\widetilde{\psi}(t)$ and $\widetilde{\phi}(t)$; the inner product be $\langle \cdot, \cdot \rangle$; and the Kronecker delta be $\delta_{j,k}$, $j, k \in \mathbf{Z}$, which is equal to 0 for $j \neq k$ and 1 for $j = k$.

Up until now, all practical wavelets of discrete transform are associated with the theory of multiresolution analysis (MRA) [4, 20, 48, 50]. For Riesz wavelets there always exist dual wavelets except for orthonormal wavelets, which are self-dual. Any discrete wavelet transform involves two convolution operations: one yields detail information; another yields smooth information [62]. Convolutions can either be implemented in a direct way in the time domain for compactly supported wavelets or in an indirect way in the frequency domain. We list the basic properties (restricted to real-valued wavelets) and give the symbols of representation for various categories and subgroups as follows.

2.4 Orthonormal wavelets

The orthonormal wavelets covered here include the following categories: Daubechies most compactly supported wavelets (denoted as ONxxA); Daubechies least asymmetric wavelets (ONxxS); Coiflets (ONxxC); Meyer wavelet (Meyer); Battle and Lemarié wavelet (B&L). Here in all the subsequent annotation x is an integer related to support length (physically, the span of mother wavelet curve).

$$\psi = \widetilde{\psi}, \tag{2.1}$$

$$\phi = \widetilde{\phi}, \tag{2.2}$$

$$\langle \psi_{j,k}, \widetilde{\psi}_{l,m} \rangle = \delta_{j,l}\delta_{k,m}, \tag{2.3}$$

$$f(t) = \sum_{j,k} \langle f, \psi_{j,k} \rangle \psi_{j,k}, \tag{2.4}$$

One MRA ladder (single set of frame bounds),

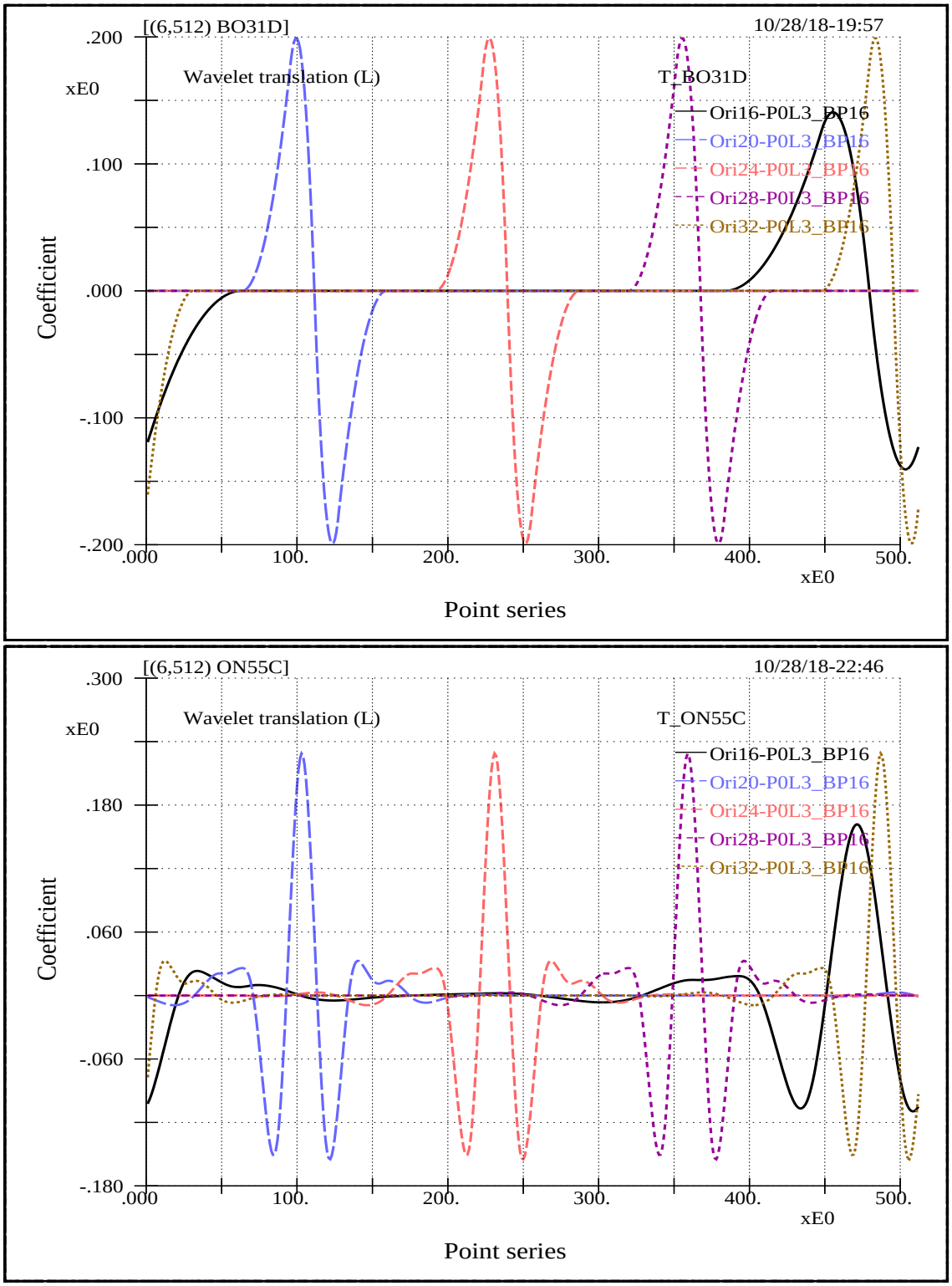

Fig 2.1 (Wavelet T&D-1) Wavelet's time-scale constructs – The time-scale concept of wavelet analysis is associated with two variables, i.e., the translation and the dilation. Here the concept of translation and dilation on the scales of transform level 3 is shown for two different wavelets (BO31D `(top)` and ON55C `(bottom)`). Individual curves are the inverse transforms of unit value at points 16, 20, 24, 28, and 32 that are situated upon level 3.

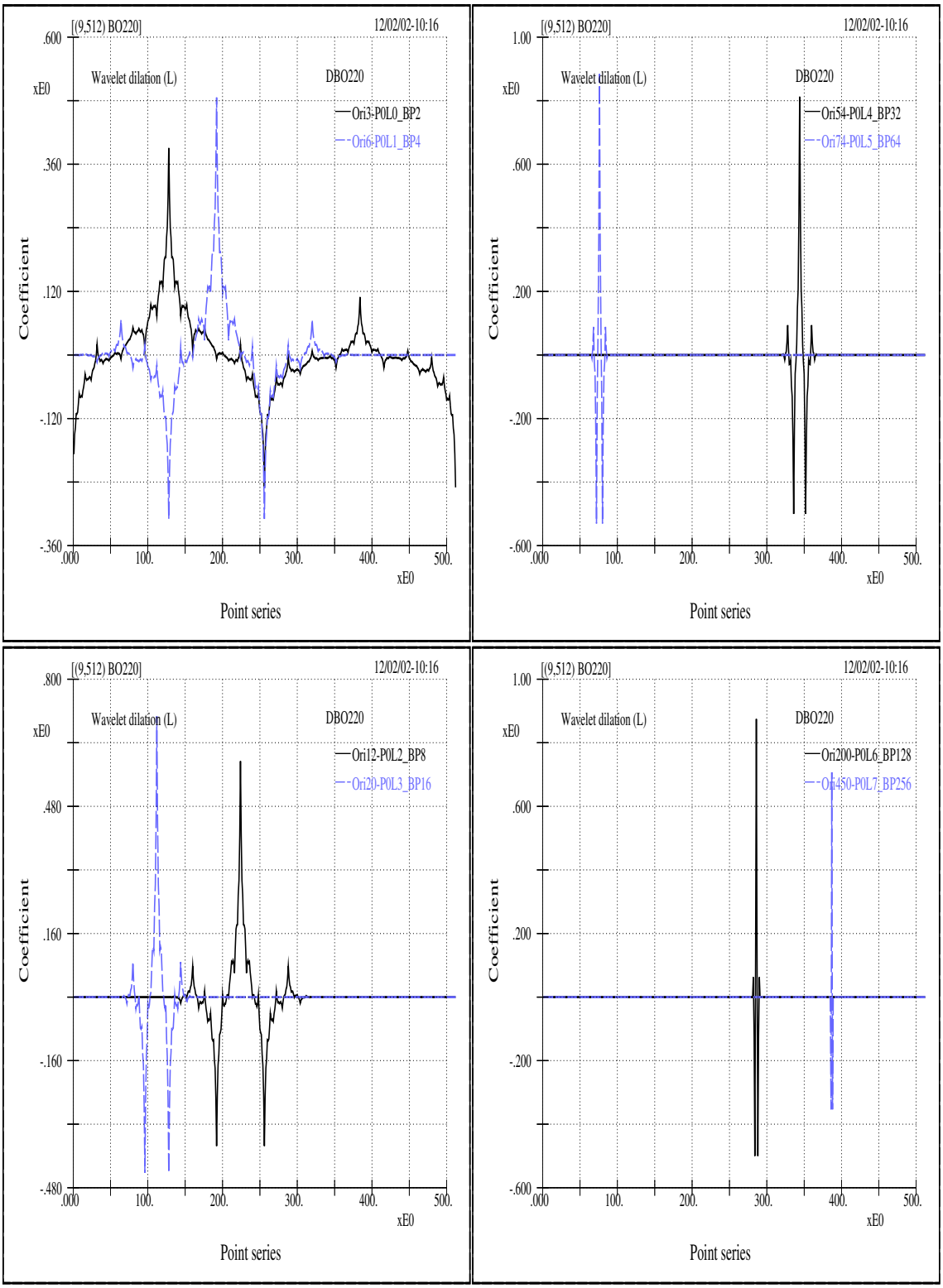

Fig 2.2 (Wavelet T&D-2) Wavelet's time-scale constructs for a bi-orthogonal wavelet – Here the concept of dilation and the fractal nature across scales of wavelet are shown for scales from transform level 0 to level 7 for the BO22O wavelet. Each curve corresponds to an individual scale and specific location as labeled in the sub-figures.

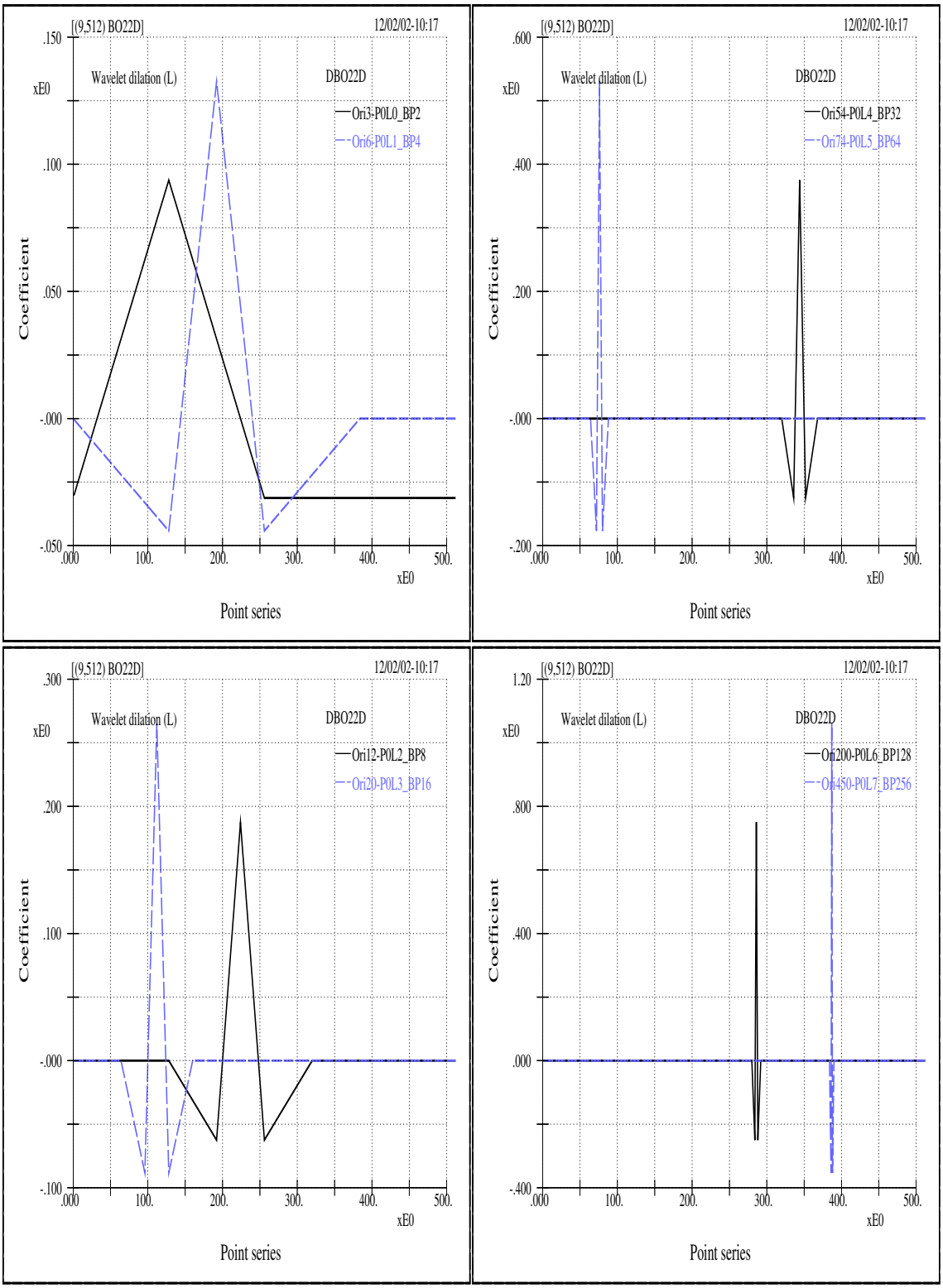

Fig 2.3 (Wavelet T&D-3) The fractal nature across scales of the dual wavelet (BO22D) and its dilation constructs are shown here. The dual wavelet refers to the wavelet used in the preceding figure (BO22O). Each wavelet curve corresponds to an individual scale (from scale level 0 to level 7) and its specific translation location as labeled in individual sub-figure.

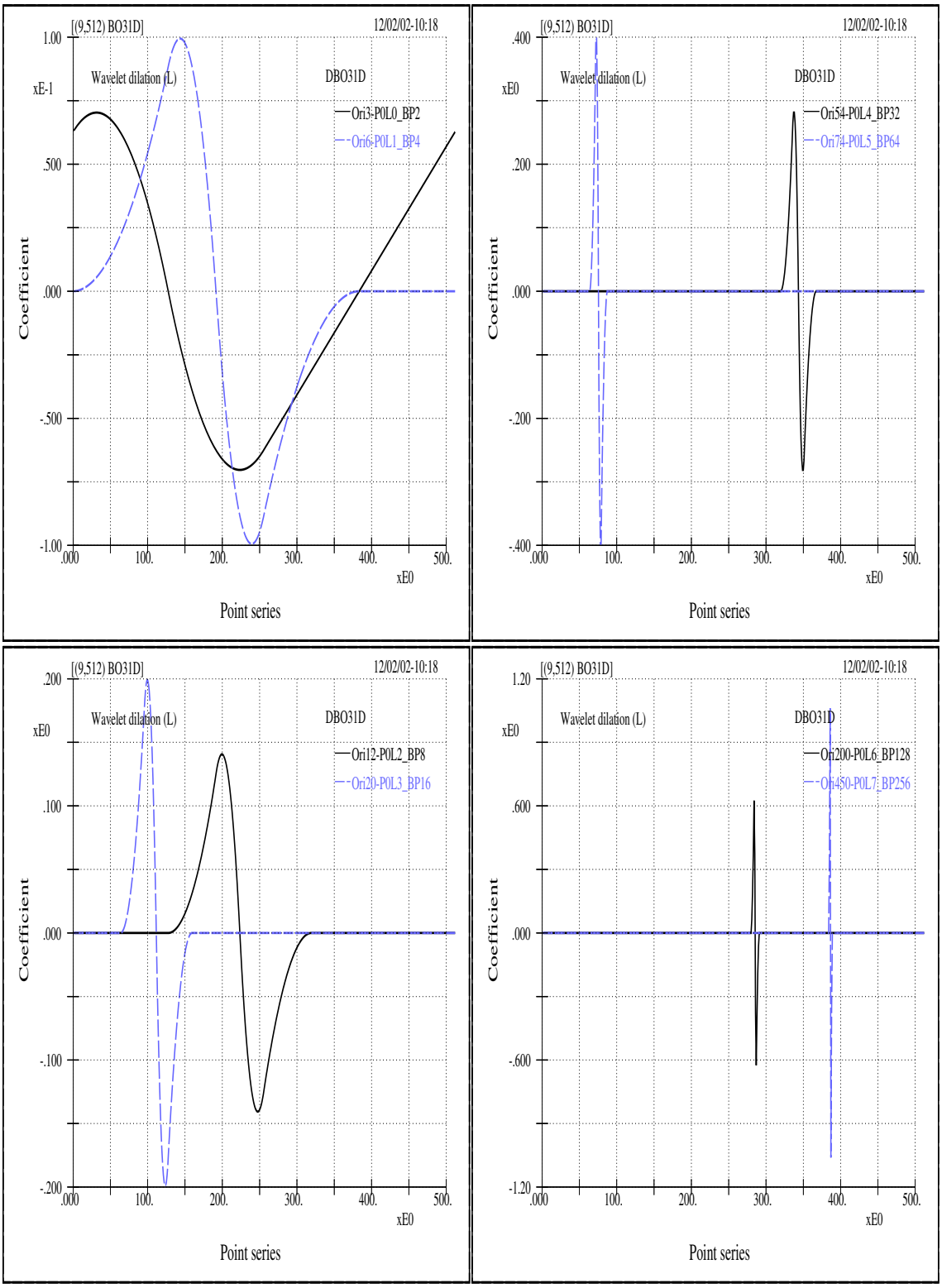

Fig 2.4 (Wavelet T&D-4) The wavelet dilation concept and smoothly fractal nature from scale level 0 to level 7 for the dual BO31D wavelet. Each wavelet curve corresponds to an individual scale and its specific time location as labeled in individual sub-figure.

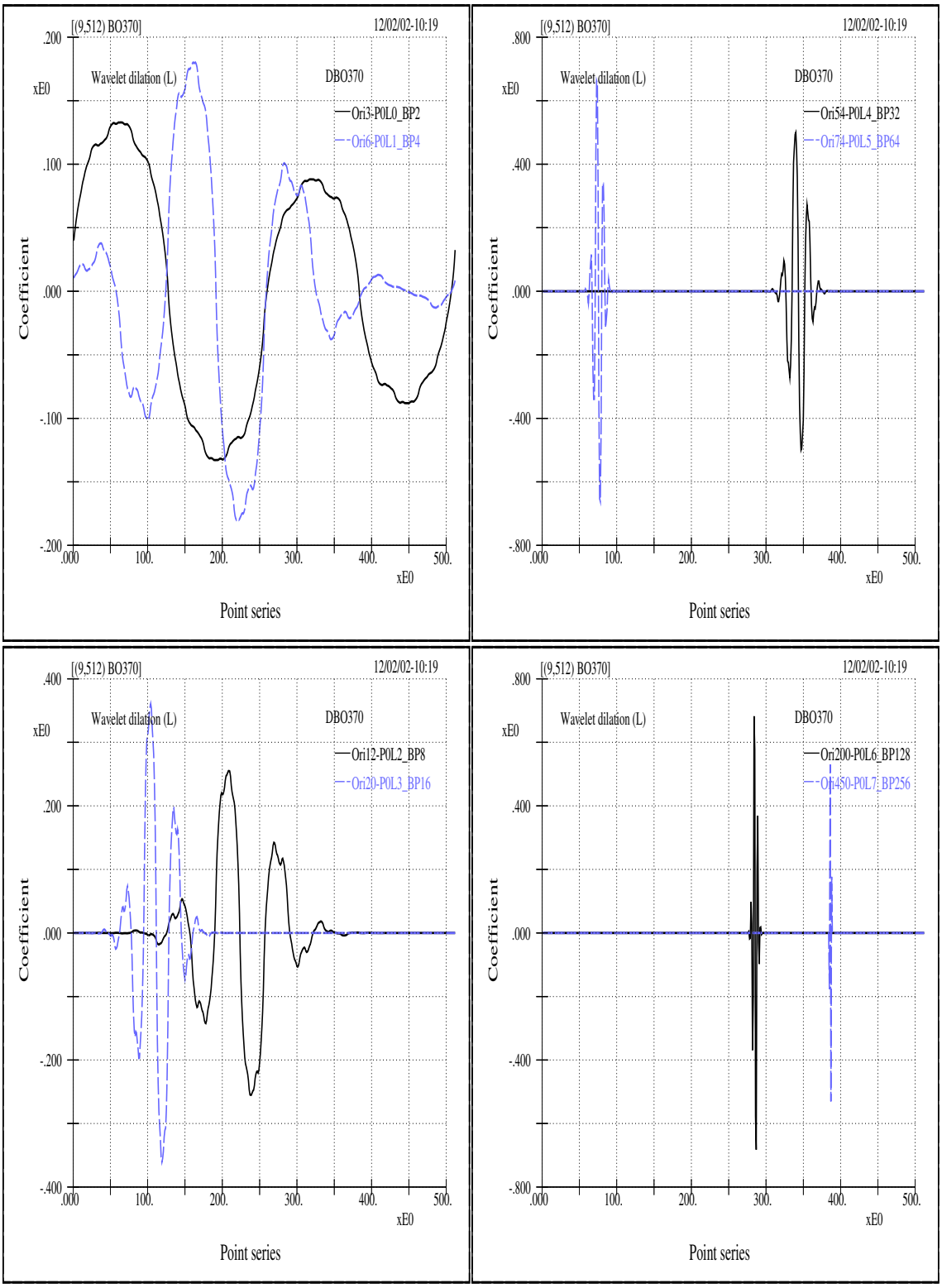

Fig 2.5 (Wavelet T&D-5) The wavelet dilation concept and the fractal nature from scale level 0 to level 7 for the BO370 wavelet. Each wavelet curve corresponds to an individual scale and its specific time location as labeled in individual subfigure.

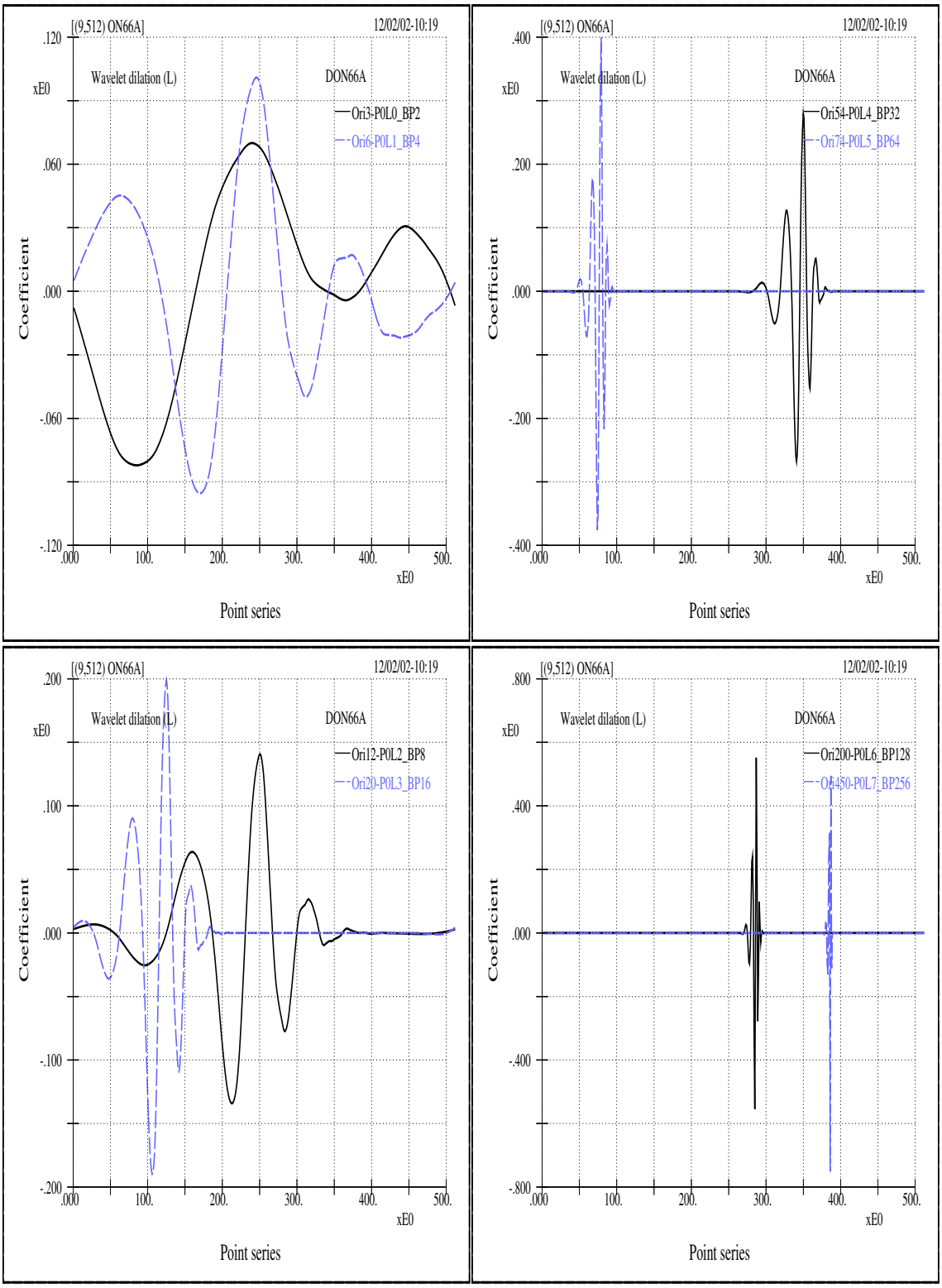

Fig 2.6 (Wavelet T&D-6) The wavelet dilation concept and the fractal nature for the ON66A wavelet, which belongs to the most asymmetric category. Each wavelet curve corresponds to an individual scale (from level 0 to level 7) and its specific time location as labeled in individual sub-figure.

One filter pair (one smooth and one detail).

2.4.1 Daubechies most compactly supported wavelets (ONxxA)

The wavelets in this group have maximum number of vanishing moments for given compatible support width. Or stated otherwise, they are the most compactly supported wavelets for given compatible number of vanishing moments. The famous most compactly supported continuously distributed wavelet belongs to this group and has only four filter coefficients. These wavelets are quite asymmetry (so, the "A" in ONxxA). The mother and farther wavelets for the group corresponding to the originating points of 12 (boundary point based on level 2) and 6 (boundary point based on level 3), respectively, for this group are shown in figures 2.7 (MW–ONxxA) and 2.8 (FW–ONxxA). The vanishing moments and the number of filter coefficients are, respectively,

$$\int_{-\infty}^{\infty} t^l \psi(t) dt = 0, \quad l = 0, 1, \cdots, x, \tag{2.5}$$

$$N = 2x, \tag{2.6}$$

where x is the integer number in ONxxA. The minimum number of x is 2.

2.4.2 Daubechies least asymmetric wavelets (ONxxS)

For a given support width, these wavelets, in contrast to those of the ONxxA subgroup, are the most symmetric ones (so, the "S" in ONxxS, but still not symmetric). They have the same representations of vanishing moments and number of filter coefficients as those of ONxxA. But the known minimum number of x is 4. The mother and farther wavelets for this group corresponding to the same originating points as the previous ones are shown in figures 2.9 (MW–ONxxS) and 2.10 (FW–ONxxS).

2.4.3 Coiflets (ONxxC)

The Coiflets have vanishing moments for both ψ and ϕ; therefore, from Taylor expansion point of views [20], they have high compressibility for fine detail information (i.e., a great portion of the fine scale wavelet coefficients are relatively small); and henceforth, they have simple quadrature rule to calculate the fine smooth information (i.e., the calculation of the inner product of a function and the fine-scale scaling functions is more efficient). Since every discrete wavelet transform involves both smoothing and detailing operations, there may exist some advantages from these two properties for certain applications such as applications that do not stress lossless of signal contents or perfect reconstructions [18, 75]. Their vanishing moments and number of filter coefficients are

$$\int_{-\infty}^{\infty} t^l \psi(t) dt = 0, \quad l = 0, 1, \cdots, x, \tag{2.7}$$

$$\int_{-\infty}^{\infty} \phi(t) dt = 1, \tag{2.8}$$

$$\int_{-\infty}^{\infty} t^l \phi(t) dt = 0, \quad l = 1, \cdots, x, \tag{2.9}$$

$$N = 6x. \tag{2.10}$$

For this group the mother and farther wavelets are shown in figures 2.11 (MW–ONxxC) and 2.12 (FW–ONxxC).

2.4.4 Meyer wavelet (Meyer)

The Meyer wavelet (denoted as Meyer or ME in figures) is the wavelet with most compact support in frequency domain (here, if without any specific assignment, "finitely supported" refers to time domain). Therefore, due to contrast properties between the two Fourier domains, the wavelet is infinitely differentiable in time domain, i.e., has an infinite Lipschitz regularity C^{∞} and does not have exponential decay. And the support length $N \to \infty$. The associated mother and farther wavelets corresponding to the same

originating points are shown in figure 2.13 (MFW–Meyer).

2.4.5 Battle and Lemarié wavelet (B&L)

The Battle and Lemarié wavelet (denoted as B&L or LE in figures) of m^{th} order is constructed from the orthonormal scaling function derived by applying the standard orthonormalization trick to the m^{th} order cardinal B-spline N_m [8, 1]. For $m = 1$, it is exactly the Haar wavelet. The latter is the only finitely supported wavelet in this group (also the case of BO11O=BO11D to be mentioned below) and is also a non-continuously distributed wavelet with the most compact support. All other wavelets in this group are infinitely supported. These wavelets have an exponential decay and possess C^{m-2} regularity. The mother and farther wavelets for the Battle-Lemarié wavelet are shown in figure 2.14 (MFW–B&L). Compared to the curves of Meyer wavelet (figure 2.13 (MFW–Meyer)), they look quite identical even though their constructions, or derivations, or formula involved (including Lipschitz regularity and decay property) are completely different.

2.5 Semi-orthogonal wavelets (SOxO and SOxD)

The semi-orthogonal wavelets are inter-scale, but not inner-scale, orthogonal. Their scaling functions are cardinal B-spline N_m and have finite two-scale relations. Although there are two distinctive (independent) filter pairs (one for the decomposition and the other for the reconstruction), there is only one MRA V_j-ladder. It was shown by Chui [1, 2] that the cardinal B-spline wavelet of an order higher than $m = 3$ is almost a modulated Gaussian (but a modulated Gaussian is not a wavelet). Therefore only the fourth order Cubic B-spline wavelet ($m = 4$) is tested. It has the following characterizations.

$$\psi \neq \widetilde{\psi}, \tag{2.11}$$

$$\phi = \widetilde{\phi}, \tag{2.12}$$

$$\langle \psi_{j,k}, \psi_{l,m} \rangle = \langle \widetilde{\psi}_{j,k}, \widetilde{\psi}_{l,m} \rangle = \delta_{j,l}, \tag{2.13}$$

$$f(t) = \sum_{j,k} \langle f, \psi_{j,k} \rangle \widetilde{\psi}_{j,k} = \sum_{j,k} \langle f, \widetilde{\psi}_{j,k} \rangle \psi_{j,k}, \tag{2.14}$$

$$N = 3x - 1 \quad \text{for SO}x\text{D}, \tag{2.15}$$

$$N \to \infty \quad \text{for SO}x\text{O}. \tag{2.16}$$

One MRA ladder ,

Two filter pairs ,

The mother and farther wavelets of the fourth order and the associated dual wavelets are shown in figures 2.15 (MFW–SO0) and 2.16 (MFW–SOD).

2.6 Bi-orthogonal wavelets (BO$x\,y$O and BO$x\,y$D)

The wavelets in this category are constructed also by Daubechies, and are sometimes called non-orthogonal wavelets. As is well known all real-valued orthonormal compactly supported wavelets, except the Haar wavelet, are not symmetrical. However, from the point of view of reconstructing a signal from its partially truncated wavelet coefficients, the symmetry is a desired property of the filter when a more natural perception or smoother variations is important. There is a very practical implication here: if non-symmetrical function bases are used, then a small change in the wave form causes significant variations of scale information. In other words, to have minor impacts to the data analysis, it is desirable to have bases as symmetrical as possible. Moreover, when considering that random errors, or noise, or uncontrolled factors are present, we should be able to comprehend the significance of this property. In fact many of the figures given in this study indicate such a feature. The symmetry can be achieved by sacrificing orthogonality; if this is the case one has dual pairs for both wavelets and scaling functions. It is obvious that conditions for semi-orthogonal cases are more general than those of orthogonal ones,

and the bi-orthogonal cases are even more general. This situation is clearly indicated by the additional freedom of dual scaling function, as is reflected by the two parameters x and y in the notations of BOxyO and BOxyD. Nevertheless, the wavelets in this category involve only one pair of independent filters for both decomposition and reconstruction even though there involve two different MRA ladders that are associated with their own individual sets of Riesz bounds. This is quite opposite to the case of semi-orthogonal wavelets where they involve one MRA ladder but with two filter pairs.

$$\psi \neq \widetilde{\psi}, \tag{2.17}$$

$$\phi \neq \widetilde{\phi}, \tag{2.18}$$

$$\langle \psi_{j,k}, \widetilde{\psi}_{l,m} \rangle = \langle \phi_{j,k}, \widetilde{\phi}_{l,m} \rangle = \delta_{j,l}\delta_{k,m}, \tag{2.19}$$

$$f(t) = \sum_{j,k} \langle f, \psi_{j,k} \rangle \widetilde{\psi}_{j,k} = \sum_{j,k} \langle f, \widetilde{\psi}_{j,k} \rangle \psi_{j,k}, \tag{2.20}$$

$$N = 2y + x - 1 \quad \text{for BO}xy\text{O and } x \text{ odd}, \tag{2.21}$$

$$N = 2y + x - 2 \quad \text{for BO}xy\text{O and } x \text{ even}, \tag{2.22}$$

$$N = 2y + x - 1 \quad \text{for BO}xy\text{D and } y \text{ odd}, \tag{2.23}$$

$$N = 2y + x - 2 \quad \text{for BO}xy\text{D and } y \text{ even}. \tag{2.24}$$

Two MRA ladders,

One filter pair,

The mother and farther wavelets for this group and the associated dual wavelets are shown in figures 2.17 (MW–BOxy0) through 2.20 (FW–BOxyD).

2.7 Wavelet packets

The wavelet coefficients derived from an orthonormal wavelet decomposition can be further decomposed by using either the set of filter coefficients (called two-scale sequence in Chui [1]) associated with the original wavelet, or different sets of filter coefficients associated with other orthonormal wavelets. Therefore, basically there can be infinitely many wavelet packet decompositions. These further decompositions are of a tree-like refinement process and are called the wavelet packet transform. The wavelet packet coefficients give better frequency resolutions with longer time supports. There are no simple formulas to describe the tree-like decompositions, but a schematic plot help elucidate the mechanism shown in figure 2.21 (WP Tree). The branch patterns and the number of branches can be chosen in any way so long as there is no repeat occurrences within any column under the stretch of the coefficients. That is to say, any column, wide or narrow, must have one and only one contribution from all levels (rows). Due to the tree-like process the computational works are dramatically increased.

Figure 2.22 (WP forms) depicts the wave forms of two wavelet packets based upon ON22A and associated with the same location point 100 at different scale levels 2 and 5. It demonstrates the typical bundled shape of distribution of wavelet packets as compared to wavelet.

For this category we have two criteria for selecting our best basis. One is still called the "best basis"; another "best level basis". Take for example, for a 1024-point signal, the finest level occurs at $j = \log_2 1024 = 10$ and there are 2^{10} different choices of bases. And within these 2^{10} choices the one which yields the minimum entropy is called the "best basis". And if we enforce the restriction that all wavelet packets be at the same level j, then we have 10 levels (0 to 9) to choose from; the level that yields minimum entropy is called best level basis. The indexes of a wavelet packet coefficient, i.e., the subscript and superscript of U labeled in the figure determine the time of occurrence of that coefficient and also associated support length and frequency resolution, i.e. the resolution, i.e., the

shape and location of the coefficient's time-frequency window within the phase plane. Concepts regarding the wavelet packet transform can be seen in figure 1.1 (TFW–WP BB). Again we also see the effects of non-symmetrical filtering. One specific feature is that the areas of all individual windows are all equal.

2.8 Wavelet nature and implications

Wavelets are fractal in nature, that is to say, no matter how detail we zoom into the wavelet curve its blowups all show similar characterization, and this is related to the wavelet differentiability, regularity, support length, and decaying property.

The **Asyst** program is written to be able to blow any wavelet constructions, such as mother and father wavelets, wavelet bases and wavelet packet bases at any point on any level. A few examples are shown in figures 2.23 (BU–BO2yO) to 2.30 (BU–BO35O).

Her we note that wavelets with fancy analytical properties are often of bizarre wave forms and not of our choice for studying water wave related physics — either judging from they entropy values to be given in the following chapter or form their stability conditions.

Moreover, this blowup exercise hints the behaviors of several numerical and theoretical aspects of wavelet analysis, such as the edge effects, the possible differences of function curves due to finite resolution, and the convergent or error propagation property.

Figures 2.29 (BU–BO31O) and 2.30 (BU–BO35O) show the blow-ups of bi-orthogonal wavelet BO31O and BO35O, respectively. Relevant data for BO31O is: Origin of wavelet curve: level 2, position 12 (i.e., element U_2^{12} in figure 2.21 (WP Tree)); Blow-up point: 150; data length: 512. Each sub-figure shows successive blow-up scale of 2^6. Here the blow-ups diverge rapidly, i.e., the wavelet fails to identify itself numerically in the refinement cascade. Relevant data for BO35O is: Origin of wavelet curve: level 2, position 12 (i.e., element U_2^{12} in figure 2.21 (WP Tree)); Blow-up point: 225; data length: 512. Each sub-figure shows successive blow-up scale of 2^6. Here the blow-ups converge but go with peculiar inclinations. Figure 2.28 (BU–WP-ON) also exhibits the grouping or bundling tendency, as

well as the fractal behavior, of wavelet packets. A few more specific or intrinsic properties and their implications might be noted in the legends of individual figures.

2.9 Summary

The purpose of this chapter is to give an idea of the comprehensiveness of the wavelet categories covered here and to provide the basic understanding of wavelet intrinsic properties as well as their possible implications in applications for water waves. It is hoped that these numerous figures suffice the robustness of the study. ❖

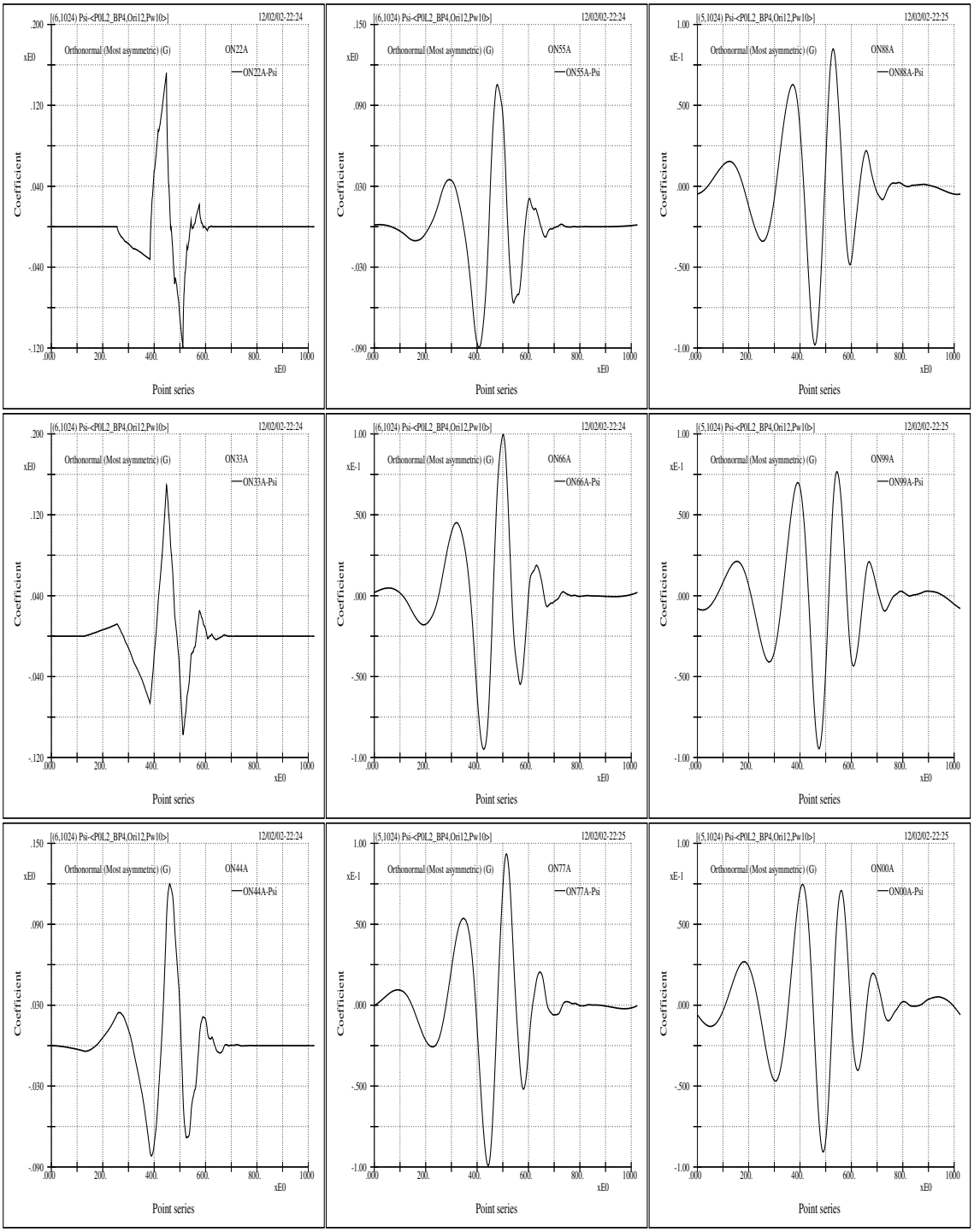

Fig 2.7 (MW–ONxxA) Any discrete wavelet transform is inherently associated with the pairing of a mother wavelet and a father wavelet (conventionally denoted as ψ and ϕ respectively). Such a pairing also links to the union of the constructs of "detail information" and "smooth information". Here the mother wavelets of the most asymmetric orthonormal group ONxxA are shown. These curves are the inverse transforms of a unit value located at point 12 for a 1024-point data. They are the constructs of the "detail information". It is noted that the "detail information" for these sub-figures is associated with a level greater than 3. That is to say the separation point between "smooth information" and "detail information" is located at point 8.

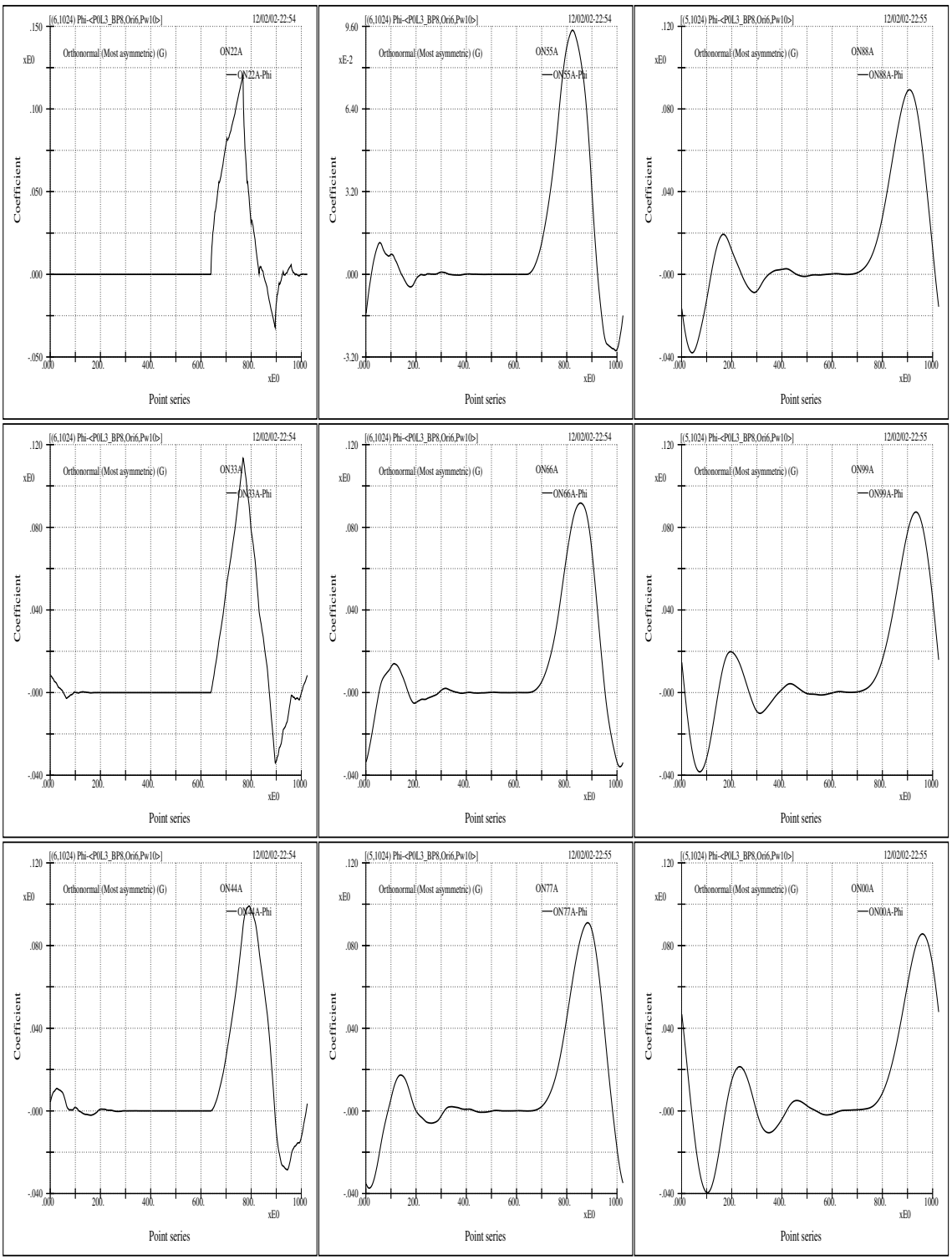

Fig 2.8 (FW–ONxxA) Here the father wavelets of the most asymmetric orthonormal group ONxxA are shown. They are the constructs of the "smooth information" corresponding to the "detail information" shown in the previous figure. These curves are the inverse transforms of a unit value located at point 6 for a 1024-point data. It is noted that the "smooth information" for these sub-figures is associated with a level less than or equal to 3. Again, the separation point between "smooth information" and "detail information" is located at point 8.

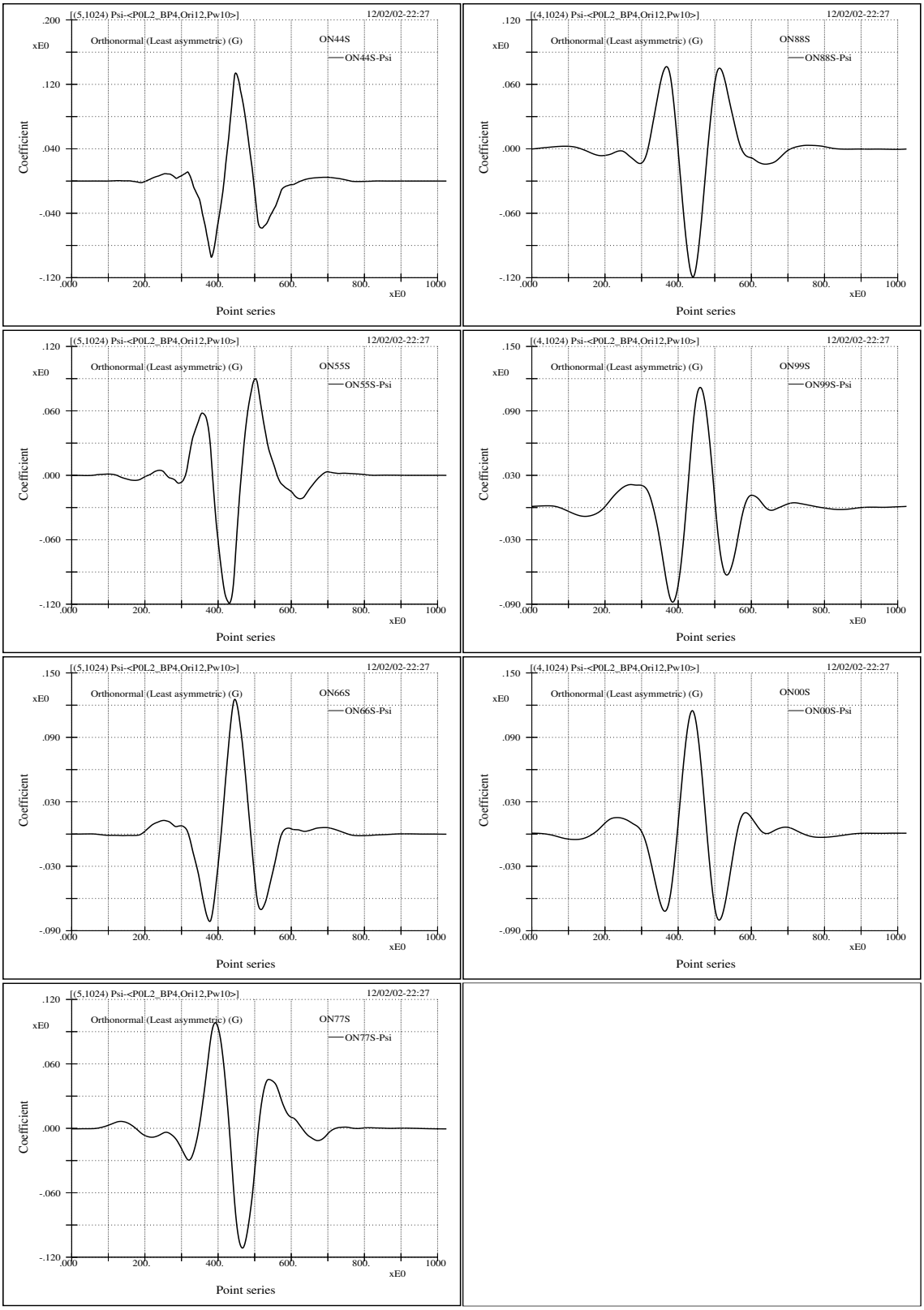

Fig 2.9 (MW–ONxxS) The mother wavelets of the most symmetric orthonormal wavelet group ONxxS are shown here. Each curve is the inverse transform of a unit value located at point 12 (at a scale level greater than 3) for a 1024-point data. Again, the separation point between "smooth information" and "detail information" is chosen at point 8.

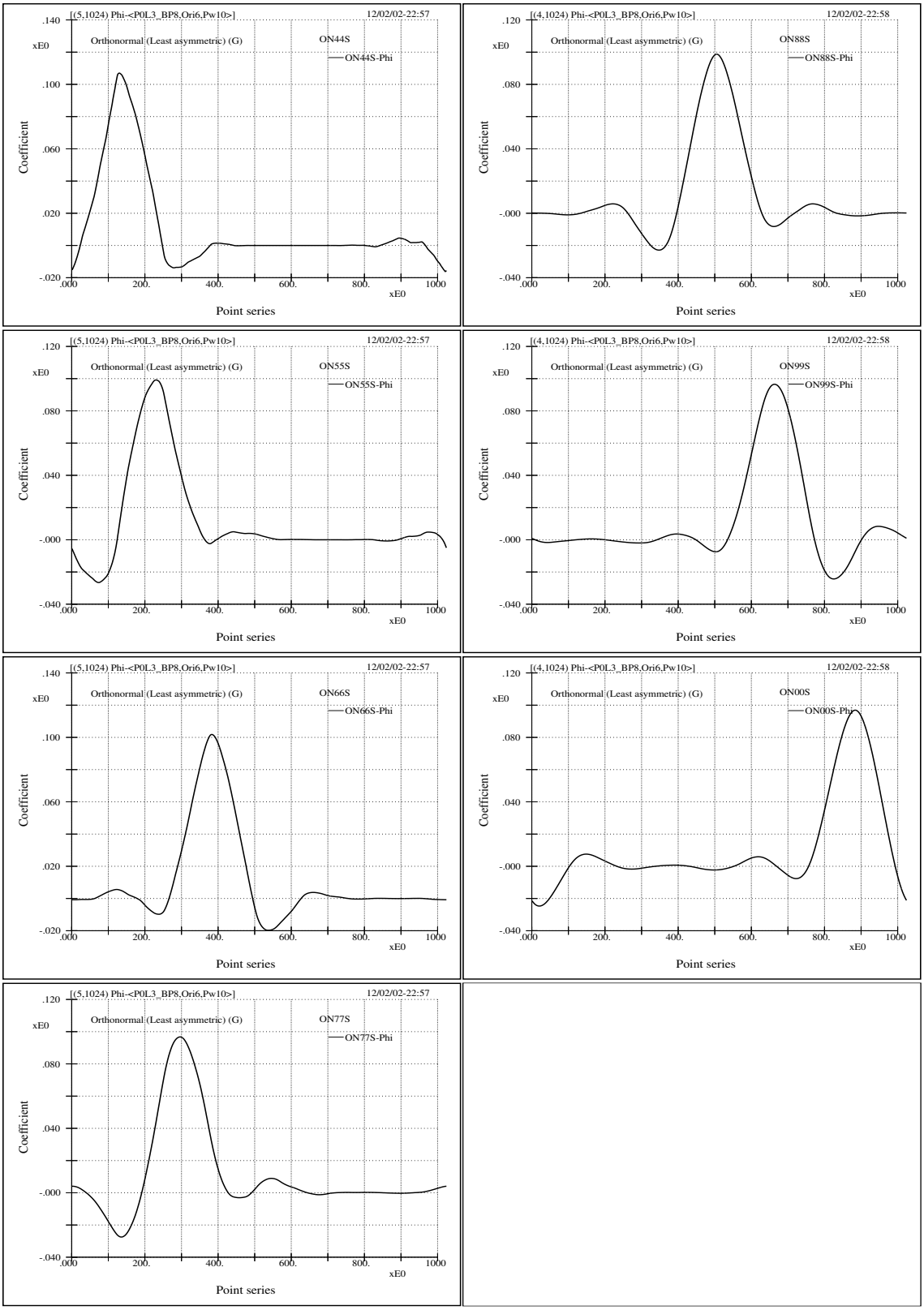

Fig 2.10 (FW–ONxxS) The father wavelets of the most symmetric orthonormal wavelet group ONxxS are shown here. Each curve is the inverse transform of a unit value located at point 6 (at a scale level less than or equal to 3) for a 1024-point data. Again, the separation point between "smooth information" and "detail information" is chosen at point 8.

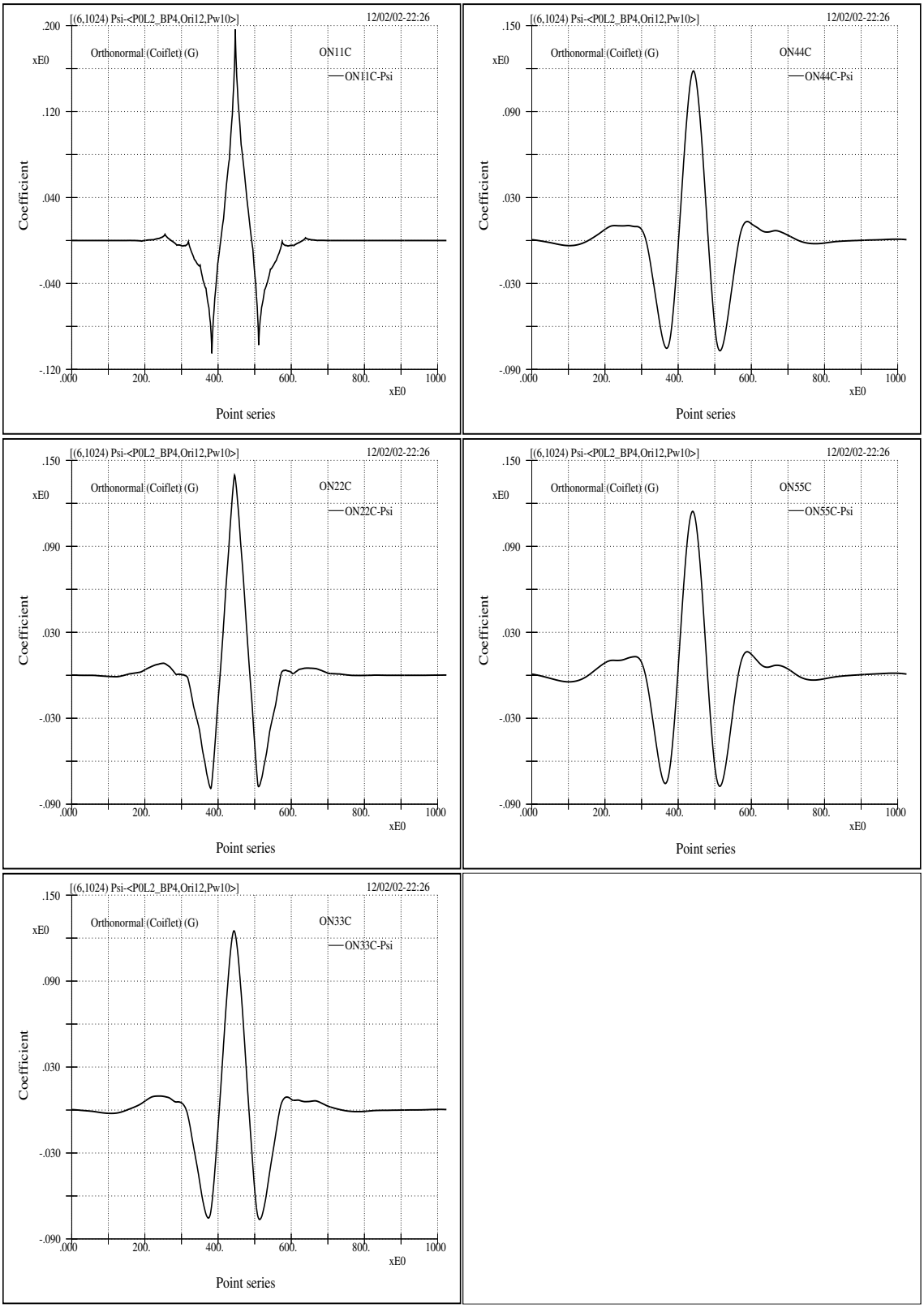

Fig 2.11 (MW–ONxxC) The mother wavelets of the orthonormal Coiflet wavelet group ONxxC are shown here. Each curve is the inverse transform of a unit value located at point 12 (at a scale level greater than 3) for a 1024-point data. The same separation point between "smooth information" and "detail information" is chosen at point 8.

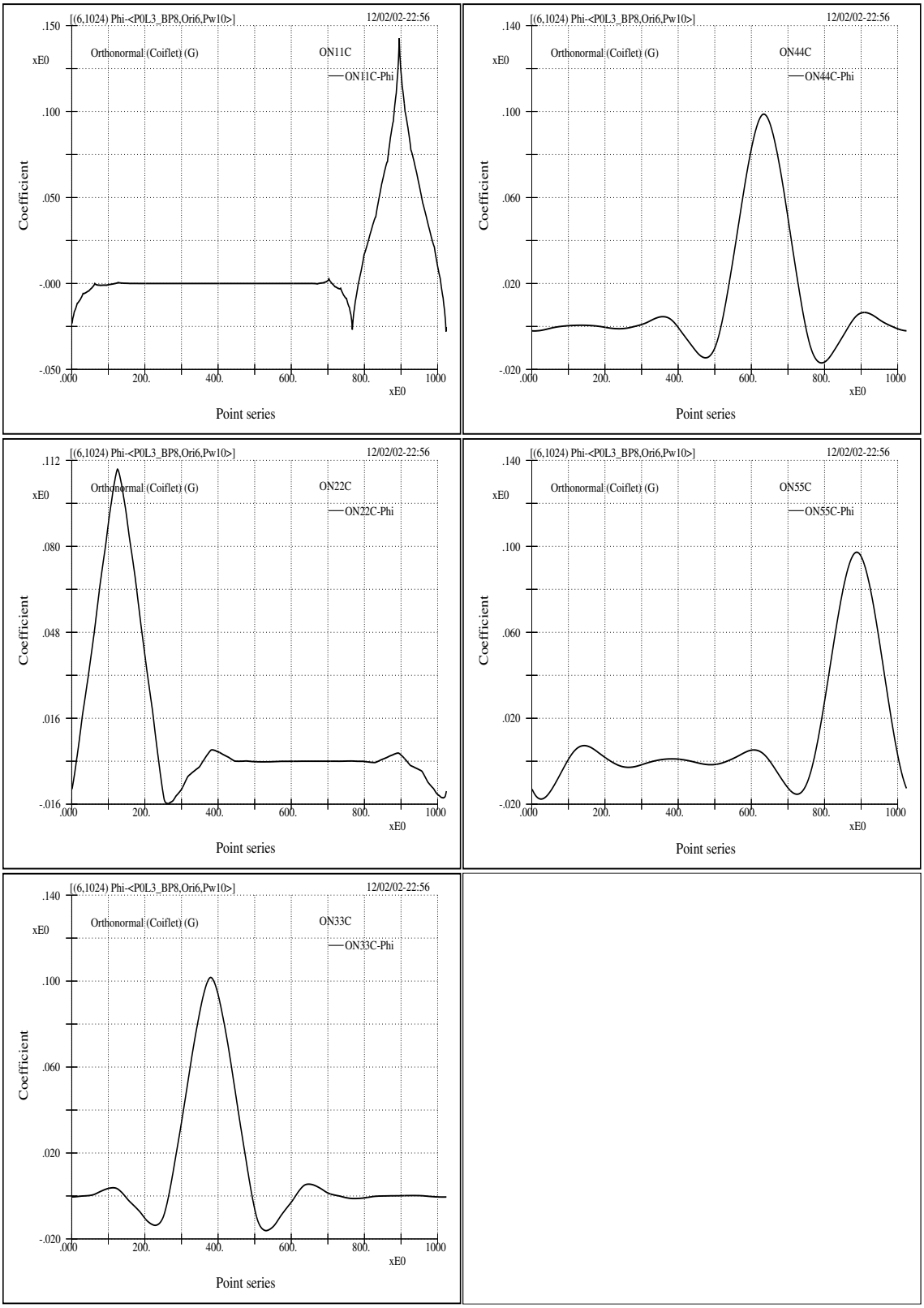

Fig 2.12 (FW–ONxxC) The father wavelets of the Coiflet wavelet group ONxxC are shown here. Each curve is the inverse transform of a unit value located at point 6 (at a scale level less than or equal to 3) for a 1024-point data. Again, the separation point between "smooth information" and "detail information" is chosen at point 8.

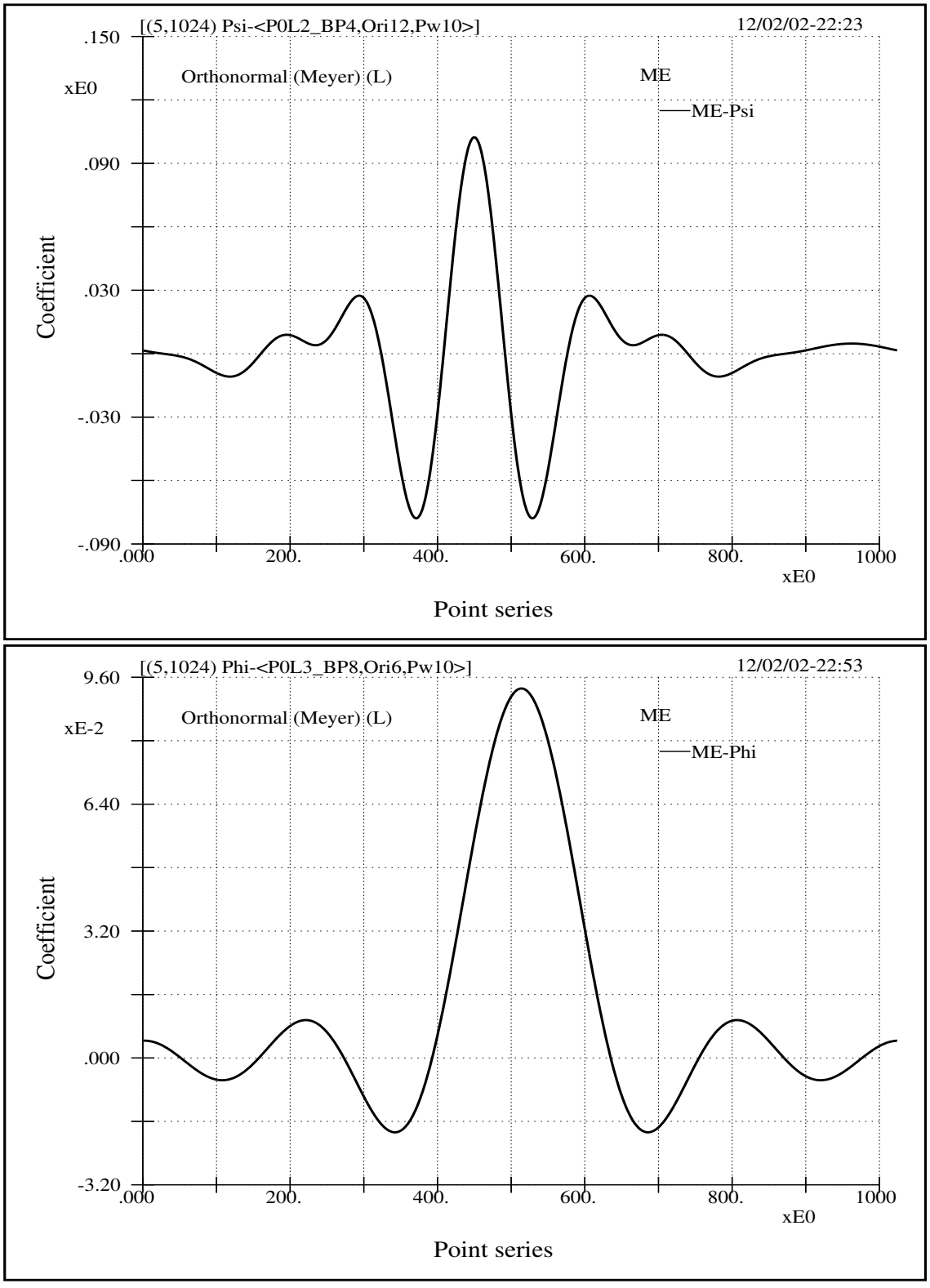

Fig 2.13 (MFW–Meyer) The mother (`top`) and farther (`bottom`) wavelets of the Meyer wavelet corresponding to the point location at 12 and 6, respectively, based upon the separation boundary point of 8 on level 3. It is noted that this figure is to be compared to the next one.

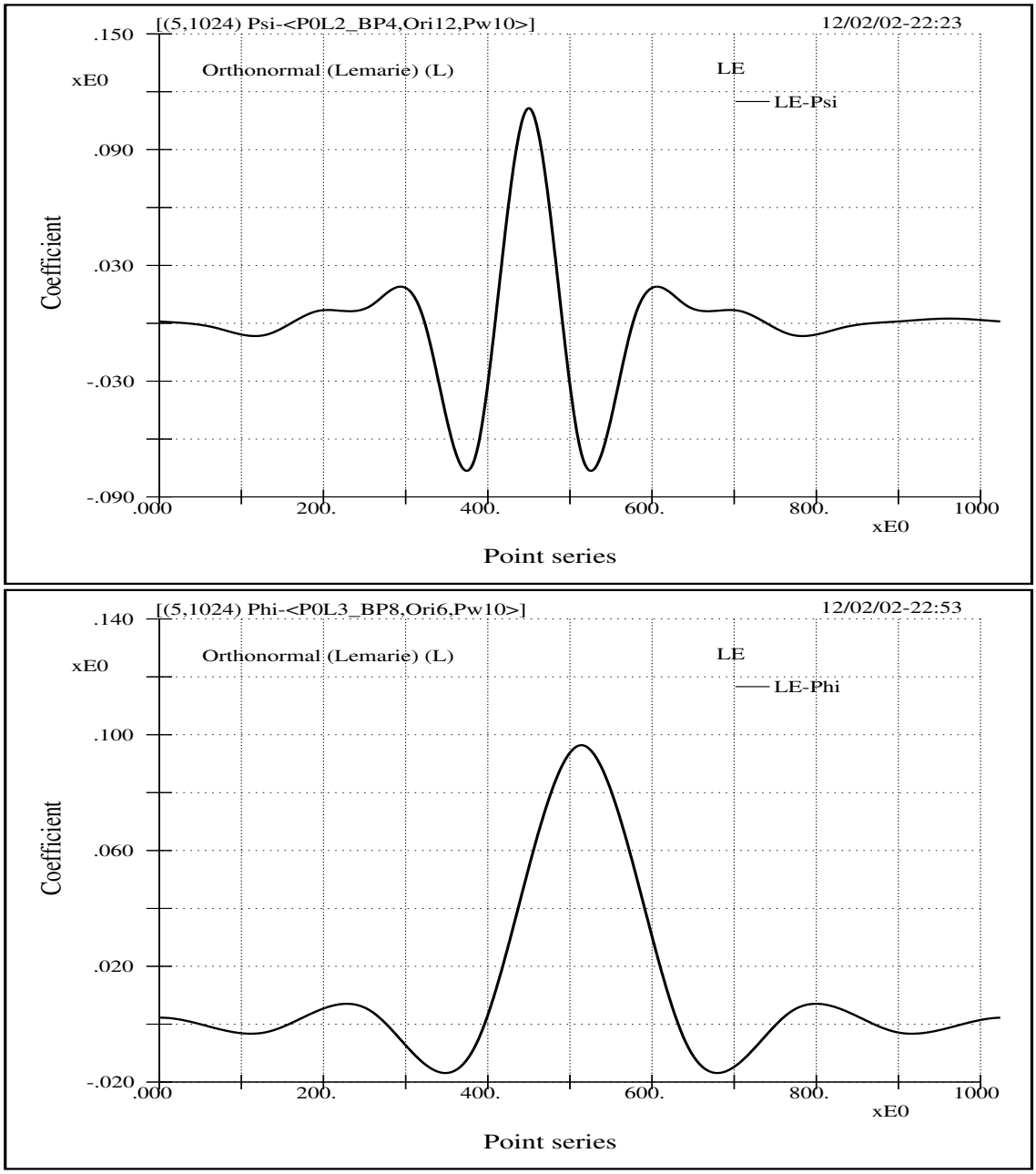

Fig 2.14 (MFW–B&L) The mother (top) and farther (bottom) wavelets of the Battle and Lemarié wavelet corresponding to the point location at 12 and 6, respectively, based upon the separation boundary point of 8 on level 3. Comparing the wavelet functions shown here with those shown in the preceding figure (figure 2.13 (MFW–Meyer)), we note the following interests. Firstly, these two different wavelets have quite similar looks, but they are associated with quite distinctive theoretical constructions and analytic properties, such as regularity, differentiability, rate of decay, support length, etc. Secondly, many intricate and complicate aspects among the discrete Riesz wavelet bases may have difficulty in their realization of practical usages, that is to say, mathematical complexity generally does not reflect our concerns about physical applications. Thirdly, water wave analysis concerns about physics, but a pure data analysis concerns only about mathematics. The important question is what is to be chosen to yield the most appropriated physics.

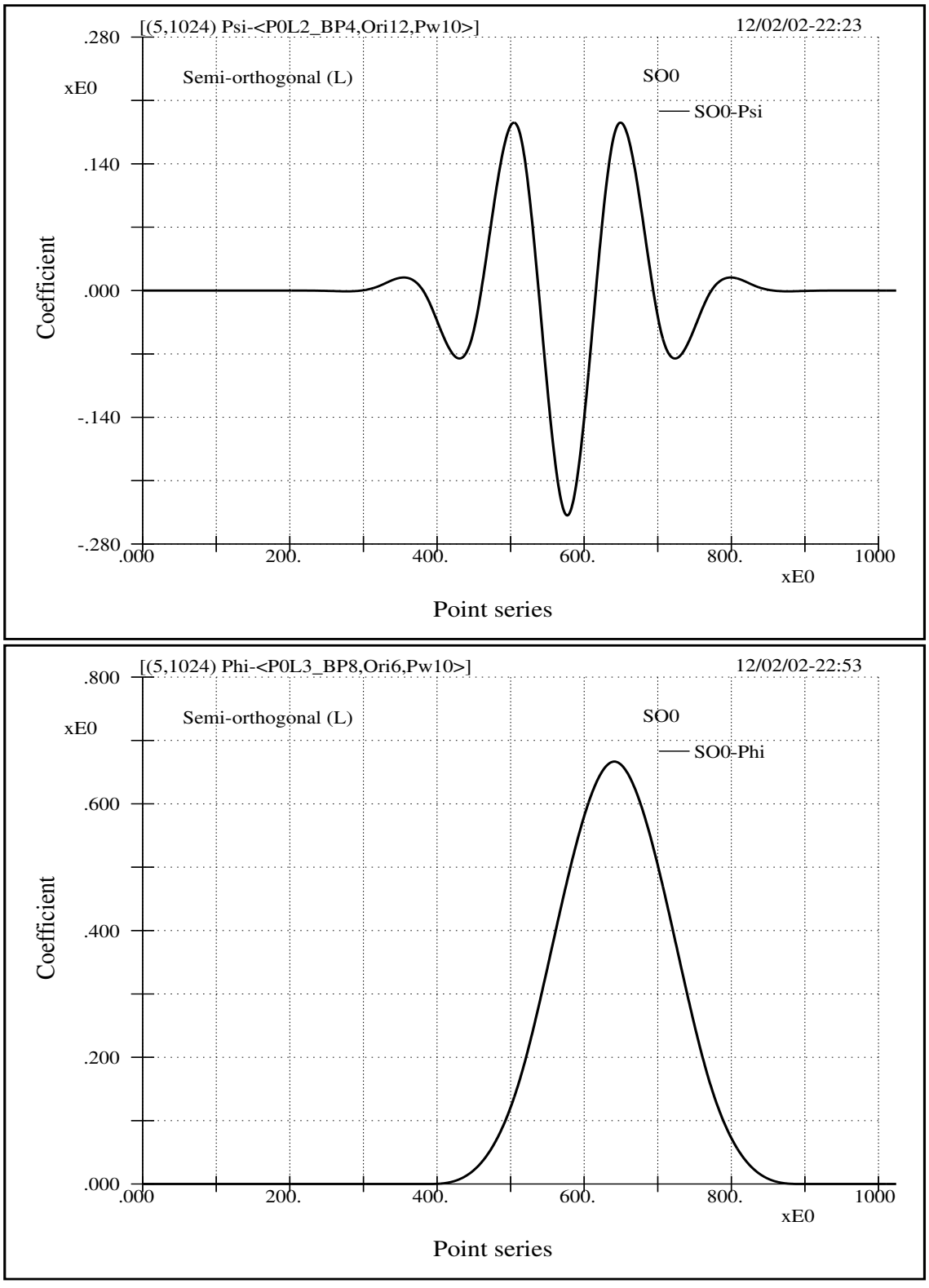

Fig 2.15 (MFW–SO0) The mother (top) and farther (bottom) wavelets of the semi-orthogonal wavelet designed by Chui (SO0) [1, 2]. The curves correspond to the same location points of 12 and 6. It will be shown that this wavelet possesses very important properties pertaining to the optimal modeling of water waves.

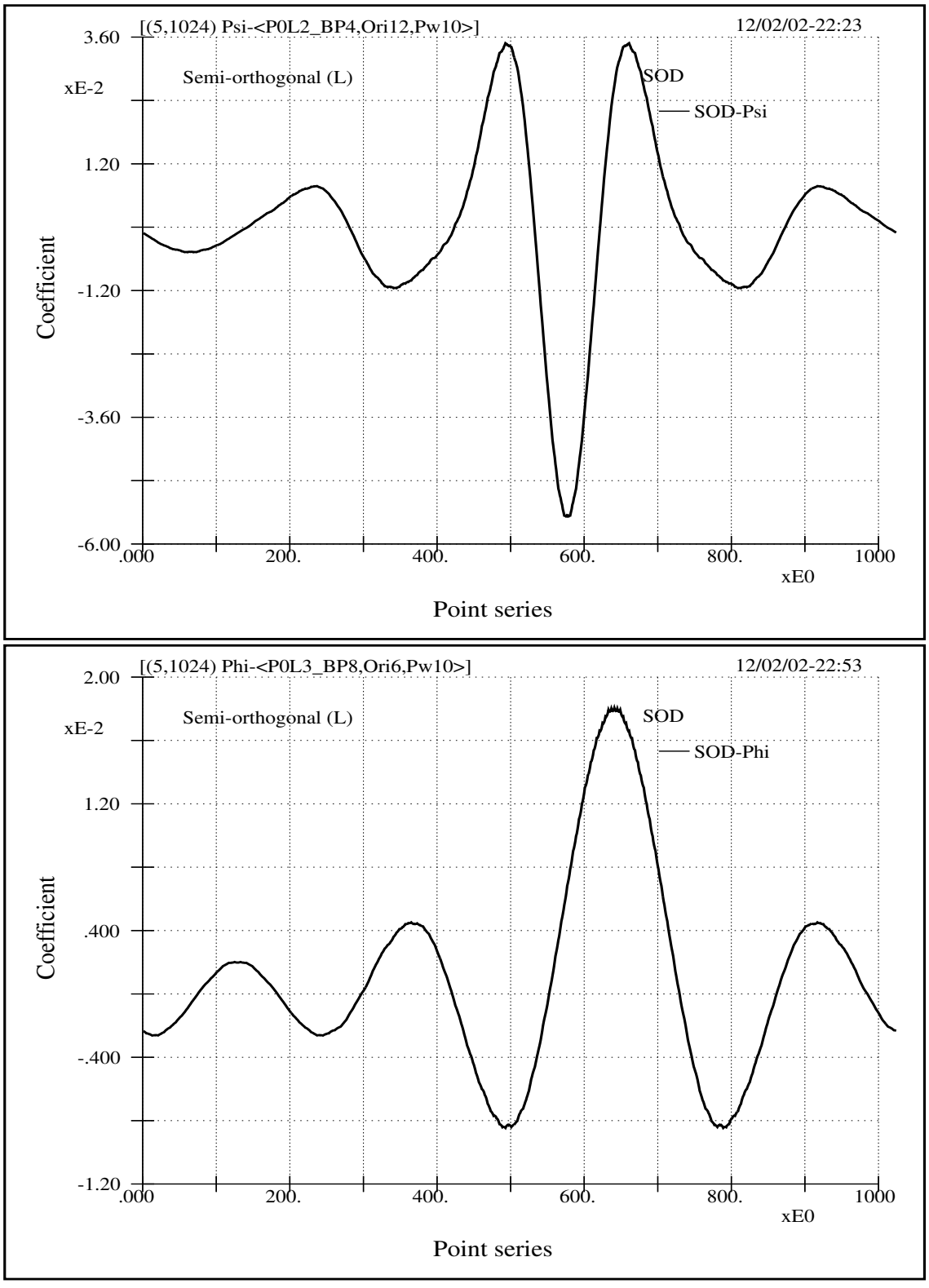

Fig 2.16 (MFW–SOD) The mother (`top`) and farther (`bottom`) wavelets of the dual of Chui's semi-orthogonal wavelet (i.e., SOD, the dual wavelet of the wavelet SO0 used in the preceding figure). Again, the curves correspond to the same location points of 12 and 6.

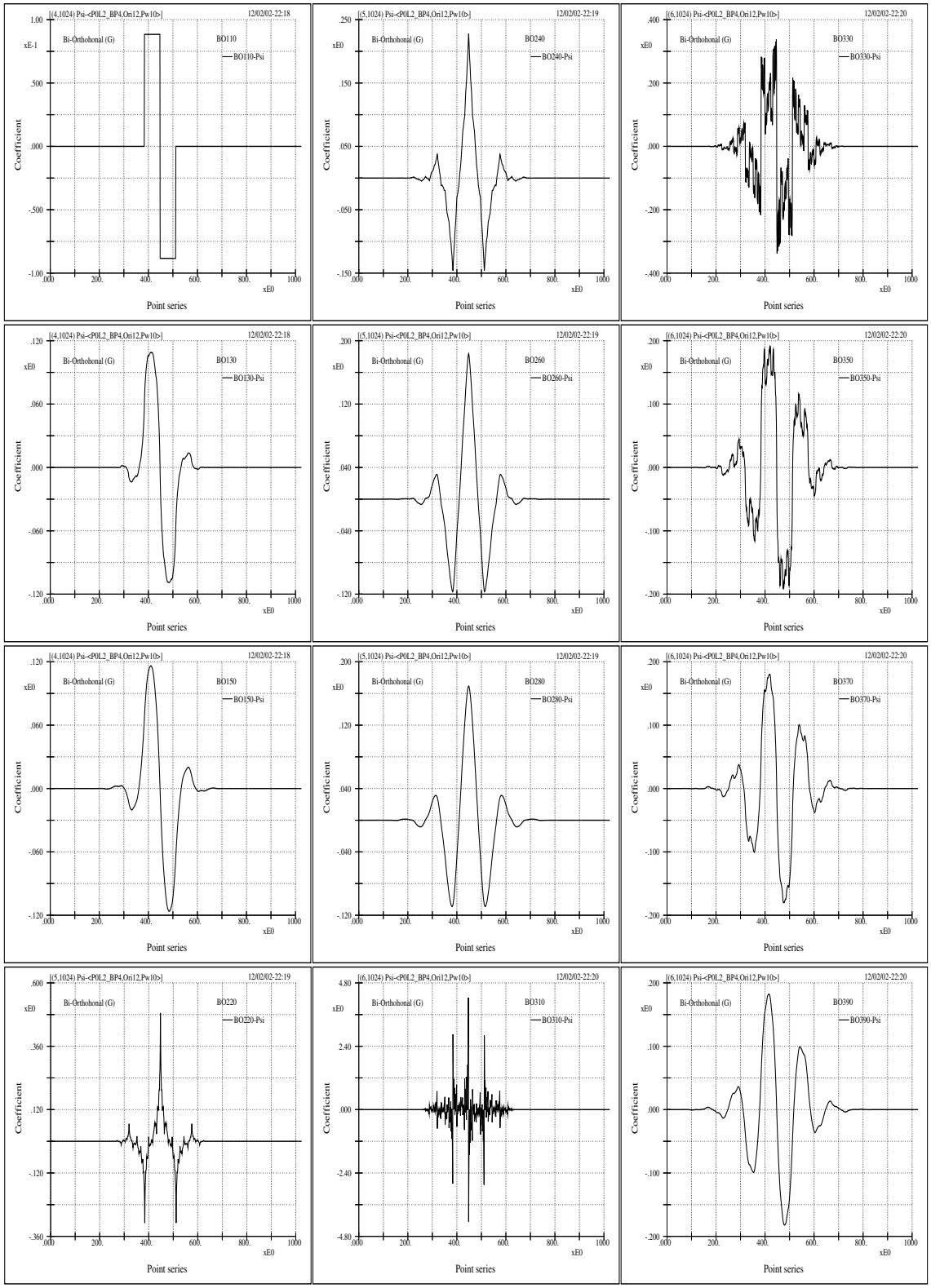

Fig 2.17 (MW–BOxy0) The mother wavelets of the bi-orthonormal wavelet group BOxyO are shown here. Again, the separation point between "smooth information" and "detail information" is chosen at point 8. And the inverse transforms are associated with location point 12. The fractal complexity of the curves depends on the configuration of the numbers of x and y.

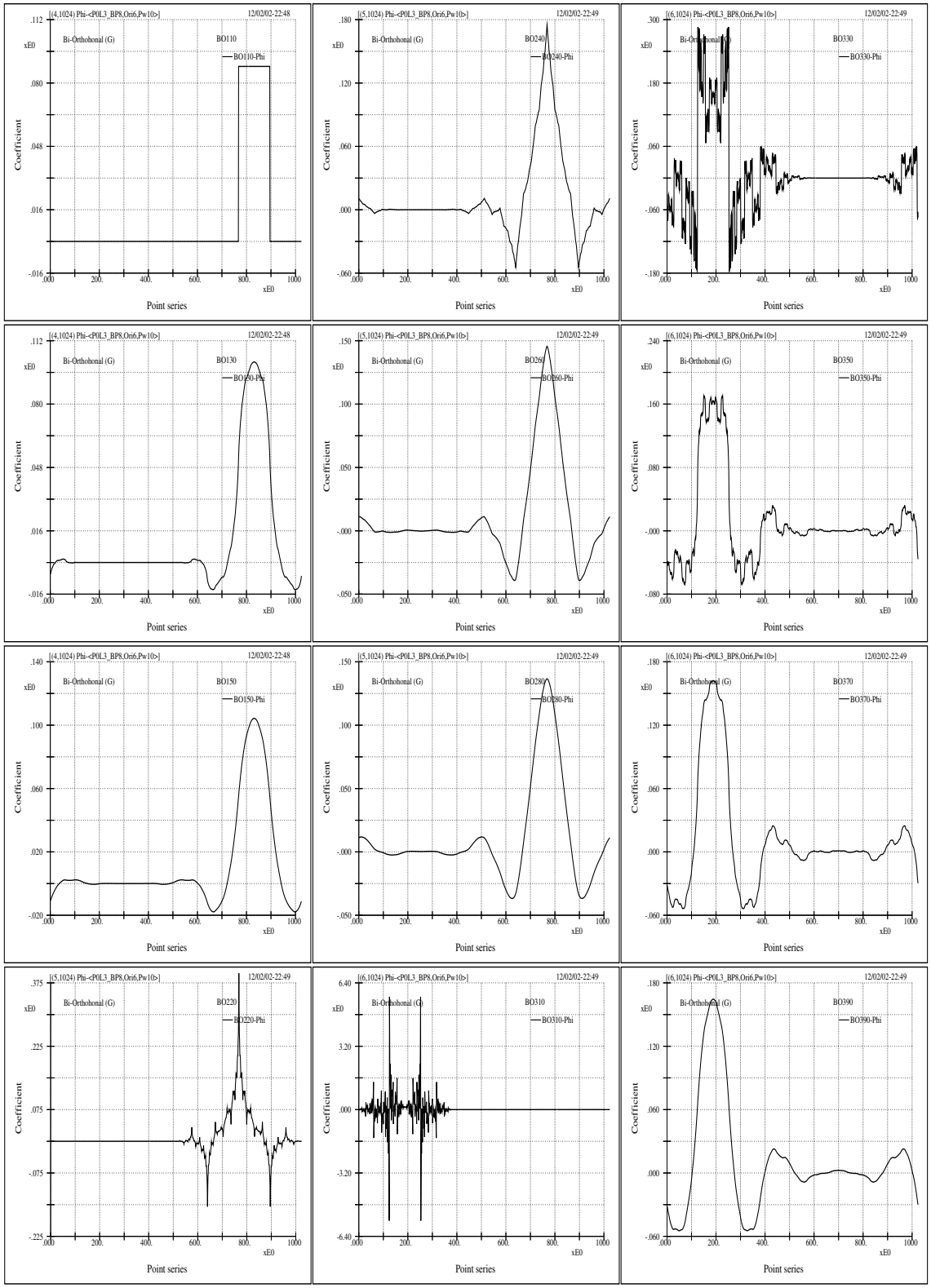

Fig 2.18 (FW–BOxy0) The farther wavelets of the same bi-orthonormal wavelet group BOxyO. The same separation point between "smooth information" and "detail information" is chosen at point 8. And the inverse transforms are associated with location point 6. Again, the fractal complexity of the curves depends on the configuration of the numbers of x and y.

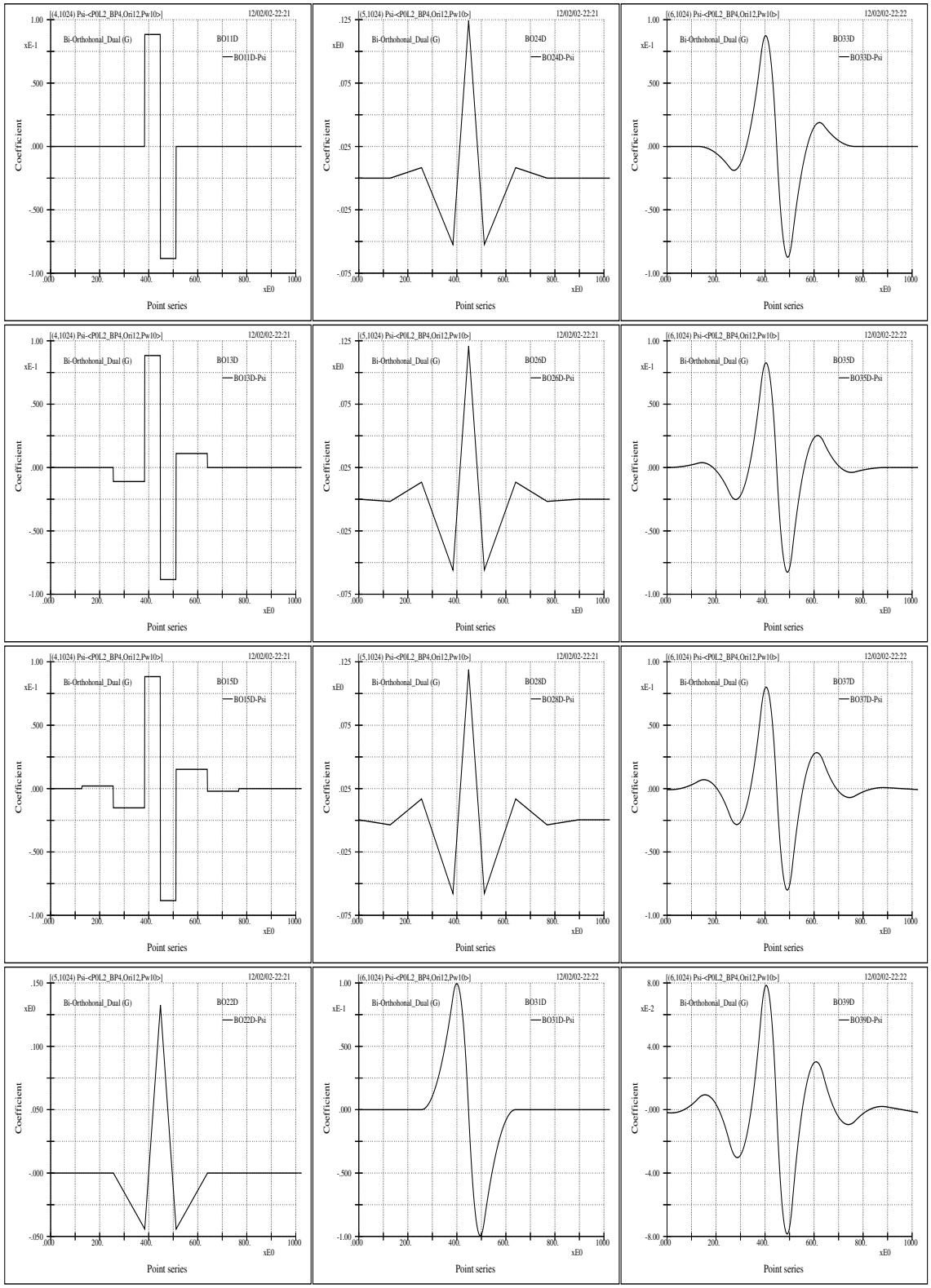

Fig 2.19 (MW–BOxyD) The mother wavelets of the dual bi-orthonormal wavelet group BOxyD. These curves are originating from the same point at 12. The fractal complexity of these dual wavelets shows much less extreme.

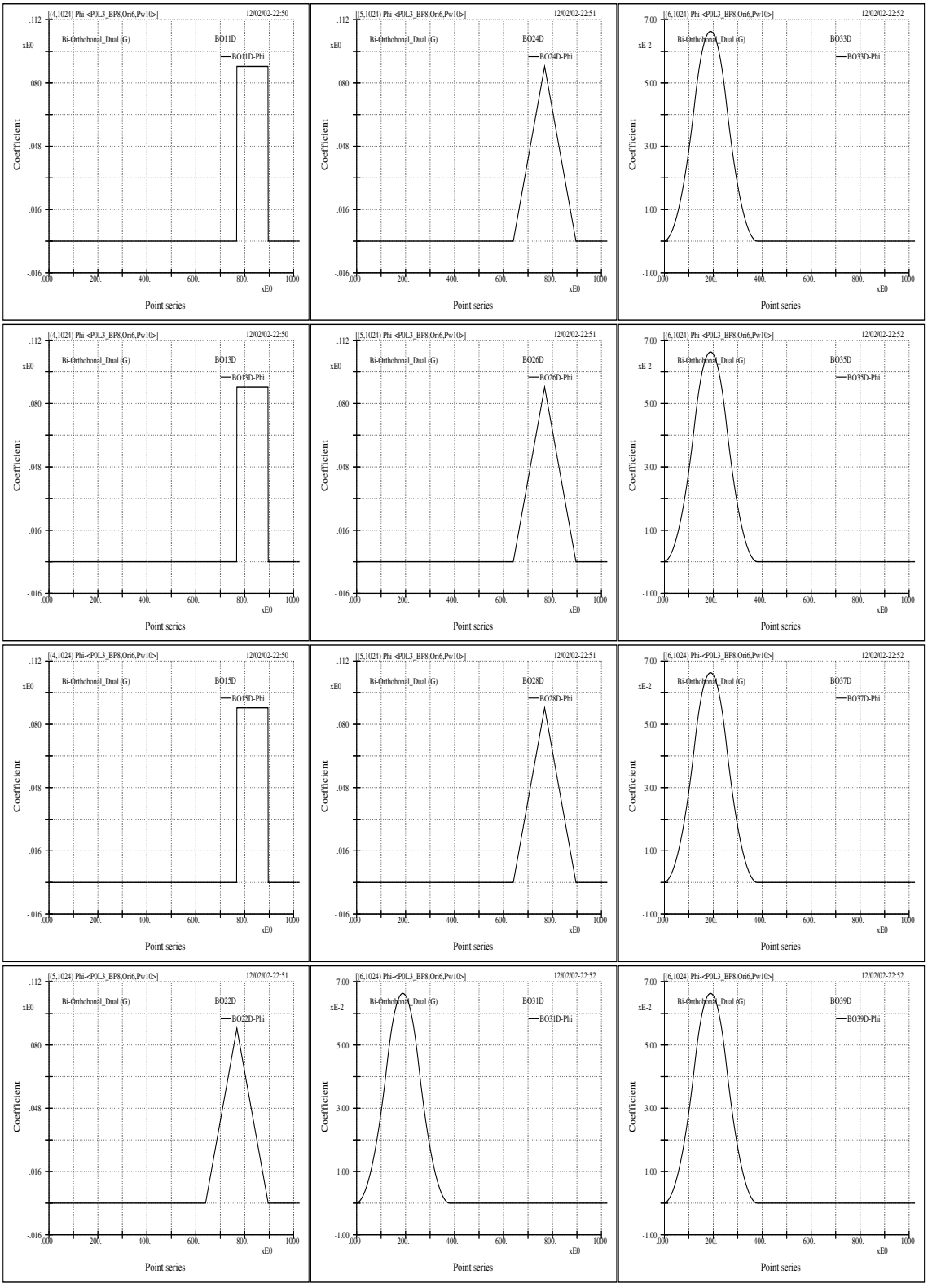

Fig 2.20 (FW–BOxyD) The farther wavelets of the dual bi-orthonormal wavelet group BOxyD originating from the same point at 12. The fractal complexity of both the mother and the father wavelets of these dual are much less extreme.

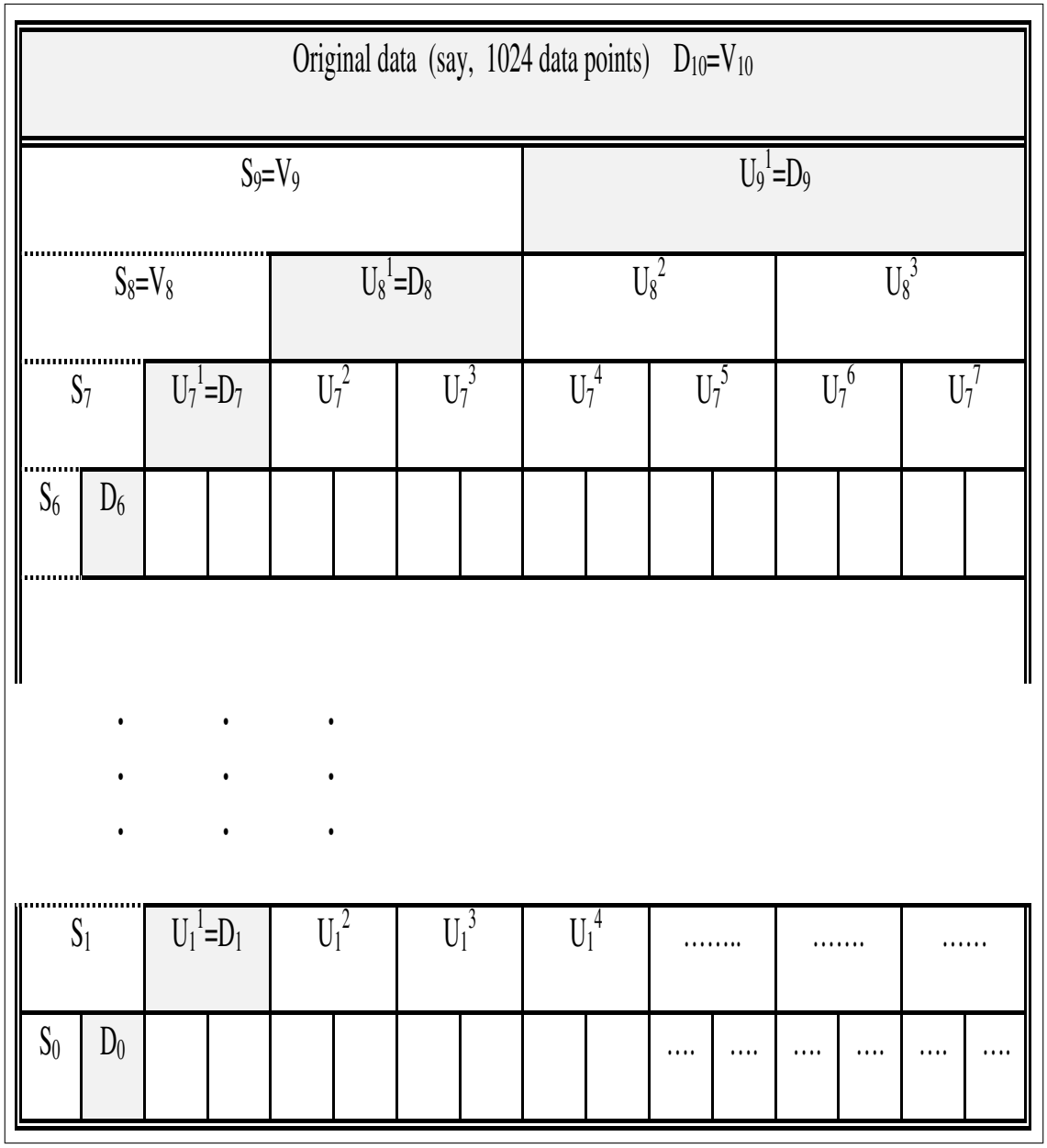

Fig 2.21 (WP Tree) The wavelet packet transform can be represented by this schematic representation of the tree-like structure of decomposition associated with orthonormal wavelets. Different branching patterns yield different transform compositions. Besides, any sub-root branch can be associated with either the same or another orthonormal wavelet; therefore, the constructs are basically unlimited. Here the schematic notations S (or *V* in the text) and D stand for smooth and detail information, respectively. The U with superscript larger than 1 stands for further decomposition of D by wavelet packets. And all subscripts of U and D mean scale levels. Besides, the superscript of U means relative location of a specific frequency band within its compatible subscript (or scale level).

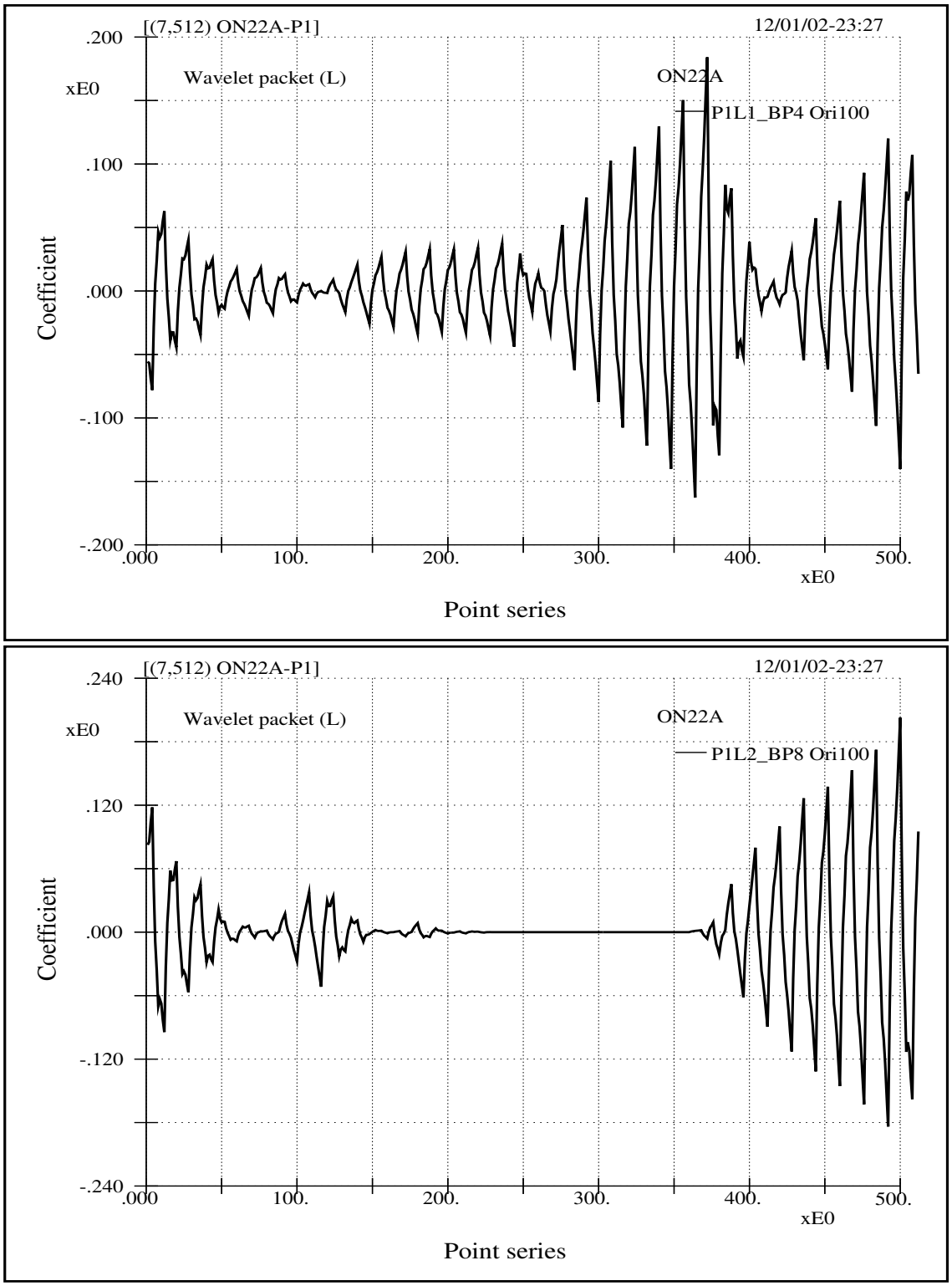

Fig 2.22 (WP forms) This figure depicts the wave forms of two wavelet packets based upon ON22A and associated with the same location point 100 at different scale levels 2 and 5, with boundary point at 8 and 64, respectively. It demonstrates the typical bundled shape of distribution of wavelet packets as compared to wavelet.

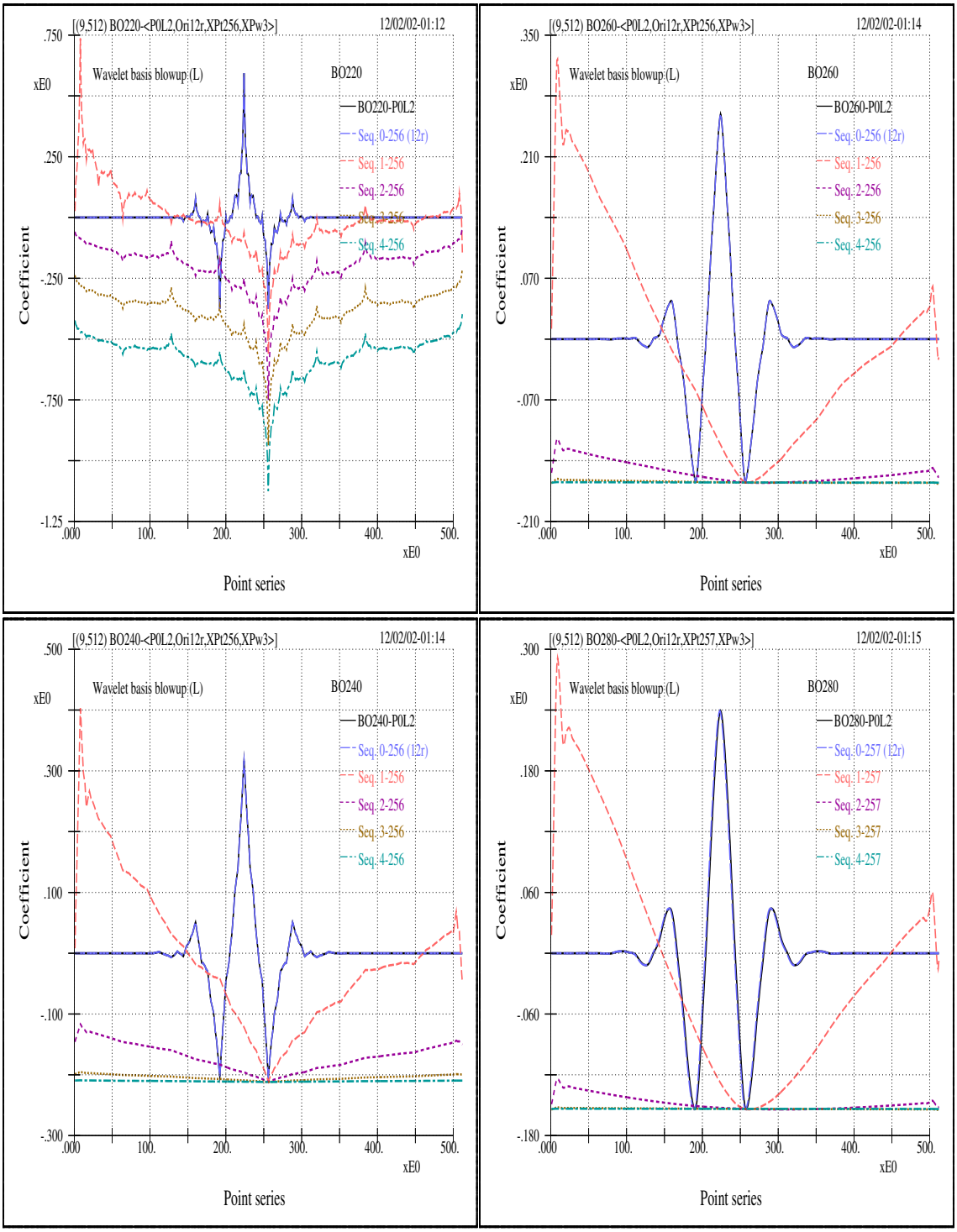

Fig 2.23 (BU–BO2yO) Wavelet's fractal nature across scales is demonstrated in various previous figures, but here the property is more appropriately shown by blowing up the wavelet at any fixed point. The curves shown here are the blowups of wavelets related to the bi-orthogonal group BO2yO. The scale interval between adjacent blowups is 2^3. The location of the blowup point is labeled in individual sub-figure (such as point 256 or 257). The scale level (which defines the boundary point between smooth and detail information) and the unit value originating point for individual wavelet to be exploded are also indicated in the sub-figures (such as L4 and Ori12).

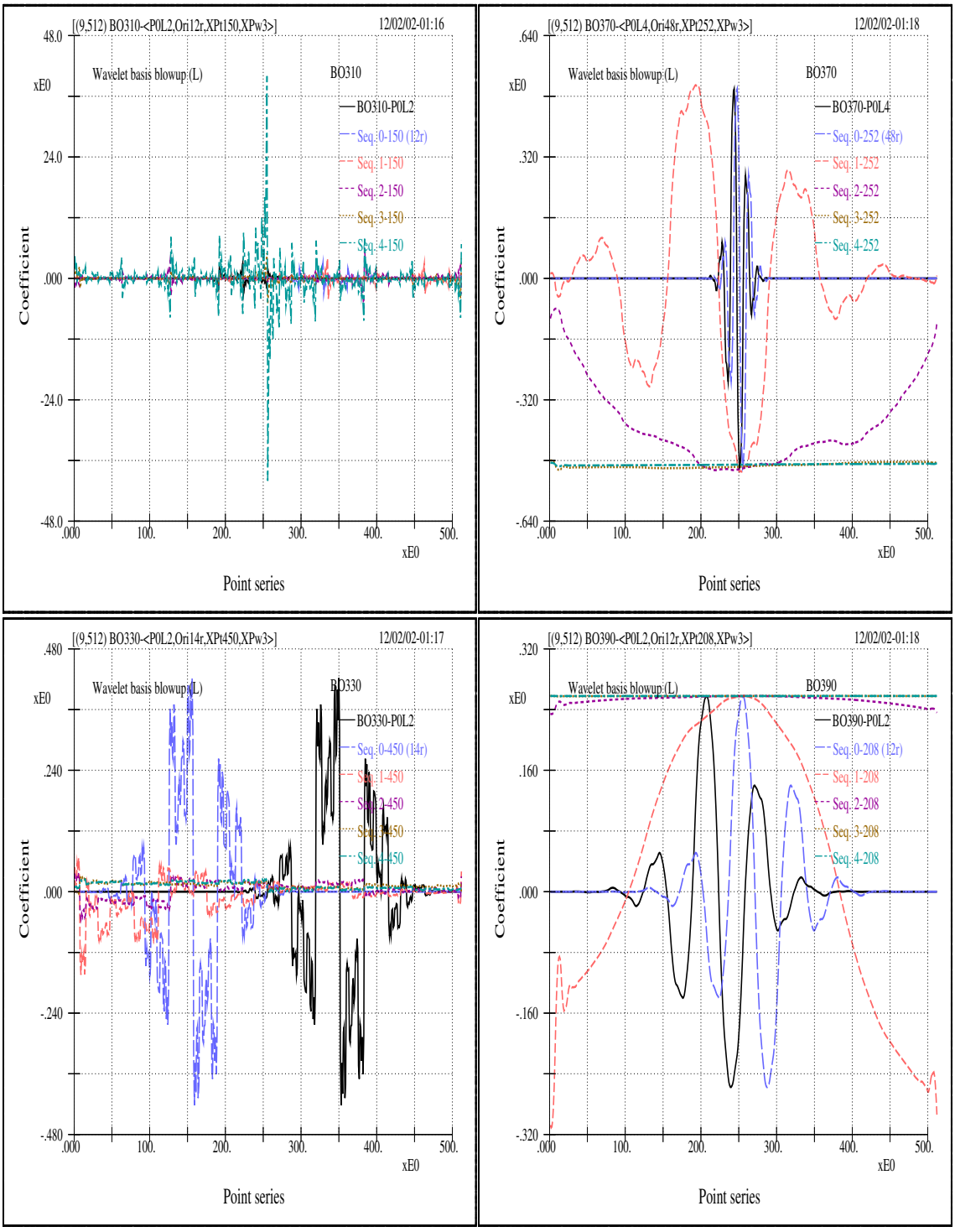

Fig 2.24 (BU–BO3yO) The blowups of wavelets related to the bi-orthogonal group BO3yO. The scale interval between adjacent blowups is 2^3. The location of the blowup point is labeled in individual sub-figure (such as point 150, 450, 252 and 208). The scale level and the unit value originating point for individual wavelet are indicated in the sub-figures (such as L2, L4 and Ori12, Ori14, Ori48, Ori12).

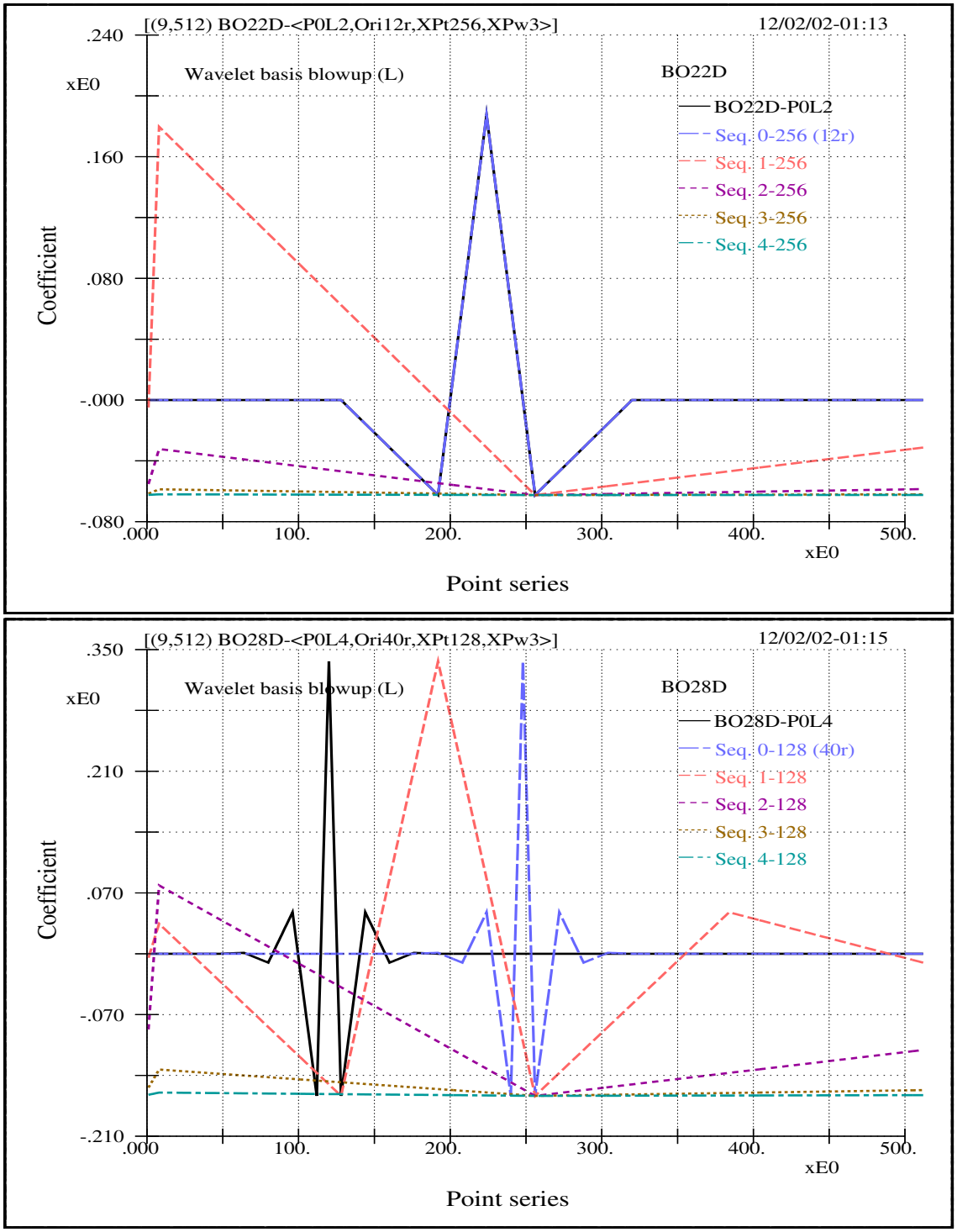

Fig 2.25 (BU–BO2yD) The blowups of wavelets related to the dual bi-orthogonal group BO2yD. The scale interval between adjacent blowups is 2^3. The location of the blowup point is labeled in individual sub-figure (such as point 256 or 128). The scale level and the unit value originating point for individual wavelet are indicated in the sub-figures (such as L2, L4 and Ori12, Ori40). In reference to the next figure, it is noted that the number of convolution weights play a part in the modeling entropy. And a too brief number of convolution weights generally yields quite unrealistic wave form.

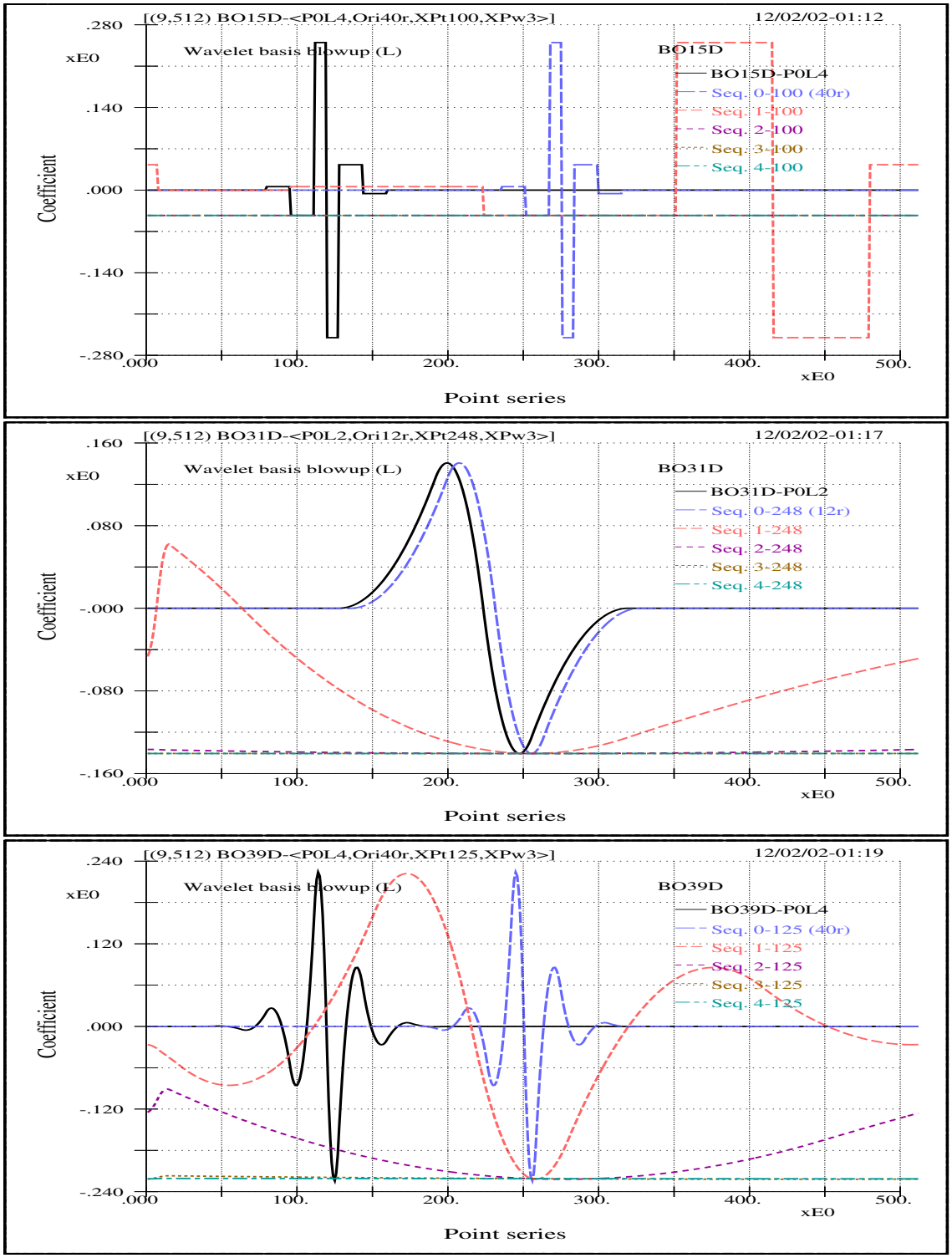

Fig 2.26 (BU–BO3yD) The blowups of wavelets related to the dual bi-orthogonal group BO3yD. The scale interval between adjacent blowups is 2^3. The location of the blowup point is labeled in individual sub-figure (such as point 100, 248, 125). The scale level and the unit value originating point for individual wavelet indicated in the sub-figures (such as L2, L4 and Ori12, Ori40). It is hinted here: comparing with the distribution curves of their counterpart group BO3yO, it is not hard to realized that the dual wavelet yields better modeling entropy as will be shown later.

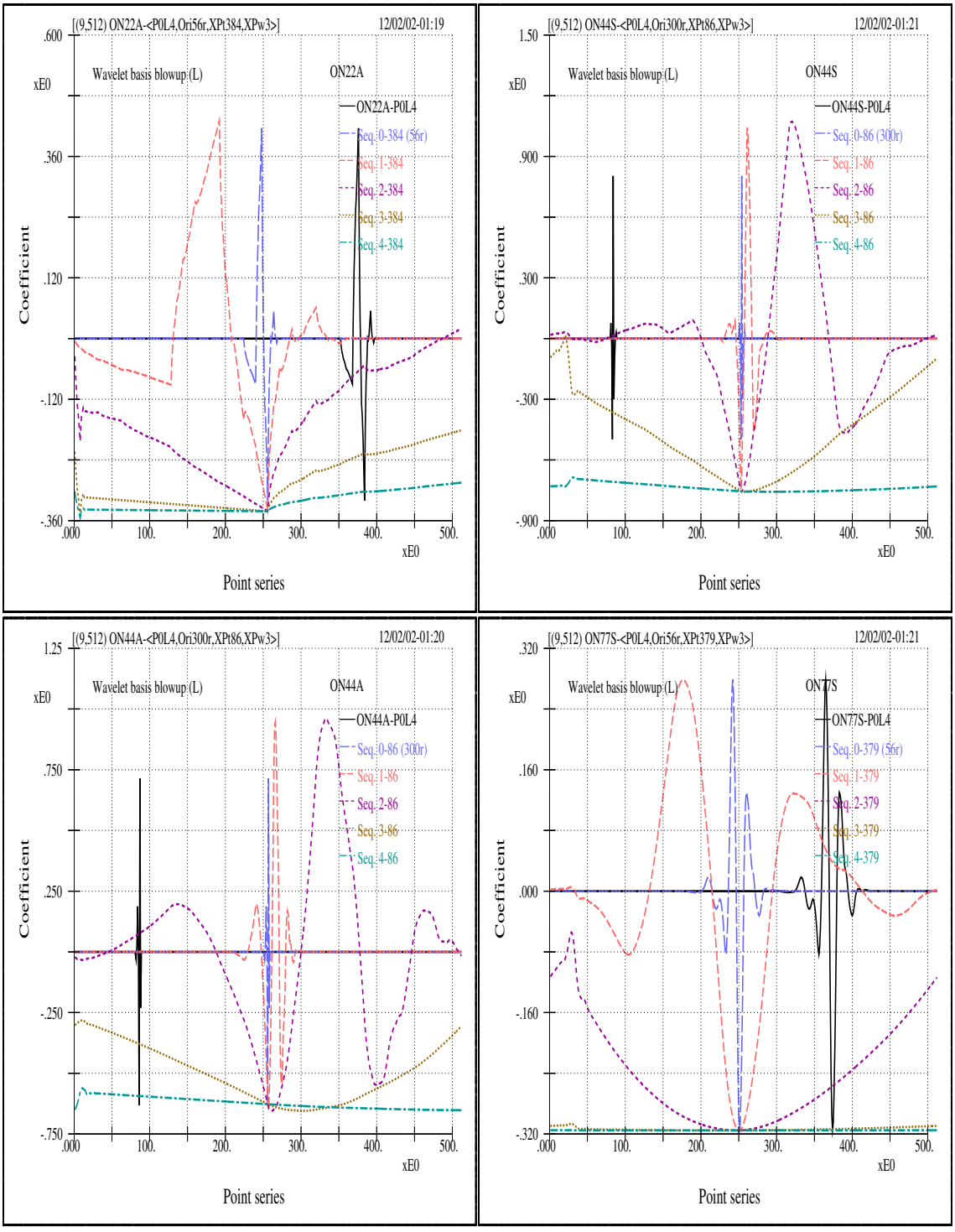

Fig 2.27 (BU–ONxAS) The blowups of wavelets related to the most asymmetric and the most symmetric orthogonal groups ONxxA and ONxxS. The scale interval between adjacent blowups is 2^3. The location of the blowup point is labeled in individual sub-figure (such as point 384, 86, 379). The scale level and the unit value originating point for individual wavelet indicated in the sub-figures (such as L4 and Ori56, Ori300). Again, it is noted that a too brief number of convolution weights yields quite unrealistic wave form.

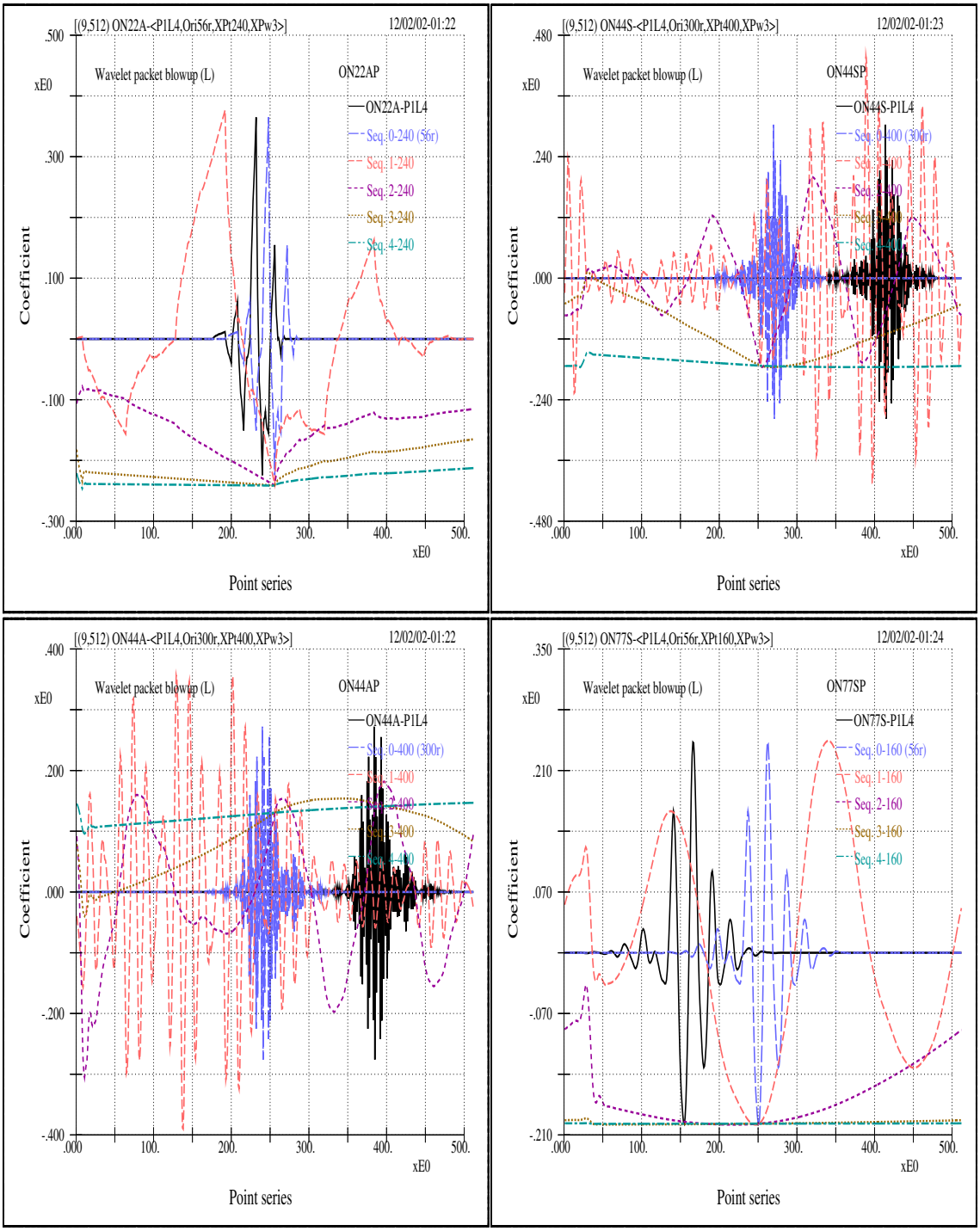

Fig 2.28 (BU–WP-ON) This figure shows the wavelet packet blowups related to the most asymmetric and the most symmetric orthogonal groups ONxxA and ONxxS. In reference to the preceding figure, it is easily comprehended that wavelet packet transform is even more unrealistic for modeling water waves. This is one – an intuitive and visceral one – of the reasons why in the later chapter we don't bother calculating the entropy of any wavelet packet. Again, the scale interval between adjacent blowups is 2^3. The location of the blowup point is labeled in individual sub-figure (such as point 240, 400, 300, 56). The scale level and the unit value originating point for individual wavelet indicated in the sub-figures (such as L4 and Ori56, Ori300).

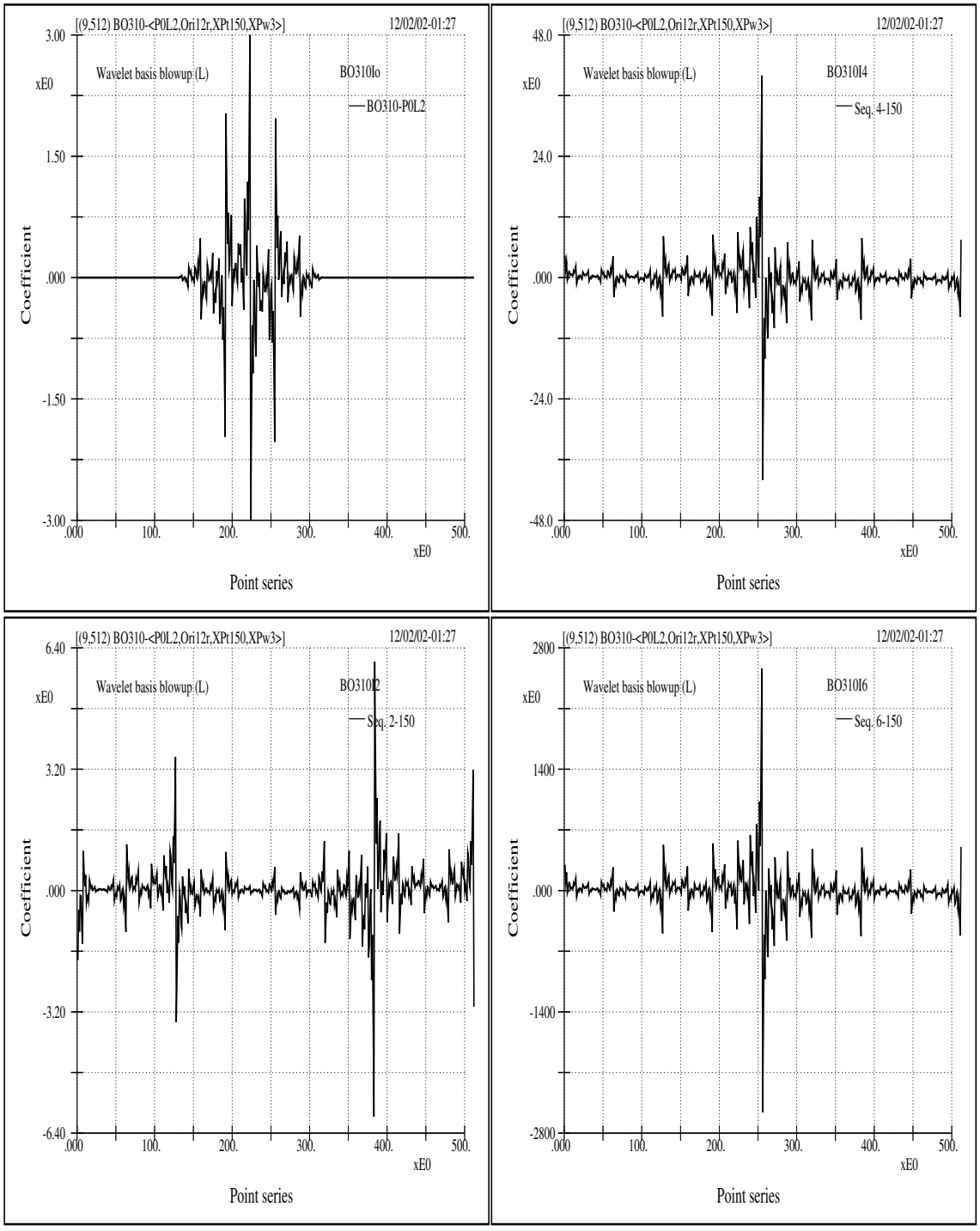

Fig 2.29 (BU–BO31O) The successive blowups of the bi-orthogonal BO31O wavelet at point 150 for scale level L2 and unit value originating point Ori12. Here the scale interval between adjacent sub-figures is 2^6. Note the vast difference in the ordinate axis. The phenomenon is related to the numerical demand of precision that is associated with a too brief number of convolution weights, as well as with its wavelet category.

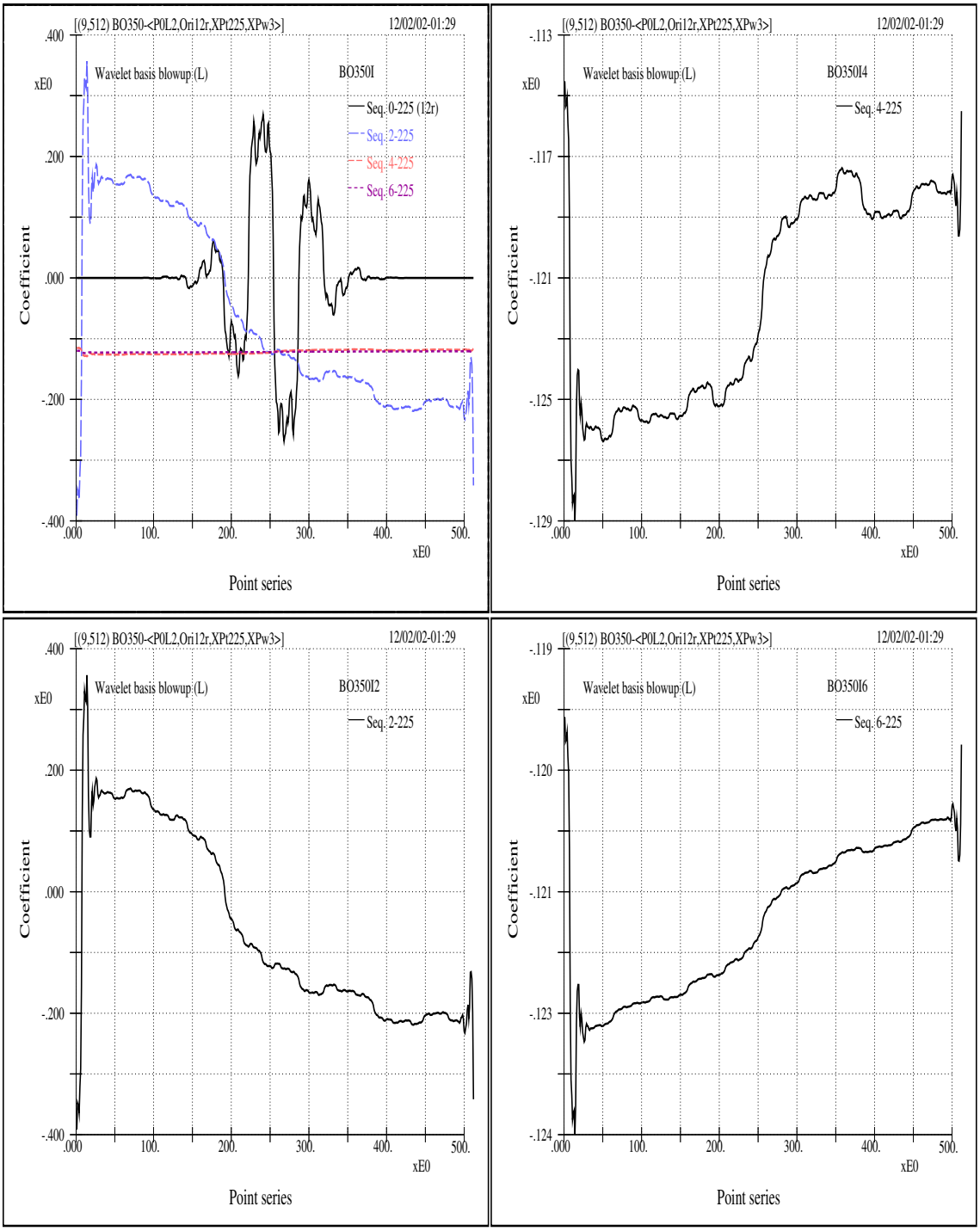

Fig 2.30 (BU–BO35O) The successive blowups of the bi-orthogonal BO35O wavelet at point 225 for scale level L2 and unit value originating point Ori12. Here the scale interval between adjacent sub-figures is 2^6. Note the completely opposite inclination of the distribution curve between adjacent sub-figures. Again, the phenomenon is related to a brief number of convolution weights, as well as the wavelet category. Overall, here it is hinted that there are many fancy wavelets but, for water wave physics, fancy sometimes is only an illusion.

Chapter 3

The Entropies and the Best Discrete Wavelet Basis

3.1 Introduction

There exist basically infinitely many wavelet bases. In studying the physics of certain phenomena using wavelets one of the most intriguing questions is how to choose the analyzing wavelet(s). The concern here is quite in contrast to those studies where they are mainly numerically or mathematically oriented. For example, in coding of images or acoustic signals the goals are straightforward: the maximum compression with minimum handling, the highest effectiveness with lowest distortion, and the most distinctiveness with lest aberration; under such circumstances mathematical relevance between signal and wavelet can be materialized much more explicitly than physical pertinence needs to be unfolded for our applications. That is to say none of the above points is focusing on our interest mainly in physics. From this point of view, by and large, for our interests in characterizing the physics of water-wave related phenomena, it seems, at first, that the aspiration is not on 'efficiency" or "compactness". However, with the understanding that, on the one hand, the compactness of a transform result means the closeness between signal components and analyzing basis functions, and that, on the other hand, the conception that basis function forms which do not look like our signals (or signal components) are obscured from intuitive perceptions of physics; it is naturally justified to seek the wavelet

that provides the most efficient or most economical representations for our signals. Still, at the end we are bringing back to the concept of entropy — the most efficient representation — different disciplines but with the same objective.

The exploits in this chapter are mainly numerical experiments on measuring the "distances" between our signals and various Riesz wavelet bases given in several wavelet treatises [1, 20, 55, 62]. No attempt to make new constructions of bases or to extend the existing constructions is made. Nevertheless, we have tried to include various categories of Riesz wavelets with a comprehensive coverage of analytical properties. And we will come to realize that there is really no need to extend the existing constructions if the associated two-scale scaling function or father wavelet is not changed, that any other individual wavelet in literature falls within our characterizations, and that a few fractal-oriented sparse wavelets [52, 50] are just as impractical as they may be in our applications.

The wavelets tested are dyadic wavelets with "mathematical sampling rate" 1 (no unit). They possess the most practical interest and easiness in applications for discretely sampled signals. Furthermore, we restrict our scope to laboratory water waves. Various criteria are used for the entropy statistics of discrete transform coefficients, including Fourier coefficients.

3.2 The entropy criteria

Entropy is a terminology in the statistical field, thus it gives indication without absolute assurance. And the entropy can be viewed as a measure of the "distance" between the original signal and its reconstructed signal using partially truncated transform coefficients. To avoid the somewhat mystified notions as one might get from some of the available readings, it may be better to give straightforward descriptions by going through the actual numerical process first and returning to its statistical implication later.

Let suppose that we have a 1024-point sampled data, then there is a set of 1024 wavelet coefficients (C=$\{c_i\}$). Take the absolute or squared value of these coefficients, sort them,

and then divide the sequence into M (say, 100 or 200 or 300) divisions which are equally spaced from 0 to the maximum value of the coefficients. Then we have the statistics of occurrence for each division, and the distribution of these normalized occurrences is the probability density distribution or probability density function (denoted by pdf), say $\{p_1, p_2, \cdots, p_{M-1}, p_M\}$. The entropy is

$$H(p) = -\sum_i p_i \log p_i. \tag{3.1}$$

Where, when $p_i = 0$, it is assumed that $0 \log 0 = 0$, since in reality one can assumed that there exists an almost zero probability in that interval without affecting the total sum of probability, after all it is only a statistics and the modification virtually has no influence on the norm value. If absolute values of c_i are taken, $H(p)$ is the L^1-norm entropy; if squared values are taken, it is squared L^2-norm entropy. Of course another power can be used, but the squared L^2-norm, being the energy, is physically the most significant. The practical aspect of this definition of entropy is: let suppose two probability distribution functions sorted in a decreasing order are p and q, if p decreases faster than q, then $H(p) \leq H(q)$ [75]. The above inequality of entropy is only one-way correct and the reverse is not always true, but smaller entropy implies that more energy is concentrated within a smaller number of wavelet coefficients. Therefore, if only a fixed percentage of coefficients is kept, the truncated error, i.e., the distance from the total sum, is likely to be smaller for set of coefficients with smaller entropy.

There is another notion for working out the entropy. It is sometimes referred as the geometric notion [75]. Again, the procedures is given first and the simple physical interpretation next. By setting the number of divisions to be the same as the number of coefficients and by defining probability density to be the normalized (with respect to the total power) value of the squared wavelet coefficient, that is to say, the total energy is $\|C\|^2 = \sum_i |c_i|^2$ and the probability density is $p_i = |c_i|^2/\|C\|^2$, we get the alternative

form of entropy by substituting P_i into Equation 3.1:

$$H(p) = \log \|C\|^2 - \frac{\sum_i |c_i|^2 \log |c_i|^2}{\|C\|^2}. \tag{3.2}$$

The notion here is simple: if one just put more weight on coefficients of small energy and less weight on coefficients of large energy (all coefficients being normalized), then the weighted energy is an indication of entropy. And since taking the log of a value is sort of a weighting operation and since the total energy is finite, small entropy therefore means that the number of significant coefficients is small, or stated otherwise, more energy is concentrated in fewer coefficients.

One equivalent indicator of entropy of a pdf is the theoretical dimension $D(p)$ and is defined as [75]

$$D(p) = e^{H(p)} = \prod_i \left(p_i^{-p_i}\right). \tag{3.3}$$

As was stated, entropy does not tell how conclusive the result is. But our numerical results yield little ambiguity regarding the judgement that we can make.

3.3 The best discrete basis for water waves

To increase the definiteness of the comparisons, we calculate entropy based on several setups: direct coefficient entropy related to L^2-norm based on Equation 3.3 (column 1 in Tables 3.1 (H–F+ON+SO) and 3.2 (H–BO0+D)), pdf entropy related to L^2-norm with 300 (column 2) and 200 (column 4) divisions, and pdf entropy related to L^1-norm based on Equation 3.1 (column 3). Theoretical dimension for one of the setups is also given (column 5). The tables show the results using a wind-wave signal from a wave tank experiment. It is noted that if the peak frequency (or the primary scale) of other signal is significantly different, then, to be consistent in comparison, the analyzed signal lengths and the sampling rates should be properly adjusted according to its peak frequency. This is because in the discrete wavelet transform we need to keep track of the actual physical size of translation

so as to have physical perception of the wave forms. Table 3.1 (*H*–F+ON+SO) give results from all orthonormal wavelets (including B&L, Meyer, ONxxA, ONxxS, and ONxxC), semi-orthogonal wavelets (Cubic B-spline, SO3O and SO3D), as well as from Fourier spectrum. Table 3.2 (*H*–BO0+D) give results from bi-orthogonal wavelets. Many distinctive features can be derived from the tables.

- The dual wavelet always gives much smaller entropy than as given by their counterpart wavelet. This certainly verifies that, for our water-wave signals, using

$$f(t) = \sum_{j,k} \langle f, \widetilde{\psi}_{j,k} \rangle \psi_{j,k} \tag{3.4}$$

  provides a much better efficiency in decomposition and reconstruction than using

$$f(t) = \sum_{j,k} \langle f, \psi_{j,k} \rangle \widetilde{\psi}_{j,k}. \tag{3.5}$$

  This also points out that dual wavelets rather than their counterpart wavelets should always be used as the decomposing basis for either better physical implications or improved computational efficiency. It may also worth noting that the practical shapes of all the listed bi-orthogonal wavelets, especially those with small x and y values, are visually quite unrealistical (such as those shown in figures 2.29 (BU–BO31O) and 2.30 (BU–BO35O)). Furthermore, for these bi-orthogonal wavelets, it can be concluded that there is going to be very little improvement by further extending the support width related to y without extending the support width related to x; since increasing the width (y) from some point on gives no effect on the shape of dual wavelets (such as $y = 7$ or 9 for $x = 3$) and since it is the dual, rather than the counterpart, wavelet that matters for better approximation.

- Entropy values of all orthonormal subgroups do not fall to the level of non-orthogonal ones. Besides, difference in entropy values of long and short supports can barely be differentiated, even though there seems to be a very slight indication that entropy

values related to longer support are somewhat smaller. Here the property reflects the role of linear phase filtering as mentioned earlier.

- Among all the orthonormal wavelets none distinguishes itself from the others. And we see no clear tendency within any subgroup. However, from the analytical point of view, the Meyer wavelet is infinitely differentiable or smooth, the B&L is second order differentiable, and the others have various degrees of differentiability or regularity [20]. It is therefore understandable that at the present stage many analytical properties of orthonormal wavelets are of little practical interests for our signals.

- The most striking result is that the dual Cubic B-spline wavelet yields a far smaller entropy value, even lower than that of the spectral coefficients. Figure 3.1 (p–W+WP+F) shows the comparisons of the cumulative probability distribution curves for several wavelet bases as well as for Fourier basis. This striking feature is reflected by the extreme flatness of the SO3D curve, nearly horizontal up until 90 percent of energy ratio. At about 96 percent of the energy ratio there is a crossing between spectral curve and the SO3D curve. These features practically imply that semi-orthogonal wavelet coefficients are better than Fourier coefficients in describing the details of the signals. Figure 3.3 (ReC–Signal) shows the reconstructions of a section of a signal from its spectral and SO3D wavelet coefficients of which 35 percent are kept. It is seen that the wavelet basis yields truer details than does Fourier basis. Again, the reasons for the SO3D's strong performance can be attributed to the following characters: total positivity of the scaling function and complete oscillation of the wavelet. That is to say, the scaling function has no oscillation or zero-crossing; the corresponding wavelet has no unnecessary oscillation, or no oscillation that is without zero-crossing. Physically, the two characteristics hint that our laboratory water waves are far less transient when compared with orthonormal or bi-orthogonal wavelets, and also imply that the description of waves based on suitable support length or life span is more likely to adhere to the physics.

- For the wavelet packet category we have the best basis and best level criteria. It may not be difficult to gain a prior idea that the chance is slim for getting better results using either of the bases. The obvious reason is due to the inherent limitation of wavelet packet transform — wavelet packet transforms are associated only with orthonormal bases. Since the primitive analyzing functions are orthonormal and since orthonormal wavelets perform poorly as just given above, it is therefore hard to anticipate the same strong performance as that of semi-orthogonal wavelets. Nevertheless, both wavelet packet criteria do show improvements when compared with the original orthonormal basis, and the performance of the best basis is certainly better than that of the best level. Figure 3.1 (p–W+WP+F)–(b) gives the wavelet packet best bases and best level curves for B&L and Meyer's wavelets; they do show improvements when compared with the corresponding curves in Figure 3.1 (p–W+WP+F)–(a) using regular wavelet transforms. It is quite certain that the improvement is not to the degree of semi-orthogonal wavelet or that of the Fourier spectrum.

- Figure 3.2 (p–WP BB+BL) shows cumulative distribution curves of the best level, best basis, and a few different levels bases wavelet packet coefficients, as well as the curve for the corresponding regular wavelet transform coefficients; here, all the curves are associated with ON77S. The curve for the best level comes close to that for the best basis. Again, wavelet packet best basis and best level yield lower entropy values than other relevant wavelet bases, but still their curves are far away from that of SO3D.

- Among orthonormal wavelets, we do not see clear differences arising from different degrees of symmetry (least asymmetric ONxxS or most asymmetric ONxxA); however, semi-orthogonal and bi-orthogonal wavelets are symmetric or antisymmetric, and their entropy values (concerning dual wavelets) are comparatively lower. It therefore indicates that the linear phase filtering is desired since symmetry or an-

tisymmetry implies linear phase of the two-scale sequence [1, 20]. Without the linear phase filtering visual impairment may occur. The non-symmetric distribution of time-frequency windows shown in figures 1.1 (TFW–WP BB) illustrates such a significant impact. Though symmetry is desired, it is hard to describe its influence since there are other factors that need to be considered (such as the support length and regularity, e.g., Meyer and B&L wavelets are also symmetric but their entropy values are not comparable to that of the ideal one).

3.4 Summary

Using various criteria of entropy statistics of transform coefficients we have identified among a vast array of Riesz wavelet bases the best basis for our water wave signals. It is found that the most prominent player is the semi-orthogonal cardinal spline wavelet with clear superiority over the Fourier basis in all criteria. And no other wavelets can ever reach the level of approximation given by Fourier spectra. Still, the results entail that many of the properties of the wavelets studied here are more of analytical interests and hard to be physically significant.

The solid performance of the semi-orthogonal wavelet indicates the usefulness of the modulated Gaussian wavelet or the Morlet wavelet in the continuous transform domain for our applications. Coupling with a few additional features that are specific to continuous wavelet transforms – such as its nature of redundancy, the flexibility in time-frequency resolutions, and the conciliatory choices of data segment of interest; there is something to be anticipated. ❖

Tab 3.1 (*H*–F+ON+SO) Entropy statistics of transform coefficients under various criteria for the orthonormal and the semi-orthogonal wavelet groups, as well as the orthonormal Fourier basis. The orthonormal groups cover the most symmetric and the most asymmetric group, as well as the most narrowly-banded (referring to frequency) Meyer wavelet and the most narrowly-distributed (referring to time) Battle and Lemarié wavelet. And the semi-orthogonal wavelet is devised by Chui [1, 2]. Note that the results in all categories for the dual semi-orthogonal wavelet are not only clearly better than the spectral ones but also far superior to any other wavelet groups.

Wavelet	L**2 coefficient entropy (0 division)	L**2 probability entropy (300 divisions)	L**1 probability entropy (300 divisions)	L**2 probability entropy (200 divisions)	Theotetical dimension (L**2 300 divisions)
B&L	4.691	1.330	3.417	1.179	3.782
Meyer	4.647	1.294	3.365	1.132	3.646
SO3O	4.833	1.669	3.756	1.488	5.307
SO3D	1.823	0.219	1.306	0.172	1.245
Spectrum	2.809	0.270	3.044	0.244	1.310
ON22A	4.993	1.761	3.891	1.516	5.815
ON33A	4.773	1.384	3.499	1.225	3.975
ON44A	4.790	1.517	3.596	1.363	4.559
ON55A	4.819	1.553	3.631	1.367	4.727
ON66A	4.790	1.373	3.456	1.203	3.946
ON77A	4.675	1.355	3.461	1.203	3.877
ON88A	4.645	1.229	3.283	1.082	3.418
ON99A	4.719	1.412	3.501	1.252	4.106
ON00A	4.787	1.423	3.511	1.244	4.149
ON44S	4.835	1.461	3.557	1.281	4.311
ON55S	4.758	1.492	3.576	1.298	4.426
ON66S	4.754	1.402	3.501	1.225	4.065
ON77S	4.751	1.336	3.331	1.188	3.804
ON88S	4.714	1.366	3.481	1.224	3.918
ON99S	4.755	1.469	3.570	1.288	4.345
ON00S	4.635	1.278	3.378	1.134	3.591
ON11C	4.938	1.696	3.832	1.457	5.452
ON22C	4.827	1.468	3.520	1.284	4.342
ON33C	4.756	1.488	3.573	1.333	4.427
ON44C	4.690	1.297	3.337	1.157	3.658
ON55C	4.644	1.309	3.405	1.154	3.703

Tab 3.2 (*H*–BO0+D) Entropy statistics of transform coefficients under various criteria for the bi-orthogonal wavelet groups. Again, none of the results here is comparable to those of the dual semi-orthogonal wavelet. And it is noted that a shorter distribution of convolution weights yields extreme and inferior value. Thus, the efficiency of computation is not pertaining to the intimacy of physics.

Wavelet	L**2 coefficient entropy (0 division)	L**2 probability entropy (300 divisions)	L**1 probability entropy (300 divisions)	L**2 probability entropy (200 divisions)	Theoretical dimension (L**2 300 divisions)
BO11O	5.395	2.623	4.502	2.299	13.777
BO11D	5.395	2.623	4.502	2.299	13.777
BO13O	4.943	1.806	3.883	1.627	6.084
BO13D	5.266	2.371	4.373	2.053	10.708
BO15O	4.866	1.678	3.755	1.495	5.357
BO15D	5.227	2.291	4.327	1.987	9.882
BO22O	5.282	2.362	4.363	2.083	10.609
BO22D	4.434	1.181	3.284	1.034	3.257
BO24O	4.963	1.862	3.985	1.634	6.438
BO24D	4.359	1.090	3.220	0.962	2.975
BO26O	4.881	1.703	3.835	1.492	5.490
BO26D	4.332	1.064	3.174	0.940	2.899
BO28O	4.857	1.624	3.782	1.452	5.073
BO28D	4.318	1.069	3.157	0.941	2.914
BO31O	5.824	3.174	4.741	2.835	23.894
BO31D	4.377	1.058	2.655	0.936	2.880
BO33O	5.084	2.001	4.062	1.756	7.393
BO33D	4.205	1.102	2.827	0.965	3.011
BO35O	4.850	1.697	3.847	1.506	5.457
BO35D	4.125	1.026	2.776	0.908	2.789
BO37O	4.790	1.658	3.821	1.442	5.247
BO37D	4.106	0.986	2.737	0.873	2.679
BO39O	4.776	1.660	3.835	1.432	5.258
BO39D	4.098	0.967	2.713	0.866	2.629

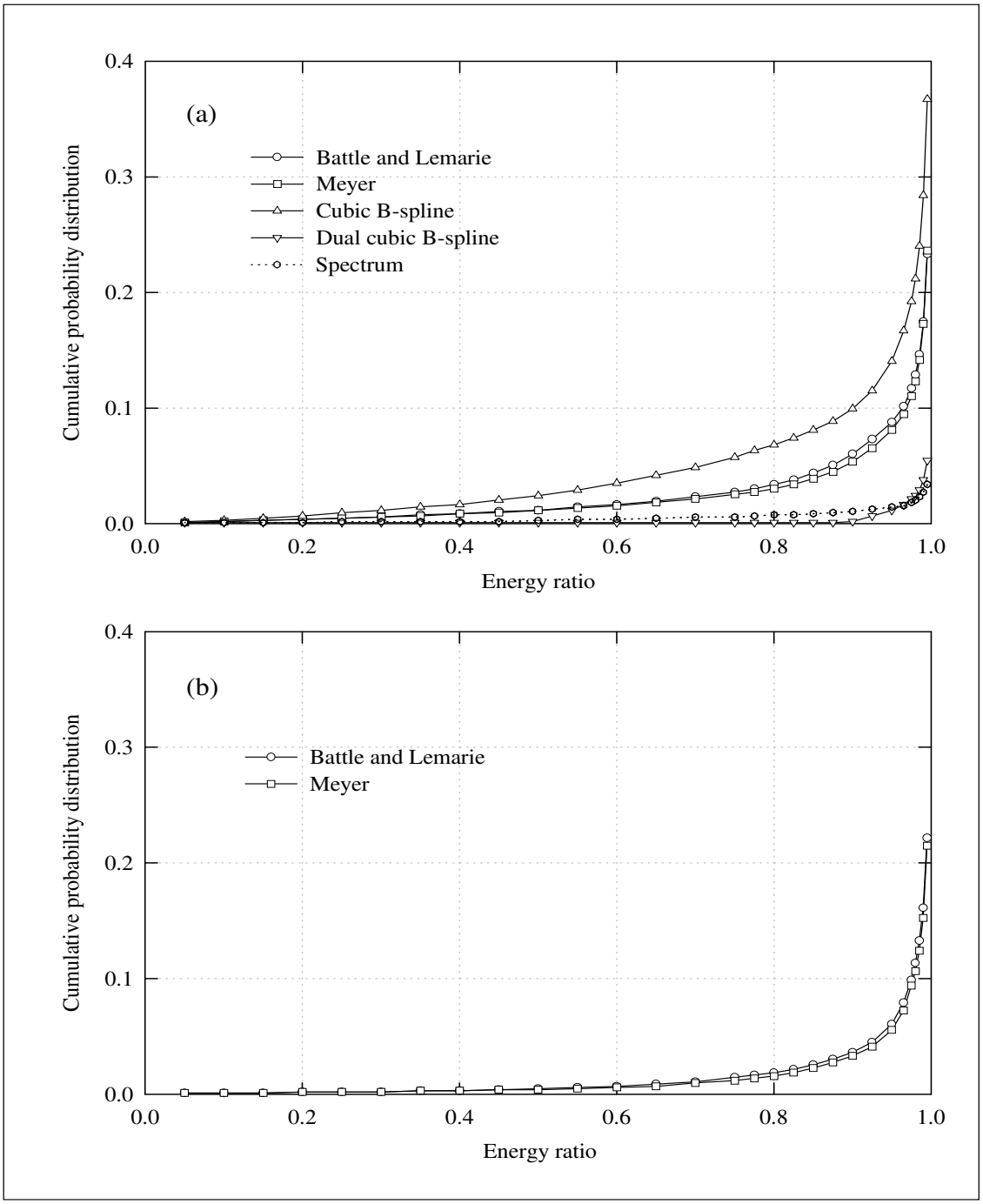

Fig 3.1 (p–W+WP+F) The cumulative probability distribution curves of the transform coefficients associated with three different transform categories. The coefficient PDFs intimately reflect L^2-norm energy relevance. Here the various bases include:
(1) Wavelets: Meyer, Battle and Lemarié, semi-orthogonal cubic B-spline, dual semi-orthogonal cubic B-spline `(top)`;
(2) Wavelet packets: those of the best packet bases based on Meyer wavelet and Battle and Lemarié wavelet `(bottom)`;
(3) Spectrum: Fourier spectral basis `(top)`.
Note the outstanding performance of the dual semi-orthogonal cubic B-spline wavelet (SOD). And its distribution clearly outperforms that of the Fourier spectrum for nearly all the energy ratio.

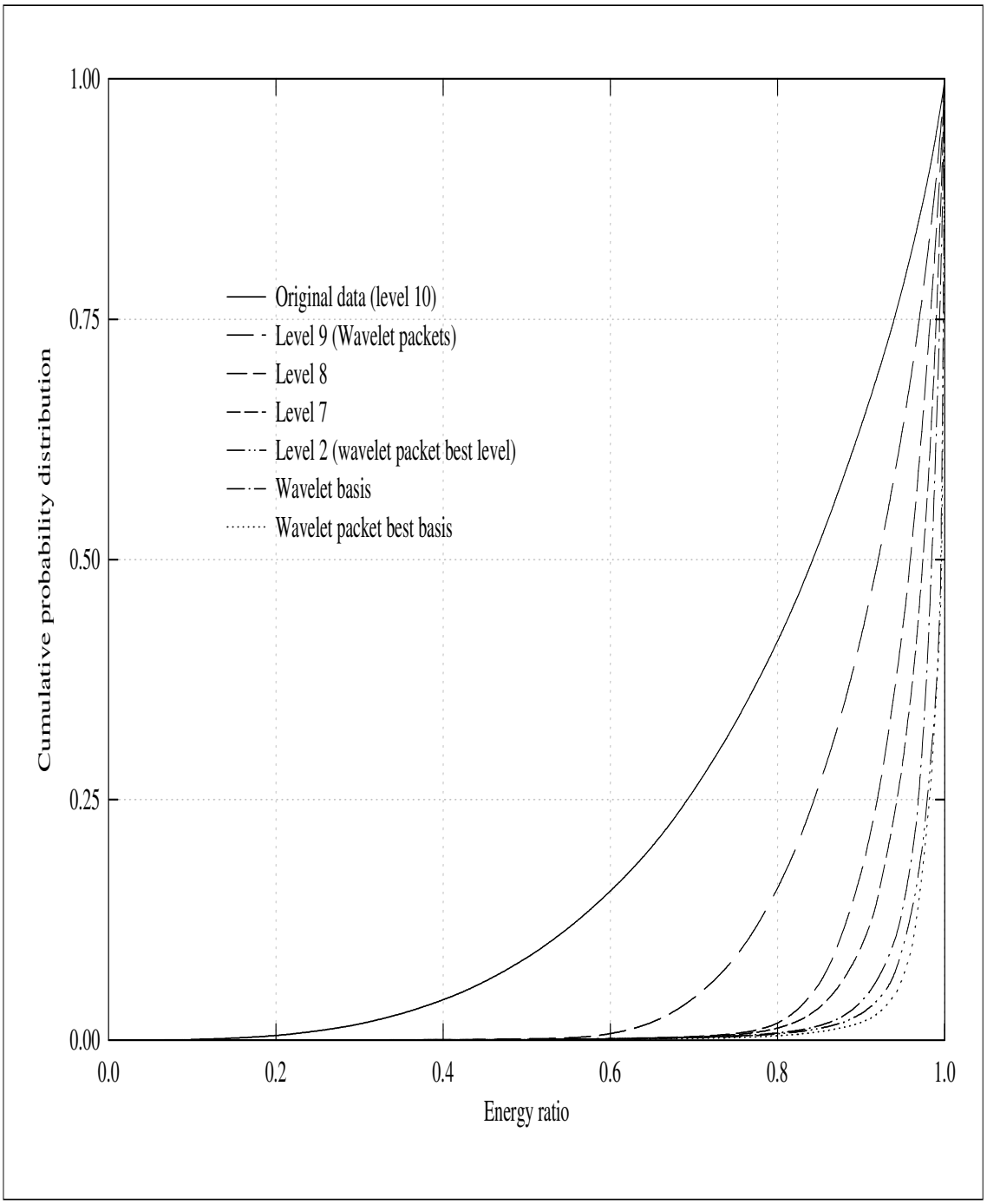

Fig 3.2 (p–WP BB+BL) The cumulative probability distribution curves of the Wavelet packet transform coefficients for the various bases derived from the seeding orthonormal mother wavelet ON77S. The PDFs are of L^2-norm energy content. The function bases include:
(1) Wavelet packet of the lowest levels (normal instance: wavelet basis);
(2) Wavelet packet of a specific level (9, 8, 7);
(3) Wavelet packet of the best level (2);
(4) Wavelet packet of the best basis (combined levels: dotted line).
Note that the best situation is the one for the best basis; but none of these curves is comparable to that of the dual semi-orthogonal wavelet (SOD) shown in the preceding figure.

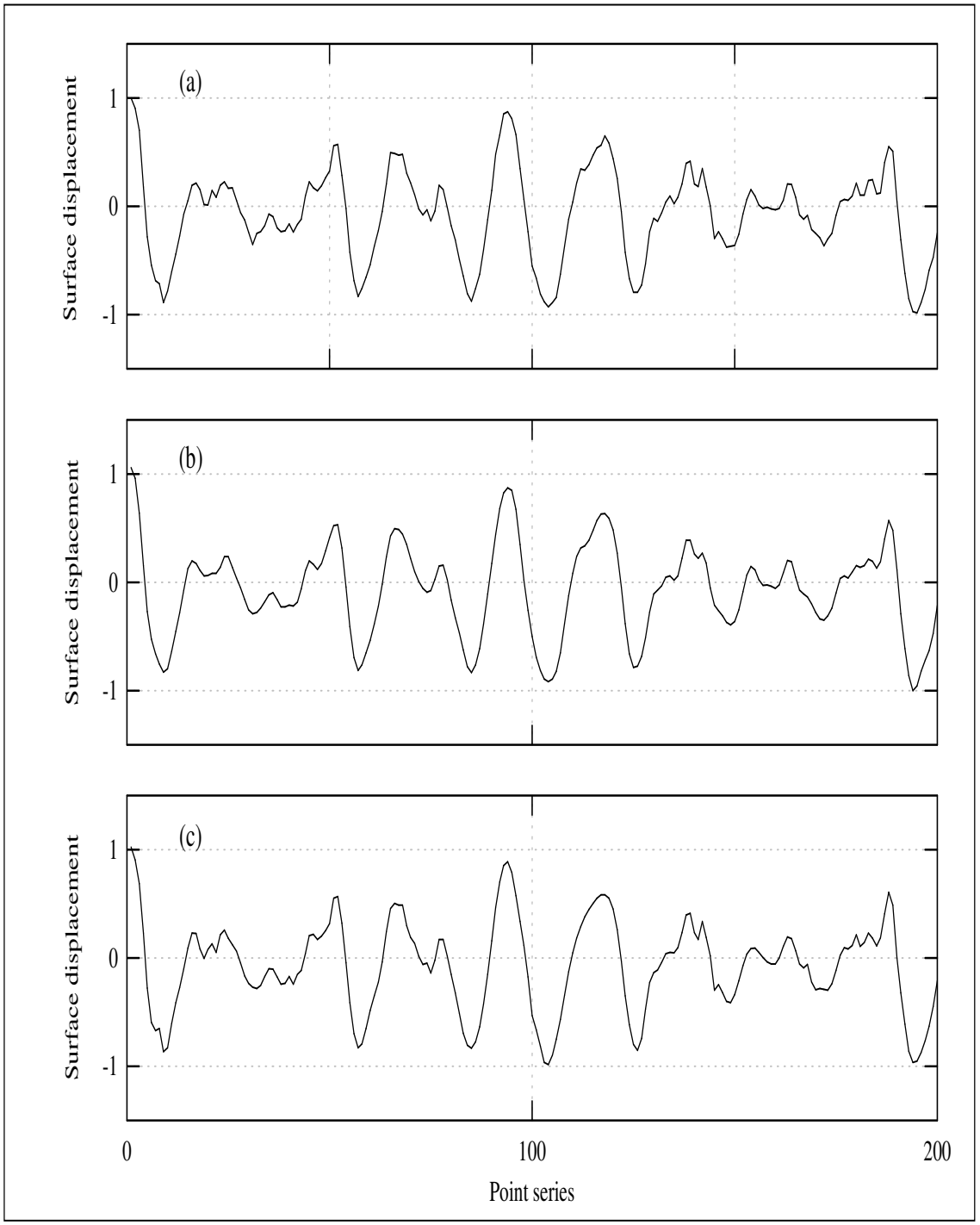

Fig 3.3 (ReC–Signal) Comparison of reconstructed signals associated with the best wavelet basis (i.e., the dual semi-orthogonal wavelet) and the Fourier basis. The semi-orthogonal wavelet is seen to better portrait the original signal, in particular, small scale transient features.
Here 35% of the transform coefficients are kept. The sub-figures show:
(1) a section of the original signal `(top)`
(2) reconstructed signal using the spectral coefficients `(middle)`;
(3) reconstructed signal using the best wavelet basis `(bottom)`.
The figure reflects the L^1-norm entropy relevance.

Chapter 4

The Role of the Characteristic Phase Distributions of Wavelets

4.1 The wavelet characteristic function m_0

In the previous chapter, the entropy of transform coefficients is used as a performance measure for wave simulation. The entropy approach is completely statistical and provides no mathematical insight of the basis property that leads to the usefulness of a basis in its modeling of water waves. Herein, we furnish the analytical essence that is connected to the modeling utility of a wavelet function basis. Moreover, practical implications of mathematical analyticity are stated. Herein the essence is concerning the phase distribution of a wavelet characteristic function for any individual basis. More specifically, the characteristic function is related to the filtering effect or convolution result associated with liner or non-linear phase filtering.

Following the convention used by Daubechies [20], the wavelet characterizing function is termed as the $m_0(\xi)$ function, which is the kernel of individual wavelet and has the following mathematical content:

A multiresolution analysis consists of a sequence of the closed subspaces V_j of the nested ladder,

$$\cdots V_2 \subset V_1 \subset V_0 \subset V_{-1} \subset V_{-2} \subset \cdots, \tag{4.1}$$

and satisfies the requirement

$$f \in V_j \Longleftrightarrow f(2^j \cdot) \in V_0. \tag{4.2}$$

The invariance of V_0 under integer translations states that

$$f \in V_0 \Longrightarrow f(\cdot - n) \in V_0 \text{ for all } n \in \mathbb{Z}. \tag{4.3}$$

Now comes the main statement that there exists $\phi \in V_0$ so that

$$\{\phi_{0,n};\, n \in \mathbb{Z}\} \text{ is an orthonormal basis or a relaxed Riesz basis in } V_0, \tag{4.4}$$

where, for all $j, n \in \mathbb{Z}$, $\phi_{j,n}(x) = \sqrt{2^{-j}}\phi(2^{-j}x - n)$, and the relaxation refers to the orthonormality. Quite often the ϕ here is formally called the scaling function of the multiresolution analysis. Furthermore, for the $\{\phi_{j,n};\, j, n \in \mathbb{Z}\}$ there exists its counterpart wavelet basis $\{\psi_{j,k};\, j, k \in \mathbb{Z}\}$, $\psi_{j,k}(x) = \sqrt{2^{-j}}\psi(2^{-j}x - k)$, such that

$$P_{j-1}f = P_j f + \sum_{k\in\mathbb{Z}} \langle f, \psi_{j,k}\rangle \psi_{j,k}, \tag{4.5}$$

where $P_j f$ is the projection onto V_j.

Since $\phi \in V_0 \subset V_{-1}$ and $\phi_{-1,n}$ are basis in V_{-1}, we have

$$\phi = \sum_n h_n \phi_{-1,n}, \tag{4.6}$$

with

$$h_n = \langle \phi, \phi_{-1,n}\rangle. \tag{4.7}$$

We therefore have

$$\phi(x) = \sqrt{2}\sum_n h_n \phi(2x - n) \tag{4.8}$$

or

$$\widehat{\phi}(\xi) = \frac{1}{\sqrt{2}} \sum_n h_n e^{-in\xi/2} \widehat{\phi}(\xi/2). \tag{4.9}$$

In an alternative form

$$\widehat{\phi}(\xi) = m_0(\xi/2)\widehat{\phi}(\xi/2), \tag{4.10}$$

where

$$m_0(\xi) = \frac{1}{\sqrt{2}} \sum_n h_n e^{-in\xi}. \tag{4.11}$$

Suffice it to say that the $m_0(\xi)$ function is intrinsic to the transcendental formulations of the mother wavelet and the two-scale equation. And it is comprised of the summation of convolution coefficients of wavelet construction (or filter coefficients corresponding to the support length of the wavelet) multiplied by the complex exponential functions of their individual scales.

4.2 Phase distributions and implications

Figures 4.1 ($m_0(\xi)$–MELE) to 4.7 ($m_0(\xi)$–BOD) show the phase distributions of $m_0(\xi)$ for all the wavelet categories listed in this study. Notable points are summarized below.

- Wavelets with similar visual appearance may possess extremal difference in the characterizing phase distributions, such as those shown in figures 4.1 ($m_0(\xi)$–MELE). Note that, regarding to the symmetrical wavelets, the Meyer wavelet is the most compactly supported wavelet in frequency domain while the Battle and Lemarié wavelet is the most compactly supported wavelet in time domain. For these two categories of wavelet, both their mother and father wavelets have quite similar distributions with respect to each other, as shown in 2.15 (MFW–SO0) and 2.14 (MFW–B&L). But the behavioral difference between their phase curves suggests that there exists theoretical complexity both in mathematics and numerics of the two wavelet constructions; moreover, it hints that physical applicabilities might not sensitive to theoretical differences.

- Combing the entropy results yielded in the preceding chapter with the phase distributions of all the wavelet categories shown here, we see that a linear phase distribution is unable to guarantee the best performance for modeling signals of water waves. What should be emphasized is that the most outstanding feature leading to the modeling usefulness of the semi-orthogonal wavelet lies in the characteristic of a peculiarly constant phase distribution for either the wavelet or its dual, as shown in figure 4.2 ($m_0(\xi)$–SO). Besides, the intuitive byproduct is that there is the strong implication that most wavelets are too exotic, as well as too alienating, to water waves.

- The more asymmetric the shape of a wavelet is the more complex of its phase distribution comes along. The distributions of the least asymmetric orthonormal group ONxxS are shown in figure 4.3 ($m_0(\xi)$–ONS) and those of the most asymmetric are shown in figure 4.4 ($m_0(\xi)$–ONA). These distributions, together with those of the previous figures, denote the relation between wavelet symmetry and water wave physics and also imply the poor performance in modeling for compactly supported wavelets (i.e., with limited number of filtering wights).

- The lengthening of the support length of a wavelet group may still yield even more irregular phase distributions as are shown in figure 4.4 ($m_0(\xi)$–ONA). And this disproves any possible benefit that may arise from further expansion of the construction concerning the support length of these orthonormal wavelets.

- The Coiflets are symmetry and have vanishing moments for both the mother and father wavelets but their phase distributions are not much different from those of the least asymmetric wavelets, as are shown in figure 4.5 ($m_0(\xi)$–ONC). It is therefore expected that their modeling capability can be of little refinement from the ONxxA group.

- The phase distribution curves for the bi-orthogonal wavelets and their duals are the same not only for all the support lengthes within their subgroups but also for the

respective crossovers, as are shown in figures 4.6 ($m_0(\xi)$–BO0) and 4.7 ($m_0(\xi)$–BOD). Again, this shows that lengthening the support length of these wavelets provides no benefit.

- Judging from all those mentioned above and that extremal mathematical properties of wavelet categories have been covered in this study, we therefore don't see any possibility that there exists other orthonormal or compactly supported wavelets that might provide suitable or better characterization for water wave physics.

4.3 Summary

Simply put, the most important and practical entailment of this chapter is to furnish the idea that water waves in their shapes or forms are intrinsically extremely "regular" and "unconstipated" when compared to those of almost all of the discrete wavelets, except the cardinal spline wavelet. And, in a simple and blunt way, those mathematical complexity of wavelet formulations do not reverberate our real world anticipations for physics and may be overkill. ❖

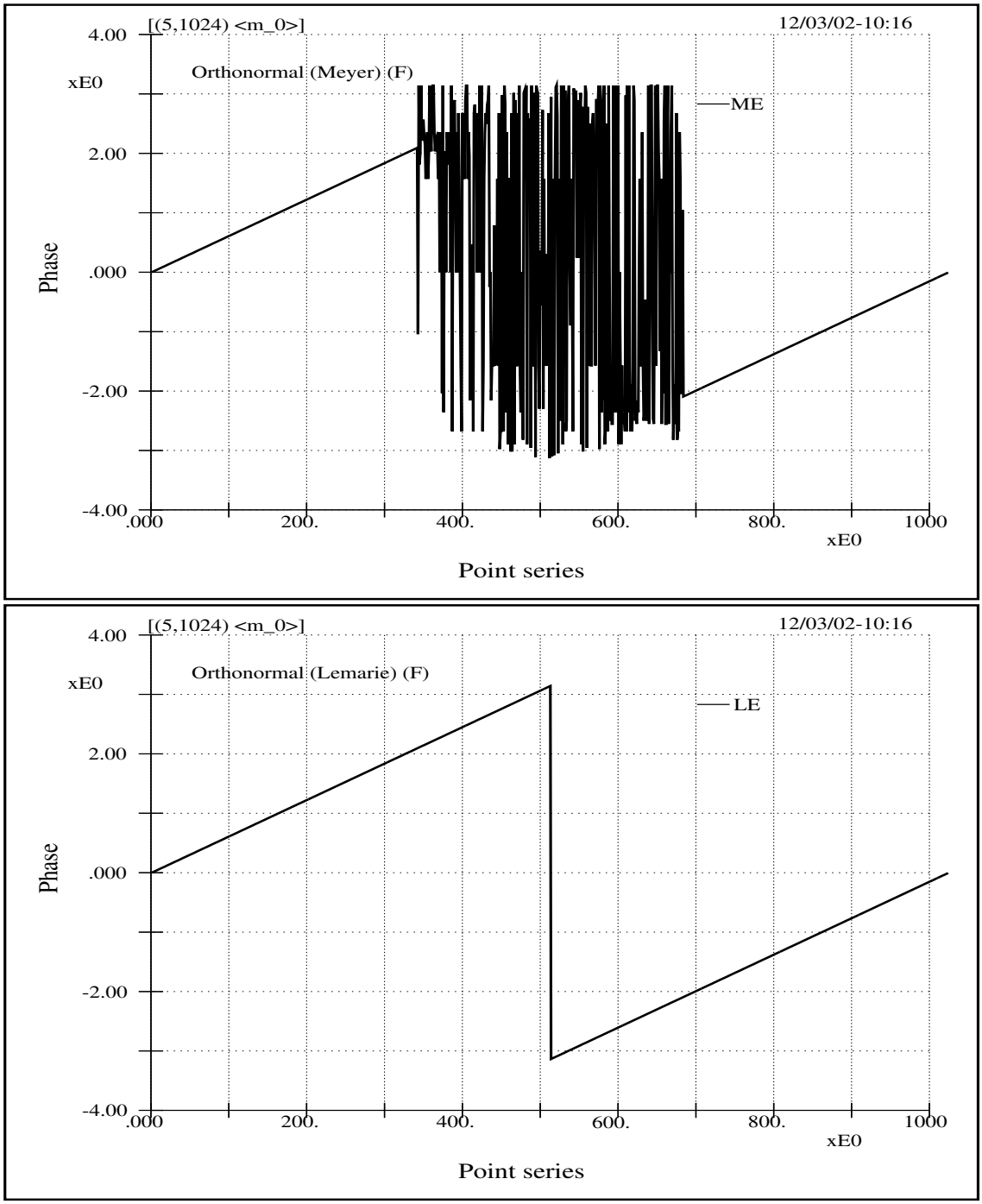

Fig 4.1 ($m_0(\xi)$–MELE) The phase distribution of the wavelet characteristic function $m_0(\xi)$ for two categories of wavelets: the Meyer wavelet (`Top`) and the Battle and Lemarié wavelet (`Bottom`). For the two categories of wavelets, both their mother and father wavelets, respectively, have quite similar distributions, as are shown in 2.15 (MFW–SO0) and 2.14 (MFW–B&L). Whereas, on the one hand, the Meyer wavelet is the most compactly supported wavelet in the frequency domain; on the other hand, the Battle and Lemarié wavelet is the most compactly supported in the time domain. Here the difference between the two distributions implies the possible ramification both in mathematics and numerics of the two wavelet constructions. Besides, it hints the intricate concerns among theoretical complexity and physical applicabilities.

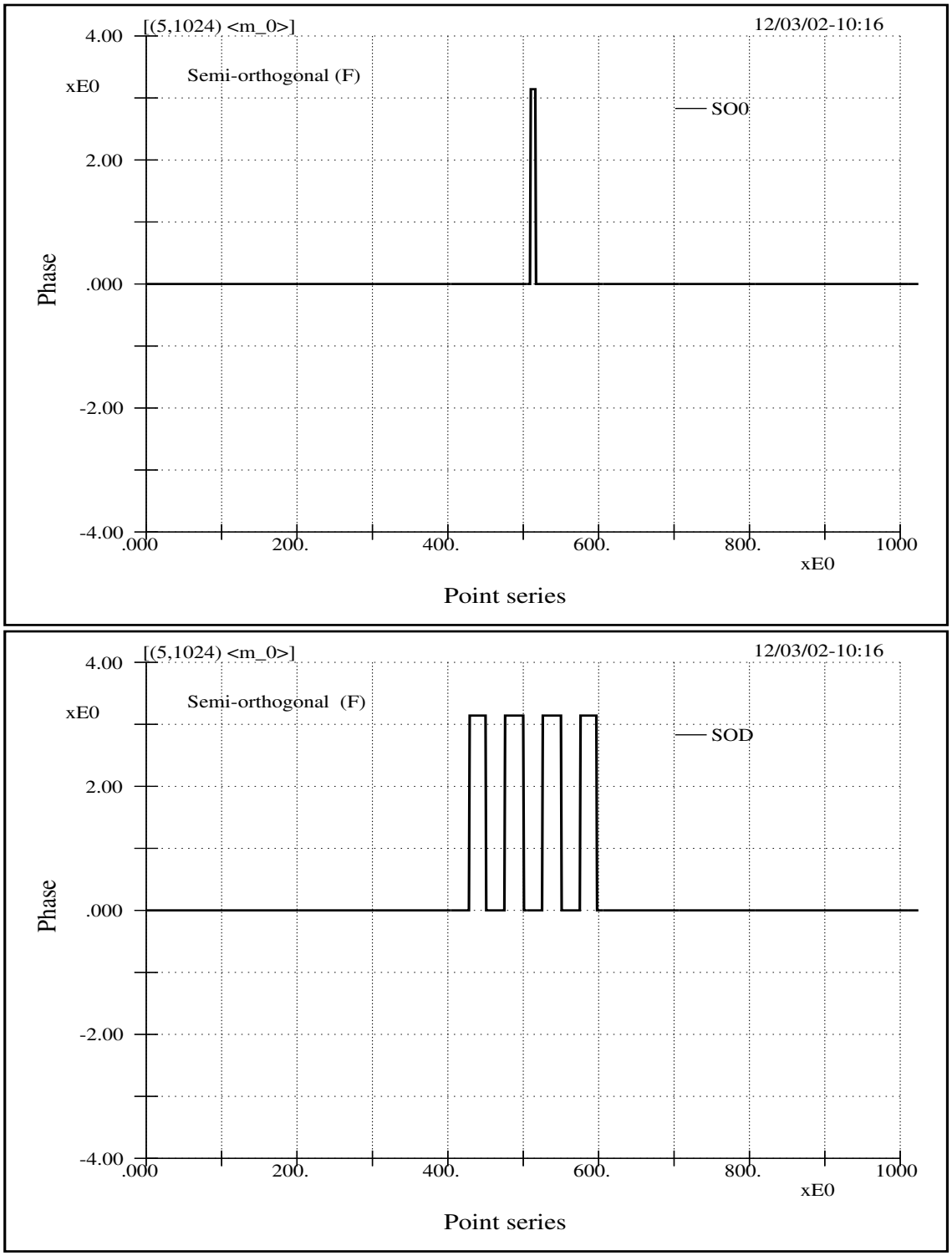

Fig 4.2 ($m_0(\xi)$–SO) The phase distributions of the wavelet characteristic function $m_0(\xi)$ of the semi-orthogonal cardinal spline wavelet (`Top`) and its dual (`Bottom`). Here the most outstanding feature, which leads to the usefulness in its modeling of water waves, lies in the peculiar distribution of a constant characteristic phase. Besides, there is an important implication that most of the wavelets are too exotic, as well as estranging, to water waves.

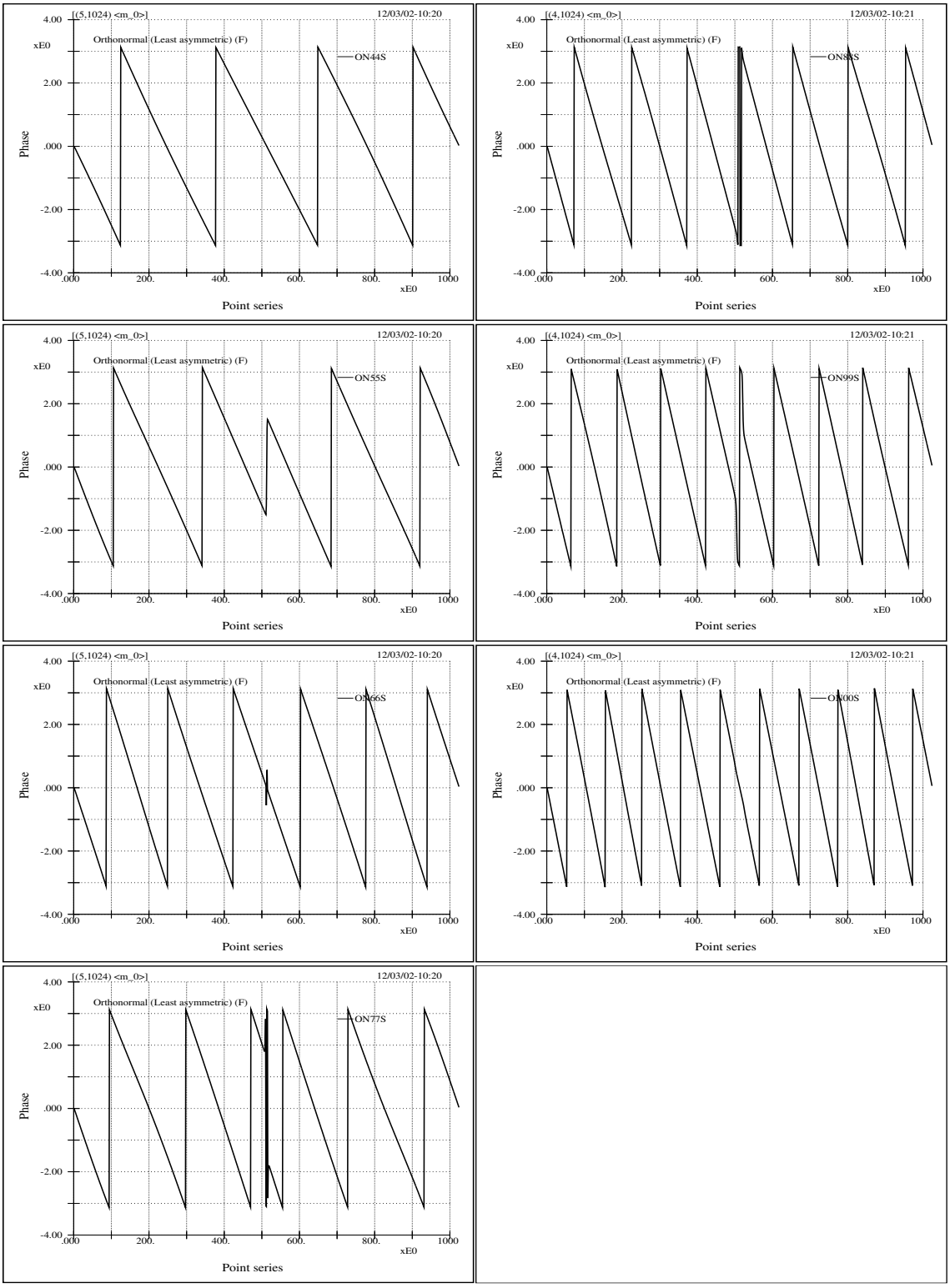

Fig 4.3 ($m_0(\xi)$–ONS) The phase distributions of the wavelet characteristic function $m_0(\xi)$ for the least asymmetric orthonormal group ONxxS. Comparing the curves here with those of the next figure we see that the more asymmetric the wavelet is the more the complication of its phase distribution comes along. This phenomenon implies the worsening modeling performance for the asymmetrical group and hints the relation between wavelet symmetry and water wave physics.

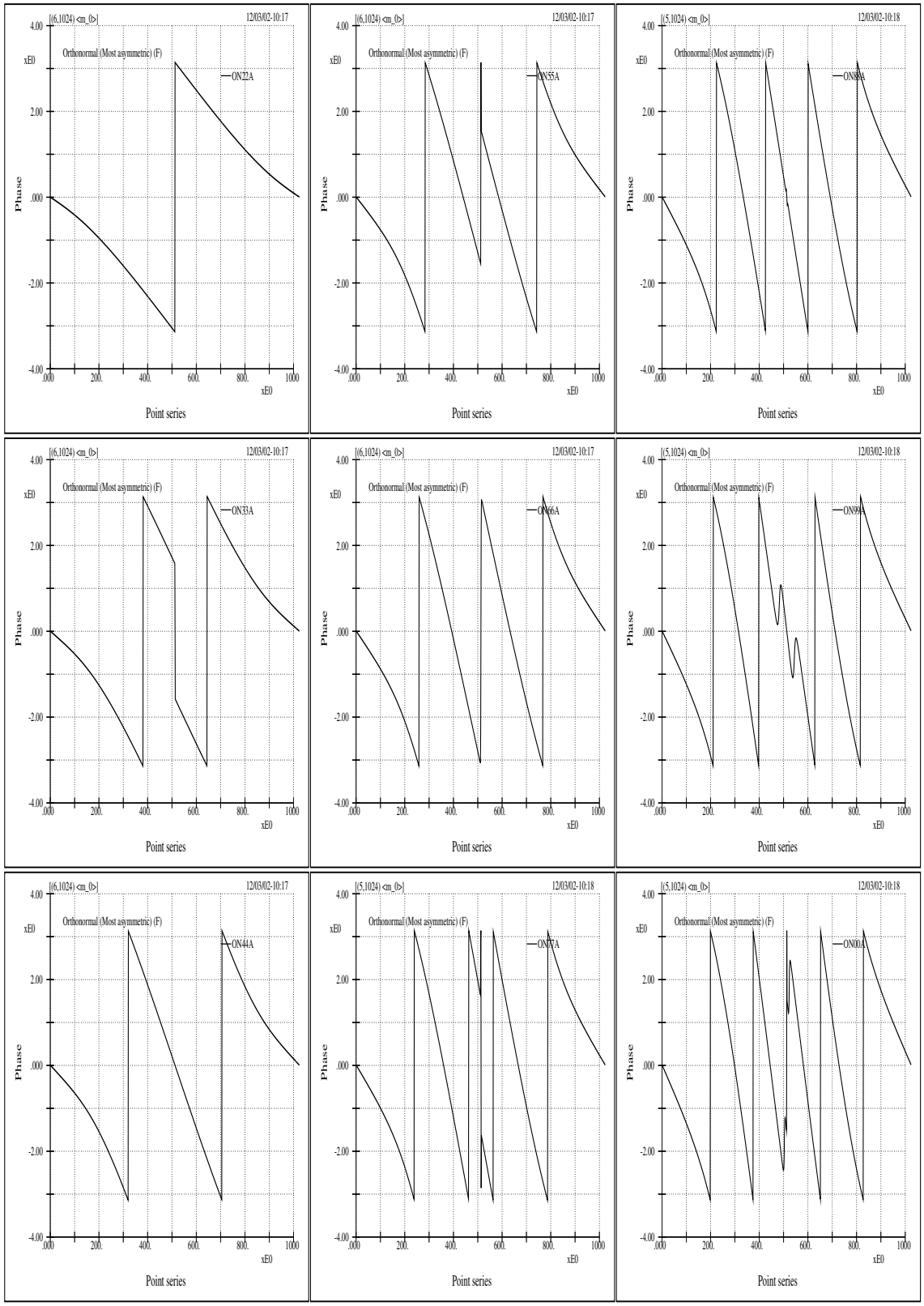

Fig 4.4 ($m_0(\xi)$–ONA) The phase distributions of the wavelet characteristic function $m_0(\xi)$ of the most asymmetric group ONxxA. Note that the lengthening of support length of the wavelet yields even more irregularity in distribution. Again, this disproves any possible benefit that may arise from any further expansion of the construction of these orthonormal wavelets.

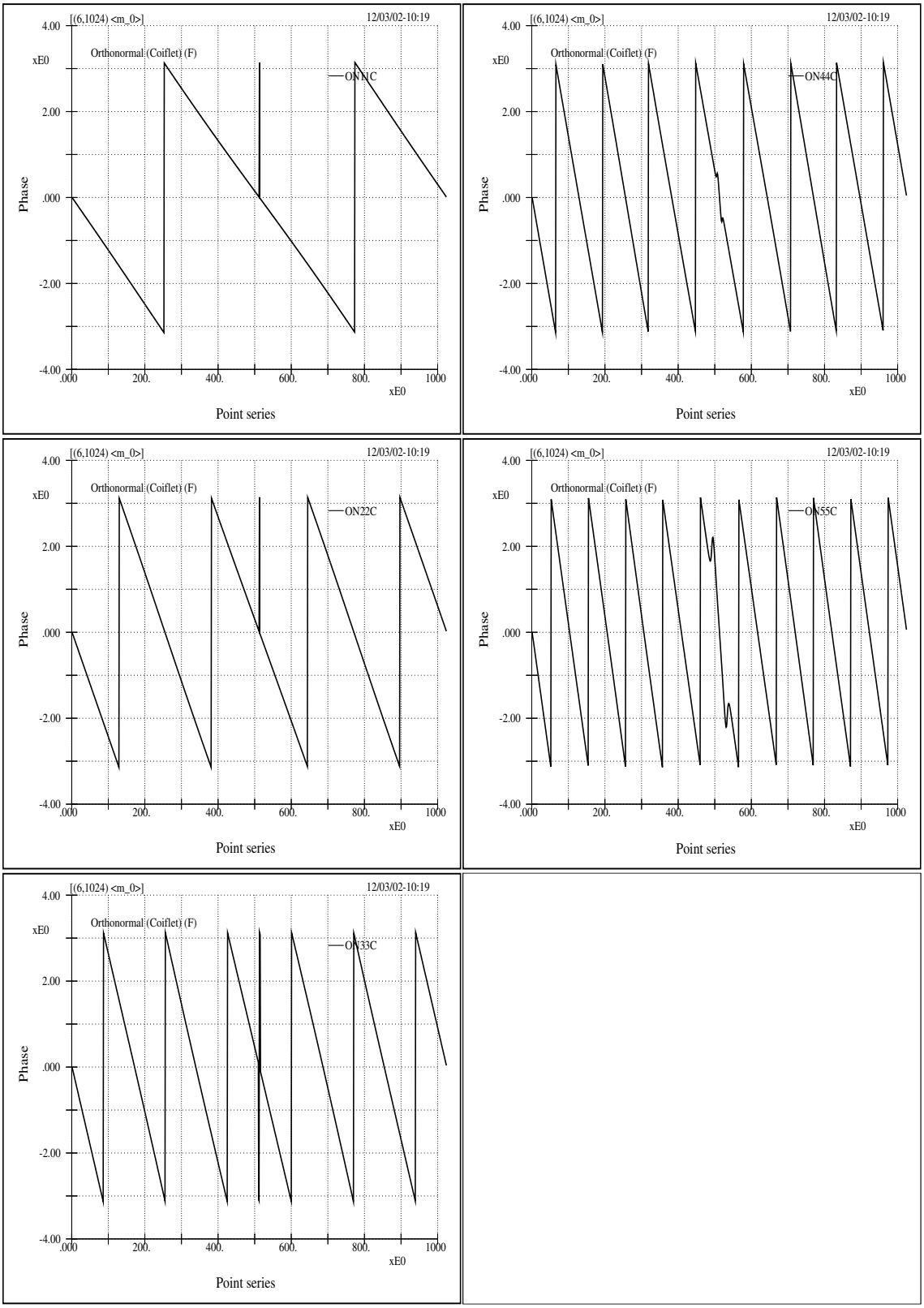

Fig 4.5 ($m_0(\xi)$–ONC) The phase distributions of the wavelet characteristic function $m_0(\xi)$ of the Coiflets. The Coiflets are symmetry and have vanishing moments for both their mother and father wavelets; but their phase distributions are not much different than the least asymmetric compactly supported group ONxxA. It is therefore expected that their modeling performance is of little betterment.

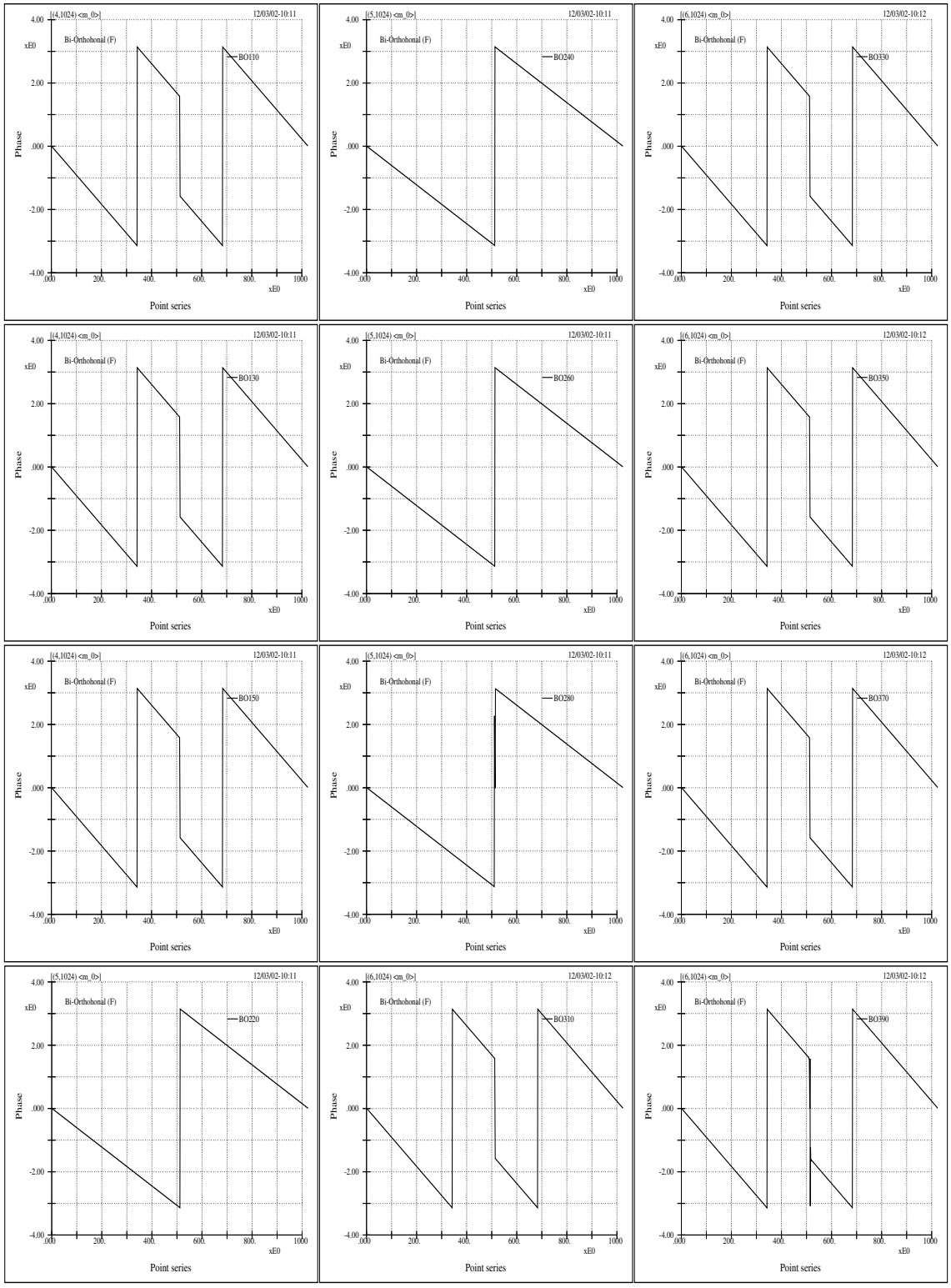

Fig 4.6 ($m_0(\xi)$–BO0) The phase distributions of the wavelet characteristic function $m_0(\xi)$ of the bi-orthogonal wavelets BOxy0. Their distributions are almost identical to those of their dual wavelets as to be shown in the next figure; nevertheless, the entropy values of these wavelets are clearly inferior to those of their dual wavelets. Again, the phenomenon implies the possible ramification both in mathematics and numerics of the wavelet constructions and hints the intricate concerns among theoretical complexity and physical applicabilities.

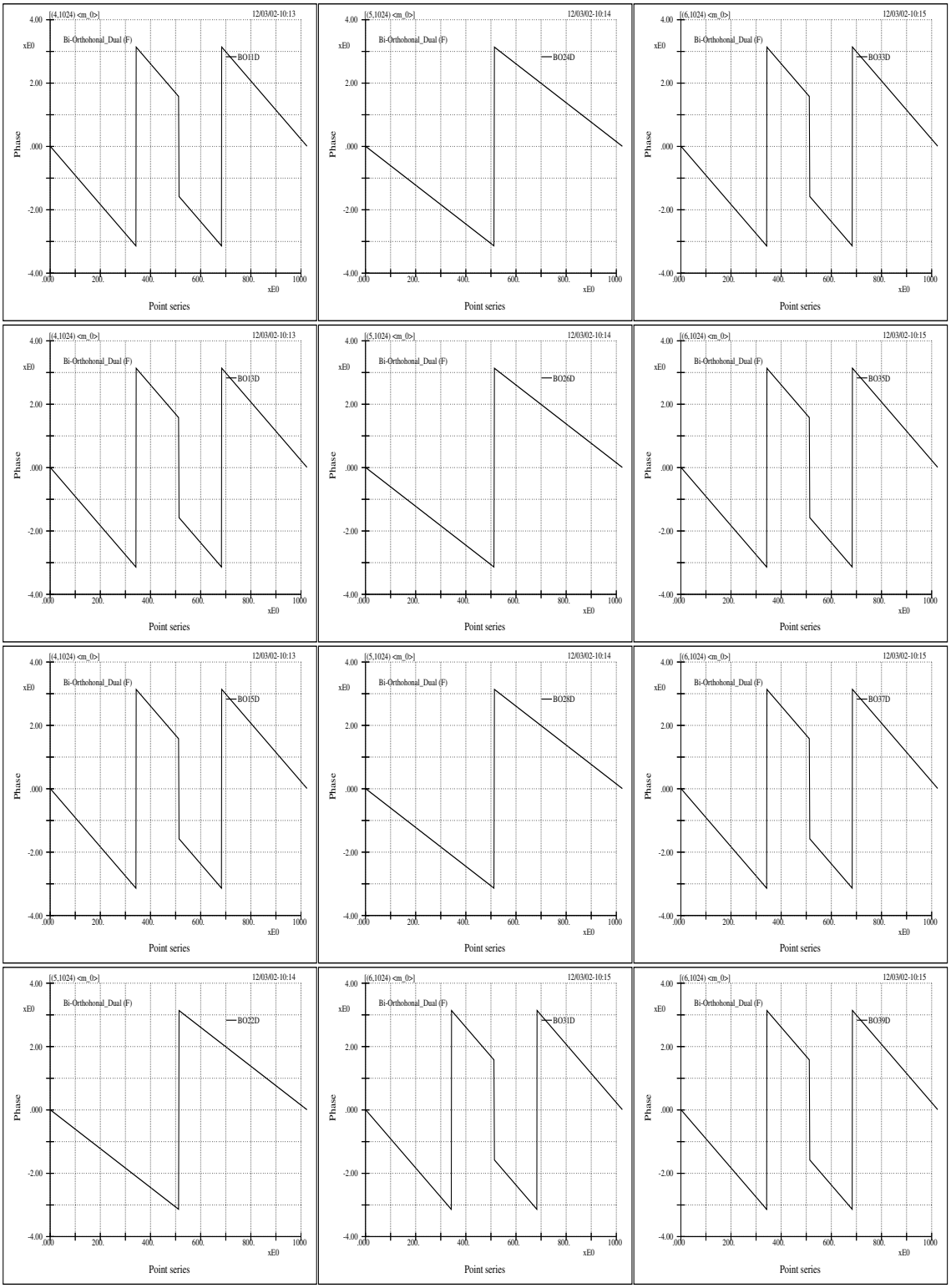

Fig 4.7 ($m_0(\xi)$–BOD) The phase distributions of the wavelet characteristic function $m_0(\xi)$ of the dual bi-orthogonal wavelets BOxyD. These phase distribution curves and those of their duals are the same not only for all the support lengthes within their subgroups but also for the respective crossovers, as shown in the last one (figures 4.6 ($m_0(\xi)$–BO0)). Moreover, here it also indicates that the mathematical complexity of wavelet formulation does not reverberate our real world anticipations and may be overkill.

Chapter 5

The Counterpart Best Wavelet in the Continuous Domain

5.1 Introduction

In the previous chapter on entropy the semi-orthogonal cardinal spline wavelet was identified as the most suitable Riesz wavelet basis for our signals. However, this discrete wavelet and its associated analyzing scheme is not what will be directly adopted in the verification of the optimality through the comparisons of coherent behaviors, as to be given later. The most fundamental concerns are in three aspects. First, the previous chapter concerns the discrete wavelet transform where each translation step is an integer multiple of the dilation scale which is in the logarithmic measure with base 2; therefore, both the translation and the dilation vary in logarithmic measure. Whereas in the study of coherences the scheme used concerns the continuous wavelet transform where the translation step can be as small as the sampling interval for all scales which can basically be specified arbitrarily. Second, the wavelets in the previous chapter handle bases with frame bounds that are either tight or relatively tight. Whereas the wavelet employed here does not involve frame bounds and might not have frame bounds at all when it is analyzed in the sense of discrete wavelet transform, i.e., not even related to a Riesz wavelet. Third, all the discrete wavelets listed here are real wavelets; therefore, they are only related to the term of "scale" and how can the phase come by so as to render a more practical term of

real physics.

Herein we will make further clarifications for these two points and try to illustrate their respective advantages and disadvantages since they are keys to the usefulness of the analyzing basis and the associated scheme for our applications.

5.2 The counterpart best continuous wavelet

Let the Gaussian function be

$$g_\alpha(t) = \frac{1}{2\sqrt{\pi\alpha}} e^{-\frac{t^2}{4\alpha}}, \tag{5.1}$$

where α is a representative value of the second moment of the Gaussian function and the constants is for the purpose of normalization, the modulated Gaussian is

$$G^\alpha_{b,\omega}(t) = e^{i\omega t} g_\alpha(t-b). \tag{5.2}$$

And the Gabor transform of a function f is

$$\left(\mathcal{G}^\alpha_b f\right)(\omega) = \langle f, G^\alpha_{b,\omega}\rangle = \int_{-\infty}^{\infty} f(t) e^{-i\omega t} g_\alpha(t-b)\mathrm{d}t. \tag{5.3}$$

As is stated by Daubechies [20] that the Morlet wavelet is almost identical to a modulated Gaussian, and as is given by Chui [1] a modulated Gaussian matches almost exactly with cardinal B-spline wavelet of order greater than or equal to three, i.e., for $m \geq 3$, the even order ψ_m's (such as the cubic spline wavelet ψ_4) match almost exactly with

$$\mathrm{Re}G^\alpha_{b,\omega}(t) = (\cos\omega t) g_\alpha(t-b) \tag{5.4}$$

and the odd order ones with

$$\mathrm{Im}G^\alpha_{b,\omega}(t) = (\sin\omega t) g_\alpha(t-b) \tag{5.5}$$

for a certain set of values α, b, ω.

In accord with these observances we therefore have an extremely natural transition from the best discrete basis to the following continuous wavelet, i.e., the Morlet wavelet,

$$\psi(t) = \pi^{-1/4}(e^{-i\omega_0 t} - e^{-\omega_0^2/2})e^{-t^2/2}. \tag{5.6}$$

Most importantly, such a correspondence introduces two terms in physics, i.e., the phase and carrier frequency, and thus make possible the enhancements of physical modeling of water wave signals, as to be provided in the following chapter.

5.3 Discrete versus continuous transforms

In the introductory chapter we listed a few properties related to different time-frequency analysis methodologies, such as Fourier transform, short time Fourier transform (STFT), Hilbert transform and the analytical signal procedure, the discrete wavelet transform (DWT), as well as the continuous wavelet transform (CWT). In fact, one of the main themes for all those discussions centered on the aspiration regarding the minimization of uncertainty effects [38]. And this is the most outstanding feature that the continuous transform comes into play. And why there is a need of the counterpart continuous wavelet with regard to the best discrete wavelet.

In this chapter, inheriting the identified discrete optimum basis, we mainly focus on the different usages of DWT and CWT concerning their practical applications to water waves related signals. That is to say, what is the counterpart wavelet in the continuous wavelet transform to the semi-orthogonal cardinal spline wavelet and why there is the need of a continuous one.

Herein we emphasize that DWT and CWT should be treated as two different entities — since, unlike the discrete and continuous Fourier transforms where they are dealing with the same basis as well as deploying basically the same formulations, DWT and CWT

generally refer to two quite different methodologies which focus on their individual function bases as well as different data treatment schemes. Most profoundly we press on the concerns of the following points:

- In general, the dilation lattice is in logarithmic measure for discrete wavelet transform (e.g., the $a_0{}^j$ in the stability condition to be mentioned) and in linear measure for discrete short time Fourier transform (e.g., the $e^{-i2\pi mt}$ in the above mentioned Gabor type frame). Continuous transforms do not involve lattice. The concept of lattice is associated with the concept of time-frequency density, which is defined as the inverse of the product of dilation and translation steps [20]. For short time Fourier transform frames, due to Shannon sampling theorem, the time-frequency density must not go beyond the value of generalized Nyquist density, $(2\pi)^{-1}$. For wavelet transform, however, there is no such a clear-cut limit of time-frequency density. Moreover, Balian-Low theorem depicts that there is no good time-frequency localization for a short time Fourier transform frame if constructed under a strict time-frequency lattice; on the contrary, numerous wavelet bases with good time-frequency localization have been given [1, 20, 55]. These physically imply that wavelet transform may provide better zoom-in.

- The existence of a lattice structure can be either practical or impractical. For water waves, if we don't anticipate any significant gaps in the scale contents, that is to say, the physical process involves time and spatial scales that are "changing" or "evolving" in a relatively continuous sense, we generally do not appreciate the use of frames. Here a continuous transform may provide better chance of success.

- Both continuous and discrete wavelet transforms implement a process of integral wavelet transform over the real line $\mathbf{R}$ in a continuous sense but they analytically emphasize the use of different integration symbols: $\sum$ and $\int$. Digitally sampled signals are certainly discrete, but this is irrelevant to the methodology of continuous wavelet transform or discrete wavelet transform. The main difference, from

the application point of view, is that there is no practical interest of reconstruction (or inverse transform) for continuous wavelet transform due to the redundant or non-orthogonal nature of its wavelet coefficients. Both methods are capable of decomposing either functions defined over the real line or signals sampled discretely. In reality, applying continuous wavelet transform to sampled data is implemented in a discrete manner; vis-à-vis, doing discrete wavelet transform for an unlimited ladder, such as that of the standard multiresolution analysis of [48], can describe any function in infinite detail, i.e., over the whole real line. The concept of unlimited ladder of discrete wavelet transform is illustrated by two examples shown in figures 2.23 (BU–BO2yO) through 2.30 (BU–BO35O) where the blow-ups of individual segments of wavelet curves are shown. The figure also illustrates possible bizarre behaviors of certain wavelets and indicates that mother wavelets with short support lengths might not be of ideal choices. In addition, a few discrete wavelet transform formulas when generalized in the limit sense are quite helpful in explaining a few continuous wavelet transform characters.

- All of the Riesz wavelets studied in the earlier chapter handle bases with frame bounds that are either tight or relatively tight; whereas the continuous wavelet does not involve frame bounds and might not have frame bounds at all when it is analyzed in the sense of discrete wavelet transform, i.e., not even qualified as a Riesz wavelet. However, we will see that there is a very natural transition from the discrete wavelet to its continuous counterpart.

- Apart form the specific features listed in the above items, there is a practical interest in what can be done to improve the physical relevance between the basis functions and the wave constituents of our signals. For example: does the decaying features of basis functions akin to the physics of component waves? And this is the topic to be discussed in the next chapter.

5.4 The physical perspective of Morlet wavelet

The combination of "Wave" and "let" hints the core concept of wavelet analysis. And the concept implies that the distribution properties of the basis functions both in time or frequency domains are at the heart of all sorts of function bases. More specifically, different intricate analytical properties of wavelets are just manifestations to these distribution features. However, since two decay properties that are analytically or mathematically quite differentiable may only have very minor visual differences in their wave forms (such as those shown in figures 2.13 (MFW–Meyer) and 2.14 (MFW–B&L)), one generally bears the feeling that wavelets' physical implications is not proportional to their analytic interests. Nevertheless, we still can benefit from the wavelet approach due to its flexibility in devising the analyzing wavelets as well as its adaptability in forging the algorithms. But versatility does not come without the price of ambiguity. For example, the power spectra of a function are shift-invariant; whereas, wavelet spectra are highly shift-variant [51]. Figure 5.1 (SNI–Phase) and 5.2 (FS–T&P) shows such a property and it gives us the idea of how significant the phase effects may be. And this figure should be regarded as the counterpart figure in the wavelet analysis to those in the Fourier analysis given in a previous study on the analytic signal approach by the author [41]. Note that all these figures indicate the possible usefulness associated with the uses of non-orthonormal or redundant function bases, as well as the drawbacks of bases with tight frame bounds.

5.5 Wavelet frame bounds and redundancy

If a function $\psi(t)$ is to be qualified as a wavelet of CWT, then the only requirement is that $\psi(t)$ meets the "admissability condition,"

$$2\pi \int_{-\infty}^{\infty} \frac{|\widehat{\psi}(\omega)|^2}{|\omega|} d\omega = C_\psi, \tag{5.7}$$

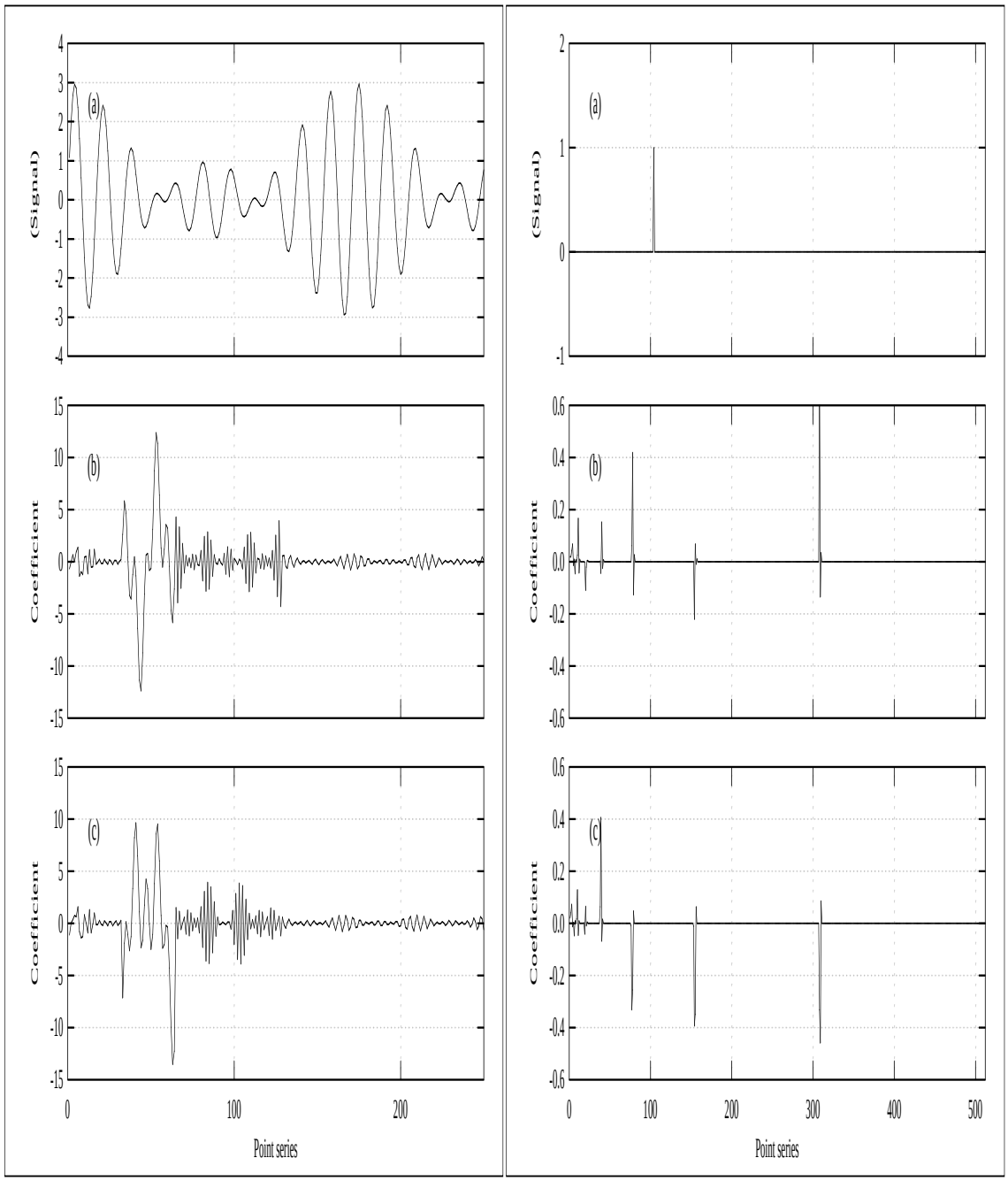

Fig 5.1 (SNI–Phase) The concerns related to the shift non-invariant property of wavelet transforms are shown in this figure. This property has important implications in the practical usefulness in physical applications of wavelets between discrete and continuous bases.
The top sub-figure in each column shows original signal individually.
The middle one shows its wavelet transform distribution.
The bottom one shows the transform result for its individually shifted signal.
For the signal in the left column it is shifted 3 points to the left and the wavelet used is ON33A. For the signal in the right column it is shifted 20 points to the left and the wavelet used is BO22D.
The property shown in this figure is linked to the vast difficulty arising from phase noise and its poor performance in coherent studies.

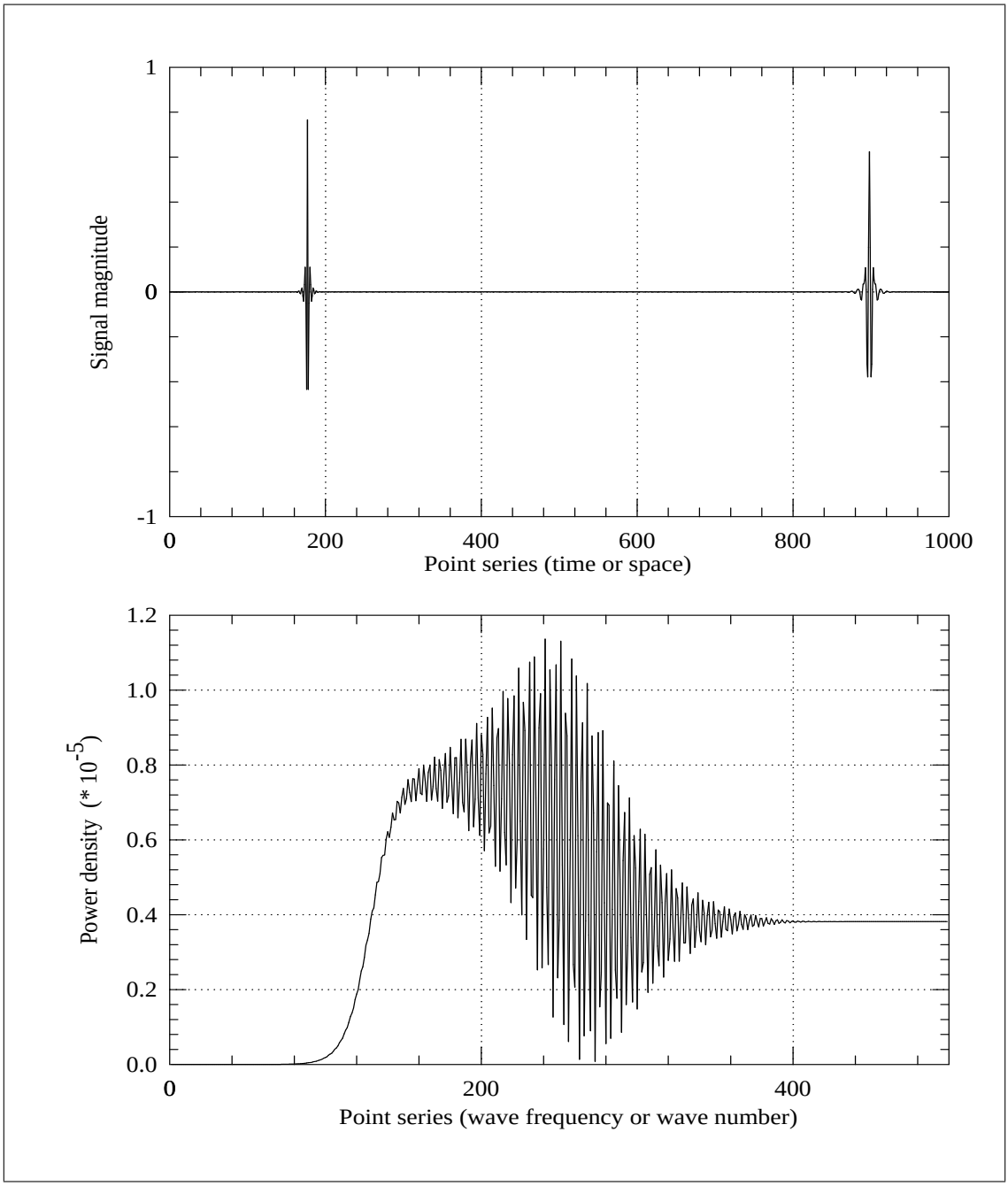

Fig 5.2 (FS–T&P) This figure shows somewhat the same concern as that of the preceding figure, but with different method of rendition. More precisely, the effects of ambiguity and phase noise arising from local transient features of a signal are illustrated using a signal comprised of two separated wavelets.

The top sub-figure shows the signal comprised of two Lemarié wavelets located at two neighboring scales (the least two scales within a 1024-point series). And the pulse at left corresponds to the inverse wavelet transform for unit wavelet coefficient at point 600, i.e., e600; the right corresponds to e470.

The Fourier power spectrum is shown in the bottom sub-figure. The distracting consequence arising from extreme variation should be comprehendible.

where C_ψ is a constant specific to individual ψ, and $\widehat{\psi}(\omega)$ is the Fourier transform of $\psi(t)$. Here, among several definitions of the Fourier transform forward and inverse pair, the adopted one is:

$$\widehat{\psi}(\omega) = \frac{1}{\sqrt{2\pi}} \int_{-\infty}^{\infty} \psi(t) e^{-i\omega t} dt \tag{5.8}$$

and

$$\psi(t) = \frac{1}{\sqrt{2\pi}} \int_{-\infty}^{\infty} \widehat{\psi}(\omega) e^{i\omega t} d\omega. \tag{5.9}$$

The admissability condition is the integration of power spectrum weighted by the inverse of the absolute value of frequency; therefore, it implies that the wavelet should have little power at low frequency and is total nil at zero frequency, i.e., the area between the wavelet curve and the abscissa integrates to zero. This feature of reasonable decay and finite support length is the outright instinct of wavelet. The dilated and translated versions of this wavelet are $\psi_{a,b}(t) = \frac{1}{\sqrt{a}}\psi(\frac{t-b}{a})$, where $a > 0$ and $a \in \mathbf{R}$ and $b \in \mathbf{R}$ are the dilation and translation parameters, respectively; and $\frac{1}{\sqrt{a}}$ is the normalization factor for L^2-norm. The $\psi_{a,b}$ satisfies admissability condition too.

The admissability condition is a very loose constrain; it does not provide a clear concept of redundancy concerning applying CWT to discretely sampled signals. To illustrate this redundancy, let us use the discrete wavelet frame (since the frame wavelet certainly qualifies as a wavelet for CWT): $\psi_{a_0,b_0;j,k}(t) = {a_0}^{-j/2}\psi({a_0}^{-j}t - kb_0)$, where a belongs to the set of discrete dilations a_0^j and b to the set of discrete translations $a_0^j k b_0$; $j, k \in \mathbf{Z}$; and $a_0 \neq 1$ and $b_0 > 0$ are fixed positive constants. For such a discrete wavelet frame we need to impose a more restrictive condition on $\psi(t)$ for its admittance, i.e., the stability condition,

$$b_0 A \leq 2\pi \sum_{j \in \mathbf{Z}} |\widehat{\psi}({a_0}^j \omega)|^2 \leq b_0 B, \tag{5.10}$$

where A and B are positive constants and $0 < A \leq B < \infty$. The fixed constants b_0 and 2π are intentionally kept since they are related to normalized wavelet basis and since the magnitudes of A and B are related to the redundancy of the basis.

The stability condition may look abstract, but we give its physical implication as: to be able to let a function be reconstructed from its wavelet coefficients, i.e., the operation is reversible, we need a process which is convergent when summing all its scales or frequency components. It is therefore necessary that the sum of the power of all the constituent elements can neither be nil or infinity. If the sum is zero, then the elements are all of zero measure — nothing exists. If the sum is infinity, then the elements are significantly overlapping in time and frequency — there is either too much dependence or too much ambiguity and tangling (just like two vectors paralleling to each other do not constitute a good vector basis for two dimensional vector space).

Speaking of the reconstruction of a function from its wavelet coefficients one always involves a dual wavelet except for orthonormal basis where the wavelet itself is its own dual — self-dual. And since the roles of a wavelet and its dual can always be interchanged in both decomposition and reconstruction, the above statements apply equally well for dual wavelet; but their frame bounds will generally be different since the sets of convolution coefficients are different as hinted by the different entropy values given in the earlier chapter.

If the basis functions are normalized and the inequality of the stability condition are optimized for both the greatest lower bound and the lowest upper bound, i.e., when A and B are defined as

$$A = \inf\left[\frac{2\pi}{b_0}\sum_{j\in\mathbf{Z}}\left|\widehat{\psi}(a_0{}^j\omega)\right|^2\right], \tag{5.11}$$

$$B = \sup\left[\frac{2\pi}{b_0}\sum_{j\in\mathbf{Z}}\left|\widehat{\psi}(a_0{}^j\omega)\right|^2\right], \tag{5.12}$$

then an indication of the redundancy is the average value of A and B, $\frac{A+B}{2}$, supposed that A and B are close to each other (almost tight). We elucidate the possible extreme redundancy of CWT as follows. If the dilated and translated versions of a function originating

from a certain set of discrete steps (a_0, b_0) constitute a frame with frame bounds A and B, then the frame bounds of a basis using the same function but with finer discrete steps, say $a_0/2$ and $b_0/2$, will contain the bounds of coarser discrete steps; therefore, the new lower and upper bounds both grow together. This nested relation can be extended infinitely and in the limit sense it is included in the algorithm of CWT. This is the reason why there is no practical value of numerical reconstruction in CWT, although CWT is reversible analytically. Another intuitive explanation is even easier to comprehend: when apply CWT to discretely sampled signal, since for each scale the number of wavelet coefficients is the same as the number of data points and since we can specify scales in whatever resolution we like, we virtually have an unlimited number of wavelet coefficients. The sum of the powers of these coefficients can be unimaginatively huge, or even unbounded; On the other hand, the sum of signal energy is fixed. If we generalize the redundancy concept of DWT, i.e., the ratio between the two sums indicates the degree of redundancy, then for discretely sampled signal a continuous wavelet transform can possibly yield immense redundancy.

Even though extreme redundancy may exist for the continuous wavelet transforms, the content of information or its usefulness may behave like a cumulative pdf curve of a Gauss function which will saturate at a later stage. Our numerical results from studies of coherent behaviors among wind, wave and current related signals vindicated undoubtedly such a situation.

5.6 Beneficial scenarios due to redundancy

Redundancy may be a nuisance in certain applications such as those that focus on the perfect reconstruction of signal or on the efficiency of coding and decoding; however it has also shown its promising aspects in several applications. Three prominent points are the results of established cases: (1) Redundancy does not mean that a whole bunch of coefficients are needed to give a good replicate of the original signal, that is to say, significant

signal contents can still be retrieved from only a comparatively small amount of coefficients with respect to that of tight or almost tight wavelet frames. (2) Redundancy means that effects of noise either embedding in the sampled signal or arising from the nature of numerical processes (such as frequency leakage) can be reduced by taking advantage of the vast sample space of transform coefficients. (3) If additional features, such as "total positivity" and " complete oscillation" of wavelet are incorporated, the effects on noise reduction or ambiguity removal may be greatly enhanced; together with the redundancy effects they facilitate the design of a very beneficial analyzing scheme. An example of the first point is Mallat and Zhong's [51] (see also Froment and Mallat [22]) signal reconstruction from local maxima using a quadratic spline wavelet. In fact, the mother wavelet they used is basically a loose wavelet (i.e., a wavelet with analytical aspects not being well defined and therefore not really to be qualified as a wavelet), but they were able to recover images quite well using only local peak values of wavelet coefficients that are associated with only dyadic scales. For the second and third points, our studies on the coherent features in the wind, wave, and rain coupling system serve as an example.

One last point to note is to compare the admissability condition of CWT with the stability condition of DWT. Here one can easily perceive the great difference in flexibility between the two. In addition, the stability condition is a necessary condition, and not all choices for ψ, a_0, and b_0 lead to wavelet frames. Moreover, stability may not guarantee a good numerical behavior. Figures 6.1 (W Quirks-1) and 6.2 (W Quirks-2) show the results of a few numerical experiments in which the problems of numerical convergence are illustrated using the blow-ups of wavelet curves. In the figures two bi-orthogonal wavelets are blown up around their individual points using refinement cascade, and the blow-up curves show the possible intrinsic absurdity arising from peculiar analytical properties associated with these wavelets. Here, the two bi-orthogonal wavelets are, respectively, with four and twenty filter weights and both are constructed from quadratic spline scaling function [20]. The top sub-figure indicates a case where the DWT fails numerically to characterize the mother wavelet (not converging) even though the associated wavelet

frame qualifies theoretically as a Riesz basis. The bottom sub-figure shows strange alternating inclinations of wavelet curves with a poor convergence. The figure also illustrates the point that, for studying water-wave related signals and their physics, most of the fancy wavelets with bizarre wave forms are not of our choice, as are also indicated by their high entropy values given in the previous chapter.

5.7 Summary

In this chapter we point out the counterpart continuous wavelet to the best discrete wavelet. It will be observed in the next chapter that the three main, as well as exceptionally important features, which do not exist in the discrete domain, i.e., the phase, the carrier frequency and the redundancy, thus introduced make possible the physical optimization and lead to the outstanding results of wavelet coherences. ❖

Chapter 6

The Further Optimization for Physics

6.1 Introduction

In addition to the various concerns about the peculiar properties specific to discrete and continuous transforms as were stated in the previous chapters, herein we focus on the practical interest in what can be done to improve the physical relevance between the basis functions and the wave constituents of our signals. For example: does the decaying features of basis functions akin to the physics of component waves? In fact, this simple question outlines another fundamental theme of this chapter: if time-frequency windows of fixed shape and size (the case of STFT) is less suitable than time-frequency windows of fixed size but with flexible shape (the cases of DWT and CWT) in characterizing multi-scale transient signals, then time-frequency windows which are flexible in both shape and size should provide even better adaptations. The theme is intuitive right, the background is not without commitments.

Based on this perception, further concerns evolving from the previous chapters can be put forward quite simply: (1) Can we utilize the redundancy of basis functions to improve the relationship between wavelet's analytical form and its physical interpretability? (2) If redundancy leads to adaptation, does the adaptation still preserve the complete information content of the signal studied? (3) Is the scheme of adaptation efficient and easy to implement? Question one is related to the distribution or the degrees of freedom of time-

frequency windows in the phase plane, and it will be reflected in the next chapter. Question two concerns the verification of the admissibility condition related to "the resolution of identity"; and ,for now, a short explanation is that, if one just applies the adaptation to finite range(s) of scale, then what is lost or unaccounted for in the adaptation process can still be recovered from some dilated and translated versions of some finer scale wavelets originating from the same $\psi(t)$ in the CWT. The success of Mallat and Zhong's case also indicates such a possibility. Question three depends on the adaptation scheme; but, based on the somewhat intuitive adaptation used here, it is fair to say that nothing complicate is introduced.

One practical aspect for all the three points is: when analyzing signal we are almost always interested in only finite scale range(s), so what is really needed is to implement the adaptation locally. Hence it may be beneficial not to stick with stubborn time-frequency windows and to adopt a scheme that is numerically with the same easiness and physically more sound.

6.2 Degrees of freedom and the uncertainty relation

The flexibility of constructing wavelet function basis, i.e., the possibility of the adaptation, is associated with the number of degrees of freedom of the time-frequency windows within a phase plane. The number of degrees of freedom for an orthogonal basis is generally defined as the total area of the phase plane divided by the area of the time-frequency window corresponding to that determined by the mother wavelet. For any time-frequency kernel the maximum number of degrees of freedom is determined by the Heisenberg uncertainty relation or Heisenberg's inequality [11]. It is illustrated here that, even though it is impossible to increase the limiting degrees of freedom, there is no further limitation imposed upon the present adaptation. Besides, this section also serves two purposes: (1) illustrate the basic functionality of the modulation mechanism for STFT, which in turn is conceptually the same as the dilation mechanism for WT; (2) outline the relation between

redundancy and the Heisenberg uncertainty using possible distribution of time-frequency windows within a phase plane.

The uncertainty relation states that the product of bandwidth Δ_ω and duration Δ_t of a signal cannot be less than a minimum value of $\frac{1}{2}$ when the Δ_t and $\Delta\omega$ are defined as the standard deviations of packet energy $|f(t)|^2$ and power spectrum $|\widehat{f}(\omega)|^2$ with respect to their centroids, respectively:

$$\Delta_t{}^2 = \frac{\int_{-\infty}^{\infty}(t-\overline{t})^2|f(t)|^2dt}{\|f(t)\|^2}, \tag{6.1}$$

$$\Delta_\omega{}^2 = \frac{\int_{-\infty}^{\infty}(\omega-\overline{\omega})^2|\widehat{f}(\omega)|^2d\omega}{\|\widehat{f}(\omega)\|^2}, \tag{6.2}$$

where $\overline{t} = \int_{-\infty}^{\infty} t|f(t)|^2dt/\|f(t)\|$ and $\overline{\omega} = \int_{-\infty}^{\infty}\omega|\widehat{f}(\omega)|^2d\omega/\|\widehat{f}(\omega)\|$. As is also illustrated in Chui's treatise textbook [1], the time-frequency window, $\Delta_t\dot{\Delta}_\omega$, of the semi-orthogonal wavelet is nearly equal to the minimum value of the Heisenberg uncertainly principal, and this very optimistically provides the opportunity for applying the adaptations. That is to say, there is an easy to way get round of the uncertainty relation by going through a modulation process (i.e., multiplying a basis function with a complex exponential). Since in Fourier analysis a modulation in one domain corresponds to a shift in the other domain, such a process causes the new variance Δ_ω to increase dramatically. Figure 6.3 (Heisenberg) shows such a mechanism. It is seen that the new $\Delta_t\Delta_\omega$ is significantly larger than $\Delta_t D_\omega$, i.e., even larger than the limiting value for Heisenberg uncertainty relation; therefore, there is quite a lot of flexibility to devise the time-frequency windows. In view of the similarity between the modulation mechanism for STFT and the dilation mechanism for WT, especially for the case of Morlet wavelet, we anticipate that there is an ample space for adapting the time-frequency windows. Furthermore, as pointed out by Bracewell [11], there exists no theorem depicting the lower limit of $\Delta_t D_\omega$, i.e., no new restriction for D_ω; therefore no further limitation on the number of the degrees of freedom is induced. Overall, it is quite flexible to draw time-frequency windows which generally

do not violate the uncertainty relation when we express a signal in its two dimensional phase plane.

6.3 Time-frequency windows and the physics

The algorithm and the physics associated with the adaptation of time-frequency windows can be illustrated easily by going through practical examples. Though the adaptation does not need to be confined to any specific type of wavelet, the Morlet wavelet readily serves for such a purpose. As was stated in the previous chapter that the Morlet wavelet is almost identical to a modulated Gaussian, and a modulated Gaussian matches almost exactly with cardinal B-spline wavelet of order greater than or equal to three, which is exactly the identified best basis wavelet. Overall we therefore, on the one hand, benefit from an extremely natural transition from DWT to CWT, on the other hand, gain the practical merit of the adaptation.

Before we go into the adaptation, let us recount more explicitly two very important features that distinguish the identified optimum basis from the other bases and that definitely contribute to the causes of the optimum basis' successful applications: (1) The best basis' cardinal spline scaling function and its associated wavelets possess, respectively, the nice properties of "total positivity" and "complete oscillation". We note that these two properties physically imply that its wave form is relatively smooth and without ad hoc variations when compared with some fancy wavelets with finite support lengths. (2) The cardinal B-spline wavelet is either symmetric or anti-symmetric. Therefore, it benefits from the linear-phase filtering. The physical implication of this is: slight differences in wavelet coefficients will not cause significant differences in their reconstructed wave forms, or alternatively, the modulations of the wave forms are comparatively less abrupt. With more natural transitions for both forward and inverse transforms under various circumstances, the impacts to our perception or visualization of an interaction process due to varying input conditions are leaning toward relatively evolutionary tendencies rather

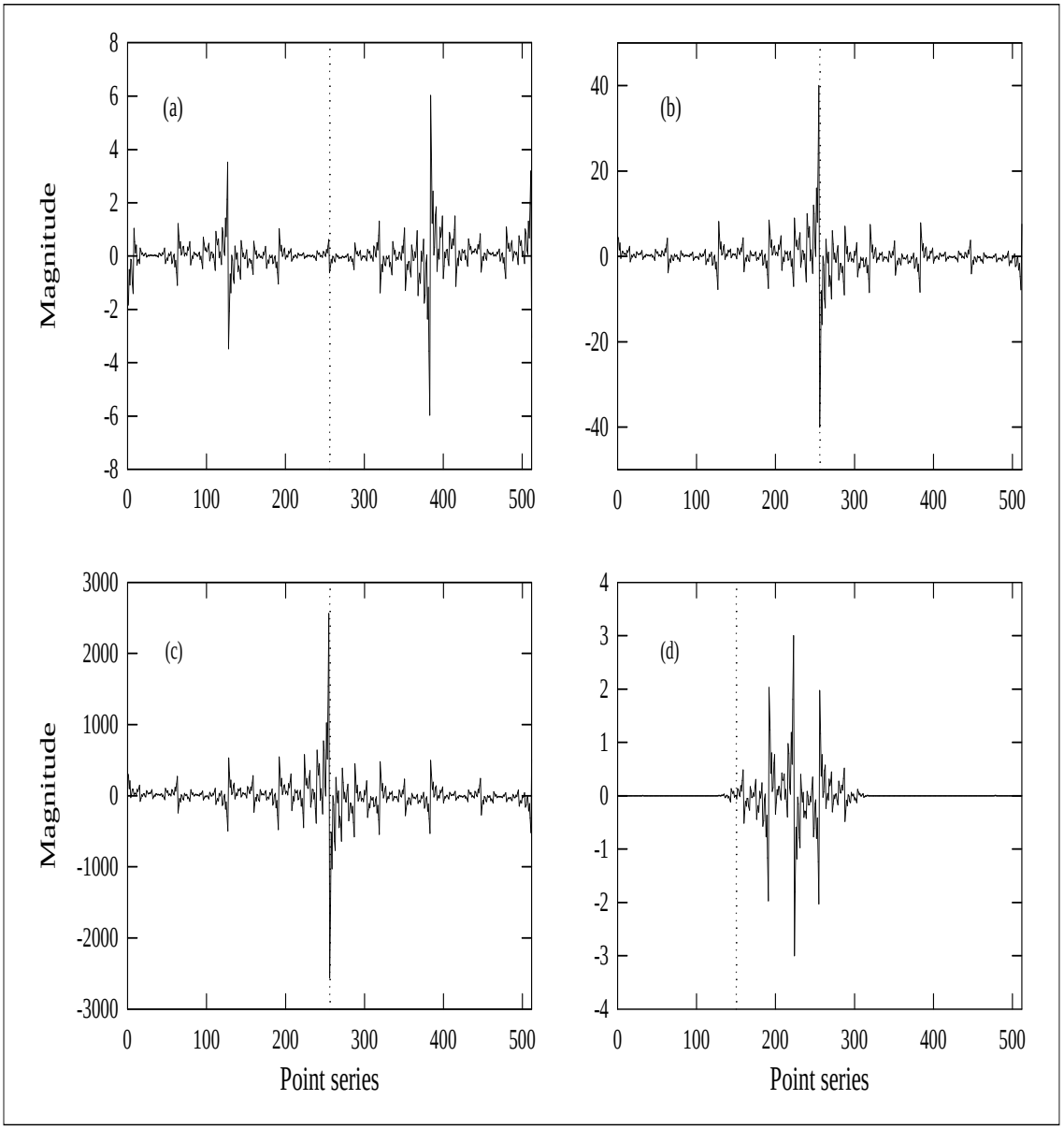

Fig 6.1 (W Quirks-1) Wavelets with fancy analytical properties are often of peculiar wave forms and are not of proper candidate for studying water-wave related physics — either judging from their entropy values given in the earlier chapter or form their stability conditions shown in this figure.

The peculiarity and the sensitivity of these types of wavelet constructions are somewhat illustrated by the phenomena appear in the blow-ups of bi-orthogonal wavelets BO31O. In this case the blow-ups diverge rapidly and fail to identify itself numerically in the refinement cascade. The blowup details are as follows.

Scale interval between blow-ups: 2^6 between subsequent sub-figures (a), (b), and (c);

Unit value originating point (the point used to obtain the curve in sub-figure (d)): level 2, position 12, i.e., element U_2^{12} in the notation of figure 2.21 (WP Tree);

Blow-up point: point 150 indicated by a vertical dotted line in the sub-figure (d).

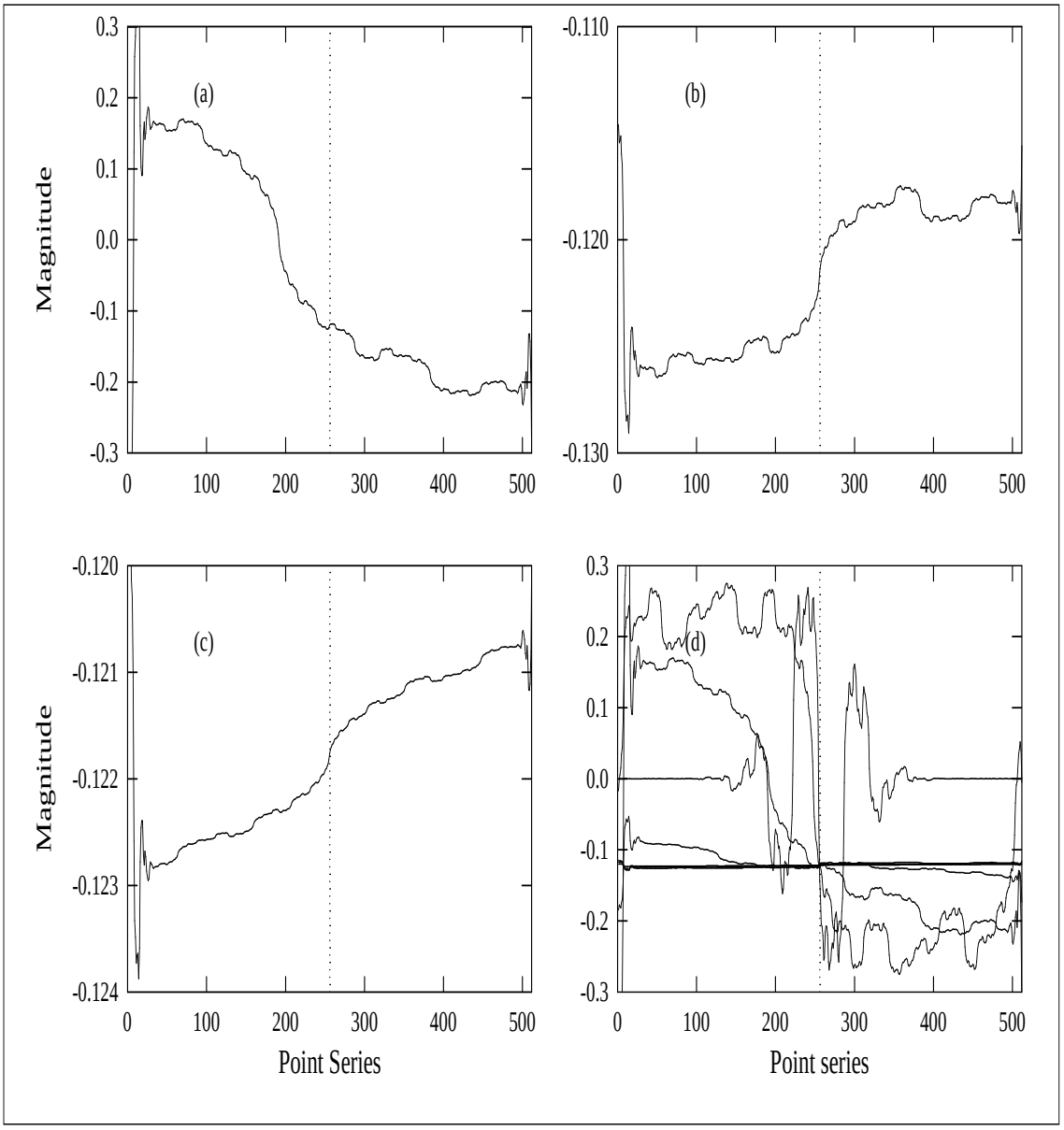

Fig 6.2 (W Quirks-2) Again, another instance of peculiarity and sensitivity arising from fancy wavelet construction is illustrated by the phenomena appear in the blow-ups of the bi-orthogonal wavelets BO35O.
The blow-ups here converge poorly and incline with opposite slopes.
The blowup details are as follows.
Scale interval between blow-ups: 2^6 between subsequent sub-figures (a), (b), and (c);
Unit value originating point (the point used to obtain the curve in sub-figure (d)): level 2, position 12, i.e., element U_2^{12} in the notation of figure 2.21 (WP Tree);
Blow-up point: point 256 indicated by the intersection point of various curves in the sub-figure (d).
It is noted that these peculiarities indicate the poor entropy values, as well as the consistently pathetic usages in water wave simulations. It is the author's belief that fancy constructions of wavelets do not adhere to the physics of water waves.

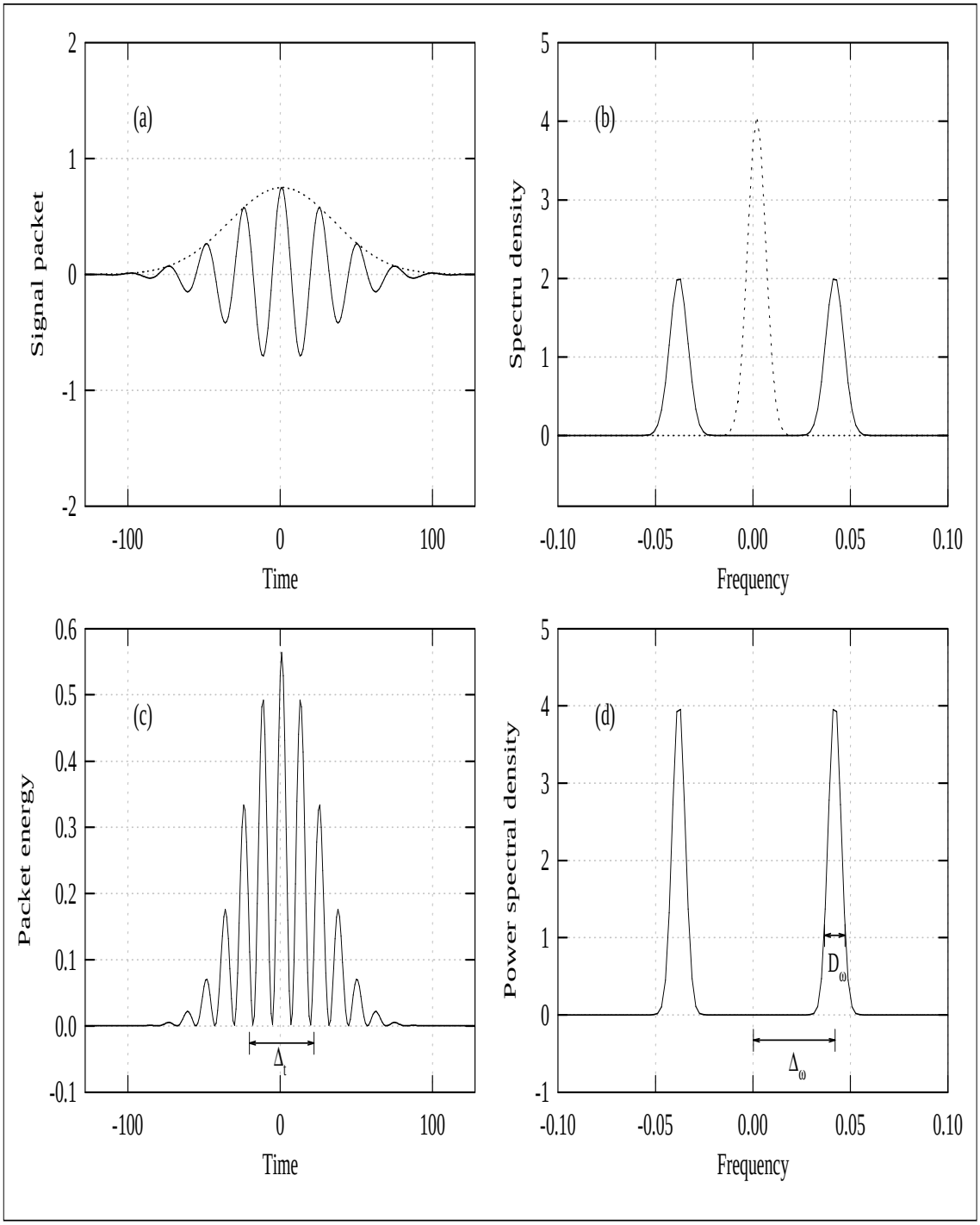

Fig 6.3 (Heisenberg) The Heisenberg uncertainty relation and the modulation versus shift property (adapted from Bracewell 1986). A modulation process renders $\Delta_t \Delta_\omega \gg \Delta_t D_\omega$. Where Δ_t, Δ_ω and D_ω are the root-mean-square departures from the centroids, respectively. The property helps significantly in possible adaptations of wavelets for the purpose of modeling water wave physics. That is to say, an adaptation generally will not violate the restriction of the minimum requirement of the product between the two moments of time and frequency distributions.

than drastic turnovers. Still, one additional implication of practical significance is: distortions are far less severe when noise and uncertainty are poignant. The phase plane in figure 6.4 (Adap–Simu) and the various blow-up curves in figures 6.1 (W Quirks-1) and 6.2 (W Quirks-2), 2.29 (BU–BO31O) and 2.30 (BU–BO35O), as well as figure 5.1 (SNI–Phase) manifest the problems and possible difficulties associated with wavelet bases that do not posses these properties.

Up to this point we have illustrated many specific properties, associated either with DWT or with CWT, that bestow upon our desires when analyzing our water wave related signals; even though their outstanding effects might only be appreciated when we get to the reality of analyzing experimental data. But here let us embark the further work on an improvement — enhancing wavelet's physical implication based on the affinity between the identified best basis and the Morlet wavelet.

The Morlet wavelet is the following complex function:

$$\psi(t) = \pi^{-1/4}(e^{-i\omega_0 t} - e^{-\omega_0^2/2})e^{-t^2/2}, \tag{6.3}$$

in which ω_0 is a constant related to the carrier frequency and the term $e^{-\omega_0^2/2}$ justifies the admissability condition. Its Fourier transform is almost a shifted Gaussian and is given by

$$\widehat{\psi}(\omega) = \pi^{-1/4}[e^{-(\omega-\omega_0)^2/2} - e^{-\omega^2/2}e^{-\omega_0^2/2}]. \tag{6.4}$$

In addition to the general meaning of the modulation frequency, the ω_0 has the physical implication of the amplitude ratio r — the ratio between the second highest peak and the first highest peak of $\psi(t)$ — i.e.,

$$r = \psi(t_2)/\psi(0), \tag{6.5}$$

in which t_2 is the abscissa of the second highest peak. The exact value of t_2 can be obtained by solving numerically the transcendental equation derived from the derivative of the ψ

function, but a fairly good estimate is obtained by simply dropping the second term of the above complex function since the second term is generally five order of magnitude less than the maximum value of the first term, i.e.,

$$\omega_0 \approx \frac{2\pi}{t_2} \approx \pi \left(-\frac{2}{\ln r}\right)^{1/2}. \tag{6.6}$$

The higher the ω_0 is, the smaller the ratio r becomes. If ω_0 is constant, then the ratio r for different wavelet dilations or scales keeps constant too. Here comes the core question: whether constituent wave components of different scales and time spans all possess this fixed decay feature? To show that this is not true, let us examine the composite water wave system that is with viscous damping.

For deep water waves with a clean surface the energy losses due to viscous dissipation arise almost entirely from the straining of the irrotational motion in the water column, and the part of contribution from viscous stresses in the surface layer is negligible. It was shown [33, 60] that the time rate of change of the energy density is

$$\dot{E} = -2\mu\sigma^2 {a_w}^2 k, \tag{6.7}$$

where μ, σ, a_w, and k are the dynamic viscosity of the water, the wave frequency, wave amplitude, and wave number, respectively. Since in deep water $E = (2k)^{-1}\rho\sigma^2 {a_w}^2$, where ρ is the water density, the attenuation coefficient

$$\gamma_\nu = -\frac{\dot{E}}{2E} = 2\nu k^2, \tag{6.8}$$

where ν is the kinematic viscosity of the water. Therefore the energy density of the wave evolves as

$$E = C_1 e^{-2\gamma_\nu t}, \tag{6.9}$$

where C_1 is a constant, and the amplitude decreases with time in accordance with

$$a_w = \sqrt{\frac{C_1 2k}{\rho\sigma^2}} e^{-\gamma_\nu t} = C_2 e^{-2\nu k^2 t}, \tag{6.10}$$

where C_2 is a constant if σ does not vary. Comparing the decay of wave amplitude of Morlet wavelet with the decay of the physical model, one sees both similarity and dissimilarity. The similarity is that the attenuation coefficients in both models have inverse square dependence on scales — the former in $(1/a)^2$ and the latter in k^2. The dissimilarity is in the time dependence of the exponent in the exponential — in Morlet wavelet it is in t^2 dependence, while in the physical model it is in linear dependence. It is therefore anticipated that Morlet wavelets based on a fixed modulation shape are not good representations of water waves of different scales. Or stated otherwise, basis functions originating form a single mother Morlet wavelet do not form a good basis.

Now the situation is clear: the constant ω_0 either overestimates the viscous decay of water waves at the low-frequency end or, otherwise, under-estimates those at the high-frequency end. Form a practical judgement of the modulation curves, it is quite reasonable to argue that the deviation is probably more significant for waves with a longer life span when a standard r value of Morlet wavelet, i.e., $r = 0.5$, is assumed. The perceptions here provide the footing for the present adaptation — with different values of amplitude ratio r for different wave scales we are really attempting to simulate the evolution process with a more realistic condition. The expansion or contraction of wavelet support length for a specific scale just reflects the devising of flexible constructions of time-frequency windows, and adjusting r is in turn using a variable ω_0. The general guideline is to use a comparatively larger ω_0 (associated with a narrower frequency band) for waves of a longer time support; and vice versa, a comparatively smaller ω_0 (a wider frequency band) for a shorter life span. Here it naturally comes to assume the ω_0 to be a function of scale, i.e., $\omega_0 = \omega_0(a)$. And the varying shapes and sizes of the time-frequency windows are

now determined by

$$\psi_a\left(\frac{t-b}{a}\right) = \pi^{-1/4}\left[e^{-i\frac{\omega_0(a)}{a}(t-b)} - e^{-\omega_0(a)^2/2}\right]e^{-\frac{(t-b)^2}{2a^2}}. \tag{6.11}$$

6.4 The carrier frequency and the adaptation

Earlier we have stated a few nice features of the identified best basis. There is one additional feature that is practically significant because of its relevance to the Morlet wavelet — the physical perception of the sizes and shapes of "scales". Without such a property everything will look obscure. In fact, we have seen a lot of ambiguities or abstractions in many studies where they only involve presentations using non-dimensional scales rather than using the more appropriate physical quantities of carrier frequency even though they are working on modulated Gaussian or Morlet wavelets. We note that the wavelet coefficient generally refers to "scale" not to "frequency". Scale has no dimension, but carrier frequency has a physical unit and is associated with a Gaussian bell modulator. Furthermore, scale generally corresponds to complicate combination of several frequency bands such as what implied by the compactly supported orthogonal wavelets shown in figure 6.4 (Adap–Simu). Therefore, in order to have a clear picture of a "scale" one needs to consider: What does the basic wavelet look like? What is the actual support length? And, what is the physical sampling interval? All these severely tangle our thought, and we get lost easily. Take as an example: the numerical processes for both discrete Fourier transform and DWT care nothing about the physical units and only the index is important; however, there is an easy conversion from index to frequency for Fourier coefficient, but not for wavelet transforms except the ones associated with the Morlet wavelet. It is totally impossible to visualize the corresponding object just from the index of a wavelet coefficient. For the best basis and the related adaptation the difficulty is avoided, since the precise and physical "carrier frequency" is easily seen to be $\omega = \omega_0(a)/a$, supposed that $\omega_0(a)$ is large enough, say above 5. Again, the point to caution is: illustrations using

scale parameter a can be confusing and misleading since the same a may correspond to different actual scales or frequencies when different adaptations or different wavelets are used.

As was stated in the previous section that the present adaptation can always be applied to finite scale range(s) and that the transform only needs to be implemented for scale range(s) that we are interested in. Still, we give an additional description of the flexibility concerning this. Since one can always regard that the set of sampled data points is derived from a certain specific function, but there are basically infinitely many functions which can pass all these sampling points. And since the functions passing through these points may be either band-limited or -unlimited but the sampled signal is always band-limited (since numerical analysis is always associated with finite scale range); therefore, the situation indicates that there exists freedom to make adaptation for ω_0 and also implies the possible redundancy when CWT is applied to the sampled signals. The remaining problem is how to define a suitable decay parameter ω_0. Nevertheless, based on the above mentioned practical concern of wave decay and the somewhat intuitive adjustment, we show the possible improvements in time-frequency resolutions when the adaptation is applied to experimental data. But let us first give a numerical simulation.

For the simulated data we use a parabolic chirp where the frequency range of interest covers the whole band width of the signal, i.e., from almost zero frequency to that corresponding to Nyquist sampling rate. And a linear variation of $\omega_0(a)$ from 10 (for large scale end) to 7 (for small scale end), as opposed to the commonly adopted fixed value of 5.3 (corresponding to $r \approx 0.5$), is assumed. As is seen from figure 6.4 (Adap–Simu), the adapted one gives better frequency localization for almost all frequencies except the lowest two carrier frequencies (in fact the adaptation can be further adjusted for this part, and to have better resolutions for these two carrier frequencies the values of their $\omega_0(a)$ should be less than 5.3, but the concern here is mainly on the serious edge effects). A phase map for the complex wavelet coefficients derived from a refined ridge extraction scheme is also shown as the top right sub-figure. Here it provides a much better identi-

fication of scales of main power contents than what can be provided by Morlet wavelet. F:TFM-WindWave

For the experimental data water waves measured in the wind blowing oval tank are used, in which reasonable frequencies should lie between 1.5 and 10 Hz. Earlier we mentioned that the Morlet wavelet is likely to overestimate the decay of longer waves in the long run; therefore, relative to higher frequency waves, we should reduce the decay parameter ω_0 for low frequency ones. Based on this understanding we heuristically assume

$$\text{Erfc}\left[\frac{4}{10}\left(\frac{\omega_0}{a}+2.5\right)-2\right]3+5=a\omega \tag{6.12}$$

where Erfc is the complimentary error function and ω is the carrier frequency. This equation may be modified according to the type of signal studied or according to the frequency range of one's interest. Figure 6.5 (Adap–Erfc) shows the curve of the function. The logic for the choice of its constants is self explained in the attached program piece. Figure 6.6 (Adap–Wave) shows results without and with the adaptation. Here, the varying $\omega_0(a)$ is from 9.16 (for the large scale end) to 5.26 (for the small scale end), as opposed to the fixed value of 5.3. Again there are less smearing effects at the lower portion of the time-frequency plane since we mainly adjust decay parameters for the low-frequency end.

A few additional points are: (1) The dominant carrier frequency is about 2.4 Hz in this case; (2) Waves of all frequencies keep constantly evolving, since light and dark regions constantly interlace; (3) There are grouping effects. Waves with significant energy contents are more enduring and the durations of darker bands are much longer than those of higher frequencies. This indicates that our adjustment for decay parameters is based on a reasonable ground; (4) There is an obvious bifurcation among scales, especially for the intermediate frequency range of about 3 to 4.5 Hz; it suggests that the phenomenon of energy cascade from where energy concentrates to neighboring areas. Judging from these characters it seems that the energy phenomenon in a multi-scale wave field is somewhat similar to that in a turbulent flow field (see Tennekes and Lumley [68]).

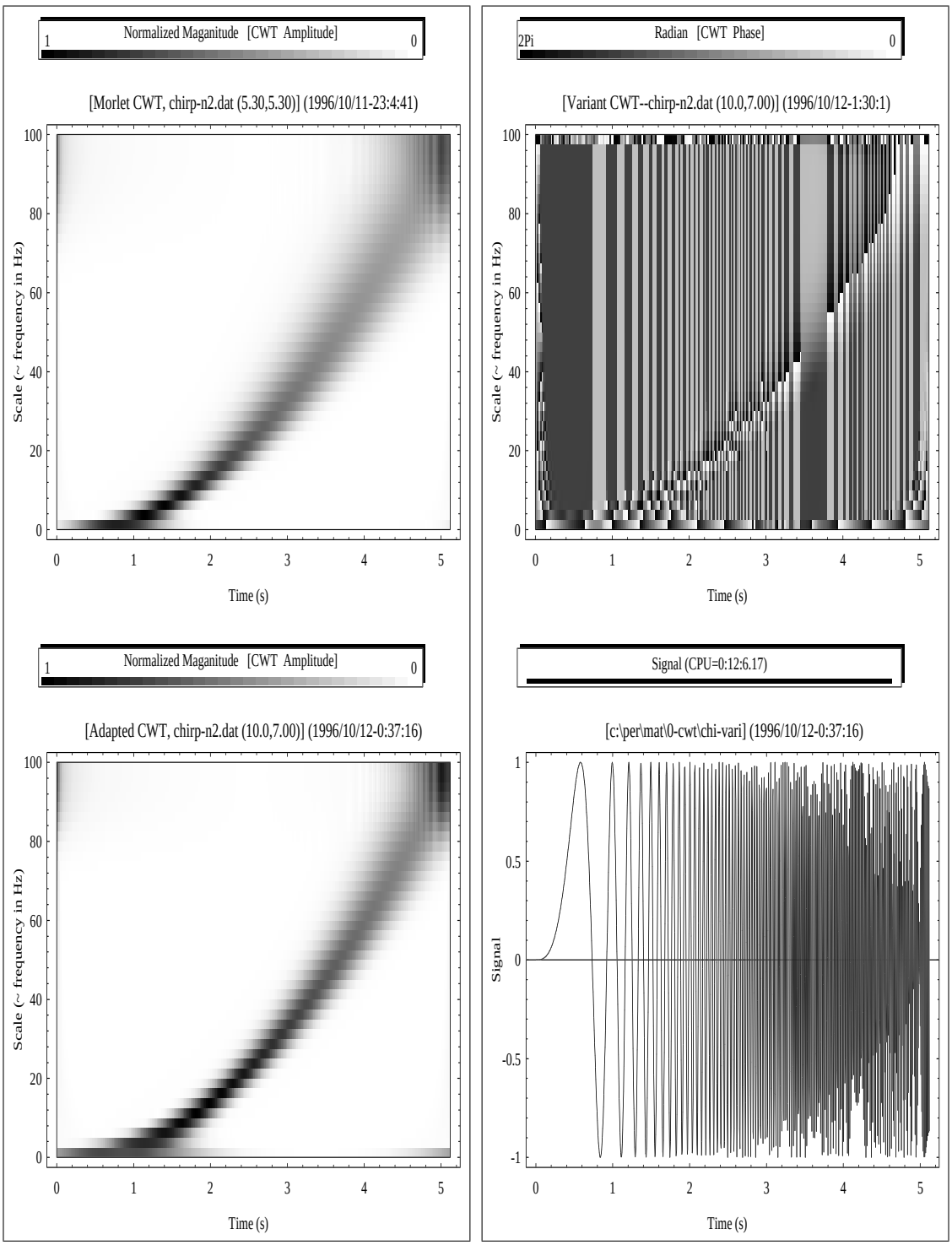

Fig 6.4 (Adap–Simu) The time-frequency distributions of a parabolic chirp `(bottom right)` with `(top left)` and without `(bottom left)` adaption of the carrier frequency parameter ω_0. In generally the adaptation yields a more concise distribution and a better coverage of frequency range.
An additional time-frequency map is shown in the top right. In which the transformation is associated with a wavelet variant devised by the author. The wavelet variant has refined capability in ridge extraction and shows less ambiguity.

```
obeg=11.;  oend=5.;
fcenter=2.5;  fdilation=10/4;   fshift=2. ;

perfc=Plot[ Erfc[(1/fdilation)* (freq +fcenter)-fshift]*
                          (obeg-oend)/2+ oend, {freq, -2.5, 8.5} ]
```

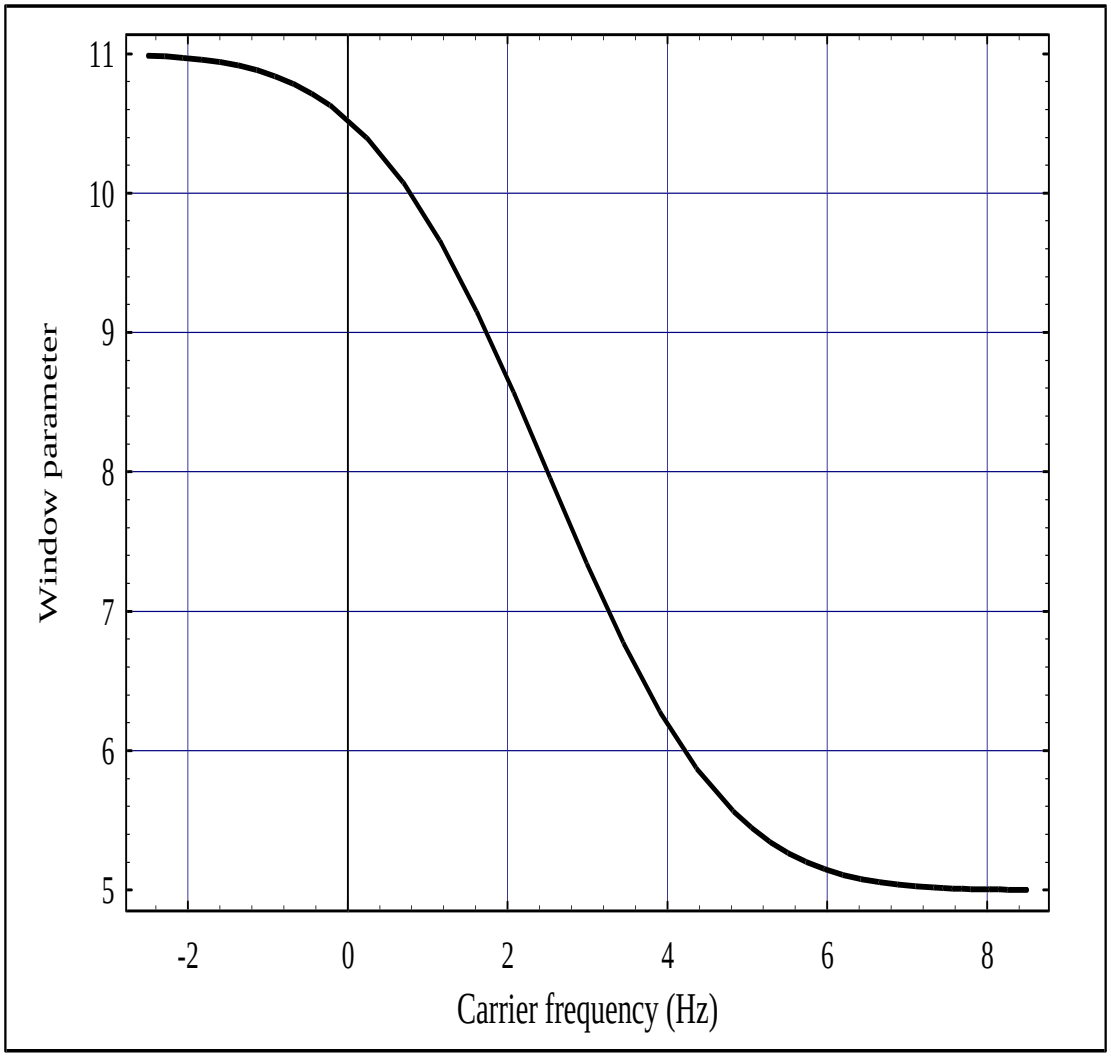

Fig 6.5 (Adap–Erfc) The ω_0 is a representative character of the wavelet time-frequency window kernel and intrinsically is the carrier frequency parameter. It has the physical indication of wave decay tendency. A constant ω_0 does not adhere to water waves of a board range of scale.

Here an adaptation of ω_0 in accordance with the carrier frequency is assumed and hinted by the program piece. The window kernel parameter as a function of carrier frequency is presumed to be the complementary Gauss error function Erfc.

And the curve can be adjusted according to several parameters of wave feature as indicated in the attached program piece: approximate peak frequency; significant range of frequency; range of decay parameter; as well as a shift adjustment parameter.

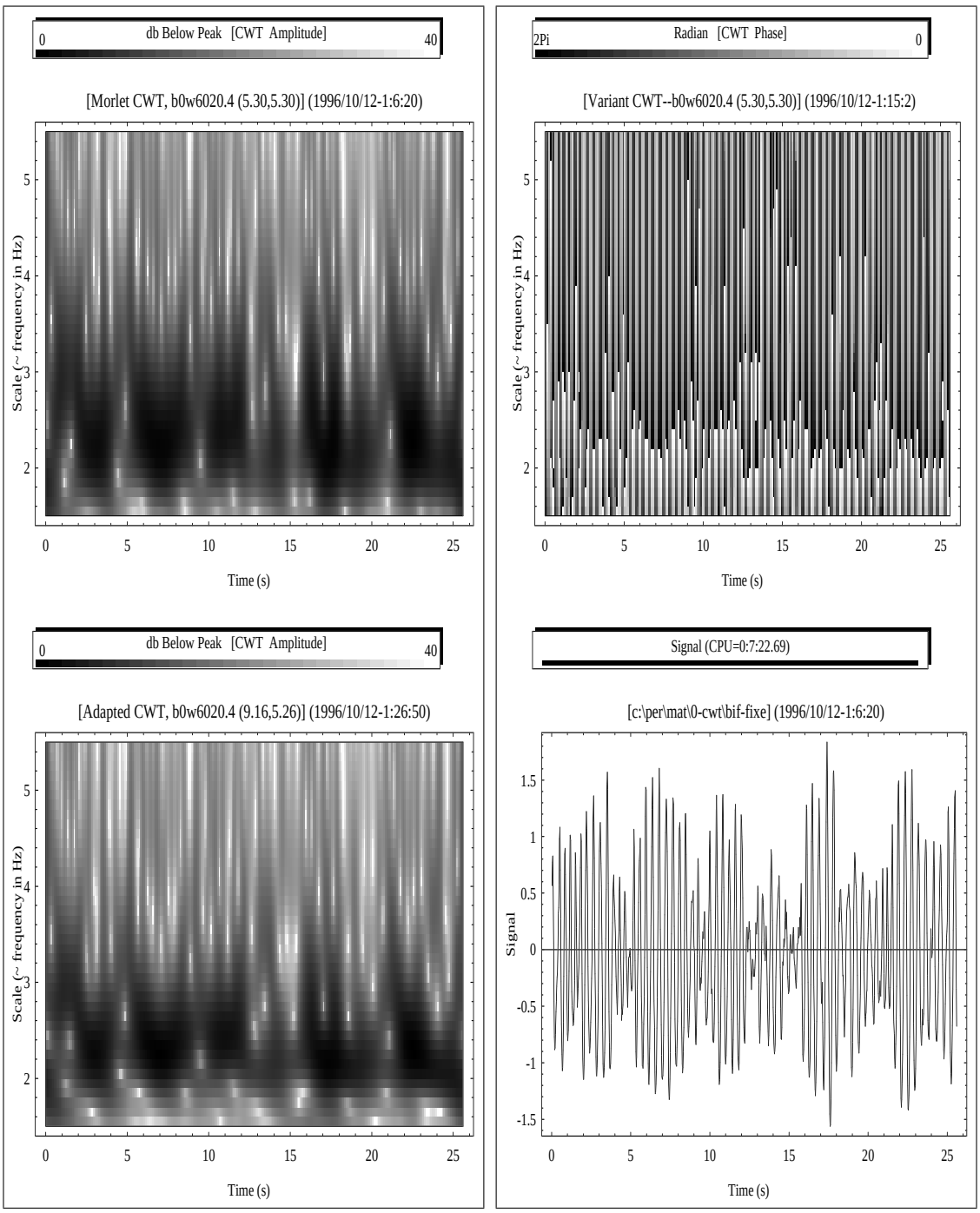

Fig 6.6 (Adap–Wave) The time-frequency distributions of a wind-generated water wave signal `(bottom right)` in a laboratory tank with `(top left)` and without `(bottom left)` adaption of the carrier frequency parameter. The assumed adaptation mainly adjusts the decay coefficients toward a mild decline for low-frequency part. Here we see less smearing for the main frequency band.
Note that due to the narrow-banded nature of the laboratory wind wave the adaptation may show more prominent effects for signals of a broad range of scales.
Besides, the time-frequency plot `(top right)` using the same wavelet variant as mentioned in figure 6.4 (Adap–Simu) provides an easy identification of the main power ridges as is generally infeasible using the Morlet wavelet.

6.5 Existence of the admissability condition

Earlier we gave a somewhat physical description on how the present adaptation manages to provide an almost "lossless" operation. Lossless means that the full information of a function is preserved during the transform and that we can recover the function from its wavelet coefficients, i.e., there exists a reverse operation. In the following we provide a more formal description through validating the existence of the identity resolution, which is basically just to show the existence of an admissability condition.

In an earlier illustration of the adaptation, a modified basis of wavelets was formed by adjusting the support length of dilated versions of $\psi(t)$ using different values of ω_0 which is further assumed to be a function of a. Furthermore, as explained in the previous section, a simple adaptation is the modification of carrier frequency according to $\omega = \omega_0/a$, i.e., $\omega_0 = a\omega$, we therefore further assume that ω_0 is a generalized function of $a\omega$ and the wavelet is

$$\psi_{\omega_0}(t) = \psi(t\,;\omega_0(a\omega)). \tag{6.13}$$

Its dilated and translated versions are given by

$$\psi_{a,b;\omega_0}(t) = \frac{1}{\sqrt{|a|}}\psi\left(\frac{t-b}{a};\omega_0(a\omega)\right). \tag{6.14}$$

And the wavelet coefficients of a function $f(t)$ are given by

$$\begin{aligned}
\mathrm{W}f_{\omega_0}(a,b) &= \langle f,\, \psi_{a,b;\omega_0}\rangle \\
&= \int_{-\infty}^{\infty} \frac{1}{\sqrt{|a|}} f(t)\overline{\psi_{\omega_0}\left(\frac{t-b}{a}\right)}dt \\
&= \int_{-\infty}^{\infty} \sqrt{|a|}\,\widehat{f}(\omega)\overline{\widehat{\psi}_{\omega_0}(a\omega)}e^{-ib\omega}d\omega,
\end{aligned} \tag{6.15}$$

in which $\widehat{\psi_{\omega_0}}(\omega) = \widehat{\psi}(\omega;\omega_0(a\omega))$. We follow the formalism to check that the inner

product of two functions f and g, $\langle f, g\rangle$, can be recovered from the integration of the projection of $\mathrm{W}f(a,b;\omega_0)$ into $\mathrm{W}g(a,b;\omega_0)$ along both real lines of dilation and translation variables. That is, whether the following equation exists:

$$\int_{-\infty}^{\infty}\int_{-\infty}^{\infty}\frac{1}{a^2}\mathrm{W}f(a,b;\omega_0(a\omega))\overline{\mathrm{W}g(a,b;\omega_0(a\omega))}dadb = C_{\psi_{\omega_0}}\langle f, g\rangle, \tag{6.16}$$

where $C_{\psi_{\omega_0}}$ is a constant. If it exists, then when g is taken as the Gaussian function with its variance approaching zero (i.e., g is practically the delta function $\delta(t)$), the inner product $\langle f(t'), g(t'-t)\rangle = \langle f(t'), \delta(t'-t)\rangle$ will recover $f(t)$ and the condition of the identity resolution is guaranteed.

The right hand side of the above equation equals to

$$\int_{-\infty}^{\infty}\int_{-\infty}^{\infty}\frac{1}{a^2}\left[\int_{-\infty}^{\infty}\sqrt{|a|}\,\widehat{f}(\omega)e^{-ib\omega}\overline{\widehat{\psi}(a\omega;\omega_0(a\omega))}d\omega\right]\times$$

$$\left[\int_{-\infty}^{\infty}\sqrt{|a|}\,\overline{\widehat{g}(\omega')}e^{ib\omega'}\widehat{\psi}(a\omega';\omega_0(a\omega'))d\omega'\right]dadb. \tag{6.17}$$

With the following two identity equations

$$\widehat{F_a}(t,\omega_0(a\omega))$$
$$= \frac{1}{\sqrt{2\pi}}\int_{-\infty}^{\infty}e^{-it\omega}\sqrt{|a|}\,\widehat{f}(\omega)\overline{\widehat{\psi}(a\omega;\omega_0(a\omega))}d\omega$$

$$= \frac{1}{\sqrt{2\pi}}\int_{-\infty}^{\infty}e^{-it\omega}F_a(\omega;\omega_0(a\omega))d\omega, \tag{6.18}$$

$$\overline{\widehat{G_a}(t,\omega_0(a\omega))}$$

$$= \frac{1}{\sqrt{2\pi}}\int_{-\infty}^{\infty}e^{it\omega}\sqrt{|a|}\,\overline{\widehat{g}(\omega)}\widehat{\psi}(a\omega;\omega_0(a\omega))d\omega$$

$$= \frac{1}{\sqrt{2\pi}} \int_{-\infty}^{\infty} e^{it\omega} \overline{G_a(\omega; \omega_0(a\omega))} d\omega, \tag{6.19}$$

one has

$$\int_{-\infty}^{\infty} \int_{-\infty}^{\infty} \frac{2\pi}{a^2} \widehat{F_a}(t; \omega_0(a\omega)) \overline{\widehat{G_a}(t; \omega_0(a\omega))} da dt$$

$$= \int_{-\infty}^{\infty} \int_{-\infty}^{\infty} \frac{2\pi}{a^2} F_a(\omega; \omega_0(a\omega)) \overline{G_a(\omega; \omega_0(a\omega))} da d\omega$$

$$= \int_{-\infty}^{\infty} \int_{-\infty}^{\infty} \frac{2\pi}{|a|} \widehat{f}(\omega) \overline{\widehat{g}(\omega)} |\widehat{\psi}(a\omega; \omega_0(a\omega))|^2 da d\omega$$

$$= 2\pi \int_{-\infty}^{\infty} f(t) \overline{g(t)} dt \int_{\infty}^{\infty} \frac{|\widehat{\psi}(a\omega; \omega_0(a\omega))|^2}{|a|} da$$

$$= 2\pi \langle f, g \rangle C_{\psi_{\omega_0}}. \tag{6.20}$$

Now the resolution of identity is fulfilled if the following admissability condition is satisfied,

$$\int_{-\infty}^{\infty} \frac{|\widehat{\psi}(a\omega; \omega_0(a\omega))|^2}{|a|} da = C_{\psi_{\omega_0}}. \tag{6.21}$$

This condition is more restrictive than Equation 5.7 in that $\widehat{\psi}(0, \omega_0(u)) = 0$ for all $u \in \mathbf{R}$. Otherwise, there is no other restriction since what is changed in the integration is limited to finite range and is anticipated to be finite. The case using Morlet wavelet complies with such a validation and therefore satisfies this condition.

6.6 Summary

The unrealistic aspect of the best wavelet in the simulation of water waves is pointed out and the importance of the existence of a physical quantity of carrier frequency is stressed. And a somewhat intuitive adaptation based on the adjustment of the time-frequency win-

dow parameter is proposed. The adaptation mainly focuses on better modeling of wave energy phenomena or energy dissipation for different wave lengthes. Such an optimization shall be more significant for board band signals. ❖

Chapter 7

Wavelet Coherences against Fourier Coherences

7.1 Introduction

Coherence connotes mutual relationship or inter-dependency; it manifests from an intimacy of complete cloning to an alienage of total irrelevance. In a multi-scale, multi-factor coupling system the levels of coherence between different target quantities symbolize the phenomena of reciprocal interactions among various playing elements. By studying variations of coherences under different experimental setups or different input parameters it is possible to show evolutions of different scales and to isolate key influential factors, as well as to identify issues thus consorted.

In this chapter solid evidences will be provided regarding the the proof of "the ultimate last word" on best wavelet concerning water wave applications and physics. What will be furnished is the absolute superiority of the wavelet coherences associated with the ultimate best wavelet over the spectral coherences associated with Fourier basis. By the way, be that as it may, the author likes to emphasize that by no means this is equivalent to saying that Fourier basis is inferior to such wavelet basis in every aspect of water wave studies. In facts, it is still vastly important in many prospects, in particular, for those that are generally stationary or without significant local transient variations and for those related to water wave instability (such as side-band instability).

In two individual studies related to the methodologies of time-frequency analysis by the author [39, 41] the viewpoints based upon Hilbert transform and the analytic signal procedure [26], [17] were used to elaborate the influences of non-stationary effects and local transient variations, as well as some of the intrinsic mathematics and their connection with the uncertainties related to Fourier spectra. Herein, we will come to realize the same drawbacks imposing upon the Fourier basis due to these effects when comparing performances of spectral coherences with those of wavelet coherences. Moreover, let state a few basic differences between the two approaches.

Apart from the most instinctive and fundamental deviation between Fourier and wavelet's viewpoints concerning the appropriateness of depicting waves as finitely supported modulating signals, i.e., waves with a life span, there are two other major differences.

First, from the viewpoint of their origins from mathematics, the formulation of wavelet coherence is a more intimate replica of its analytical form than is the Fourier spectral coherence. Specifically, the wavelet coherence is a direct and natural extension of the wavelet "resolution of identity", and therefore involves less artificial intervention.

Second, the wavelet coherence presented here is derived from a set of coefficients with an extreme redundancy associated with no orthogonality whatsoever; while spectral coherence is derived from a set of coefficients associated with orthonormal basis functions. Such a redundancy is capable of providing not only a fine scale resolution but also a huge population space needed for outstanding coherent statistics; since it reduces impacts related to histogram processing, noises, and a few additional uncertainty factors, etc [62], [78]. Most importantly, being based upon the basis with minimum entropy that clearly outperforms the Fourier basis, the wavelet transform coefficients possess utmost information contents and lead to clear and superior tendencies in coherent features.

Overall, what presented in this chapter will come to the conclusion: for water waves, the ultimate best wavelet in the discrete domain is the semi-orthogonal cardinal spline wavelet; and in the continuous domain it is the Morlet wavelet.

7.2 The Fourier spectral coherence

The cross correlation function of two functions $g(t)$ and $h(t)$ is the following inner product $c(t)$

$$c(t) = \langle g(t+\tau), h(\tau) \rangle, \tag{7.1}$$

where τ is a dummy variable with respect to t. The correlation coefficient function of $c(t)$ is $r_s(t)$,

$$r_s(t) = \frac{c(t)}{\|g(t)\| \|h(t)\|}. \tag{7.2}$$

For real $g(t)$ and $h(t)$, its Fourier transform is

$$\frac{\widehat{c(t)}}{\|g(t)\| \|h(t)\|} = \frac{G(\omega)\overline{H(\omega)}}{\|G(\omega)\| \|\overline{H(\omega)}\|}. \tag{7.3}$$

The Fourier spectral coherence is the following induced form,

$$R_s^2(\omega) = \frac{|\mathbf{E}[G(\omega)\overline{H(\omega)}]|^2}{\left(\mathbf{E}[|G(\omega)|^2]\mathbf{E}[|H(\omega)|^2]\right)^{1/2}}, \tag{7.4}$$

where the symbol $\mathbf{E}$ stands for taking expected value. Comparing the two equations above, the artifacts introduced into the spectral coherence are associated with the form of expected values and the introduction of normalization.

This equation is in fact identically unity for all component frequencies if no additional man made manipulation is adopted. Since expected values take no action without introducing one more dimension. As such, the introduction of an additional dimension is the manipulation of data segmentation, that is to say, the whole data sequence is segmented, and each segment is individually transformed and arranged in a matrix thus creating the one additional dimension. The process of this segmentation is completely identical to that commonly implemented in calculating Fourier power spectra, and it aims to reduce the uncertainty or standard deviation of the spectral estimation. There is no doubt that various inherent properties of the discrete Fourier analysis inflict their symptoms and impose

similar limitations to the conclusiveness of spectral coherences.

7.3 The wavelet coherence

It was a stumbling when the subject of both wavelet and spectral coherences caught the author's attention. Reading a paper by Liu [44], the author was dissatisfied with the paper's definition of wavelet coherence and the ambiguity and lack of information thus yielded. And it turns out that the derivation of wavelet coherence is even much simpler mathematically and more intuitive theoretically, along with fewer artifacts.

The wavelet's "resolution of identity" of two functions (g and h) is

$$\langle g, h\rangle = \frac{1}{c_\psi}\int_0^\infty \frac{1}{a^2}\int_{-\infty}^{\infty}\langle g,\, \psi_{a,b}\rangle\overline{\langle h,\, \psi_{a,b}\rangle}dbda, \tag{7.5}$$

in which c_ψ is a constant and $\psi_{a,b}$ is a wavelet with scale a and translation step b. For a component scale a

$$\langle g_a, h_a\rangle = \frac{1}{c_\psi}\frac{1}{a^2}\int_{-\infty}^{\infty}\langle g,\, \psi_{a,b}\rangle\overline{\langle h,\, \psi_{a,b}\rangle}db. \tag{7.6}$$

Here the integration with respect to the translation parameter b is physically, as well as intuitively, similar to the operation of taking an expected value by summing up the elements in the population space. It is therefore quite straightforward to define the wavelet coherence as the natural extension of the normalized equation of resolution of identity:

$$R_w^2(a) = \frac{|\mathbf{E}_b[\langle g,\, \psi_{a,b}\rangle\overline{\langle h,\, \psi_{a,b}\rangle}]|^2}{\left(\mathbf{E}_b[|\langle g,\, \psi_{a,b}\rangle|^2]\mathbf{E}_b[|\langle h,\, \psi_{a,b}\rangle|^2]\right)^{1/2}}, \tag{7.7}$$

where $\mathbf{E}_b$ stands for sampling average with respect to the translation parameter, the subscript b.

It is clear that the wavelet coherence has a more direct linkage to its analytical counterpart than does the spectral coherence.

Unlike the spectral coherence, there is no need to segment the data. The expected values can be obtained in a sense of summing up all the results of wavelet transforms at all locations. And each elemental transforms can be obtained through simple convolution, i.e., an operation of time reversal and time shift if the data is a time sequence. Therefore, the population size of the sample space of wavelet coefficients for any given scale (or carrier frequency as adopted here) is generally two or three orders of magnitude larger than that for spectral coherence. That is to say, the amount of available sampling coefficients is generally not a concern for the wavelet scheme.

In fact the fundamental difference between the present definition based on equation 7.7 and the one adopted by Liu [44]) is the state of subsistence of the expected values. Without the statistics of an expectation the results seemed scanty and the depictions sounded skimpy.

Although the equation of the wavelet coherence (eq. 7.7) applies equally well to a discrete or a continuous basis, there is one significant and practical advantage that facilitates the use of the continuous one. Since we can focus only on the portion of scale range that is meaningful and substantial to us. Nevertheless, for the spectral coherence, in the handling we have no control at all over the frequency range of interest. As such, a great portion of the spectral result might be entirely irrelevant to our concerns.

Judging from the fact that we generally only want to, and are just able to, focus on a finite scale range or some frequency bands in practically any real world situation. Even though computation efficiency is not our concern, We know that the spectral approach wastes its effort and resource in the unwanted while the wavelet coherence does just the most appropriate.

7.4 The experimental data

The data involved in this chapter is related to a subset of experiments that aims at the study of the energy cascade phenomenon and the interaction scales in the wind, wave and

rain coupling system. Details will be given afterwards.

The coherence comparisons include both wind and Stokes waves. Major wind speed was 6.0 $\sec^{-1}$, and Stokes waves with different wave steepness were mechanically generated. The wind speed was measured with a Pitot tube located 50 cm upwind of the rain section and 11 cm above the still water surface. Water surface displacements were measured with the capacitance type tantalum wire probes. Aqueous flows at several depths in two sections along the tank were measured with a laser Doppler velocimeter.

7.5 Comparisons and implications

The performance comparisons of the two approaches provided here concern the coherences between the surface wave and aqueous flow fields for both wind wave cases and Stokes wave cases.

These comparisons fully warrant the entropy results and vindicate the ultimate best wavelet for water waves. There must be reasons and implications.

- The absolute superiority of the wavelet coherences — The wavelet coherences using three different analyzing data lengthes of 1024, 2048, and 4096 points are shown in figure 7.1 (WC–$2^{10,11,12}$). The individual curve in each sub-figure indicate individual measurement depth for aqueous flow at 2, 3, 4, 5, and 9 cm, respectively, below the still water surface. It is seen that all the corresponding curves for the three different analyzing data lengthes are extremely consistent. In contrast, figure 7.2 (FC–$2^{10,11,12}$) shows the Fourier spectrum coherences for the same data sets. The difference in performance of the two methods is quite obvious and can be grasped without explanation. Additionally, figure 7.3 (FC–2^{13plus}) shows the spectral coherences using a lengthy 9126-point with individual FFT segmentation length of 256- and 1024-point. It is noted that, when extremely lengthy data is used, the Fourier coherent curves may possibly come close to those of wavelet coherence but the trend is surely slow and costly, yet with certain defections still.

- The fitness of the nature of a life span — For short wind waves (such as the tank data here) the description of a life span fits the physics better. Component waves are inherently evolving and mutual interaction among them is a norm. And this is the basics that the wavelet depiction comes into play. Moreover, life spans of component waves are shorter than any analyzing data length used. That is to say, even the shortest data length of 1024-point sufficiently cover the support lengthes of all wave components in the experiments.

- Wind waves in the tank soon lose their identities — Figure 8.5 (ACC ~ ID) shows the auto-correlation coefficient distributions of two wind-wave signals in the oval tank measured at upstream and downstream location, respectively, and it provides the evidence of the life span argument. Here the correlation level is low and diminishes rapidly. A sensible feeling is that these waves lose their identities extremely fast when viewed from Fourier spectral perspective. Put differently, the behavior indicates the trouble related to the level of uncertainty of the Fourier decomposition.

- Spectral repeatability — Even with the acquaintance of the above explanations one might not grasp to what extent the problem of Fourier spectral repeatability may affect the conclusiveness in data interpretations, as well as the coherent performances shown here. Measurements of the signals in the wind blowing oval tank provide further explanations. But let first present the data in a fundamental perspective based on zero-upcrossing statistics; compared with the spectral point of view, it helps illuminate different specific features that are associated with individual perspectives. Table 8.2 (Zeroup–Sta) shows the statistics from such a conventional method for three sets of measurements. These three measurement sets were made under the same wind velocity and the signals were sampled at a rate of 40 samples per second for a duration of 240 seconds. Channel 1 is for aqueous flows measured with LDV at a depth of 3, 4, and 5 cm, respectively, from the still water surface. Channel 2 is for water-surface displacements measured at nearly the same transverse cross

section of the tank as that of the LDV measurement point (with a separation of 0.6 cm). Therefore, statistics for channel 2 can therefore be regarded as the results from repeated measurements. As are seen from the table, of all individual runs various statistical values for channel 2 are extremely consistent; hence, from the point of view of zero-upcrossing statistics, the wave field under the experimental setup is quite stationary. In contrast, figures 8.3 (FS–RP–L_1) and 8.4 (FS–RP–L_2) show that the idea of stationarity is hardly substantiated when viewed from the spectral perspective. In the two figures, the spectra are for the same data sets but with different values of one of the FFT parameters, i.e., two different segmentation lengthes. The top sub-figures are the power spectra for the repeated measurements of water-surface displacements. The bottom sub-figures are the LDV aqueous flows at each depth. Choices of parameters for these standard spectral numerics are labeled in the figure. For all cases the total length of data is multi-segmented with 50% overlapping, and the Blackman window is applied to each segment. A segment length of 512 points (with an approximate degrees of freedom of 36) is used for the left figures and 1024 points for right figures (with an approximate degrees of freedom of 17). As are shown in the top sub-figures, the repeatability of spectra is rather poor, not to mention the discrepancy arising from different length of segmentation. The spectral resolution for those on the left is insubstantial, while the variations of spectra on the right is much more defective. In fact, the illustrated problem is the manifestation of the symptom associated with the deconvolution mechanism of a spectral blackbox operation [38].

- Phase effects — If we compare corresponding curves (surface wave and aqueous flow signals) in the top and the bottom sub-figures it is seen that the shapes of the two are generally in agreement. This provides a lucid illustration of the phase effects. Since the two signals are acquired at the same time and at almost the same cross section, there is little phase effect between the two spectra. On the contrary, we just do not have any control over the phases of component waves for differ-

ent runs under the same experimental setups. An extreme illustration and further explanation for those effects can be found in figure 5.2 (FS–T&P).

- Stationarity prerequisite — The truly remarkable point for the wavelet coherences is that the 1024-point data length has almost fulfilled the statistics of stationarity. There is little difference among the three analyzing lengthes. Such a behavior is even more proficient than that of the zero-upcrossing statistics (Table 8.2 (Zeroup–Sta)).

- The role of the redundancy — The Fourier basis is orthonormal and the discrete wavelet bases are either orthonormal (self-dual) or orthogonal to their duals (dual mother wavelet and dual farther wavelet). There is no redundancy for orthonormal transforms and little redundancy for those discrete transforms based on nonorthogonal bases. However the continuous wavelet transform is an extremely redundant operation. Without the redundancy a small change in signal causes enormous variation in scale information or transform distribution. The redundancy is able to yield purified coherences by minimizing effects from unrelated scales while provide a fine scale resolution. Redundancy is therefore a much desirable property for studies of coherent behaviors.

- Length requirements — There is no need to acquire lengthy data when wavelet approach is adopted, whereas for the spectral approach the need for more data sees no ending. In this regard, for the wavelet coherences, the lengthening of data provides not much additional information and the information content of redundancy saturates quickly.

- Water waves are inherently "regular" from wavelets' perspective — And again, it is emphasized that this statement is based upon the wavelets' point of view. Since, we have the facts:

  – that most of the wavelet basis functions other than one identified here look

quite odd when compared to the Fourier sine and cosine functions;

- that the various properties outlined in the previous chapter on phase distributions indicate the simplicity requirement of the wave forms and bespeak no ambiguity;
- that the optimal continuous wavelet here is quite like a modulated Gaussian;
- that, in the end, the fourier spectral coherences and the wavelet coherences somewhat approach similar distributions.

7.6 Summary

The absolute superiority of the wavelet coherence fully vindicates the optimal simulation of a best basis. And the outstanding performances lie upon the two main core factors that reflect the truly best both from the best discrete basis and from the most upright continuous counterpart. That is to say, first, it is based on a clear-cut minimum entropy associated with the best discrete wavelet (the semi-orthogonal cardinal spline wavelet) for water waves; second, it further employs the beneficial property of the redundance and engages the existence of a meaningful physical quantity of the carrier frequency associated with the phase of the counterpart continuous wavelet (the Morlet wavelet). ❖

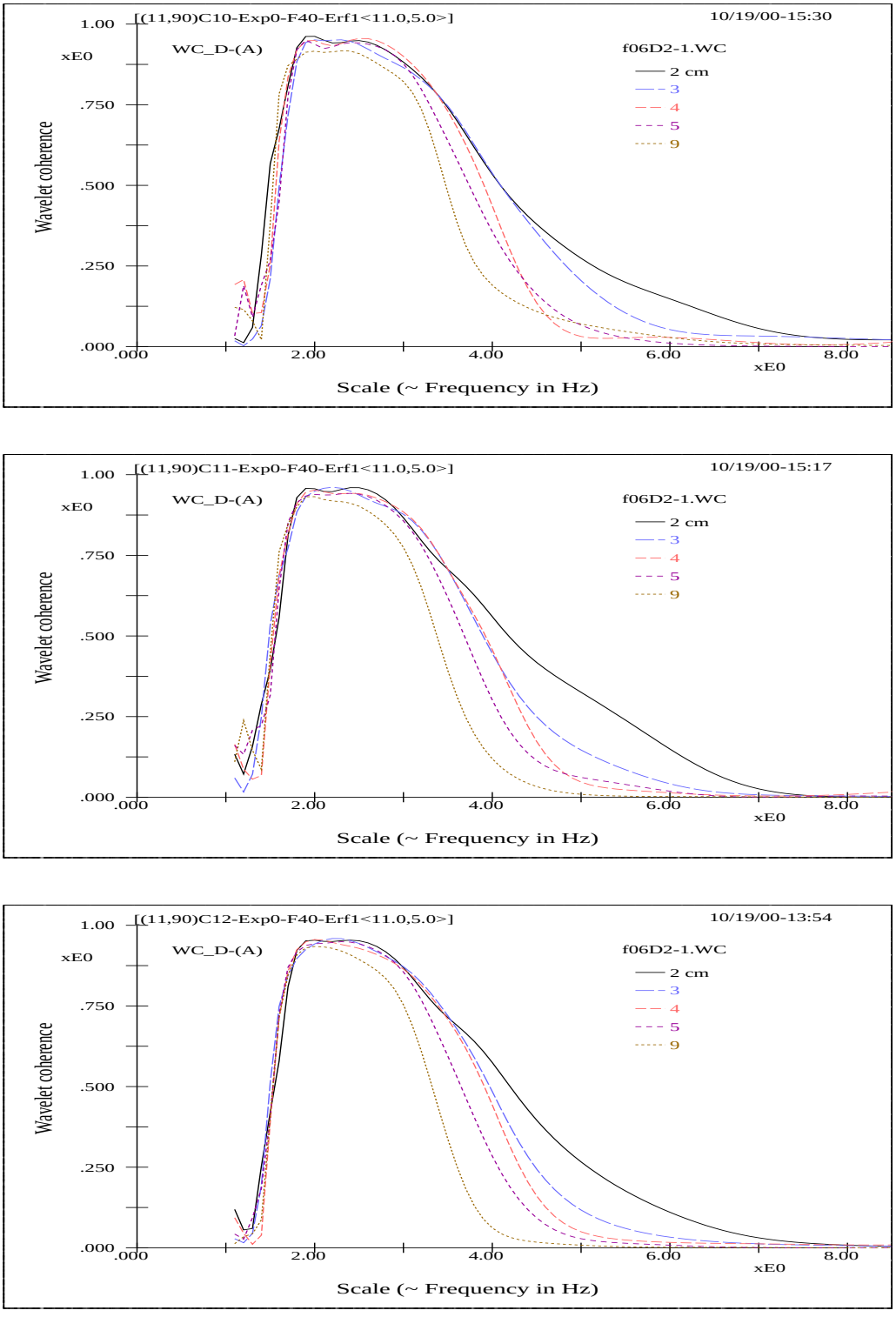

Fig 7.1 (WC–$2^{10,11,12}$) The wavelet coherences between the wave and aqueous flow using three different data lengthes: 1024 (`top`), 2048 (`middle`), and 4096-point (`bottom`). Each individual curve represents a different measuring depth of aqueous flow at 2, 3, 4, 5, or 9 cm, respectively, below still water surface as labeled in the sub-figures. Note the well consistency and behavior among curves.

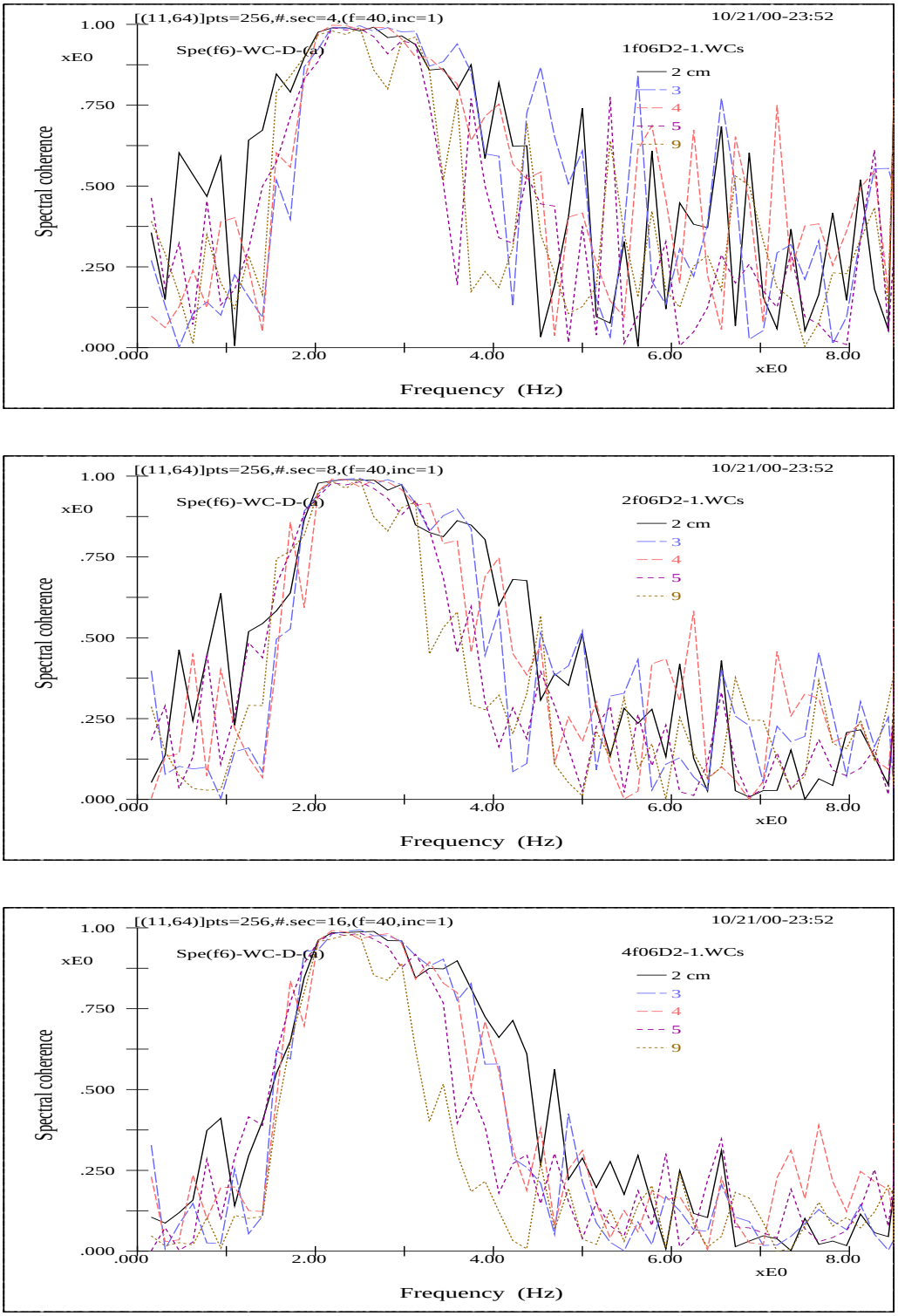

Fig 7.2 (FC–$2^{10,11,12}$) The Fourier spectral coherences between the wave and aqueous flow for the same set of data as that of the wavelet coherences (figure 7.1 (WC–$2^{10,11,12}$)). Note the extreme variation for all the curves.

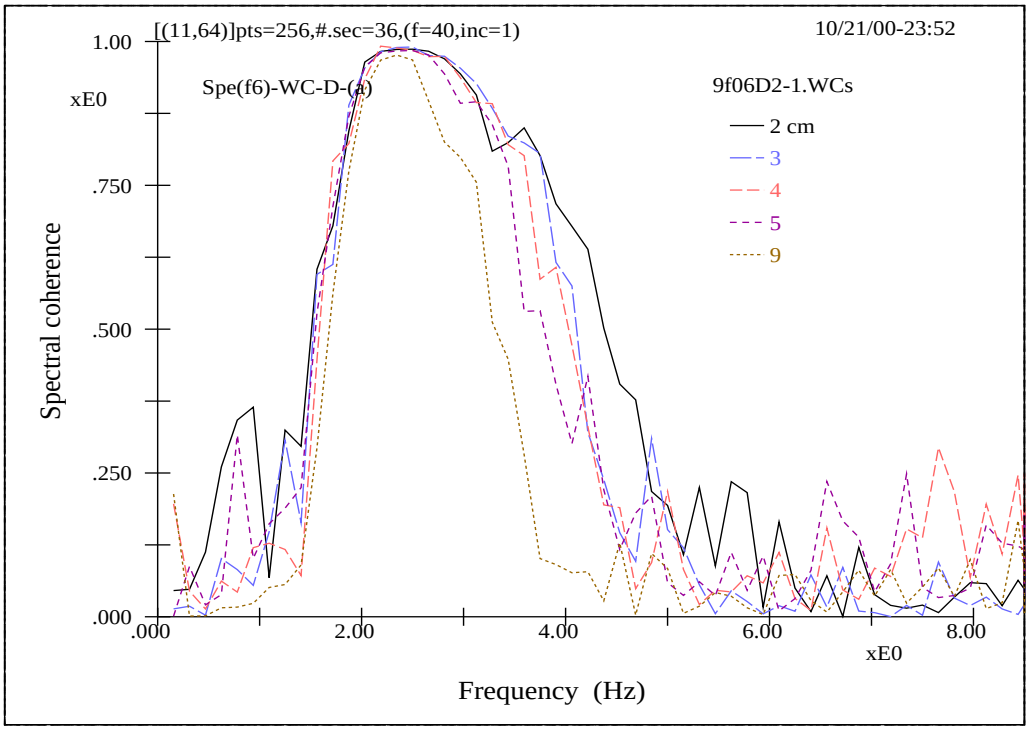

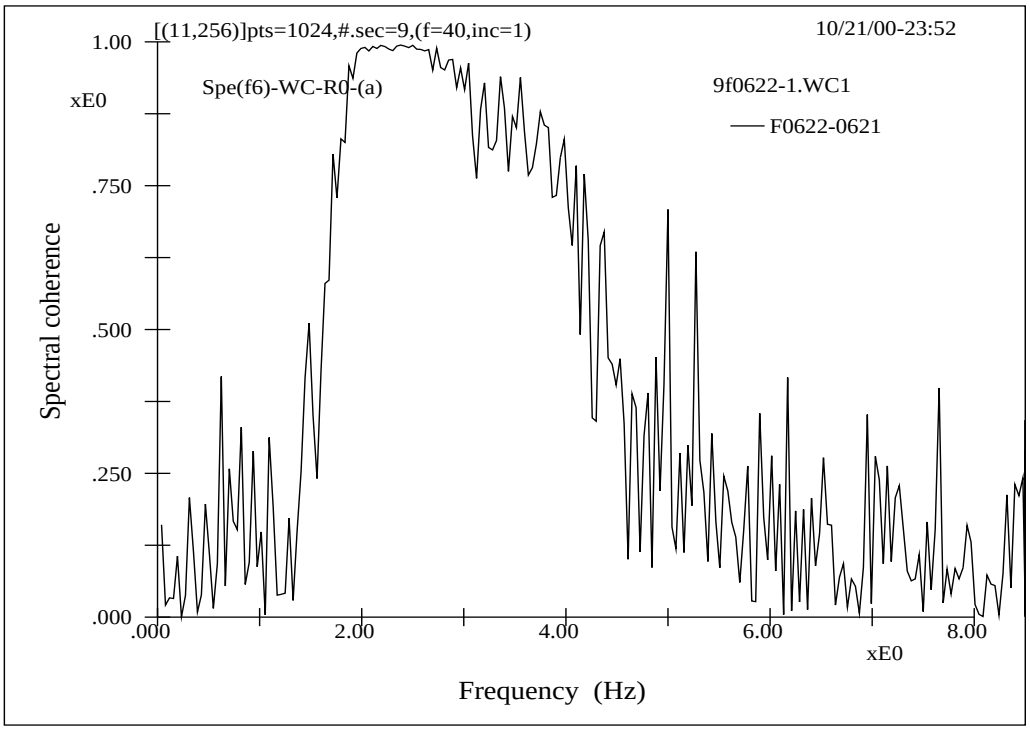

Fig 7.3 (FC–$2^{13 plus}$) The Fourier coherences using a data length of 9126-point for two different lengthes of spectral segmentation, 256 `(top)` and 1024 `(bottom)` points. It is seen that extremely lengthy data may possibly yield a somewhat similar distribution curve as that of the wavelet coherence `(top)`, but note the effects of degrees of freedom of the spectrum `(bottom)`.

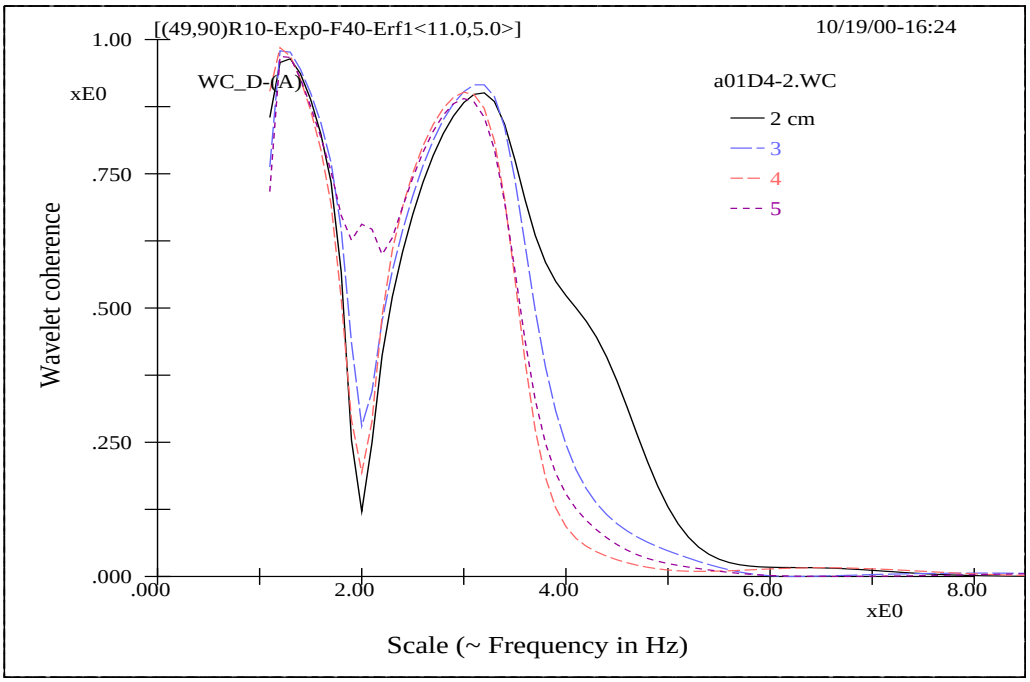

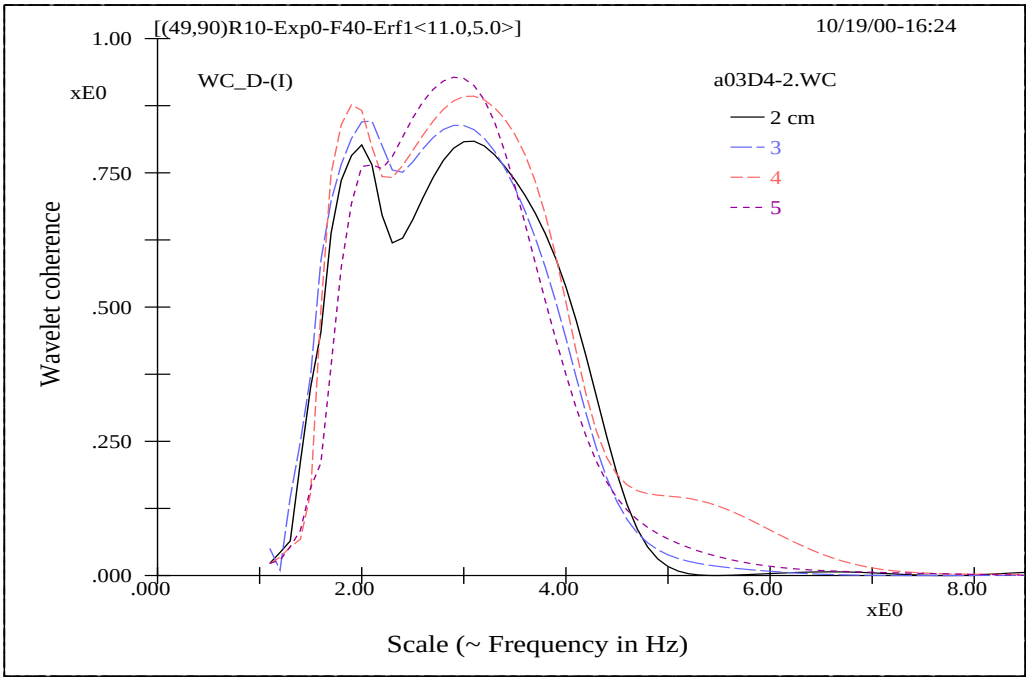

Fig 7.4 (WC–Stokes) The wavelet wave-current coherences at several depthes for two Stokes waves with wave steepness of 0.06 (top) and 0.30 (bottom) for a data length of 1024 points — Some prominent physics here may involve:
(1) the band distribution and degree of separation;
(2) the coherent level for individual band at individual depth;
(3) the tendency or the phenomena attributed to the side-band instability or nonlinear effect of water waves.

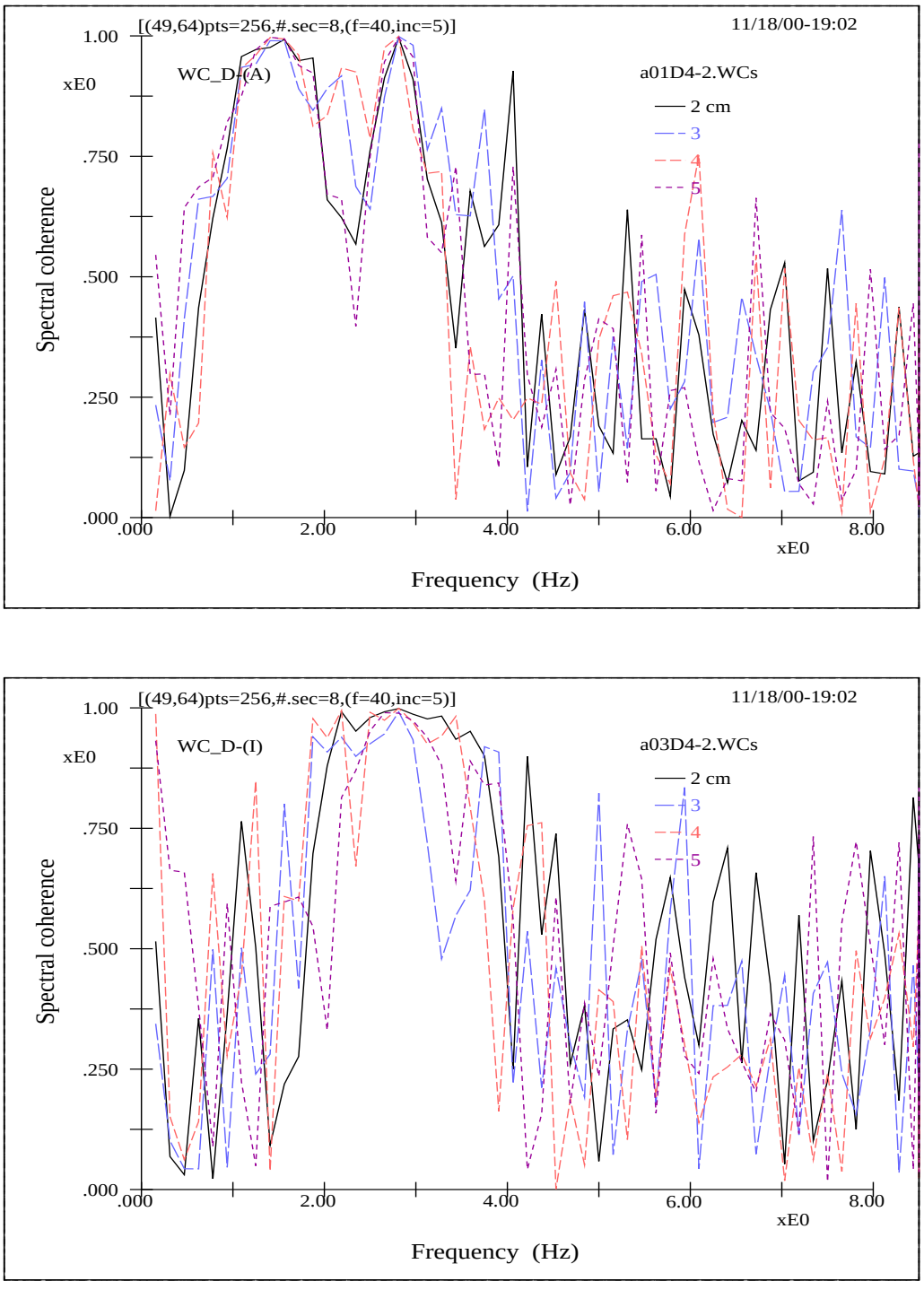

Fig 7.5 (FC–Stokes) The Fourier spectral coherences for the same data as in the last figure (7.4 (WC–Stokes)) (FFT parameters are labeled in the figure) — Can we infer anything?

Chapter 8

An Energy Cascade Model for the Wind, Wave and Rain Coupling System

8.1 Introduction

To serve as an example of possible applications of the identified best wavelet basis and the proposed coherence approach, we study the physics concerning the rapid damping of surface waves in the wind, wave and rain coupling system, and an energy cascade model involving both the surface and internal waves is proposed.

In the fluid dynamics of turbulent flows, a well accepted theory for its energy phenomena is the cascade of energy among scales (e.g., Tennekes and Lumley [68]). In this chapter, apart from a few concepts related to classical wave generation and dissipation mechanisms, we are engrossed to see that many similar features exist between turbulent flows and the wave field of a rain coupling system:

- Catalyst: Both phenomena are caused by the existence of boundary condition or disturbances.

- Diffusivity: In turbulence it is the mixing; in the coupling system it is the induced waves through wave-wave interactions of both surface and internal waves.

- Three-dimensional phenomena: In fluid flows, turbulence is characterized by high levels of three-dimensional rotational motions; in the wave fields, the stratifica-

tion induces diversified wave energy propagation directions and internal local wave breakdowns.

- Continuum: Turbulence is a continuum phenomenon, governed by the equation of fluid mechanics. In this regard, energy phenomenon of the rain coupling system must also be a continuum process since the rain boundary layer is relatively thin when compared with scales of main energy content; without mechanisms acting in the continuum, wave energy of the underlying mainly irrotational motions is isolated.

- Dissipation: Turbulence needs a continuous supply of energy to sustain its viscous losses. If no energy is supplied, turbulence decays rapidly. In this regard, if waves of main energy content cascade their energy into short dissipation scales of either surface or internal waves, the rain calms down the sea very effectively.

- Irregularity: The developed stages have a characteristic of randomness in common.

8.2 Previous studies and the status of data analyses

Van Dorn [72], on his observations of wind-induced stress over a pond, incidentally found that rain can significantly enhance wind stress. He gave the rain-induced horizontal stress over the water surface as $\rho U_r R$, where ρ is the density of water, U_r is the horizontal rain drop speed just before hitting the water surface, and R is the rain intensity. One may regard this quantity as a macroscopic formula in the understanding that the momentum flux is in the form of stress involving neither temporal nor spatial scales in the water side. Moreover, it recognized that the rain drop speed vanished eventually, so the net momentum change is of U_r.

Caldwell and Elliott [14, 15] modeled the interaction of wind and rain in the atmospheric surface layer and concluded that although the wind is only mildly modified by the rain (for the extreme case the increase is about 15%), there is an increase in the

stress communicated by the air. Furthermore, the speed of the rain drop right before hitting the water surface is hardly influenced; so, in the coupling system there is significant enhancement of surface stress over the water surface. These results also suggest the likelihood of more momentum transfer to waves.

LeMehaute and Khangaonkar [42] (henceforth, L&K), in their theoretical treatment of the dynamic interaction between rain and waves, modified the rain-induced stress by taking into account not only the rain falling angle but also the wave orbital velocity in the momentum exchanges. In their attempts they have tried to involve temporal as well as spatial variations into the interaction process. However, these involvements seem only partial and lack scales too. They assumed an instantaneous adaptation of the rain drop speed to the wave orbital velocity upon touching the skin of the water surface. In other words, they have virtually assumed that both the interaction time and the coupling space between rain and waves are zero (a surface without a volume). In fact, another practical and also intuitive concern originating from these is: since the analytical model is based on small amplitude wave theory and since there are no realistic coupling scales, most of their theoretical results would be of little difference from what van Dorn provided — the analytical model introduced only higher order correction terms related to wave orbital motion that is of small amplitude when compared with the first order term the same as in van Dorn's formula. It is therefore quite natural to anticipate that their results predict mainly the wave growth too. Furthermore, the coupling is for monochromatic wave.

On the other hand, seafarers have long observed that rain knocks down the sea, and a few experimental results also indicate that rain causes the damping of waves. However, available experimental results are scattering and generally not comparable since individual experiments were quite different in setups and sometimes limited in modeling conditions. Tsimplis and Thorpe [70] and Tsimplis [69] both used monochromatic waves without considering wind and rain falling angles. Due to the size of their tanks they studied only waves within a narrow frequency range of 2.6 – 4.4 Hz. And in Tsimplis' experiment the size of the receiving water was only 2.35(L) $\times$ 0.10(D) $\times$ 0.33(W) m and

most of their experiments have wave steepness of about 0.3, which is quite large; to our experiences, instability of these waves should be significant and breaking might occur. Moreover, as is generally conceived that the energy dissipation is of multi-scale processes (Tennekes and Lumley [68]), for monochromatic waves the power content may be quite different from that of the corresponding component that is represented in a natural spectral distribution, thus introducing a distortion of the dissipation process. For example, in our wind-blowing oval tank, the total energy content for frequencies higher than 3.5 Hz is generally less than 10% of the overall energy content for wind velocities higher than about 5 m s^{-1}. So, if the main power is not taken into consideration, one can imagine that the proper mechanisms would not show up.

Poon et al's [61] experiments took into account wind and rain falling angles. The spectral results of their damping coefficients are not definite and often deviate from those of Tsimplis and Thorpe [70] by more than 100%. Even though a short 128-point overlapping sections was used in Poon et al's spectral analysis, the spectral comparisons suffer from the uncertainty symptoms that are common to orthonormal function bases, as are related to figures 5.1 (SNI–Phase), 5.2 (FS–T&P), and 8.2 (Faulty BB (F)). .

In what follows we give a brief description of L&K's theoretical treatment to introduce a few related basic mechanisms and provide a framework for subsequent discussions.

By taking into account the rain falling angle and wave orbital velocity on the water surface L&K first derived the horizontal and vertical components of the stress acting on the water body, and then decomposed these into components acting normally and tangentially on the water surface. The tangential component was further converted into the equivalent normal pressure (Longuet-Higgins [45]) acting on the surface, and then added to the original normal component as the equivalent total normal pressure acting on the surface boundary of the irrotational wave field. With this equivalent normal stress as an input of the kinematic and dynamic boundary conditions of waves, a transcendental equation for the complex wave frequency was derived and solved numerically based on the assumed exponential power form of the wave-height evolution. The imaginary part of

the complex frequency (σ_i in Figure 8.1 (σ—L&K)) gives the coefficient of wave growth or decay as appears in the power of the exponential.

A modified plot of L&K's wave decay or growth coefficients for deep water condition is shown in Figure 8.1 (σ—L&K). It is noted that we have made a slight correction about a sign error occurring in the transformation process of the equivalent total pressure, but this happened to affect the relatively higher order terms as compared to that of the major (i.e., equivalently, the macroscopic stress given by van Dorn, as will be further explained). Since it affects higher order terms, the plot here only has minor differences from theirs. Although numerical values were given, they provided no physical explanation on the practical aspects of their outcomes. It seems that their results are neither quite satisfactory for a great portion of wind speed range, nor for the important parts of waves with shorter wavelengths; the latter play a significant role on the dynamics of the air-sea interaction processes, as well as account for major characteristics of a great portion of remote sensing data. For most practical parts of waves under the action of rain with inclined incident angles, L&K's results mainly predict wave growth, and, for shorter waves, the growth rate can be unimaginably huge. Even though one of L&K's figures seems to suggest wave decay, the data are not of practical interests since the case only applies to shallow water and since the illustrated water depth is 3 m with the range of wavenumber reaches only about 0.6 rad m^{-1} (i.e., the wavelength must be large than about 6 m). For relatively shorter wavelengths the curves in their figure turn upward and possess the same tendency as in Figure 8.1 (σ—L&K).

An additional illustration of the impractical aspect of L&K's wave decaying cases is the comparison of their e-folding decay times with those of Nystuen [58]. The equation that Nystuen used to estimate the attenuation of waves by rainfall is $(1/E)dE/dt = -4\nu k^2$, in which E is the total energy density of the wave, k is the wave number, and ν is the viscosity (additional forms were also provided by Nystuen, but this form is particularly true and fits for short waves (see also Atlas [5]). This equation is the theoretical energy dissipation arising from the straining of the irrotational motions due to waves un-

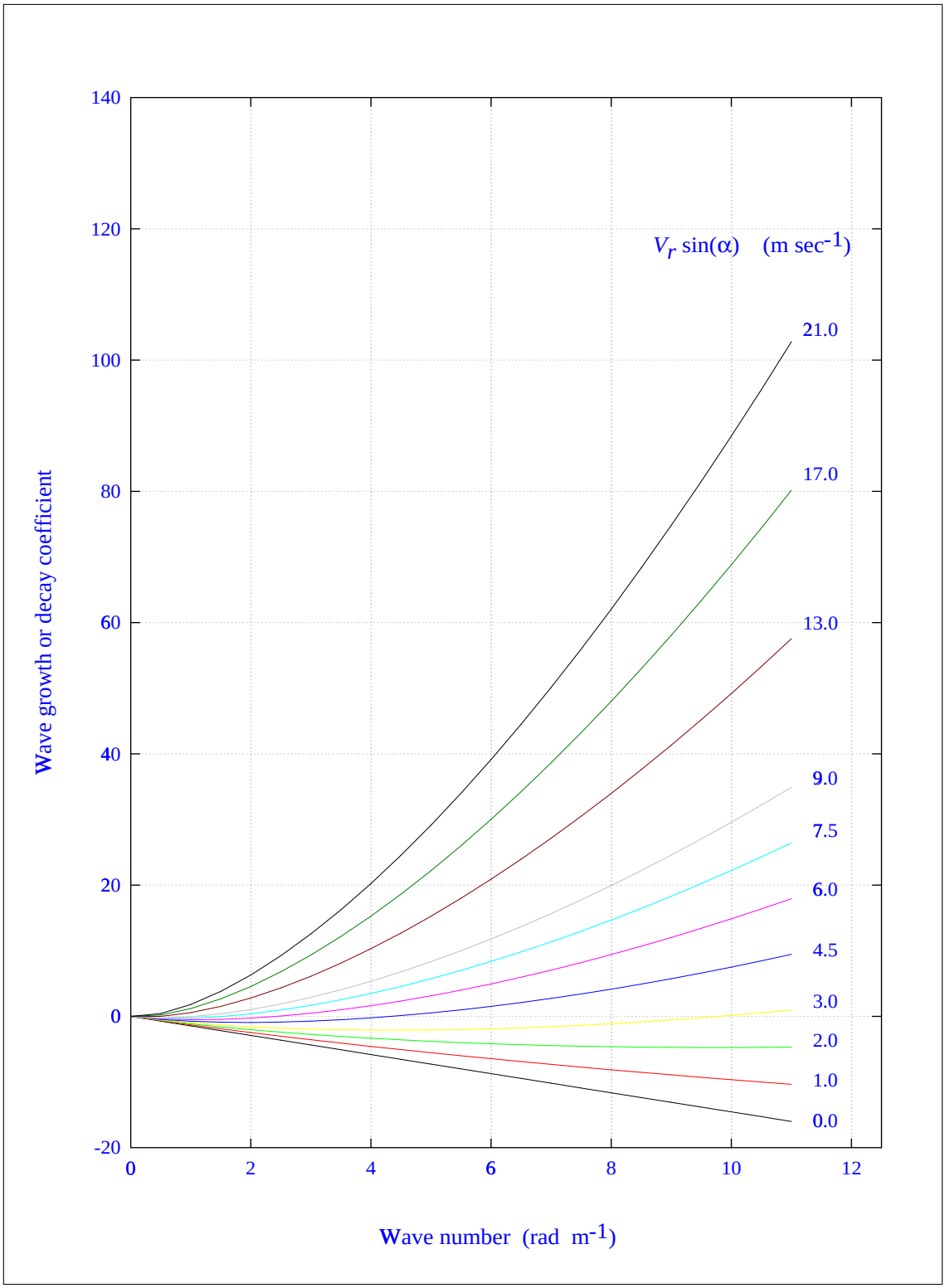

Fig 8.1 (σ—L&K) The wave growth or decay coefficient σ_1/R as a function of wave number k under different values of the parameter $V_r \sin(\alpha)$, where α is the rain falling angle with respect to the gravity line, V_r is the rain drop speed, and R is the rain intensity. A deep water condition of 300 meters is assumed. (Modified from L&K [42])

der the deep water condition. Values of the kinetic viscosity Nystuen assumed are 0.01 and 0.3 $cm^2\ s^{-1}$, respectively, for molecular and turbulent mixing. Note that there are additional sets of viscosity given by the author which yield almost nonexistent life span for short waves (such as 30 cm wavelength); therefore, only the estimations related to the two coefficients are presented here. It should also be emphasized since the turbulent mixing due to rain is confined in a quite thin surface layer the appropriateness of the use of an eddy viscosity for the whole water column in some of Nystuen's cases is also subjected to doubt. The role of viscous dissipation will further be discussed in the following chapter that concerns an energy cascade model. Table 8.1 (*e*-decay–N+K) gives their e-folding decay times (all are converted to values based on the wave amplitude) for selected wavelengths. A rain intensity of 150 mm hr^{-1} and vertical rainfall are assumed for L&K's case (corresponding to an extreme decay condition). If non-vertical rainfall is used, the decay times of L&K's estimations will become even longer. One may notice that the e-folding decay times of L&K are even larger than those due to molecular dissipation, and for shorter wavelengths there may be orders of magnitude differences. One may also notice that if Nystuen's eddy dissipation for relatively short wavelength is true, it is difficult to obtain significant data related to these waves due to its near invisible short life spans in time and space. Moreover, results from radar backscatter experiments do not entirely agree with these. Moore et al's 2.1 cm radar wavelength [57], Bliven et al's 2.2 cm [10] and Bliven and Giovanangeli's 0.8 cm [9] showed no sign of such wave damping; whereas Atlas [5] gave reasons why these experiments failed to show evidence of wave damping.

8.2.1 A problematic blackbox mechanism of direct deconvolution

Spectral comparison is commonly adopted in envisioning phenomenological evolutions of a complex process; however, there is a concern regarding how detail it can go. Figure 8.2 (Faulty BB (F)) illustrates such a concern as explained in the following.

Tab 8.1 (*e*-decay–N+K) Comparison of the e-folding decay times of wave amplitude from LeMehaute and Khangaonkar's [42] and Nystuen's [58] estimations.

Source of e-folding decay time (s)	Wavelength (m)			
	0.02	0.1	0.3	1.0
LeMehaute and Khangaonkar$^{\star\,\dagger}$	158.0	788.0	2362.0	7880.0
Nystuen's molecular viscosity†	4.8	120.0	1080.0	12000.0
Nystuen's turbulent layer eddy viscosity‡	0.034	2.1	37.8	800.0

*With 150 mm hr^{-1} rain intensity and vertical rainfall (implying maximum decay rates)
†Molecular viscosity: 10^{-6} m^{2}s^{-1}
‡Eddy viscosity: 3×10^{-5} m^{2}s^{-1} (for cases with a 0.1 m turbulent layer thickness)

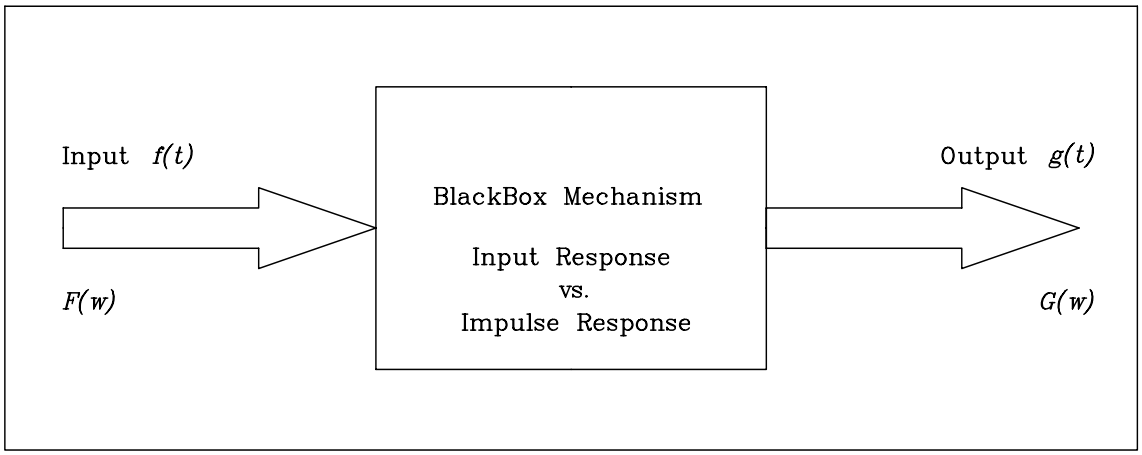

Fig 8.2 (Faulty BB (F)) The simple blackbox here is to illustrate the following problem: Does direct quotient of spectral coefficients of two spectra make any sense? If a direct division of two spectra is taken, this blackbox implies that the output is the convolution of the input signal and a certain impulse response function, or alternatively speaking, the blackbox mechanism is the deconvolution between the output and the input signals. The concept is intuitively simple, but it is generally of little use due to the fact that the process is extremely error prone, as explained in the text. The figure also indicates the inherent problems regarding a direct comparison of two spectra when there are concerns of non-stationary effects and other possible uncertainties (implied by figures 5.1 (SNI–Phase), 5.2 (FS–T&P), 8.3 (FS–RP–L_1), 8.4 (FS–RP–L_2), 8.5 (ACC ~ ID), as well as various figures given in the chapter on cohherences).

Let suppose we have an input signal and an output signal. The input signal is, say, an original signal without being influenced by external factors or measured prior to the introduction of influences; and the output signal is, say, the altered signal when those external factors or influences are introduced. One simple intuitive thinking regarding the identification of effects of these influential factors on constituent components of the signal is to compare the input and output spectra. The concept is simple, but generally it is quite problematic. The reason is that the idea of such a spectral comparison is just a manifestation of a deconvolution process, as illustrated by the convolution duality property of Fourier transform,

$$h(t) \iff H(\omega), \tag{8.1}$$

$$h(t) \star f(t) \iff H(\omega)F(\omega). \tag{8.2}$$

Here the double arrow sign means that the role of t and ω can be inter-changed. Referring to Figure 8.2 (Faulty BB (F)), if one assumes that

$$H(\omega)F(\omega) = G(\omega), \tag{8.3}$$

it seems, therefore, quite straightforward to say that the individual effect on each frequency component is simply the division of two spectra,

$$H(\omega) = \frac{G(\omega)}{F(\omega)}. \tag{8.4}$$

And the response function $h(t)$ induced by the external factors is simply the inverse Fourier transform

$$h(t) = \mathcal{F}^{-1}\left[\frac{G(\omega)}{F(\omega)}\right]. \tag{8.5}$$

The problems here are two-fold, both practically and analytically, and they are mainly

associated with the $F(\omega)$ in the denominator. Practically, due to finite discrete resolution scheme, together with many unavoidable side effects in numerical processing, the spectral results are of periodogram estimations and reflect only the expectation values of the power spectrum of a continuous distribution. These estimators generally suffer severely from having large variance with efforts to improve it being rather inefficient (Press et al. [62]). Moreover, in many physical situations the power spectra are often quite narrowly banded, or stated otherwise, peaked only around a small region within the whole range of frequencies; therefore, for frequency components with little energy the division of two spectral coefficients is extremely error prone. Analytically, if there exists only a single resolution point where the power content is nil, then the inverse transform is simply non-existent. Overall, the symptom here is the so-called direct source deconvolution and is generally referred as the "effects of amplitude equalization"; it results in a high-pass window in the frequency domain. In the presence of additive noise, this window further amplifies the uncertainties significantly (Soumekh [64]). Though such inherent limitations exist, it is not uncommon to see that the tactic is used to judge the details of scale evolutions for cases with complicated processes. The following two sections also serve as further elaborations.

8.2.2 Transient effects and phase noise

In a wind, wave, and rain coupling system both the water surface and the flow field are quite irregular and possibly turbulent, and there are always sharp and violent local features. Figure 5.2 (FS–T&P) conceptually illustrates the power spectral phenomena that are caused by these features. But, let us first have a physical description of the analytical aspect; it helps explain why many of the outcomes of data analyses are scattered.

If there is no autocorrelation (or cross-correlation), there is no power spectrum (or co-spectrum); therefore, if the life span of a wave (or wave components) is short, then the correlation of variables related to that specific wave soon loses and the corresponding spectral content is relatively minor or undistinguishable, and with insignificant spectral

contents the deconvolution is hardly meaningful.

The corresponding parts that Figure 5.2 (FS–T&P) conveys can be given quite straightforwardly, even though the condition shown may be somewhat extreme. In the figure two Lemarié wavelets in the two least (smallest) scales are used to represent the short local transient pulses of a signal. The left pulse corresponds to the result of the inverse wavelet transform from a unit wavelet coefficient at element 600 within a 1024-point series, and the right pulse corresponds to that of a unit wavelet coefficient at element 470. The choice of the least two scales is to emphasize the effect of transient locality — which renders a very board distribution of power spectrum. The choice of positions 600 and 470 is somewhat intentional and somewhat arbitrary — just to show the symptom related to the occurrences of the pulses, i.e., the phases, which are responsible for the wiggling of the spectrum. By "intention" we mean that the greater the separation distance, the more severe the wiggling; By "arbitrariness" we mean that for a practical situation where complexity and randomness exist we generally do not have control over either the timings of occurrences or the positioning of local features. Overall, once more, these symptoms simply reflect properties of the following Fourier transform pairs:

$$f(t-\tau) \iff e^{-i\omega\tau} F(\omega), \tag{8.6}$$

$$|f(t)+g(t)|^2 \iff |F(\omega)+G(\omega)|^2. \tag{8.7}$$

Again the double arrow sign means that the roles of t and ω may be inter-changed, except there may exist different multiplication constants. Now, causes of the wiggling of the spectral curve can be explained more specifically. First, since "a shift in one domain corresponds to a modulation in the other domain (one of duality properties of the Fourier transform)", relative locations of individual pulses introduce serious wiggling of the overall spectrum. Moreover, even the modulus of the modulated spectral coefficients for the second pulse alone is the same as that of the spectral coefficients for the first pulse alone, the modulus of the spectral coefficients for the pulses combined differs from the

direct summation of the two individual modulus values. Second, even though the Fourier transform is a linear operation on component signals (or component waves), the power spectrum is not a linear operation. That is to say, the power of combined pulses does not equal to the sum of individual powers for the two pulses.

Still, the above statements do not count for side effects arising from actual numerical process; there are always uncertainties that are associated with the discrete nature of a transform, due to finite resolution and limited data length. In addition, these is not without artificial inputs, such as the practical concerns regarding proper explanations of complex results of the Fourier transform as well as from double-sided into single-sided spectrum, as are most obviously reflected when dealing with two-dimensional spectrum where the symmetry of power spectrum can hardly be practically explained — in this regard, the wind waves in the tank are somewhat two dimensional.

8.2.3 Spectral repeatability

Even with the acquaintance of the previous phenomena one might not grasp to what extent they might affect the conclusiveness in the interpretation of spectra. Measurements of the wind-wave signals in our wind blowing oval tank provide the explanations. But first let present the data in a different perspective based on zero-upcrossing statistics; compared with the spectral point of view, it helps illuminate specific features that are associated with individual perspectives.

Table 8.2 (Zeroup–Sta) shows the statistics from such a conventional method for three sets of measurements. The data sets are acquired in the oval tank to be described in a later chapter. These three measurements were made under the same wind velocity, with signals being sampled at a rate of 40 samples per second for a duration of 240 seconds. Channel 1 is for aqueous flows measured at a depth of 3, 4, and 5 cm, respectively, from the mean water surface using a laser Doppler velocimeter (LDV). Channel 2 is for water-surface displacements measured at nearly the same transverse cross section of the tank as that of the LDV measurement point (with a separation of 0.6 cm). Statistics for channel 2 can

therefore be regarded as the results from repeated measurements.

As are seen from the table, of all individual runs various statistical values for channel 2 are extremely consistent; therefore, from the point of view of zero-upcrossing statistics the wave field is quite stationary. On the contrary, the idea of stationarity is hardly substantiated when viewed from the spectral perspective. Figures 8.3 (FS–RP–L_1) and 8.4 (FS–RP–L_2) show the spectra for these same data sets as well as additional ones: the top sub-figures are the power spectra of the repeated measurements of water-surface displacements. The bottom sub-figures show spectra of the LDV aqueous flows measured at several depths (3, 4, and 5 cm from the mean water surface). As is shown in the top sub-figures, the repeatability of spectra is rather poor. Nevertheless, when comparing the top and the bottom sub-figures the spectral shape of the water-surface displacement is seen to match well with those of the aqueous flow for each individual run. This provides a lucid illustration of the phase effects — since the surface displacement and the aqueous flow are acquired at almost the same cross section, there is little phase effect between the two spectra associated with a single run; while, on the contrary, we just do not have any control over the phases for different runs.

Choices of parameters for these standard spectral calculations are labeled in the figure. For all cases the total length of data is multi-segmented with 50% overlapping, and the Blackman window is applied to each segment. A segment length of 512 points (with an approximate degrees of freedom of 36) is used for the left figures and 1024 for right figures (with an approximate degrees of freedom of 17). The spectral resolution for those on the left is inferior, while the repeatability of power spectra for those on the right is much worse. Again the figure illustrates problems highlighted by the blackbox mechanism.

And again, as a supplemental explanation in plain terms, we can attribute causes of the repeatability problem to the rapid diminishing as well as the irregularity of the auto-correlation coefficient distributions, as are shown in Figure 8.5 (ACC ~ ID). In the figure the auto-correlation coefficient functions for two wave gauges located at upwind and downwind positions are shown. The correlation levels are quite low; it simply states that these

waves lose their identities extremely fast and that there are profound transient local phenomena.

8.3 Scale complications and mechanism

8.3.1 Questions restated

All phenomena in nature have their own scaling laws, though the scales involved may either be relatively simple or extremely complex. Here on the one hand, we discussed the problems concerning the proper scalings both in space and time for a few existing studies; on the other hand, we pointed out the deficient aspects concerning the current status of data analyses, and these deficiencies are amplified owing to scale complications. Therefore, the motivation here should be clearer: On one hand, we need to venture a broader spectrum of mechanism such that interaction scales are more faithfully accounted; on the other hand, we need to facilitate a tool or methodology that is both apathetic to existing shortcomings and in accord with the nature of the our signals, such that evolutions of scales can be discerned.

In this complex coupling system of ours the energy phenomena are certainly anticipated to be the results of intertwined processes that involve interactions of various characteristic dimensions and originate from individual causes. For example, both in the wave and flow fields the energy is related to large scales and is therefore contained in a large volume of water body; while the turbulent dissipation is limited to a local surface layer of relatively small scale, and its locality is further restricted by the existence of a stable stratification. So, if it is true that rain does not hinder the wind (Caldwell and Elliott [14, 15]) but suppresses the sea, then there must exist some kinds of energy transfer or dissipation mechanisms. One pivoting issue is the energy cascade among waves; monochromatic wave fields lack the mechanism. Furthermore, the patterns of energy propaga-

Tab 8.2 (Zeroup–Sta) The zero up-crossing statistics for three different sets of measurement under the same wind condition. Channel 1 is for LDV aqueous flows measured at different depths from the still water surface. Channel 2 is for surface displacements measured at the same location. Statistics for channel 2 can basically be regarded as results from repeated measurements. Comparisons of data related to channel 2 indicate that the wave statistics is in good stationary condition. Whereas, this is certainly not true when viewed from the Fourier spectral perspective, as shown in the power spectrum figures (figures 8.3 (FS–RP–L_1) and 8.4 (FS–RP–L_2)).

Case : f0w6030.dat (f1 p3 c1 s9)
Date : 01/05/96
Time : 02:19:05.48 Sampling frequency : 40 Hz
Specifics : Sampling time length : 240 Sec

Ch	#_W	H.1	H.2	H.3	H1/10	H1/3	H1/2	H.ave	H.rms	T1/10	T1/3	T1/2	T.ave	T.rms
1.	554	26.74	23.67	23.04	20.20	17.38	15.92	12.03	12.93	.44	.44	.44	.43	.44
2.	572	2.90	2.69	2.61	2.33	2.04	1.89	1.44	1.54	.44	.44	.43	.42	.42

Case : f0w6040.dat (f1 p3 c1 s9)
Date : 01/05/96
Time : 02:14:05.76 Sampling frequency : 40 Hz
Specifics : Sampling time length : 240 Sec

Ch	#_W	H.1	H.2	H.3	H1/10	H1/3	H1/2	H.ave	H.rms	T1/10	T1/3	T1/2	T.ave	T.rms
1.	546	22.81	20.65	20.52	17.04	14.48	13.32	10.35	11.01	.45	.44	.44	.44	.45
2.	563	2.98	2.88	2.72	2.35	2.04	1.89	1.46	1.55	.44	.43	.43	.43	.43

Case : f0w6050.dat (f1 p3 c1 s9)
Date : 01/05/96
Time : 02:00:30.72 Sampling frequency : 40 Hz
Specifics : Sampling time length : 240 Sec

Ch	#_W	H.1	H.2	H.3	H1/10	H1/3	H1/2	H.ave	H.rms	T1/10	T1/3	T1/2	T.ave	T.rms
1.	546	17.62	16.49	16.30	14.02	11.94	10.97	8.22	8.88	.45	.44	.44	.44	.45
2.	562	2.83	2.74	2.72	2.36	2.06	1.91	1.45	1.55	.44	.44	.44	.43	.43

Units:: Aqueous flow (Ch1:H): cm/s
Surface wave (Ch2:H): cm
Period (T): s

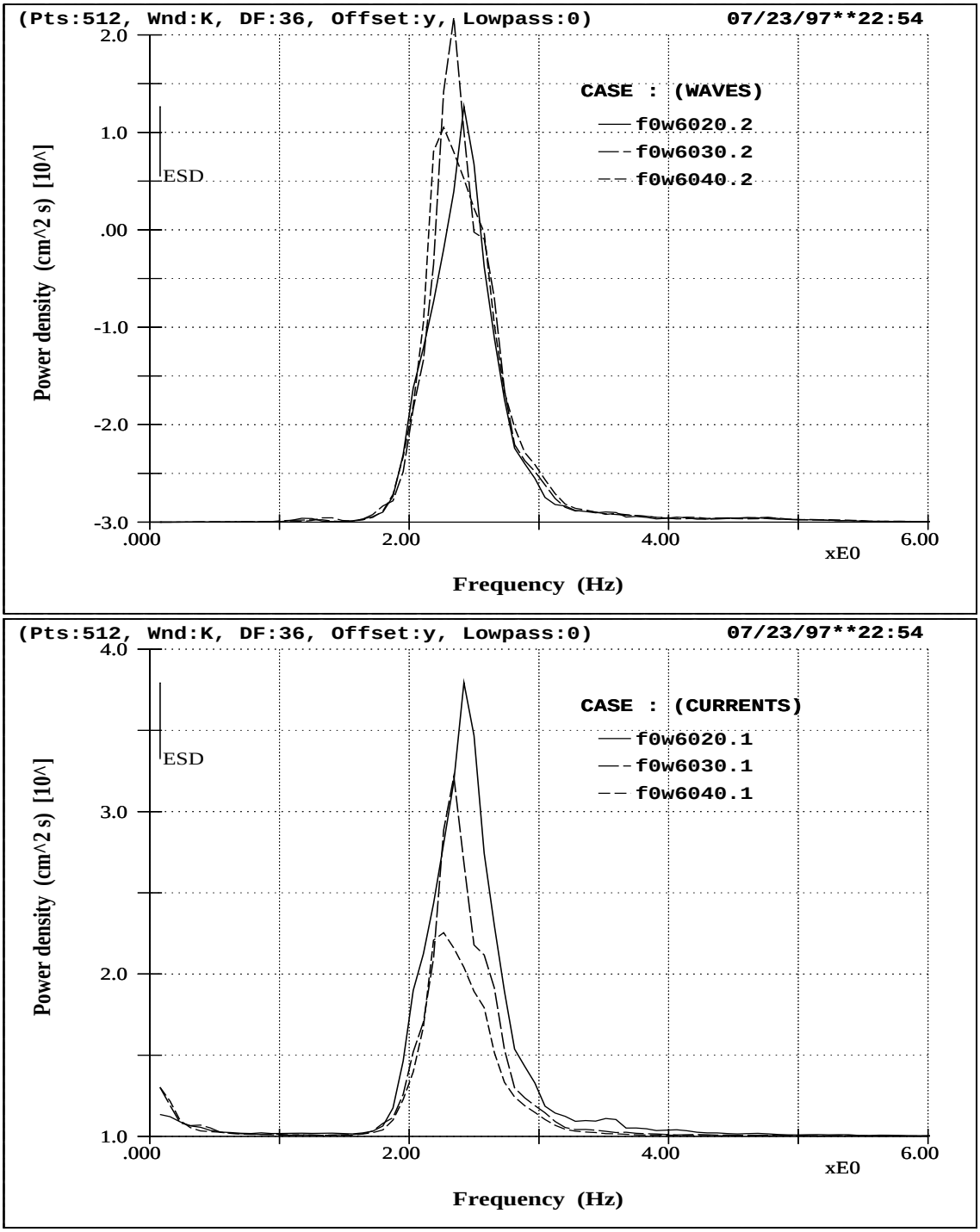

Fig 8.3 (FS–RP–L_1) Spectra of the surface displacement and aqueous flow for the same three sets of measurements as shown in table 8.2 (Zeroup–Sta). The top sub-figure shows power spectra of the repeated measurements of surface displacement. The bottom sub-figure shows power spectra of the LDV aqueous flow measurements at different depths. It is seen that the repeatability of power spectra is rather poor even though the zero up-crossing statistics has indicated the existence of a good stationary condition. This has profound entailment of the poor performances of spectral coherence, as well as the sure unfruitfulness of the blackbox deconvolution mechanism for two signals under any circumstance.

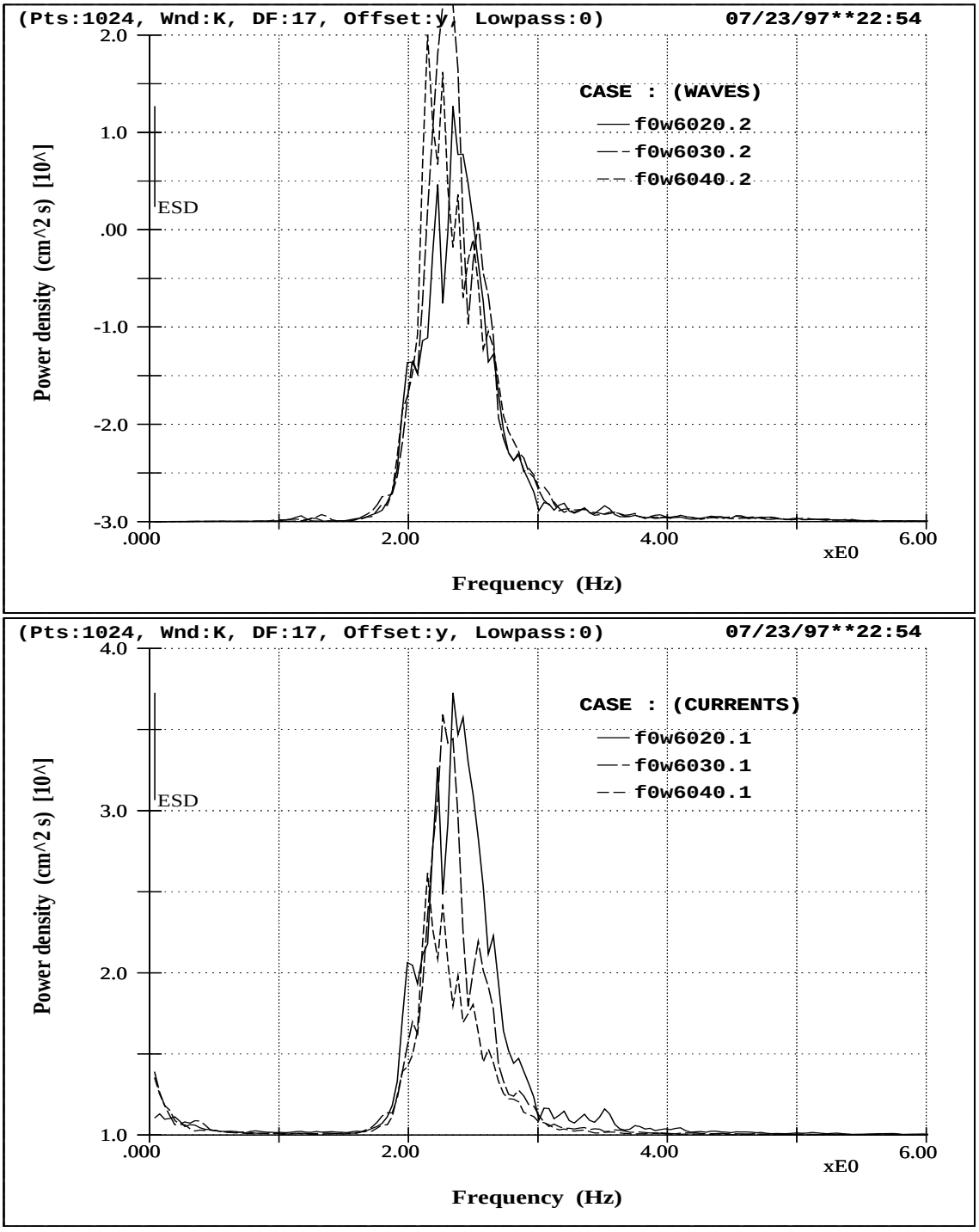

Fig 8.4 (FS–RP–L_2) Spectra for the same data sets as in the previous figure but with different FFT parameters. Here a longer 1024-point segmentation is used and the degrees of freedom is approximately halved. Whilst the resolution is increased the standard deviation intensifies. Again the figure shows the profound implication of the problems of Fourier spectral repeatability and the poor performances of spectral coherence.

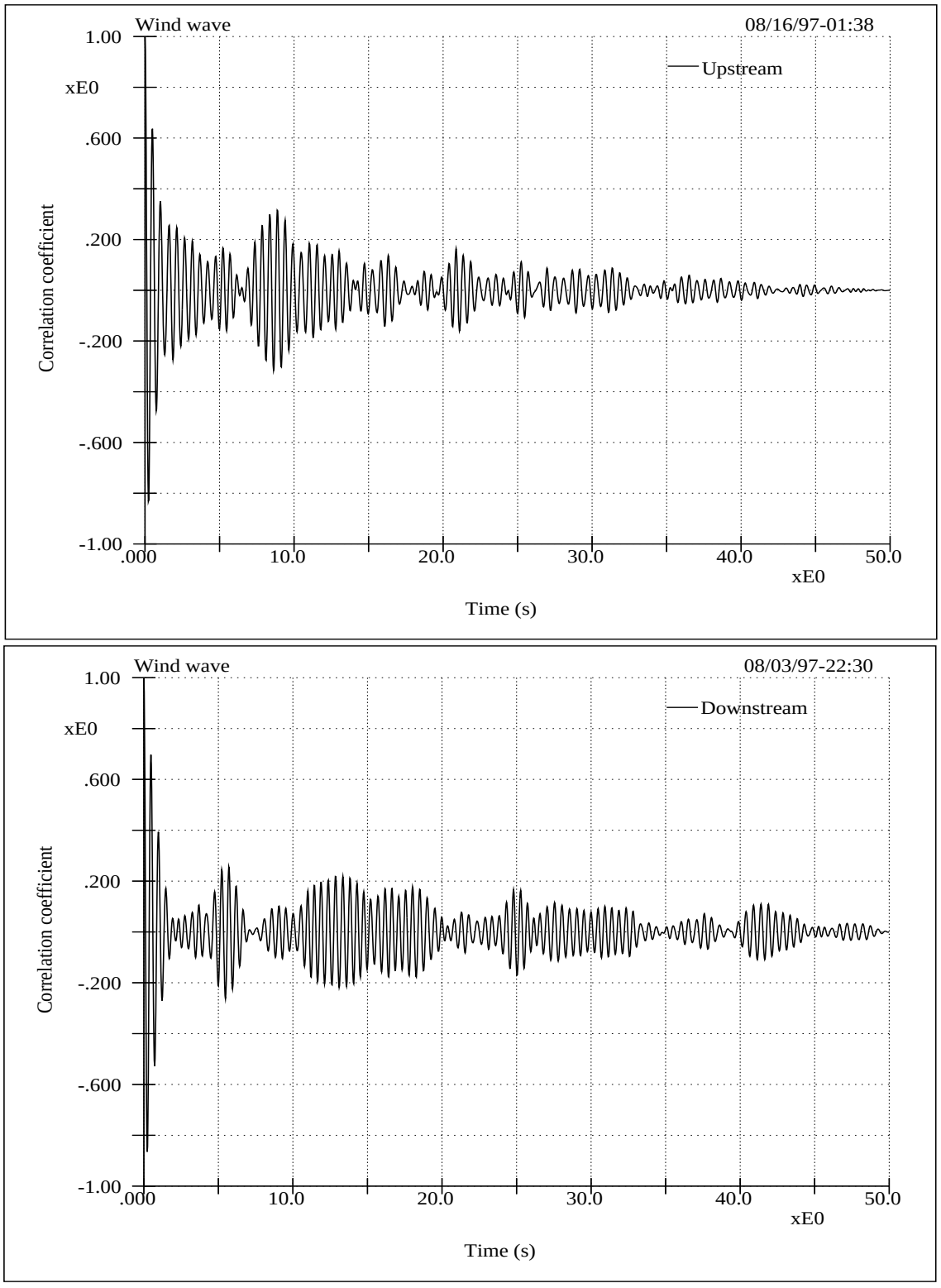

Fig 8.5 (ACC ~ ID) Wind waves in the tank soon lose their identities — The auto-correlation coefficients of two series of wind-wave signals measured at upstream and downstream locations in the oval tank. The correlation level is low and diminishes rapidly. A sensible feeling is that these waves lose their identities extremely fast when viewed form Fourier spectral perspective.

tion of waves for homogeneous and stratified fluids may be quite different. And in almost all natural water bodies stratification almost always exists either due to thermal or salinity effects or both. Besides, in most rainfall cases the rain further induce favorable conditions for stratification when fresh water falls into the sea (Houk and Green [28]; Green and Houk [25]). Now it is natural to put forward the following questions: What are the roles of the interfacial surface layers with the addition of rain action, and can they trigger the speedy calming of the sea? What are the mechanisms induced by the stratification of the receiving water body? How are local and global mechanisms intertwined, and does energy propagate into the small thin surface mixing layer? Are energy phenomena at different depth regions different? In brief, what are the interactions and their scales that facilitate the physics involved?

8.3.2 The wavelet connection

In view of the discrepancies among the various studies, the blunders arising form the inherent complexity of the coupling system, the unavoidable limitations in model experiments, as well as the aforementioned deficiency in data analysis, we sense the need of an optimum tool and its related scheme if they should ever be useful. In this regard the connection between the optimum wavelet basis and the study of the coupling mechanism can be outlined. Suffice it to say that the fundamental concept here is: If we perceive our signal as composed of waves which are limited in life span and evolving with time and in space, then it is natural to take advantages of the property of the finitely supported lengths of analyzing basis functions. In this regard, the localized transform of wavelet approach meets the basic appeal. Moreover, if we also acknowledge that intrinsic instability (Benjamin and Feir [13]; Whitham [73]; Melville [53]), which may be due only to nonliner surface boundary condition, is inherent to almost all dispersive waves, either initially regular or not; then, not only for non-stationary but also for stationary signals, the wavelet decomposition is clearly better consolidated to modeling of the physics than is the Fourier decomposition.

8.4 Local mechanisms — Physics in the rain boundary layer as well as in the air boundary layer

8.4.1 Instability in the surface shear layer

It was mentioned earlier that L&K's rain and wave interaction model mainly predicts the wave growth. It seems that there is some kind of wave generation or enhancement mechanism inherent in their model. A review of Phillips' [59, 60] and Miles' [56] theories on the wave generation due to wind and the coupling mechanism between wind and waves may help to identify the problems related to the generation rather then damping caused by rain in L&K's model. Phillips and Miles divided both the normal pressure and the tangential stress acting over the water surface into the phase averaged variations (called directly induced stress) and the randomly varying component associated with eddies of the atmospheric turbulence. Due to the zero dimension (in depth) of the rain boundary layer that L&K assumed the dynamics of the two cases are of the same nature — the same type of boundary conditions acting on the water surface. The correspondences of the boundary conditions are: (1) The basic rain-induced stress (term) in L&K's model corresponds to the phase averaged stress in the wind model and is given by the macroscopic stress $\rho U_r R$, i.e., the horizontal momentum flux of rain, as proposed by van Dorn [72]. (2) Those stress modifications to the basic macroscopic stress correspond to the random turbulent components of the wind stress of the wave generation model; however, these modifications are not related to turbulences, but related to the wave orbital velocity of a monochromatic wave.

Given the inherent mechanisms involved in L&K's model, we should be able to discussed the inadequacy of their model more clearly. Let explicate in two aspects.

First, let us explain why the major term of the stresses is the macroscopic stress and the terms related to wave orbital velocity are of higher order. On one hand, since small amplitude wave is assumed in L&K's model, the surface slope is relatively small; there-

fore, there is not much modification on both the normal and tangential pressures acting on the water surface caused by the imposed boundary condition of wave orbital velocity. On the other hand, since the imposed boundary condition of wave orbital motion is periodically oscillating, there are symmetrical cancelations in its influences on both the normal and tangential stresses; therefore, the net effects are negligible. The above two points apply to both long and short waves. For short waves there is the additional concern: since the magnitude of the wave orbital velocity is relatively small as compared to the rain drop speed (suppose that the rain drops are falling with somewhat noticeable angle) the effect of wave orbital velocity is certainly negligible.

Second, let us explain why the calculated wave growth coefficients of L&K are going to render unimaginably huge waves and why the shorter are the waves the greater the effects are introduced. On one hand, as shown analytically in Phillips' wind and wave resonant theory: if the momentum transfer is dominated by turbulent stress fluctuations the energies of the wave(s) increase linearly with time; whereas, if the system is dominated by induced surface stresses the rate of growth of wave becomes more rapid and is characterized by an exponential form that is associated with an instability depicting a time scale determined by the wave length and water viscosity, and the shorter the wavelength the sooner the physics collapses. In fact Phillips' results also manifest the physics intrinsic to the Kelvin-Helmholtz instability (Lamb 1932 [33]): in a forced system of flow field if the surface dominating stress is shear rather than normal pressure the system is in an unstable mode and variables grow exponentially rather than in an oscillating form. On the other hand, from practical point of view, even without considering the abrupt intrusion of rain drops, when shear stress is applied to a free surface the critical Reynolds number for the transition from laminar to turbulent flow drops drastically and the eddy viscosity of the fluid comes into play (so, non-viscous irrotational is no longer suitable) and the energetic vortex dynamics develops; Moreover, there is another concern that two-dimensional flow field is not able to provide such a mechanism (Tennekes and Lumley [68]). In the later section we will mention a weak vortical motion induced by surface boundary condition.

8.4.2 The match layer concepts

As stated earlier, one of the major problems concerning the interaction between rain and wave is the inadequacy of the zero-depth assumption of the rain boundary layer which causes the wave orbital velocity to be treated as the turbulent fluctuations. Furthermore, since rain-induced stress hardly exists without wind, it is inadequate to study rain effects without considering wind altogether. In this section, based on the match layer concept (Phillips [60]) we explain that the rain boundary layer on the water side does not give favorable condition for the developments of large scale waves, but does provide promising conditions for the turbulent dynamics that is associated with short waves. The match layer concepts as adopted in the wind and wave coupling system proposed by Phillips concern the turbulent dynamics in the air boundary layer, but here by extending the arguments to the water side we try to explore the physics in the rain boundary layer superimposing upon an irrotational wave field.

Let the frame of reference be taken as that moving with the phase speed c of wave. The mean surface speed of the water of the wave will be $-c$; on the air-water interface the mean surface speed will be $-c+q$, where q is the mean surface drift. For relatively short waves the mean speeds on the upper and lower boundaries, i.e., $-c+q$ and $-c$, respectively, are very likely to be of opposite signs as viewed by an observer moving with the wave. Under such a situation the streamlines of the phase averaged turbulent flow (a phased averaged two-dimensional incompressible flow suffices the existence of a stream function for the velocity field) form closed loops centered at a zero relative speed. The layer that covers the thickness for these closed loops is the so-called matched layer. For the matched layer to play an important role in the energy transfer from the rain boundary layer to the waves the matched layer must be located in the region where a large curvature of the mean speed profile exists. However, unlike the air boundary layer, the rain boundary layer is generally relatively thin; so the matched layer is likely to cover a great portion of the rain boundary layer. Under such a condition the dynamics will be either of "viscous dynamics" or of "vortex force dynamics" (Phillips [60]). The viscous dynamics is for the

matched layer to fall near the wave surface (especially for small c) and the vortex force dynamics (in which the flux of energy from phased averaged mean flow to the fluctuating motion is coming from the working of the vortex force on the phase averaged velocity field) for c somewhat larger (but still of short wave).

As for longer wave, due to the large c value, the match layer will not exist in the rain boundary layer (but there may still exists a match layer in the wind boundary layer); and the direct energy input to the underlying irrotational wave field form the rain boundary layer arises from the Reynolds stress variations in the turbulence induced by the impact of rain. However, with long waves, for a system that contains only wind and waves there may exist in the air boundary layer large scale turbulent pressure (or total equivalent normal stress) fluctuations that have the convection velocities approximately in phase with the slope of the underlying wave so as to give resonant effects; but, with the addition of rain action, in the rain boundary layer it is unlikely to have such large scale phase averaged turbulent structures that may in phase with the surface slopes of such long waves. In other words, on one hand, the rain boundary layer is too thin to provide resonant mechanism that can contribute to wave growth for long waves; and, on the other hand, the rain boundary layer acts as a barrier to the transferring of the momentum from the air boundary layer.

Overall, for shorter waves, the rain-induced stress or the vortex dynamics in the rain boundary layer may have more effects on the energy transfer to or from waves; and, for long waves, it may seem that the rain boundary layer is only "skin deep" and therefore negligible, and the induced Reynolds stresses (in the terminology similar to that used by Phillips [59, 60], Miles [56], and Lighthill [43] which is not quite the same as the turbulent Reynolds stress) in the interface regions under the combined action of rain and waves have been greatly altered from what without rain. In summary, therefore, the original mechanism for the energy transfer from wind to waves no longer exists when there is rain.

The arguments here point out that scale laws are at the heart of understanding the mechanisms governing such a complex system.

8.5 Extensive mechanisms — Energy phenomena induced by stratification

In the above sections local coupling mechanisms are provided, but they are far from satisfactory due to their inability to provide a global view of the energy phenomena. In the following we will provide energy transfer and dissipation mechanisms that have the scope of the whole water body, and show that all these are closely related to the existence of stratification.

Green and Houk [25], using a laboratory scale close to that of natural processes regarding rain falling distance and rain intensity, investigated the mixing of rain with the near-surface water under thermally stratified condition. Though their experiments did not focus on the present context of rain and wave interaction they observed the temporal irregularities of the thermocline and attributed these to the existence of internal waves. This mechanism of exciting internal waves due to impact of rain, together with the peculiar characteristics pertaining to internal waves, provides important clues for explaining the energy phenomena in the coupling system. Since we are aiming to provide the mechanisms of surface wave attenuation and since the spatial scale of most energetic surface waves are generally quite larger than the depth of the surface rain mixing layer, we need some kinds of connections between surface waves and internal waves. We will give reasons why the stratification, which occurs in almost all natural water bodies and is further intensified in the near surface region in a raining system, is a bridge for this and illustrate a few interesting aspects associated with it.

But, let us first seek the most direct consequence caused by the impact of rain and explain the stimulus coaxing the development of interaction among various factors within a stratified fluid system.

8.5.1 The tuning and de-tuning of interactions near the air-water interface

Initially we have the coupling of the wind and waves. The wave system has its particular composition corresponding to the state of development under the wind forcing. For a water body under the surface forcing of both the pressure and shear stress, the energy transfer to waves as given by a boundary layer argument (Longuet-Higgins 1969 [45]) is

$$-\overline{(p+\mathrm{i}\tau)w} = \overline{\mathbf{c}\cdot(p+\mathrm{i}\tau)\nabla\zeta}, \tag{8.8}$$

in which p and τ are, respectively, real-valued surface stress components acting normally and tangentially on the air-water interface; w is the particle velocity on the boundary; $\mathbf{c}$ is the phase velocity; and ζ is a complex-valued surface displacement (they all may be in a sense of either an individual component or a combination of Fourier components.) Here the overbar means either a spatial or a temporal average. This equation suggests that for the wave to grow the pressure variation should be in phase with the wave slope and the shear stress variation should be in phase with the wave elevation. Such a mechanism for wave growth or decay is essentially the tuning or de-tuning of phase relations among the air-flow structure and air-water interface. The existence of a surface boundary layer, which communes between the air-flow boundary layer and the underlying irrotational flow field is vitally important, since the positive contribution of shear stress to wave energy is equivalent to a situation in which a thicker boundary layer forms on the rear slopes and a thinner boundary layer forms on the forward slopes. Now, with the incorporation of the falling rain and the associated Rayleigh jets, vortex rings, splash drops and ring waves, even though Caldwell and Elliott [14, 15] have shown that the wind was only slightly modified, we should be able to ascertain that the configuration of air-water interface is dramatically changed and that the structure of the air-flow boundary layer is also altered. Thus the original interactions among wind and waves are completely disrupted and phenomena evolving from perturbation or disturbance are given impetus. Therefore,

along with the match layer effects, the existing dominant waves lose their energy sources and minor waves, either of surface waves or of internal waves, energize their activities.

In addition to the above conceptual reasonings on physics, we have a physical justification to follow. Using dyed rain drops falling vertically to a receiving water, our laboratory observations showed quite dramatic differences in movement patterns of rain drops (moving within the receiving water) among cases with either the same uniform freshwater or a stratified salt water. When rain drops impact onto the water body with a uniform density they penetrate without bouncing back and somewhat stay where they go, and there is more assimilation during the process. But, an entirely different picture showed up for the rain drops to hit a stratified receiving water. Not only rain drops definitely bounce back due to buoyancy, less assimilation was observed during their movements. More interestingly, we observe that drops coming from the same hypodermic needle do not repeat the same penetration depth each time but once a while they have the same deepest scale of penetration. I suggest that buoyancy effects appear to play a role of beating, with the impact of rain drop on stratified fluid being conceptually similar to the beating of a drum; the timing and position of the beating will render different tones. Similarly, consecutive drops do not repeat the same penetration pattern. Physically, one may think that there may exist cyclic fluid motion that interact with the drops. Moreover, judging from the depth of penetration, the bouncing distances, and their horizontal spatial distributions (e.g., those observed by Green and Houk [25] using a near physical scale and those observed in our experiment using a smaller scale, as well as the match layer arguments), it is reasonable to argue that impacts are going to favor the transfer of energy to motions of high wave number and this is a strong catalyst for the several factors that contribute to the damping and the energy cascade of waves as will be illustrated subsequently. Not only these, let us first provide a most direct mechanism for the damping of waves that is due to the inherent property of fluid and is caused by a strong stratification.

8.5.2 The vortical contributions to wave attenuation

We mentioned that the turbulence induced by the direct impact of rain exists only in a thin surface layer and the buoyancy effects enhanced by the stratification further reduce the thickness of the rain boundary layer and increase the temporal rate of change in the flow field. The creation of a surface region that has entirely different flow features from those of the underlying region of wave motions is similar to the placement a densely packed layer of surface film on top of the region of wave motions. As we know, the existence of a boundary, even it is a free surface, always induces vortical motion. Here we should examine this vortical contribution to wave attenuation under conditions with and without a distinct surface layer. The dissipation here is due to molecular scale, not to turbulent eddy scales as faultily assumed in some of Nystuen's (1990) estimations of background eddy dissipation where no attention was paid to vertical scales. Even though in the deeper interior region of the flow field there may be, as explained later, local turbulence introduced by sporadic breaking of resonated internal wave, this concept of energy dissipation is still different from what Nystuen perceived as eddy dissipation.

The existence of a boundary induces a term of vortical velocity modification, $\mathbf{u}^{'}$, to the irrotational motion $\nabla\phi$, i.e., $\mathbf{u} = \nabla\phi + \mathbf{u}^{'}$. Without surface film the energy loss of waves arises almost entirely from the straining of $\nabla\phi$ since the vortical strain rates are no larger than that in the irrotational flow and the thickness of vortical influence is relatively small, so we have the classical law of viscous decay (Lamb 1932)

$$\dot{E} = -4\mu\sigma^2 a^2 k = -4\nu k^2 E = -\gamma_\mu E, \tag{8.9}$$

where μ and ν are the dynamic and kinematic viscosities of the water, respectively; and γ_μ^{-1} is the e-folding decay time of wave energy density due to irrotational motion. If there is a surface film, the vorticity induced by $\mathbf{u}^{'}$ is the main contribution to rate of strain in the vortical boundary layer with an e-folding characteristic depth of $\beta^{-1} = (\sigma/2\nu)^{-\frac{1}{2}}$. This

portion of mean energy dissipation per unit area is (Phillips [60])

$$\dot{E} = -\frac{1}{2}\mu\sigma^2 a^2\beta\coth^2 kd, \; = -\nu\beta k(\coth kd)E = -\gamma_f E, \tag{8.10}$$

where γ_f^{-1} stands for the characteristic decay time of wave energy density due to a packed film. The ratio of γ_f to γ_μ, say in deep water, is

$$\frac{\gamma_f}{\gamma_\mu} = \frac{\beta}{4k} = \frac{\sqrt{\sigma}}{4\sqrt{2\mu}k} = 2^{-5/2}\sqrt{\mathbf{R}_w}, \tag{8.11}$$

in which

$$\mathbf{R}_w = \sigma/\mu k^2, \tag{8.12}$$

is the wave Reynolds number. We have the physical values shown in Table 8.3 (*e*-decay–N+P).

Tab 8.3 (*e*-decay–N+P) Comparison of the e-folding decay times of wave amplitude between present estimation and Nystuen's [58] estimations.

Source of e-folding decay time (s)	Wavelength (m)				
	0.02	0.1	0.3	1.0	2.0
Present estimation†	1.0	8.0	33.0	140.0	330.0
Nystuen's molecular viscosity†	4.8	120.0	1080.0	12000.0	47000.0
Nystuen's turbulent layer eddy viscosity‡	0.034	2.1	37.8	800.0	5800.0

†Molecular viscosity: 10^{-6} m^2s^{-1}
‡Eddy viscosity: 3×10^{-5} m^2s^{-1} (for cases with a 0.1 m turbulent layer thickness)

It is seen from the table that the present estimations give more likely values for all the wavelengths from the view point of energy dissipation. Especially, when we are focusing at the short wavelength excited by resonance as will be stated later or by the forcing of the newly tuned disturbances as mentioned above, we should be able to appreciate

the existence of a strongly stratified surface layer, which plays a role of surface film and contributes significantly to the vortical energy dissipation that is still due to molecular viscosity. We may also note that this dissipation mechanism is still weak for small wave number, but, if there exists a cascade phenomenon of waves from low to high wave number, this element, given the points mentioned in the previous sections as well as those follow, is certainly a highly possible mechanism for the calming of the sea.

8.5.3 Interactions among surface waves and internal waves

We have pointed out that the impact of rain provides seeds of disturbances for the growth of minor waves. Of course these minor waves must be of short wave lengths since low energy contents are certainly associated with short waves. Rapid growth and decay is a character of short waves; motions of large temporal and spatial scales need more energy to spread and more time to develop.

In the followings we illustrate the phenomena of a chain of reactions in the fields of both surface and internal waves, and explain how energy is transferred based on the following sequence of arguments. First, the most early interaction should be wave-wave interaction of surface waves; next, we have the excitation of near-surface internal waves through surface-wave and internal-wave interaction; and then the resonant interaction of internal waves that promote the cascade of surface-wave energy from the near-surface region into the deeper region or even in an opposite direction that bring the wave energy in the deep region into the rapid energy damping zone of the rain mixing layer.

The highest order resonant interaction among waves is the quadratic interaction in which two waves interact to give a third one — the product of a quadrature forcing term through the weak non-linear interaction. The three waves must form a triad with the following wavenumber vector and frequency relationships:

$$\mathbf{k}_3 = \mathbf{k}_1 \pm \mathbf{k}_2, \tag{8.13}$$

$$\sigma_3 = \sigma_1 \pm \sigma_2. \tag{8.14}$$

The $\pm$ signs in the two equations should be in pair. Note that these triads hold for surface waves, internal waves, or even among surface waves and internal waves since there is always a surface wave mode solution for the single set of governing equations for internal waves, i.e., analytically speaking, a single equation of the form $\mathcal{L}(y) = \epsilon\mathcal{N}(y)$, fits for the components of the triad. In the equation $\mathcal{L}$ stands for a linear operator, $\mathcal{N}$ stands for a nonlinear operator, y for dependent variables, and ϵ means a perturbation condition corresponding to weak nonlinear interaction. However, for purely surface waves which satisfy the dispersion relation of $\sigma_r = (gk_r)^{\frac{1}{2}}$ there are no non-trivial solutions. Therefore, the only possible resonance is of next order, in which triple product forcing terms resonance with a fourth wave. One possible solution sets for this tetrad is (Hasselmann [27])

$$\mathbf{k}_3 + \mathbf{k}_4 = \mathbf{k}_1 + \mathbf{k}_2, \tag{8.15}$$

$$\sigma_3 + \sigma_4 = \sigma_1 + \sigma_2, \tag{8.16}$$

$$\sigma_r = (gk_r)^{\frac{1}{2}}. \tag{8.17}$$

Although the tetrad interaction being of third order is relatively weak, it is still efficient enough for low energy surface waves to excite internal waves. This is one of the special characteristic of internal waves, since we know that the surface displacement for an internal wave system is nearly null so that it can often be treated as a rigid lid. In summary, only very small potential or kinematic energy changes are needed to produce internal waves, implying that small imposed disturbances at the surface can be very effective generators of internal waves. Together with the tuning and de-tuning processes stated above, these two phenomena match very well. Another hinted point here is that, even we perceive that the sea surface is calmed by the rain, it is still possible that there is enhanced internal wave motions.

Next we attempt to link between the tetrad of surface waves and triad of surface waves

and internal waves to allow the passage of energy from surface waves to internal waves. Links here lie on another property of internal waves: the frequencies of internal waves are generally much lower than those of surface waves with the same wave number. This is equivalent to state that, for two surface waves (subscripts 1 and 2 in the following equation) to produce an internal wave (subscript 3), the two surface waves should have approximately the same wavenumber (so their frequencies are also close to one another) and interact in the following format

$$\mathbf{k}_3 = \mathbf{k}_1 - \mathbf{k}_2, \tag{8.18}$$

$$\sigma_3 = \sigma_1 - \sigma_2. \tag{8.19}$$

Besides, we need to apply dispersion relationships to each component of the triad. It is now appropriate to include the tetrad interaction in order to determine whether it is the dominant waves or the minor waves that are responsible for the transfer of energy from surface waves to internal wave. The answer of this can be best explained by the schematic diagram of the conditions for resonant interaction given by Ball [7] as shown in Figure 8.6 (WNV–Triad), as well as by our understanding that the nature wave fields are generally quite narrow banded regarding their energy contents. It is unlikely for a wave field to have wavenumber vectors that are of small values (i.e, longer dominant waves) while oriented in appreciable different or diversified directions. Nevertheless, it is suitable for minor waves of low energy to have more diverse directions of propagation since only one normally distributed bell shape two dimensional spectrum suffices to provide this configuration, although this diverseness is not a requirement.

The results of this is that the two surface waves should be of higher frequencies. This is equivalent to the case that points A and B_1 in Figure 8.6 (WNV–Triad) (or points A and B_2) should lies at the upper parts of the curves, and the line connecting the points is somewhat horizontal so as to produce an internal-wave frequency that complies with the requirement for the resonant length scale. So now we can draw the region for the tetrad interaction

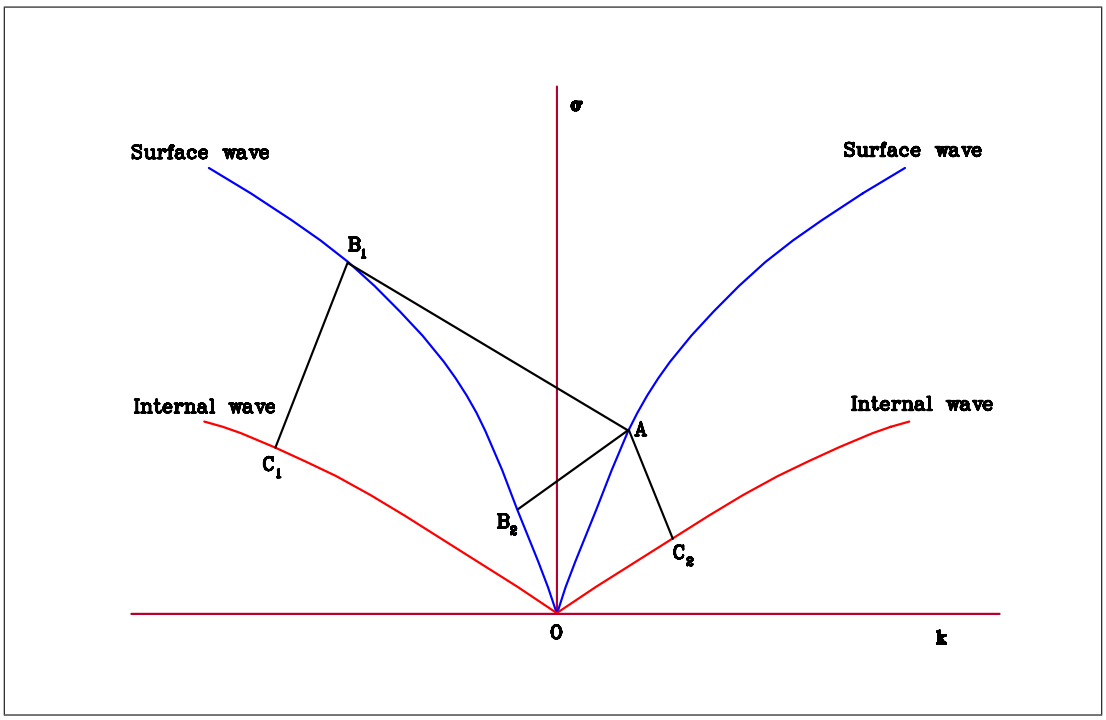

Fig 8.6 (WNV–Triad) Schematic representation of the resonant conditions for triad composed of surface waves and internal wave. The various curves revolve around the wave frequency axis, and configurations should be viewed in a three dimensional sense. The AB_1C_1 and AB_2C_2 are two resonant componenets of the triad with a common surface wave component, after Ball [7].

among surface waves as shown in Figure 8.7 (WNV–Tetra) and the region for the triad as shown in Figure 8.8 (WNV–Loci), noting the scales and directions of waves in the figures.

Several more points can be drawn from the figures. First, the most likely growth of short minor waves (long wavenumber vectors) are those propagate at about the same direction of dominant waves. Second, the most likely resonant near-surface internal waves should propagate in the near perpendicular direction to the major waves, i.e., also perpendicular to the propagation of minor waves.

8.5.4 The cascade of energy

Up until now we have not exploited several important and interesting features of internal waves. The first and, maybe the most, significant feature is that the direction of energy propagation of internal wave is perpendicular to its wavenumber vector (the direction

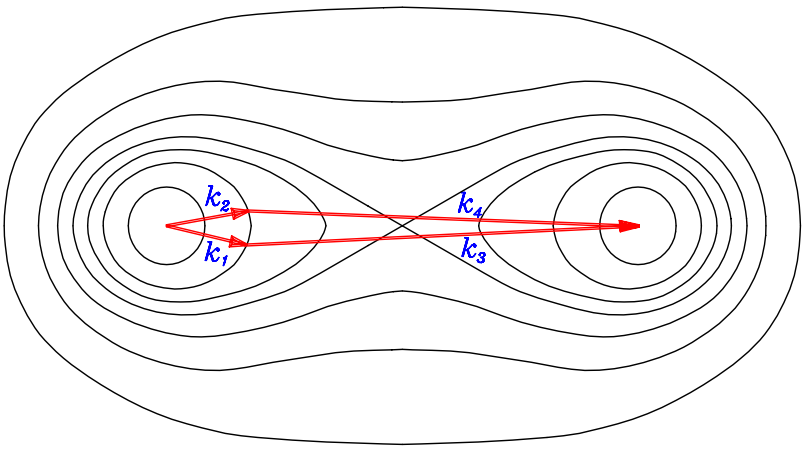

Fig 8.7 (WNV–Tetra) Schematic representation of the family of curves for the tetra resonances. Resonant wave number vectors should locate at the same figure-of-eight curve. The vectors shown here are most likely to be associated with the triad interaction depicted in the previous figure, after Simmons [63] and Phillips [60].

of phase speed) suppose that the stratification is not an exactly ideal two-layer system. So the energy of excited near-surface internal waves propagate either into the turbulent rain boundary layer or into the deeper region. This is another mechanism to diverge (cascade) or to dissipate the energy of the surface waves. Secondly, we know that there are enormous differences between the density gradients near the rain mixing layer and those at deeper region and that the internal wave frequency must be less than the local Brünt-Väisälä frequency, N, for the internal waves to propagate further. The Brünt-Väisälä frequency is

$$N^2 = -\frac{g}{\rho(z)}\frac{\mathrm{d}\rho(z)}{\mathrm{d}z}, \tag{8.20}$$

in which $\rho(z)$, in precise meaning, is the potential density, but in a strongly stratified region due to significant difference in salinity, e.g., in the interfacial region of the irrotational wave motion and the rain boundary layer, the general sense of density can be used. If the rain falls into the sea, than the limiting internal wave frequencies at the water depth near (and under) the rain mixing layer can be of the same order as those of surface dom-

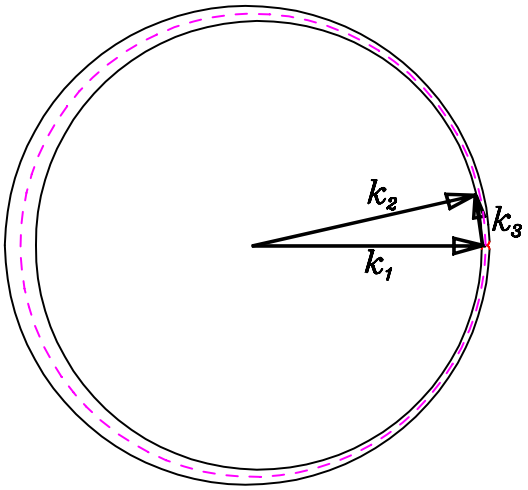

Fig 8.8 (WNV–Loci) The loci of wave number vectors for two surface waves with approximately equal wave number magnitude. The configuration of k_1, k_2 (surface waves) and k_3 (internal wave) and the closeness of the two loops are for the coherence between the triads and the tetrads in the coupling system, after Turner [71].

inant waves provided that the surface waves are well developed, so in this near surface region there is possibility of diversification of internal waves. But those internal waves of higher frequencies must soon breakdown as they propagate into deeper region either by energy concentration or by an alternative process of triad resonance since they encounter the dramatic reduction of density gradient. There are two kinds of mechanisms here. The local breakdown is for higher frequency internal waves. The resonant triad interaction is for low-pass internal waves and the possible mechanism for this is the disintegration of high-wavenumber internal waves into low-wavenumber internal waves and this process is enhanced by the diversified components of internal waves generated around the thermocline or halocline. Moreover, judging from the governing equations for triad for purely internal waves — since the strict condition of dispersion relations is greatly relaxed now due to a rather loose requirement of frequency and wavenumber relation for an internal wave, i.e., one frequency can corresponding to many modes — the frequency of internal wave can be independent of the wavenumber magnitude but dependent only on its direction. One may also note that, for any stratification, theoretically, there are an unlimited

modes of internal waves and, practically, several experiments have indicated the existence of diverse internal waves modes (Turner [71]; Phillips [60]) — it is anticipated that the diversifications of interaction have the phenomena of chain reaction and energy is thus cascaded in the wave fields.

8.6 Summary

In this chapter we provide the physics for the energy phenomena in the wind, wave, and rain coupling system. Problems related to a few studies (LeMehaute and Khangaonkar [42]; Nystuen [58]; Tsimplis and Thorpe [70]; Tsimplis [69]) are clarified further. Attempts to give physical arguments about the mechanisms of wave growth or decay in the coupling system are exploited in two senses.

First we provide local coupling mechanisms that are confined in the rain and air-flow boundary layers and that are similar to those in the classical wave generation mechanisms. Their key aspects are the tuning and de-tuning processes as well as the vital role of a match layer in the rain boundary layer, which commute between the air-flow and the underlying irrotational wave field.

Later we focus the energy phenomena that are associated with the existence of stratification. Here our scope covers the whole region of the water body but with a sequence of interactions from the top layer to the inner region. The key concepts are: (1) The dissipation mechanism induced by the strong stratification simulates that induced by a surface film and the resulted vortical contribution to dissipation that is still of molecular scale is shown to be a very competitive factor for the calming down of the sea, especially, when the mechanism of the wave cascading is incorporated. (2) The physical concepts of a beating process due to impact of rain drops are used to give catalysts for the tetrad interaction of surface waves and these further provoke the triad interaction among surface waves and internal waves. (3) Among these interacting component waves their relative scales hold some restrictions. However, at the last stage of interaction, the interaction among

internal waves is so diversified, owing to the relaxation of constrain of the dispersion relation of the internal waves, that it ignites a board spectrum of interaction and feedback to the surface-wave-internal-wave interactions. The overall consequence is thus of a board range of interactions with energy transfer to scales of dissipation — a somewhat turbulent phenomenon in the wave field. ❖

Chapter 9

Experiments

9.1 Introduction

There are basically two series of experiments when classified from their usages: one focuses on the Fourier perspective of the surface waves and the measurements of momentum flux due to rain — this serves to reaffirm what will be stated in the next chapter; the other focuses on the coherent feature of surface wave fields and aqueous flow fields — this serves to provide evidences of the proposed energy phenomena. For the second series of experiments both wind waves and Stokes waves are adopted and a couple of cases are performed using a stratified receiving water body. The overview of the experimental setups is shown in Figure 9.1 (Oval Tank).

9.2 Facilities

9.2.1 The oval tank

The experiments were carried out in an circulating oval tank equipped with wind blowing facilities and a mountable mechanical wave generator (Air-Sea Interaction Lab., University of Delaware, USA). The tank is 31 cm wide and 45 cm high and has a 5-meter observational straight section. The water depth was kept at 24 cm in all experiments. A fan of continuously variable rotation speed was located at the opposite side of the obser-

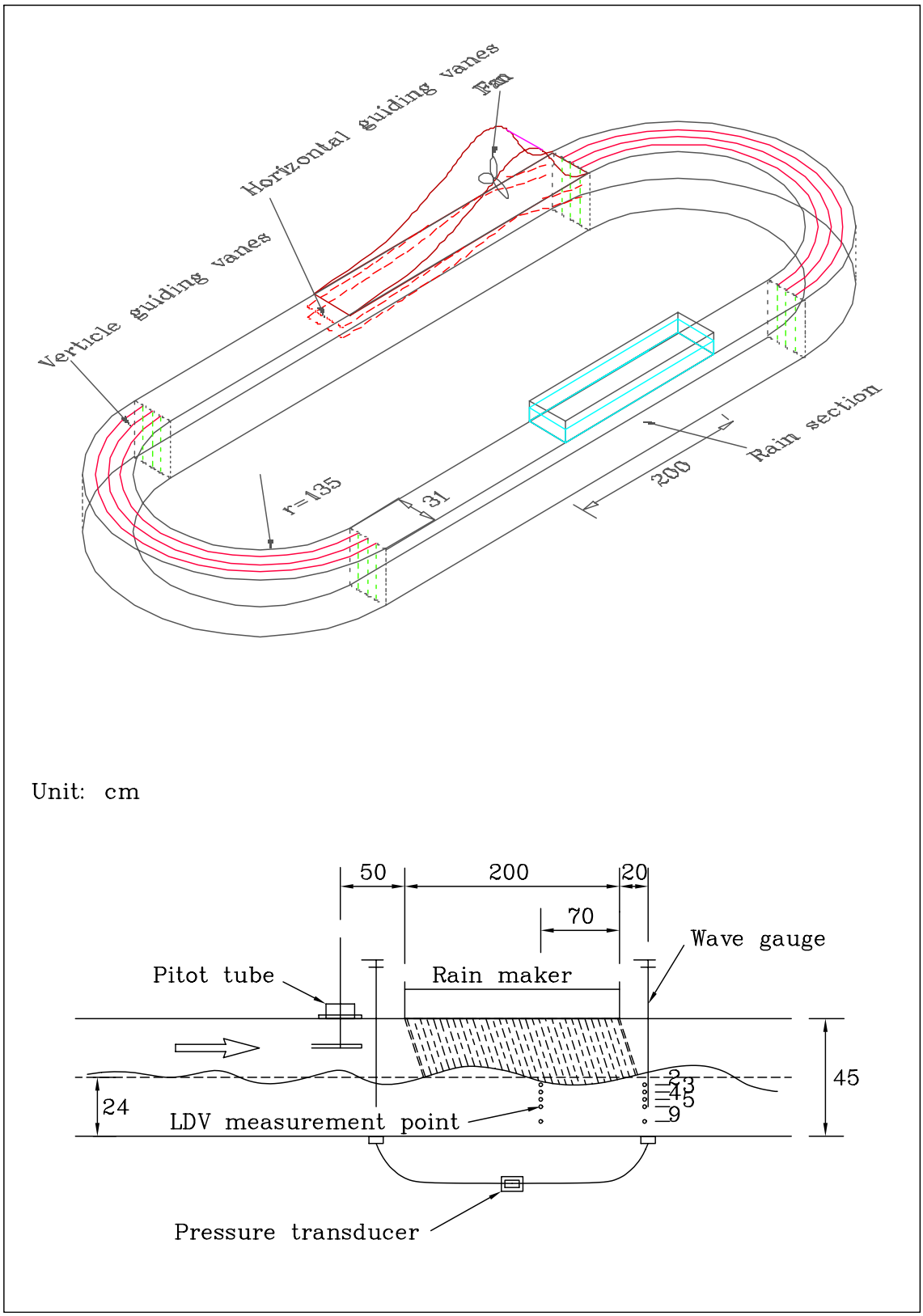

Fig 9.1 (Oval Tank) Schematic layout of experiment

vational section. Horizontal guiding vanes were installed in front of the fan to regulate the airflows. And vertical guiding vanes were installed at the two semi-circle sections to reduce secondary flows in both air and water. The mechanical waves were generated by the plunger type motion of a wedge shape piston controlled by a variable-speed rotor. And the mechanical setup could be placed along the observational section.

9.2.2 Artificial rain simulators

Two one-meter rain modules (Poon et al. [61]) were mounted atop the tank. Hypodermic needles of gauge 23 were uniformly spaced in the bottom of the module and arranged in an equi-lateral triangular shape with a spacing of 3 cm from center to center. Rain intensity was controlled by the water head above the needle tips. The calibrated size of raindrops is about 2.6 mm in diameter, assuming a spherical shape of drops. The drop size depends only on the needle gauge and the wind condition but not the water heads; this character is consistent with the feature of rain intensity calibration curves to be shown later.

9.2.3 Pressure transducer

For the first set of experiments, a differential pressure transducer (Validyne model DP15) was connected to two bottom holes of the tank locating at the upstream and downstream wave gauges before and after the rain module. The pressure sensor is a typical variable reluctance stress transducer which consists of a diaphragm of magnetically permeable stainless steel clamped between two blocks of stainless steel. To ensure that no air was trapped in the transducer so that a proper dynamic response could be secured, the transducer was flushed with a long steady water flow through its bleed port and was tilted or shaken somewhat randomly. In addition, a relatively rigid (compared with the magnitude of the pressure concerned) plumbing connection was used, such that effects of the low-pass filtering could be avoided. With these precautions, the small rain-induced stress due

to the differential water surface displacement can be faithfully extracted. The accuracy of the transducer measurements will be illustrated through the discussion of the natural frequency of the oval tank to be given later.

9.2.4 Laser Doppler velocimeter

Aqueous flows at several depths in two sections along the tank were measured with a laser Doppler velocimeter (LDV) [3]. The LDV system is a TSI four-beam, two-component system with two-color, dual-beam backscattering, and counter type signal processor configuration. A few auxiliary instruments and accessories were also used in fine-tuning the whole system and in achieving optimum control of data quality. The main system components and the auxiliary instruments are: (1) Fiberoptic transmitting and receiving probes (TSI Model 9115, 9182, and 9140); (2) Photodetector and photomultiplier system (Model 9160); (3) Frequency shifter with acousto-optic modulator and electronic down-mix module (Model 9180A); (4) Signal input conditioner (Model 1994C); (5) Fringe timer (Model 1995B); (6) Frequency to analog conversion module (Model 1988). (7) Digital readout module; (Model 1992); (8) Intermittent burst data recording interface; (Model 1998); (9) Light-power meter; (10) TI Dual channel oscilloscope for high-end fast and sensitive real time monitoring.

9.2.5 Wave gauges

Measurements of water surface displacements were done with the ASI self-design capacitance type Tantalum wire probe. For measurements in a stratified water body a laser wave gauge devised also by the ASI Lab was arranged, but it was found that the concurrent measurements with LDV is not feasible, besides, there are additional concerns to be given later. Main components of the laser gauge are: a laser gun, a line scanner with 512 photodiodes, and a multibus computer interface. The laser gun, with special mirror arrangement and precise alignment, projects vertically a laser beam from under the bot-

tom of the wave tank. When the beam crosses the water surface, a bright spot is formed on the water surface and scatters light in all directions. The line scanner, with proper lens and PC interface, traces the position of the light spot through its cyclic scanning. To minimize geometric errors and attain a suitable resolution, the line scanner should be arranged at a suitable angle relative to the beam axis (about 45 degrees) and should also be placed at a proper distance (about 1 meter away from the light spot for the current hardware setup) in order to observe various optical principles or restrictions such as the depth of field, aperture size, photodiode cell resolution, light intensity, non-unform focusing problem (associated with the tilting of photodiode array relative to the laser beam), etc. The resolution of the laser wave gauge must be calibrated on site and is about 0.0031 cm per pixel for the arrangement. Due to the size of the light spot and various afore mentioned factors, there exists an inherent low-pass mechanism (a blurring effect) that filters out the detail of the variations of surface displacement. Several factors add to the difficulties of the experiments: (1) There is sever interference caused by the flares from LDV laser beams; (2) The relatively low sampling rate due to the scanning mechanism makes it not feasible to synchronize with the LDV measurement; (3) The top cover of the oval tank interferes with the detection of feeble scattering light; a special arrangement of a slit is needed, but such a slit arrangement affects the wave field right at the vicinity of the measurement area. These difficulties rendered a not quite satisfactory use for the present application; it was therefore decided that simultaneous measurements using a Tantalum wire probe be taken. However, to minimize the uncertainty caused by the density gradient, a deep submergence of the wave gauge that almost reached the bottom of the tank was adopted. The gauge was mounted on a vernier support and calibrations were done on-site just before the experiments started.

9.3 Measurements

9.3.1 The real time system

A highly automated and specifically optimized PC-based real time system for both data acquisition and data analysis was developed by the author. Parts of the details can be found in the previous section on "*Program and workbench developments*", as well as on an earlier report on the experiments of comparison studies of different armor types [80].

As was hinted in van Dorn's (1959) observations of wind-induced setup in a pond, the rain-induced setups for our experiments may be less than the order of a fraction of a millimeter (even for the wind-induced part). And in view of the complicated factors or mechanisms involved in the experiments, as well as in anticipating difficulties in distinguishing differences incurred by the short raining section, both accuracy and precision in measurements are needed.

A few key features of the system are: (1) Data acquisition is real-time monitored on PC with multi-tasking programming; (2) Multi-channel calibration capability; (3) On-site automated data analysis, such as zero-crossing statistics, reflection coefficients, correlations, spectral analysis, and software filtering, etc.; (4) On-site generations and printouts of various statistical results and graphics; (5) All the real time processes are controlled through a menu-driven interface; (6) Friendliness and optimization of control are considered, such as: the number of keystrokes is minimized specifically for our experiments, automated inputs are considered to prevent human errors, and sounds are added for stage reminding.

It is noted that the major programming languages used in the present study are **Asyst** and **Mathematica**. For the control of the laser wave gauge **Fortran** is also used.

9.3.2 Winds and rains

For the first set of measurements, in order to maximize the momentum input into the receiving water so that more obvious setup effects due to rain can be discerned, a large

impact angle of rain is desired. Therefore, a large wind speed of 6.8 m s^{-1} was used. The speed corresponds to the capacity of fan with a 24 cm water depth. And the wind was measured with a Pitot tube located 50 cm upwind of the rain section and 11 cm above the still water surface. Rain intensities covered a range from 34 to 104 mm hr^{-1}. Data were sampled at 40 Hz for a duration of 200 seconds.

For the second set of measurements, wind speeds of 4.10, 5.10, and 6.00 m s^{-1} and three rain intensities of 36, 50, 68 mm hr^{-1} were adopted. Most data were sampled at 40 Hz (some data were hardware sampled at a higher rate and than software sub-sampled at 40 Hz) for a duration of 120 seconds.

9.3.3 Aqueous flows

LDV measurements are located at two cross sections: One is right in the vicinity (0.6 cm away) of the wave gauge located behind the rain section, another right under the raining segment which is 70 cm ahead the end of the rain module. Depths of the measurement points are 2, 3, 4, 5, and 9 cm below the mean water surface (in fact some other locations are also measured, but we have not found a way to shed some peculiar information mainly due to the nonconcurrent nature of measurements as to be stated in results of data analysis).

Successful aqueous flow measurements using the current LDV system involve a few stringent requirements both in instrument setup and control. A few key points in optimizing these measurements are explained as follows: (1) Power outputs of laser are critically affected by the alignment of optical elements and are quite sensitive to the adjustments of various interacting knobs. A light power detector was used to ensure that maximum power outputs were achieved. Such a process generally took a couple of hours. (2) Fringe bias was minimized by setting the possible maximum frequency shift according to a calculation based on flow conditions. (3) Velocity bias was handled by sampling the analog frequency output at a fixed rate. (4) Without affecting the Doppler bursts, the pedestal signals were completely removed by setting allowable maximum values of the

high-pass filter. The decisions of these filter values should reference to point (2), and the condition be real-time monitored in the oscilloscope. (5) High-frequency noises have significant impacts on the accuracy of results registered by the frequency counter and are closely related to the amplification process of the photomultiplier tube (and also to the seeding conditions). They in turn are determined by extraneous background light (such as laser flare and reflection from glass walls) and by the inherent electronic shot noise. The minimization of these noises was controlled by adjusting the gain setting together with low-pass filtering; in addition, a dark background was carefully arranged for this purpose. (6) In these measurements most of the LDV signals can be put in the category of continuous burst mode with both high burst rate and high data density. This could be inferred in-site from the oscilloscope display as well as from the output of the digital readout module. Non-uniformly spaced counter data rate of about 800 to 1000 points per second was typical for the green channel. For the blue channel, the emitting light power was about 2/3 of that of the green one; this power difference gave a critical blow to its data quality; therefore the data rate was generally less than half of the green one and the sampled signals were often of step shapes. Due to this, only the green channel signals are used in the data analysis. (7) For helping to optimize the choice of parameters and various instrument settings a spreadsheet was designed (Table 9.1 (LDV-IPs)). The spreadsheet embeds various instrument specifications and formulas needed for LDV measurements and computations.

9.3.4 Stratified cases

As indicated in the energy cascade model, stratification of the receiving water body plays a key role in the energy phenomena. A couple of experiments with stratified receiving water were also performed. Considering that a stratification with small density gradient is difficult to setup and that stratification acts as a film that hampers the development of

Tab 9.1 (LDV-IPs) A spreadsheet for optimal control of LDV setups. The sheet embeds various instrument parameters and related LDV formulas. When desired velocity range is filled in, the spreadsheet will give the appropriate setup parameters.

ITEM	BLUE	GREEN
Wave length (nm)	488	514.5
Half angle (degree)	3.4204	3.3594
Beam width (mm)	7.1717	7.0440
Fringe spacing (micro m)	4.0897	4.3900
Focal length (mm)	60.1030	60.1034
Number of fringes	24	22

Pedestal Filter (kHz)	1	3
High limit filter (kHz)	300	300
Shift (kHz)	50	50
Cycles/Burst	8	8
Out (Time/F10:1/F100:1)	F10:1	F10:1
EXP	M10	M10
Comparison (%)	1	1
Data rate / Amp. limit	/	/

Velocity - Min. (cm/sec)	-20	-20	-20	-20	-20	-20	-20	-20
- Max.	20	20	25	25	30	30	40	40
Doppler freq.(fd)- Min. (kHz)	-48.90	-45.56	-48.90	-45.56	-48.90	-45.56	-48.90	-45.56
- Max.	48.90	45.56	61.13	56.95	73.35	68.34	97.81	91.12
Freq. shift (kHz)	50	50	50	50	50	50	50	50
Shifted freq.(fe)- Min. (kHz)	1.10	4.44	1.10	4.44	1.10	4.44	1.10	4.44
- Max.	98.90	95.56	111.13	106.95	123.35	118.34	147.81	141.12
Cycles/Burst	8	8	8	8	8	8	8	8
Freq. EXP <- Max. fe + Floor	10	10	10	10	10	10	10	10
X (Trans. fun.) (kHz)	152.59	152.59	152.59	152.59	152.59	152.59	152.59	152.59
10:1 Freq output (kHz/V)	15.26	15.26	15.26	15.26	15.26	15.26	15.26	15.26
Min. voltage (V)	0.07	0.29	0.07	0.29	0.07	0.29	0.07	0.29
Max. voltage <- Max. fe	6.48	6.26	7.28	7.01	8.08	7.76	9.69	9.25
0V velocity (cm/sec)	-20.45	-21.95	-20.45	-21.95	-20.45	-21.95	-20.45	-21.95
5V	10.75	11.54	10.75	11.54	10.75	11.54	10.75	11.54
10V <- X	41.96	45.04	41.96	45.04	41.96	45.04	41.96	45.04
Time EXP <- Min. fe + Ceiling	14	12	14	12	14	12	14	12
X (Trans. fun.) (kHz)	9.54	38.15	9.54	38.15	9.54	38.15	9.54	38.15
Min. voltage (V)	0.10	0.40	0.09	0.36	0.08	0.32	0.06	0.27
Max. voltage <- Min. fe	8.69	8.59	8.69	8.59	8.69	8.59	8.69	8.59
0.5V velocity (cm/sec)	-12.65	11.54	-12.65	11.54	-12.65	11.54	-12.65	11.54
5V	-19.67	-18.60	-19.67	-18.60	-19.67	-18.60	-19.67	-18.60
10V <- X	-20.06	-20.28	-20.06	-20.28	-20.06	-20.28	-20.06	-20.28

Velocity - Min. (cm/sec)	-20	-20	-20	-20	-20	-20	-20	-20
A54 - Max.	20	20	25	25	30	30	40	40
Doppler freq.(fd)- Min. (kHz)	-48.90	-45.56	-48.90	-45.56	-48.90	-45.56	-48.90	-45.56
- Max.	48.90	45.56	61.13	56.95	73.35	68.34	97.81	91.12
Freq. shift (kHz)	100	100	100	100	100	100	100	100
Shifted freq.(fe)- Min. (kHz)	51.10	54.44	51.10	54.44	51.10	54.44	51.10	54.44
- Max.	148.90	145.56	161.13	156.95	173.35	168.34	197.81	191.12
Cycles/Burst	8	8	8	8	8	8	8	8
Freq. EXP <- Max. fe + Floor	10	10	9	9	9	9	9	9
X (Trans. fun.) (kHz)	152.59	152.59	305.18	305.18	305.18	305.18	305.18	305.18
10:1 Freq output (kHz/V)	15.26	15.26	30.52	30.52	30.52	30.52	30.52	30.52
Min. voltage (V)	3.35	3.57	1.67	1.78	1.67	1.78	1.67	1.78
Max. voltage <- Max. fe	9.76	9.54	5.28	5.14	5.68	5.52	6.48	6.26
0V velocity (cm/sec)	-40.90	-43.90	-40.90	-43.90	-40.90	-43.90	-40.90	-43.90
5V	-9.70	-10.41	21.51	23.09	21.51	23.09	21.51	23.09
10V <- X	21.51	23.09	83.91	90.07	83.91	90.07	83.91	90.07
Time EXP <- Min. fe + Ceiling	9	9	9	9	9	9	9	9
X (Trans. fun.) (kHz)	305.18	305.18	305.18	305.18	305.18	305.18	305.18	305.18
Min. voltage (V)	2.05	2.10	1.89	1.94	1.76	1.81	1.54	1.60
Max. voltage <- Min. fe	5.97	5.61	5.97	5.61	5.97	5.61	5.97	5.61
0.5V velocity (cm/sec)	208.72	224.04	208.72	224.04	208.72	224.04	208.72	224.04
5V	-15.94	-17.11	-15.94	-17.11	-15.94	-17.11	-15.94	-17.11
10V <- X	-28.42	-30.50	-28.42	-30.50	-28.42	-30.50	-28.42	-30.50

LDV Parameters ASI, CMS, UD

surface waves (i.e., a strong stratification induces stabling effects so that the same wind speed may not create the same wave field), as well as that too small a stratification will not yield noticeable effects; it was decided that a density gradient from one half of the salinity of sea water to freshwater be used when filling the tank from bottom to top.

To fill the tank, the silicone carbide seeded saline water was prepared in 11 batches (11 layers) and pumped into a bowel placed in a lump of plastic straw located at the opposite side to the observational section of the oval tank. The water then spilled over the brim of the bowel and flowed through the lump straw to spread into the stretch of the tank. The lump also acted as a wave absorbing ramp. It took more than eight hours to fill the tank to the desired water level.

As to LDV measurements under stratified conditions, due to settling of particles associated with the long filling process, the proper seeding was quite difficult. A few experiments failed to yield acceptable counter data rate. Measurements were only done for 5 cm depth point under wind velocities of 4.1 and 5.1 m s^{-1}.

9.4 A few intrinsic aspects of the experiments

In this section we discuss a few experiment-related details that might not akin to the key interests of the topics, but they help illustrate some intrinsic aspects of the experiments and thus solidify the data analysis given later. The points here concern a few understandings, such as the response characters of the instruments, the accuracy of the measurements, awareness of the degree of control in the experiments, as well as different inherent properties associated with different numerical processes.

9.4.1 Calibration curves for the rain module

It is generally accepted that orifice flows follow the principle of Bernoulli equation, that is to say, the flow rate is proportional to square root of the water head. However, for the hypodermic flow of the rain module a linear relationship rather than the Bernoulli

principle provides the best fit for the data. This is given by the almost perfect straight line shown in Figure 9.2 ($r \sim$ head), in which the instantaneous flow rate is calculated from the time derivative of the water head. For this straight line, both the second order polynomial and exponential fits (between the water head above the bottom of the rain module and the elapsing time) can provide quite reasonable fits. However, for the low water head region, the exponential curve provides a much better fit, even down to the tip of the hypodermic needle; while the second order polynomial curve does not fit well and yields a negative rain intensity. Obviously, the needle and the wind have caused the flow mechanism to deviate from the potential theory.

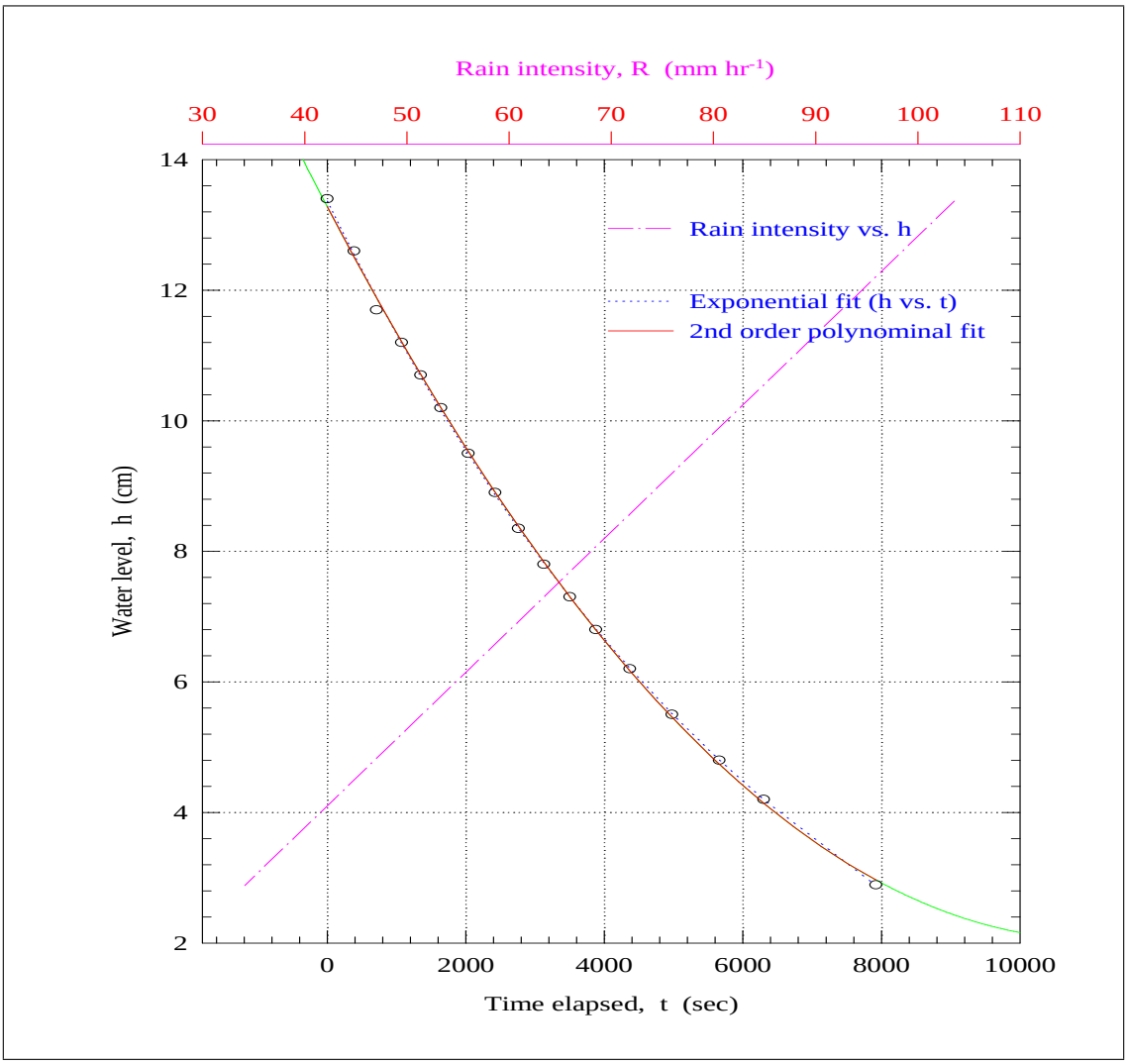

Fig 9.2 ($r \sim$ head) Characteristic curves for the rain module.

9.4.2 Natural frequency of the wind-wave tank

It is generally true that any structure or instrument setup is associated with specific natural frequencies and can even induce noise that may interfere with the desired signals. The identification of these should be helpful. For example, with the help of the real-time laboratory system it was found that the running of fan motor interferes with the wave gauge when the gauge is placed within a specific region of the tank. In addition, the natural frequency of the tank was also identified; this helps to illustrate some informative points.

When the wind is blown for a period of time and then stopped, short wind waves die away rapidly and only sustainable phenomena remain. For the oval tank, if not blocked (for measurements associated with rain-induced setups, its reasons to be stated later), there does exist an energy pickup from the relatively short wind waves by the relatively low natural frequency which is about one thirteenth of the typical peak frequency of the wind waves in the tank. Figure 9.4 (NF ~ Noise) shows a wave gauge signal recorded under such a condition. The signal is associated with the most noisy wave gauge we used (nevertheless, using the developed real-time software system, the gauge is calibrated to have a good linearity, as is shown in one of the curves in Figure 9.3 (Cal–WG & PT)). As is seen the signal corresponding to the natural frequency is relatively weak and is almost submerged in the noise of the gauge. However, when the signal is smoothed and auto-correlation coefficients are calculated, the period for the natural frequency is easily identify as 13.3 sec as shown in Figure 9.5 (NF ~ ACC). The period is in good agreement with the time needed to travel the tank using the celerity formula for the shallow water wave limit, i.e., $c_g = c = \sqrt{gh}$, where c_g is the group speed, c is the celerity of the wave, g is the gravitational acceleration, and h is the water depth. In the figure the tapering of the curve is associated with zero padding when calculating the coefficients.

In a different perspective, the pressure transducer records a much less noisy signal as shown in Figures 9.6 (NF ~ PT), in which the cyclic period can easily be identified. A few points can be said here: First, they show that both the wave gauge and pressure transducer

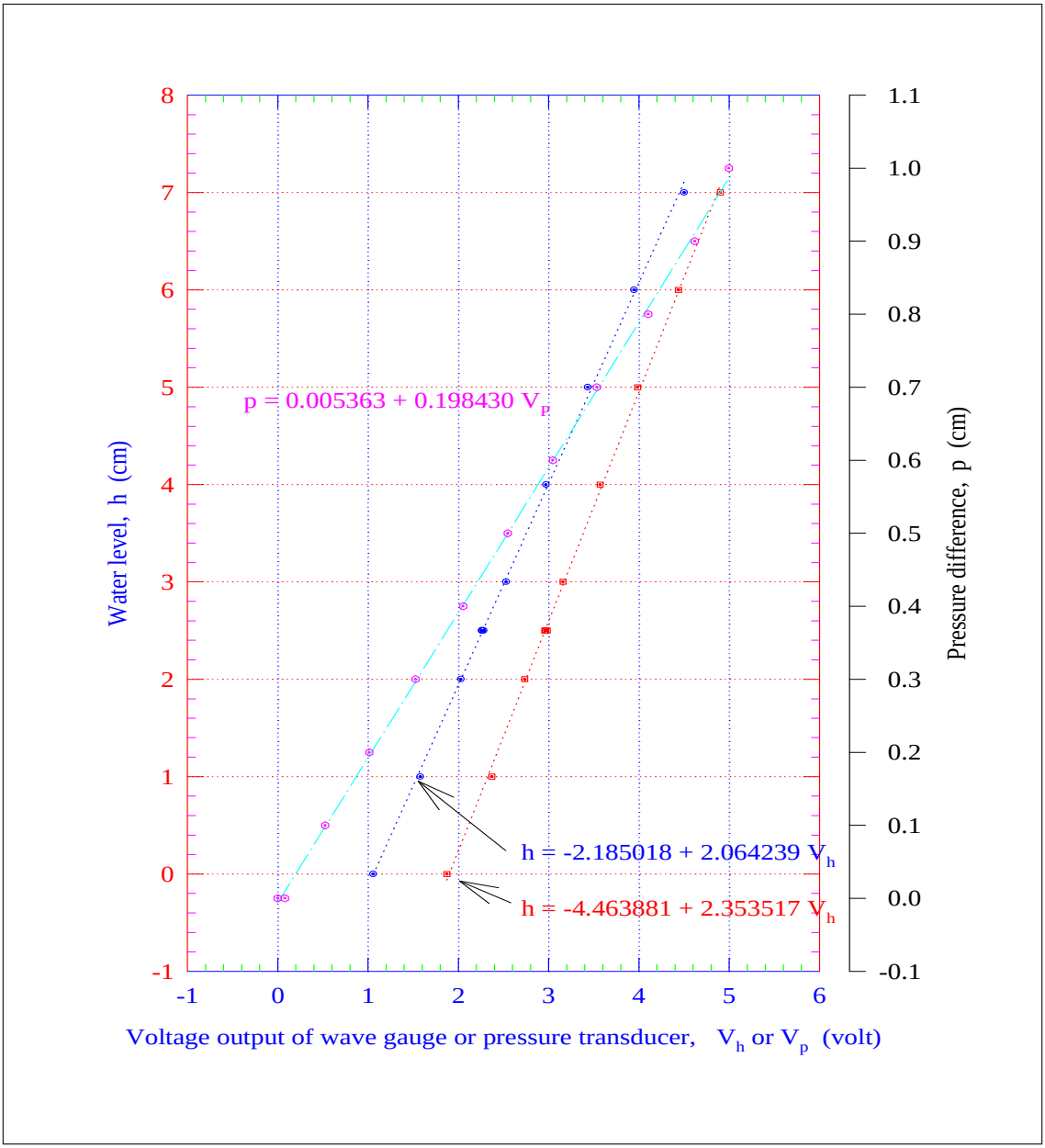

Fig 9.3 (Cal–WG & PT) One set of calibration curves for the wave gauges and pressure transducer.

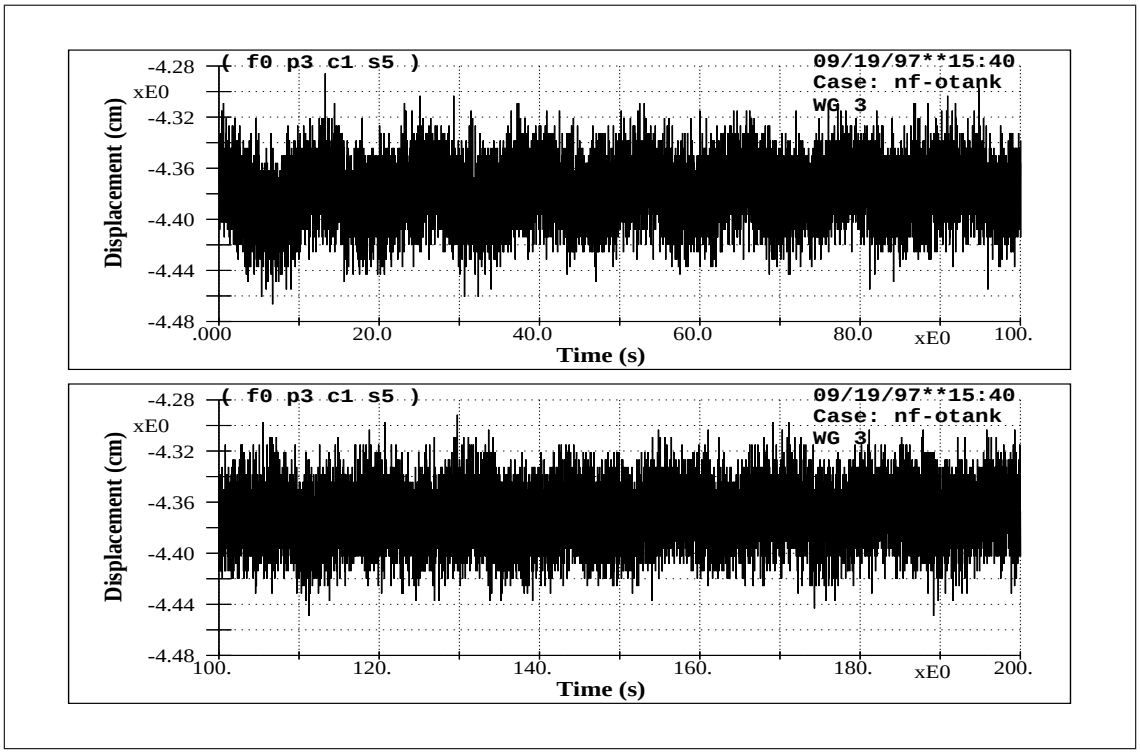

Fig 9.4 (NF ~ Noise) A noisy wave form that embeds the natural frequency of the oval tank.

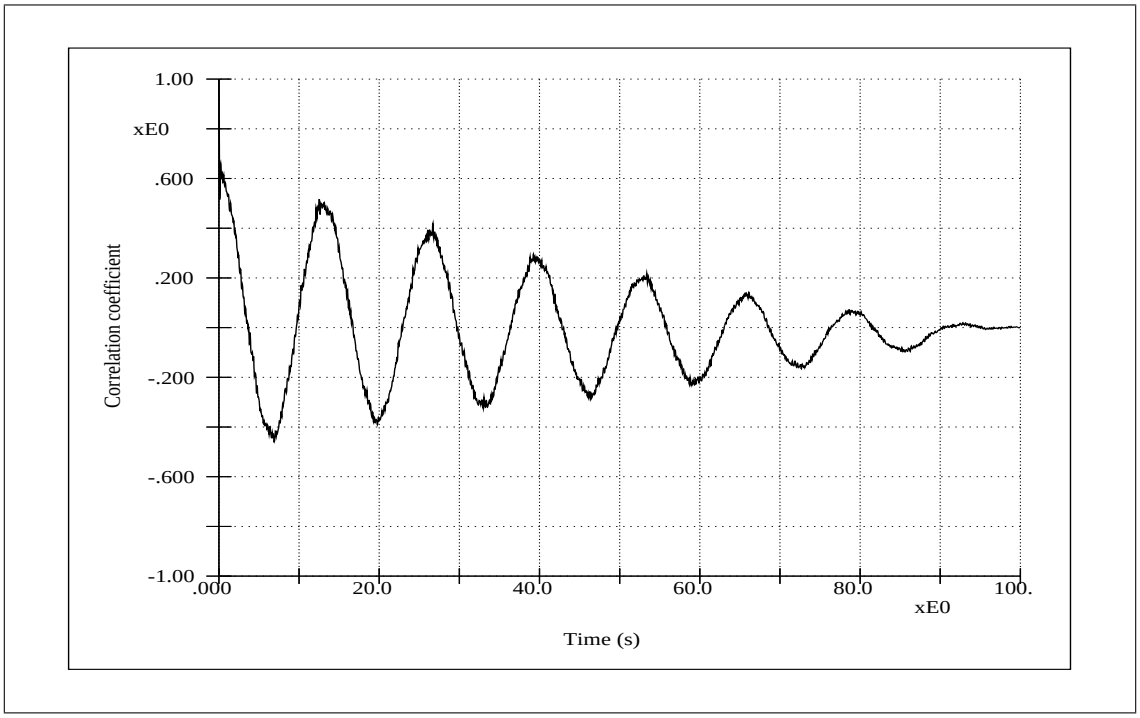

Fig 9.5 (NF ~ ACC) The auto-correlation coefficient function of the noisy wave form which clearly shows the natural frequency of the oval tank. The tapering of the curve is mainly due to zero padding of the numerical process.

are able to provide accurate and consistent measurements. This is justifiable from the minimally filtered wave gauge signal shown in Figure 9.7 (NF ~ MLP), where the convolution filtering is associated with the use of a maximum allowable cutoff frequency of 3-point and the Blackman window. Second, even for such an extremely small wave steepness the wave is much more of a Stokes wave, as shown by the surface displacement curve where it has flatter troughs and sharper peaks as well as the curve of differential pressure where it has slower rises and steeper descends (which are corresponding to troughs and peaks of the wave form, respectively). Concerning the natural frequencies, this also indicates the existence of a multi-mode. Third, judging from the curves in 9.6(NF ~ PT) and Figures 9.7(NF ~ MLP), it is anticipated that the measurements meet the accuracy requirements of less than the order of 0.01 cm.

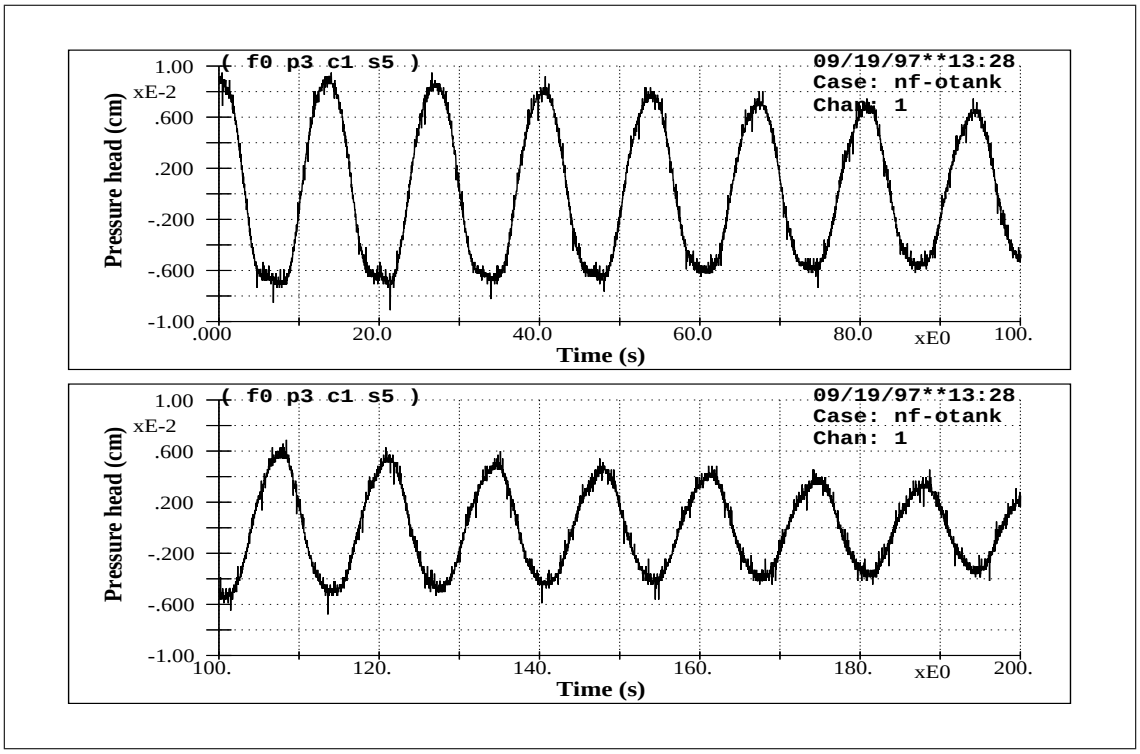

Fig 9.6 (NF ~ PT) Raw signal of the pressure transducer related to the natural frequency. Even for the extreme smallness of wave steepness the wave is more like a Stokes wave with flatter troughs and sharper peaks, which in turn yield slower rises and steeper descends of differential pressures as shown in this figure.

As a supplemental explanation of the uncertainty arising from the Fourier numerical process, it is also noted that, even though analytically the power spectrum is the Fourier

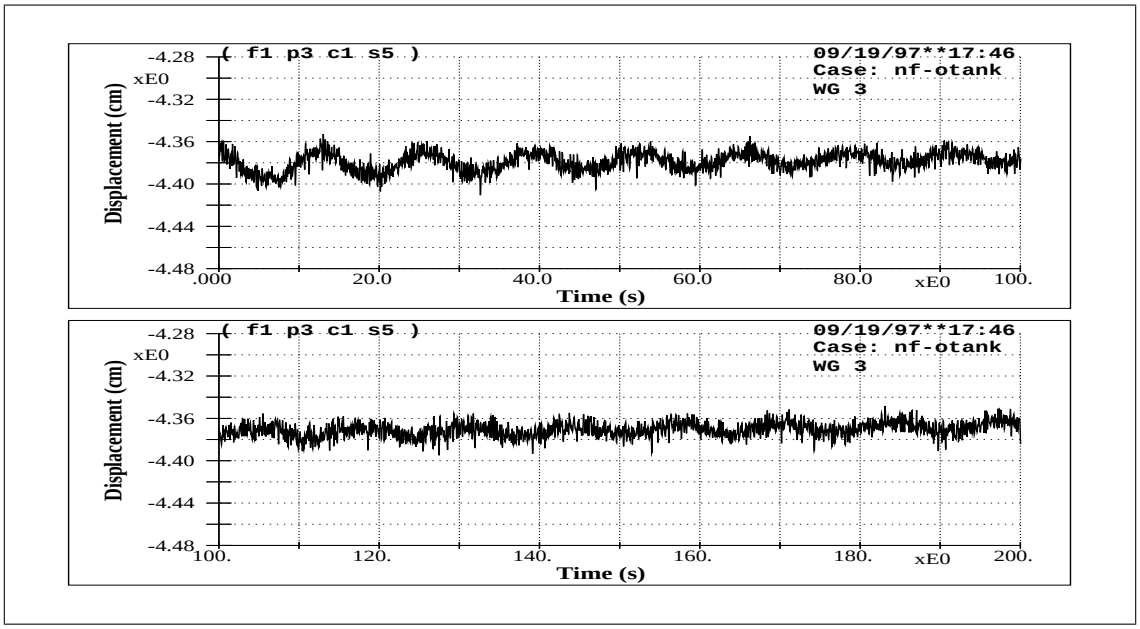

Fig 9.7 (NF ~ MLP) The minimally low-passed wave gauge signal associated with the natural frequency of the oval tank. Here the Blackman filter with maximum cutoff frequency of 3 points is used. Compared with Figure 9.4 (NF ~ Noise) one sees that most of the noise is associated with relatively high frequency. In reference to the pressure transducer measurement (Figure 9.6 (NF ~ PT)) they show quite consistent results.

transform of the auto-correlation function, the spectral curves seem not to have as a clear identification of the natural frequency as the auto-correlation curve has. This is mainly due to added side effects of the numerical process. And it manifests a few practical limitations associated with numerical aspects of the discrete Fourier transform such as segmentation, frequency leakage, edge effects, windowing, and the deviation of actual frequency from spectral resolution point. Figure 9.8 (NF ~ PS) shows two power spectra under different segmentation lengths. The spreading of the peak makes it hard to identify the frequency unambiguously.

Some additional points are given as follows: The noise level for the surface displacement is generally higher than that of measurement accuracy, but it is of high-frequency and can mostly be filtered out. Calibrations of surface displacements were all done with verniers with an accuracy of 0.005 cm. Response characters of instruments, including resolution and time responses of the acquisition hardware and pre-filtering instruments are verified using a WaveTek signal generator. No deterioration of signals can be identi-

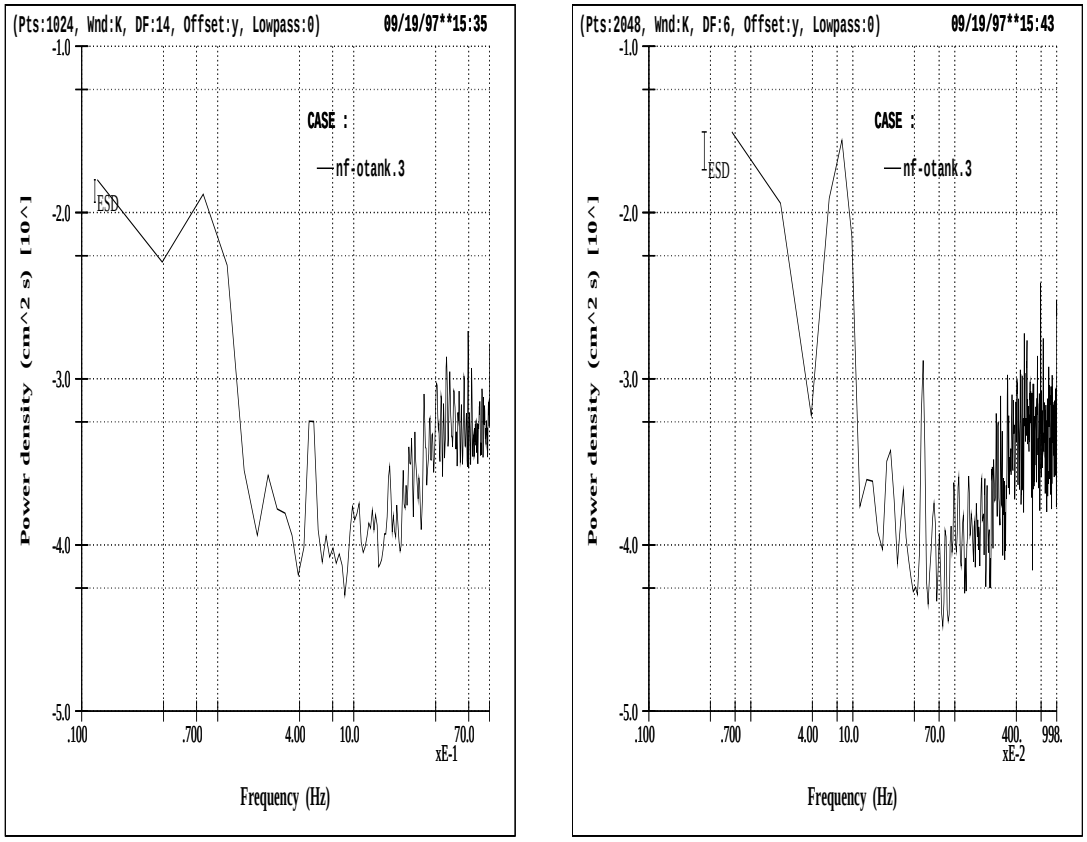

Fig 9.8 (NF ~ PS) Power spectral curves for the signal shown in Figure 9.4 (NF ~ Noise). Though analytically power spectrum is the Fourier transform of the auto-correlation function, side effects of the numerical process cause ambiguity and render judgemental difficulty.

fied for the instrument setups. For those experiments focusing on the momentum transfer, the oval tank was not blocked by wave absorber so as to minimize influences induced by setup or back flows (this concerns the accuracy of estimation from the formulation of the rain-induced stress to be stated in the next chapter); for those related to LDV measurements the oval tank is blocked with an wave absorbing ramp so as to reduce circulating drifts.

9.4.3 Wave reflection coefficient in the tank

Wave reflections from the curving section of the tank and possibly from the wave absorber ramp are estimated using the wave separation technique proposed by Goda and Suzuki

[23] (cf. Lee [80]). For such an estimation, the mechanical wave generator is used and the coefficients are calculated based on the energy contents of separated incident and reflected component waves. Table 9.2 (Tank Reflection) shows the statistics of a case where the significant wave period (less than 2 Hz) is somewhat longer than those of typical wind waves in the tank; this therefore provides a conservative estimation. The energy reflection level is about one percent, which is no larger than the uncertainty associated with the numerical calculation (such as a few concerns mentioned before as well as phase complications); therefore, influence of reflection is negligible.

9.5 Summary

Setups of Experiments are detailed. A few informative aspects or intrinsic natures of the experiments are also illustrated. From these we gain a general idea concerning the control of the experiments. ❖

Tab 9.2 (Tank Reflection) Energy reflection level for a mechanically generated wave in the oval tank. It is calculated by separating the incident and reflected waves using Goda and Suzuki's method [23].

Case : Kr_Oval.dat (s1p3c1)
Date : 04/29/95
Time : 13:50:27.84 Sampling frequency : 200 Hz
Specifics : Oval tank Kr Sampling time length : 52 Sec

Ch	#_W	H.1	H.2	H.3	H1/10	H1/3	H1/2	H.ave	H.rms	T1/10	T1/3	T1/2	T.ave	T.rms
1.	110	31.95	30.77	30.61	30.61	29.09	27.69	23.31	23.99	.49	.48	.48	.46	.47
2.	106	31.10	30.60	28.11	28.84	26.41	25.82	24.05	24.17	.48	.48	.48	.48	.48
3.	112	3.47	3.40	3.35	3.27	3.01	2.88	2.48	2.54	.47	.47	.48	.45	.46
4.	106	3.44	3.43	3.38	3.38	3.27	3.21	2.96	2.97	.47	.48	.48	.48	.48
5.	108	3.42	3.17	3.13	3.19	2.99	2.90	2.65	2.67	.49	.49	.49	.48	.48

Energy reflection level (%): 0.8424
Program parameters etc. ::

Kr	: .0918	r.ch1	: 4	r.ch2	: 3		
		depth	: 24.0000	del.L	: 9.0000		
L.min	: 20.0000	T.min	: .3581	M.max	: 57		
L.max	: 180.0000	T.max	: 1.2983	M.min	: 16		
smo.flag	: 1	f.cut	: 67	aR.sq	: 57.6631E	3	
fft.point	: 4096	b.pnt	: 1	aI.sq	: 68.4510E	5	

Reconstructed incident and reflected waves :

Ch	#_w	H.1	H.2	H.3	H1/10	H1/3	H1/2	H.ave	H.rms	T1/10	T1/3	T1/2	T.ave	T.rms
4	42	3.79	3.55	2.85	3.26	2.28	1.85	1.45	1.59	.48	.48	.48	.48	.48
4	42	.34	.31	.26	.28	.21	.16	.12	.14	.49	.48	.48	.47	.47

Units:: Aqueous flow (Ch1&2:H): cm/s
Surface-wave (Ch3&4&5:H): cm
Period (T): s

Chapter 10

Rain-Induced Stress and Its Effects on Surface Waves

10.1 Introduction

Rain over the ocean is usually accompanied by wind. Observations (van Dorn [72]) and analytical studies (Caldwell and Elliott [14, 15]) showed that the rain-induced stress can be of comparable magnitude to the wind stress, especially for light and intermediate winds. However, it is unclear about the partition of rain-induced stress into different components such as currents, water-surface setups, waves, or turbulent features in the air-sea interface (such as ripples, vortex rings, bubbles, stalks, and mixing). Added to the complexity of this coupling system are variety of real ocean conditions, such as density differences, thermal effects, surface films, etc. It is therefore not surprising to have inconsistent or even contradictory descriptions about rain's effects on waves among various researchers (e.g., Moore et al. [57]; Tsimplis and Thorpe [70]; LeMehaute and Khangaonkar [42]; Tsimplis [69]; Poon et al. [61]; Bliven and Giovanangeli [9]; Atlas [5]). In this chapter a few experiments are used to furnish some of the evidences concerning the deficient aspects of existing studies. These experiments focus on rain induced stress and its effects on surface waves. And, with an intention to minimize the uncertainty as much as possible, data are processed in a manner focusing on globally oriented rather than finely resolved features.

10.2 Macro perspectives of rain-induced stress and surface setup

Expanding van Dorn's [72] formulation of rain-induced stress, by taking into consideration a more reasonable reference basis, which helps to remove the influences of unrelated quantities and improve accuracy of estimates; the rain-induced stress is reformulated as the followings. Let consider a control volume of water right under the raining segment and take the system to be a two-dimensional steady case with x- and z-axis being along the tank and vertically upward, and let us further assume the horizontal mean speed u is much larger than the vertical mean speed v (therefore, for these experiments involving setups the tank is not blocked), the momentum equation integrated over the water depth under no rain action is:

$$\frac{\partial}{\partial x}\int_0^{D+h} u^2 dz = -g\int_0^{D+h}\frac{\partial h}{\partial x}dz + \frac{\tau_w - \tau_b}{\rho_w}, \tag{10.1}$$

where D is the still water depth, h the setup of water level, g the gravitational acceleration, τ_w the wind stress, and τ_b the wall friction of the tank. Further integrating along the rain section l, since $D \gg h$, one has

$$\int_0^{D+h} u^2 dz\Big|_0^l = -gD(h_l - h_0) + \frac{\tau_w - \tau_b}{\rho_w}l. \tag{10.2}$$

With the addition of rain, the formula modifies to

$$\int_0^{D+h'} u'^2 dz\Big|_0^l = -gD(h_l' - h_0') + \frac{\tau_w' - \tau'_b + \tau_r}{\rho_w}l, \tag{10.3}$$

where values with superscript $'$ represent those with the influences of rain, and τ_r is the rain-induced stress. Since the change made by the rain to the initially wind-driven current u in the circulating tank is of relative magnitude of 10^{-3} or even less, $u' \approx u$. And since changes of the wind and current speeds due to rain are very small, it is reasonable to

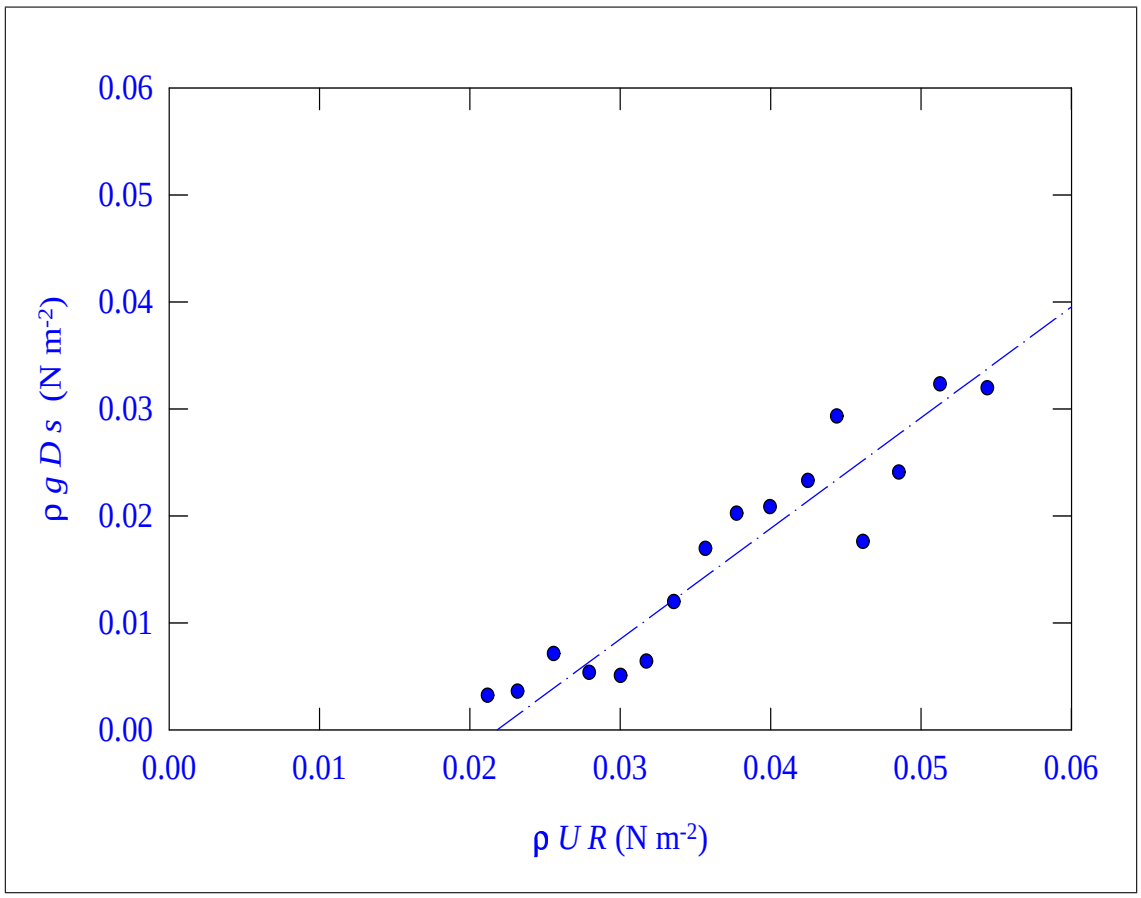

Fig 10.1 (RIS–P&V) Indirectly measured rain-induced stresses versus van Dorn's [72] theoretical values. The fitted straight line is in parallel to the diagonal line. This indicates the existence of a threshold wind and rain condition for rain-induced setups and implies that the momentum flux does not act only on the water surface; therefore, proper temporal and spatial scalings need to be considered.

assume that $\tau_w^{'} - \tau'_b$ is almost identical with $\tau_w - \tau_b$. Therefore, we have the estimation of rain-induced-stress as

$$\tau_r = \rho g D \frac{(h_l^{'} - h_0^{'}) - (h_l - h_0)}{l} = \rho g D s, \tag{10.4}$$

here s denotes a slope representing the relative change of the mean water surface.

Figure 10.1 (RIS–P&V) shows the relation between the experimental results based on the above formula and the theoretical values given by van Dorn [72]. The magnitudes of the two are comparable, but the measured values are smaller with a large relative reduction for a lower rain intensity, and a small relative reduction for a higher rain intensity. The

straight line fitted for the data points is in parallel to the diagonal line of the plot. This seems to indicate the existence of a threshold for rain-induced setups and implies the fact that the momentum flux does not act only on the water surface, i.e., there involve temporal and spatial scales. And it also suggests that the partition of the rain-induced stress into different physical elements is dependent on wind and rain conditions. Additional wave statistics and spectral analysis also support this implication, as will be explained later.

10.3 Fourier perspective of rain's effects on energies of surface waves

Figure 10.2 (Gain–FSI) shows the normalized relative gain of the power spectrum integration versus the rain intensity. This normalized relative gain is defined as the difference

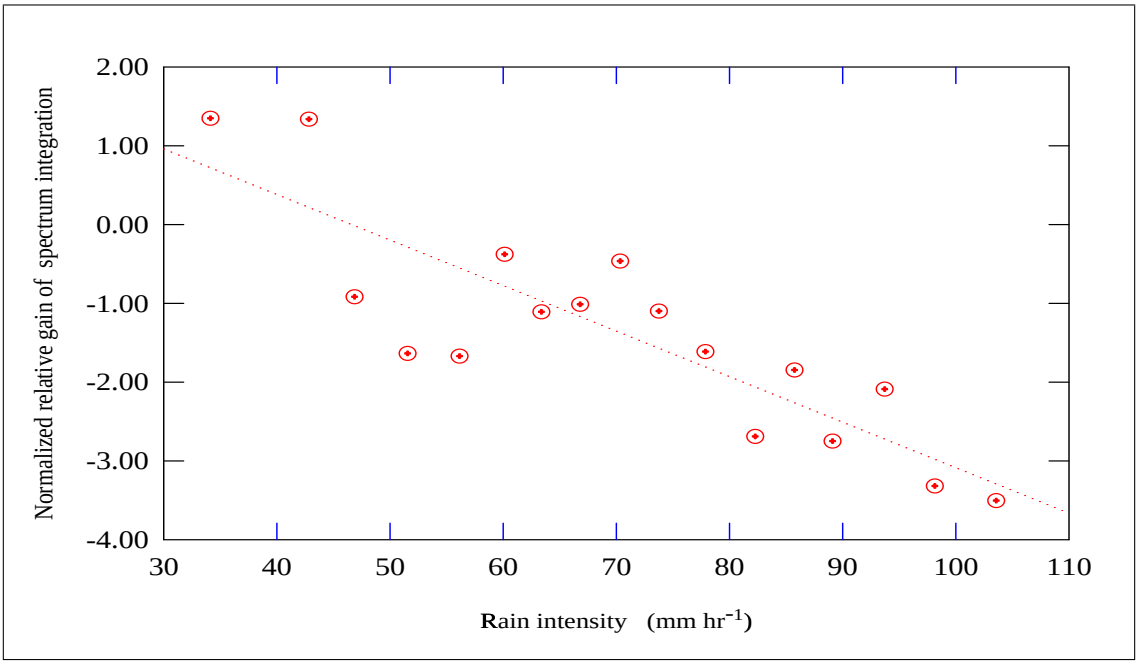

Fig 10.2 (Gain–FSI) Normalized relative gains of power spectrum integrations for various rain intensities. The values have the physical meaning of the relative magnitude of the rain-induced energy gain to that of wind-induced gain.

between the power spectrum integrations of the upwind and downwind wave gauges under the rain action with the subtraction of the difference of spectrum integrations under

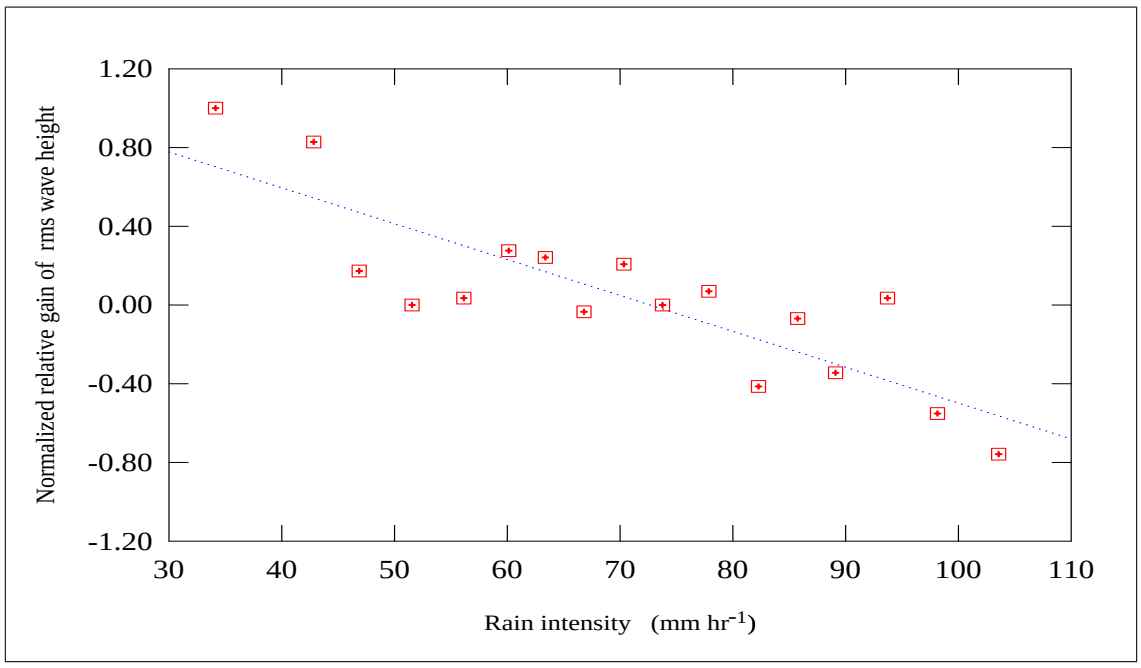

Fig 10.3 (G – $H_{rms} \sim r$) Normalized relative gains of root-mean-square wave heights from zero-upcrossing statistics for various rain intensities. Though completely different approaches are used for this and the previous figures, they give a quite consistent tendency concerning the distribution of data points. Since the statistics of this figure is based on zero-upcrossing, its energy implication is not as intimate as the previous one.

no rain action, and then normalized by the latter difference. It has the physical meaning of the relative magnitude of the rain-induced energy gain to that of wind-induced gain (again, here effects due to bottom and sidewalls of the tank or even other factors are implicitly removed). Figure 10.3 (G – $H_{rms} \sim r$) additionally shows the normalized relative gain based on root-mean-square wave heights derived from zero-upcrossing wave statistics. The two figures, which are associated with completely different statistics, show a quite consistent tendency. This fact hints the unambiguous effects of damping of waves of main energy contents. Figure 10.4 ($H_{dist} \sim r$) shows the cumulative wave height distribution curves of the downstream gauge using zero-upcrossing statistics for rain intensities equal to 0.0, 67.0 and 104.0 mm hr^{-1}, respectively. Again, these experimental results are opposite to L&K's theoretical predictions. It is also noted that our experiments are of a three-element interaction (wind, waves, and rain; or even with the forth element – currents) while L&K's theory mainly focuses on rain and waves only (but they do in-

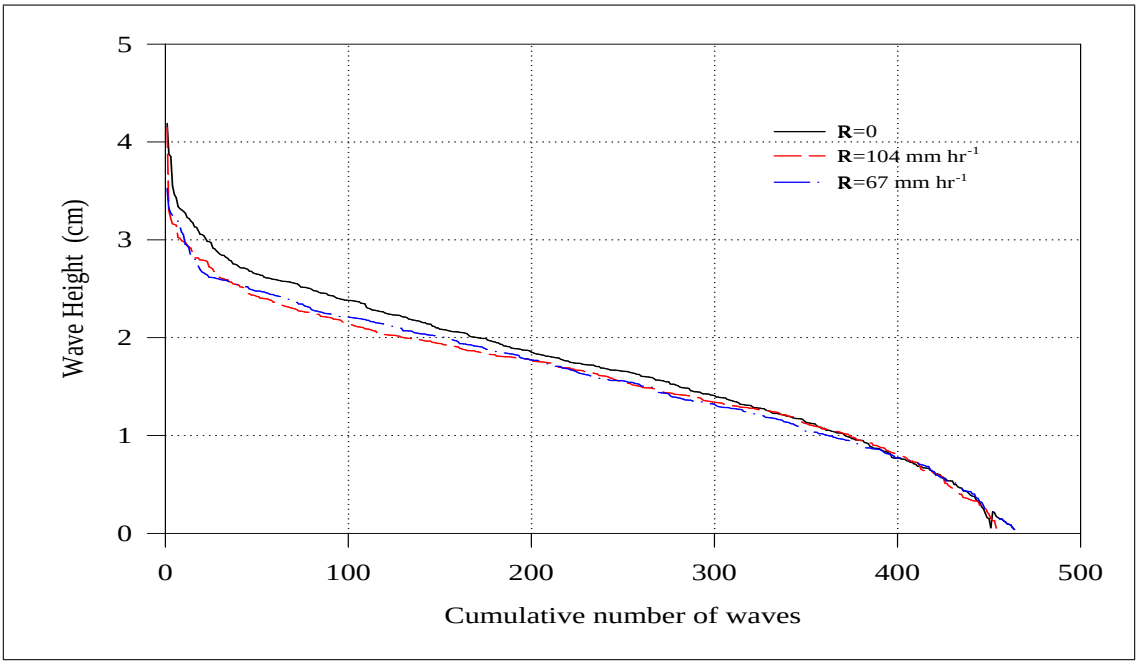

Fig 10.4 $(H_{dist} \sim r)$ Distribution curves for zero-upcrossing wave heights under three different rain intensities as labeled in the figure.

clude rain angles). Nevertheless, our processing methods have tried to extract only the rain-induced parts.

In addition, these figures suggest that, for a high rain intensity, although its rain-induced stress may be larger, there is more wave energy loss; and, for smaller rain intensity, though the rain-induced stress may be smaller, the energy loss of waves is smaller and can even turn to a gain (but with a relatively small net effect). Altogether, all these indicate that different wind and rain conditions involve different scale interactions.

Let us further provide statistic values of waves distributions under different rain intensities using Rayleigh distribution parameters. Figures 10.5 (RDP $\sim H_{rms}$) and 10.6 (RDP $\sim H_{ave}$) show two different Rayleigh distribution parameters based, respectively, on root-mean-square and averaged wave heights for the upwind and downwind wave gauges. They indicate that the zero-crossing wave height distributions in the wind blowing oval tank deviate from the Rayleigh distribution and that the wave heights are somewhat less normally distributed after the action of rains since the coefficients generally become larger.

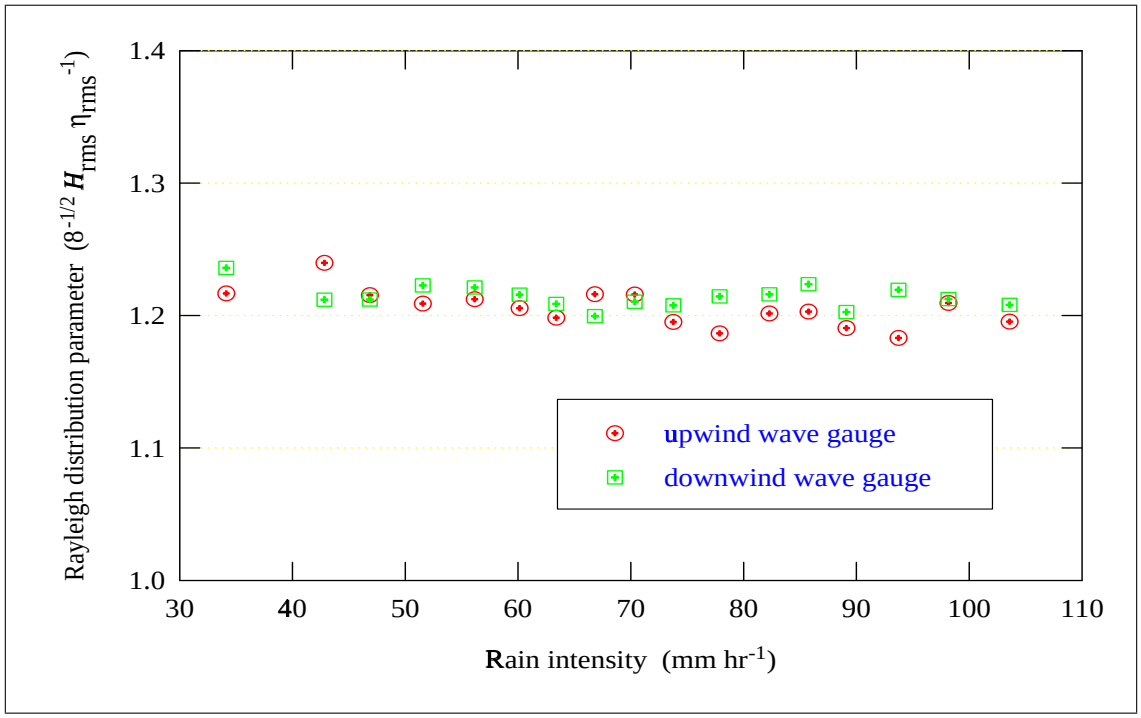

Fig 10.5 (RDP ~ H_{rms}) Rayleigh distribution parameters based on statistics of root-mean-square wave heights for different rain intensities.

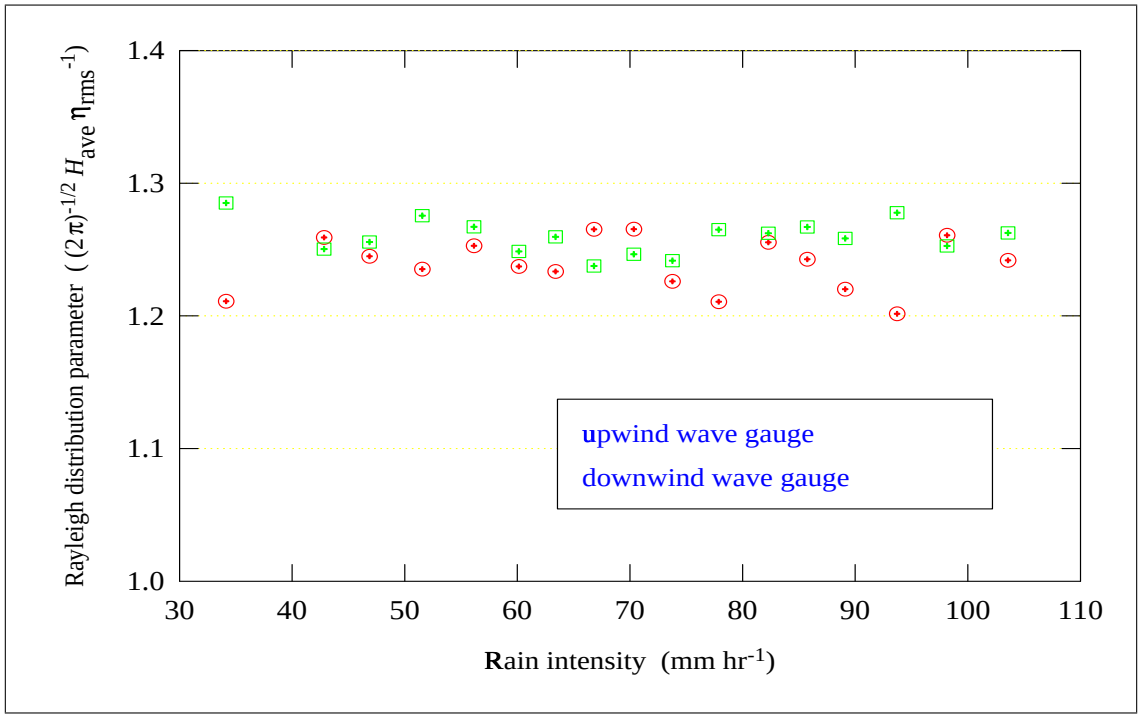

Fig 10.6 (RDP ~ H_{ave}) Rayleigh distribution parameters based on statistics of average wave heights for different rain intensities.

The above discussions focus on global parameters, i.e., not focusing on component waves. They should have less ambiguity or uncertainty concerning rain's overall effects on waves. A few spectral features of the signals are stated in the followings. Figure 10.7 (FS – U&D) shows power spectra of the upstream and downstream wave gauges under 104 mm hr^{-1} rain intensity. Here a scheme of 15 1024-point overlapping sections with Bartlett window is used. The general features are: (1) The spectrum curves have steep drops at both sides of the peak and the dropoffs on the high-frequency side have quite large slopes (larger than 5.0 power exponent); (2) For frequencies higher than about 2.5 Hz the dropoffs can be represented by the -4 power law quite well. Poon et al.s' [61] spectral curves showed quite mild slopes for both regions; this might be due to the shorter segmentation length they used.

With an intention to reduce the uncertainties, the following spectral perspective takes into consideration two following points: (1) Rather than making comparison for data with and without rain at downstream alone, which are related to different runs (therefore, induced additional uncertainties), the upstream and downstream data measured at the same time are used and further referenced to the upstream and downstream data without the rain action. (2) Rather than considering each frequency component, we consider the frequency bins of the spectra. Figures 10.8 ($BG_{0.5hz} \sim r$) and 10.9 ($BG_{0.1hz} \sim r$) show the relative gain (or loss) factor of the energy at each frequency bin for two different bin resolutions (a coarser and uneven resolution as marked in the axis is used for Figure 10.8 ($BG_{0.5hz} \sim r$); a finer 0.1-Hz resolution is used for Figure 10.9 ($BG_{0.1hz} \sim r$)) under various rain intensities. Here the relative gain is defined as the difference between the downstream and upstream energy contents, with first the removal of the difference without the rain action and then divided by that without the rain action (in a sense similar to the definition used for Figure 10.2 (Gain–FSI)).

For the practical wind conditions in our oval tank, most of wave energy concentrates in a narrow band from 1.7 to 3.0 Hz (accounts for more than 92% of the energy) with spectral peak around 2.0–2.8 Hz. And for lower wind speed the peak shifts to a higher

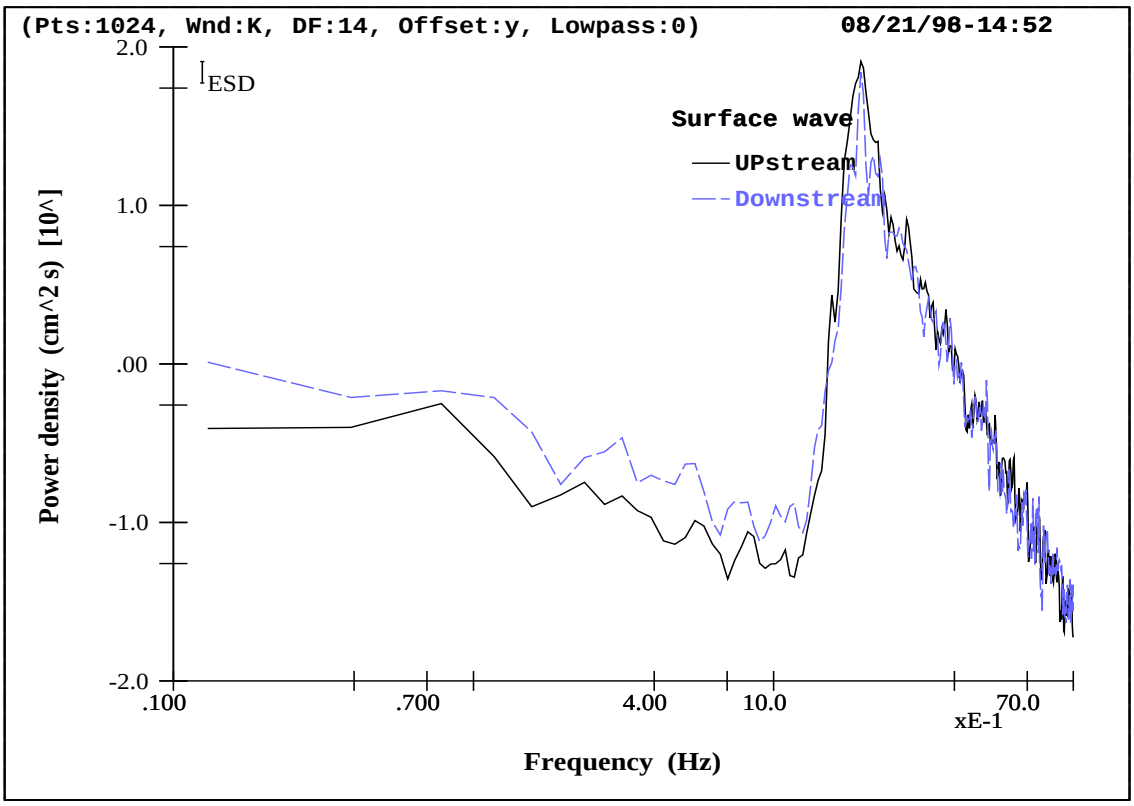

Fig 10.7 (FS – U&D) Power spectrum densities for upstream and downstream wave gauges.

frequency and becomes flatter or wider. Under the present wind speed, if the Doppler shift due to drift current is accounted (Wu [76], the main energy wave is about 50 cm long or 1.8 Hz in frequency. Poon et al.s' [61] results at high wind velocities showed an extensive damping at frequency around 3.5 Hz, and around 3.5 Hz the energy is of little importance. In this regard, our results show the same general decay for high frequencies (about greater than 3.2 Hz), but for those lower frequency bins with more significant energy contents the features are somewhat complicated (Figure 10.8 ($BG_{0.5hz} \sim r$)). It worths mentioning that there is a trench around bins 2.0 and 2.1 Hz (Figure 10.9 ($BG_{0.1hz} \sim r$)). And since there is a high energy concentration there, energy dissipation is anticipated to be significant. It is also noted that the significant wave period as well as the root-mean-square wave period based on zero-upcrossing statistics fall in this trench. This spectral feature is consistent with the globally oriented characterizations discussed earlier. Moreover, there exist regions with positive gain around the trench, and this highlights the possibility of an energy cascade mechanism.

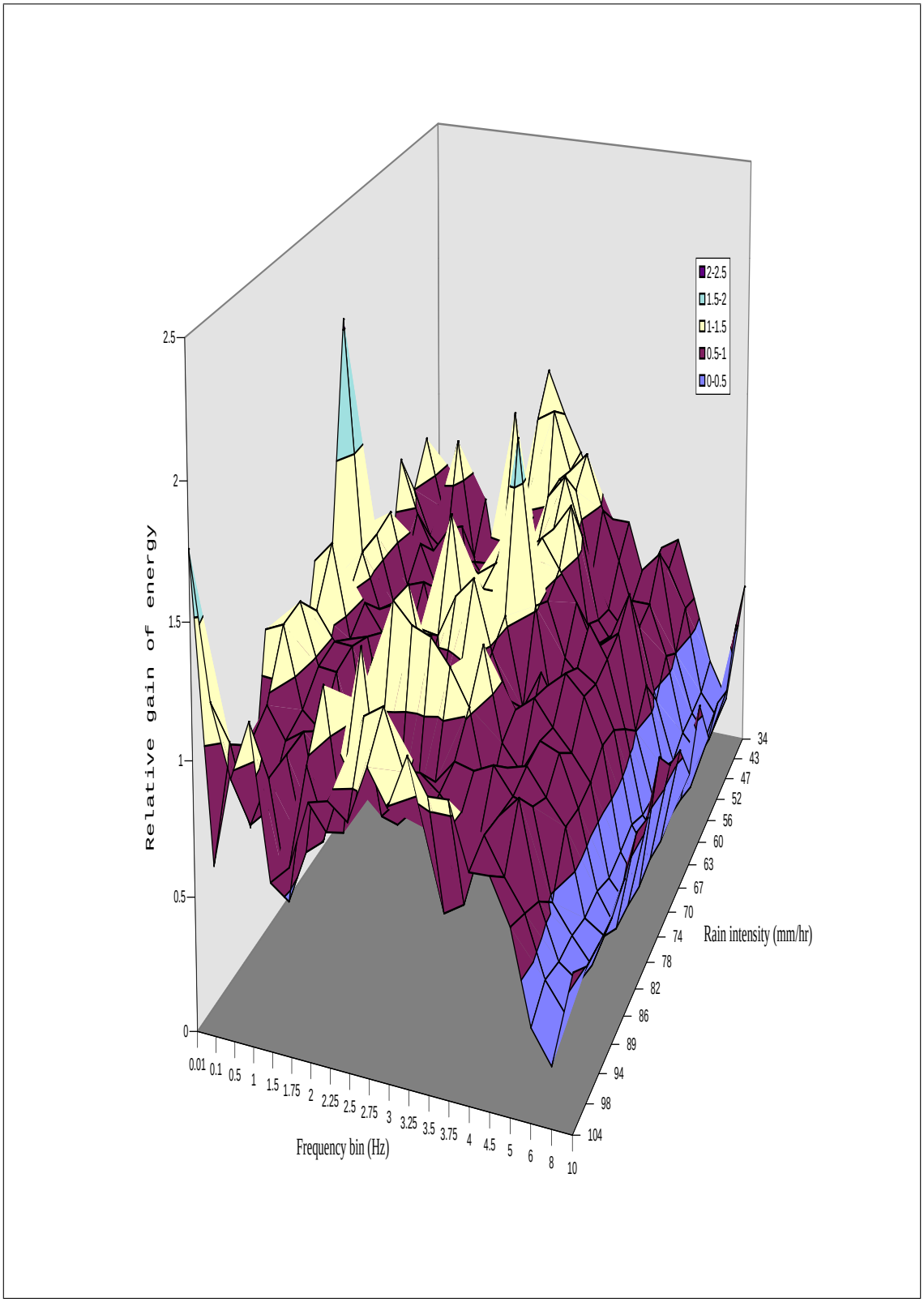

Fig 10.8 $(BG_{0.5hz} \sim r)$ Relative gains of the spectral energy for individual frequency bins (bin width 0.5 Hz) under various rain intensities.

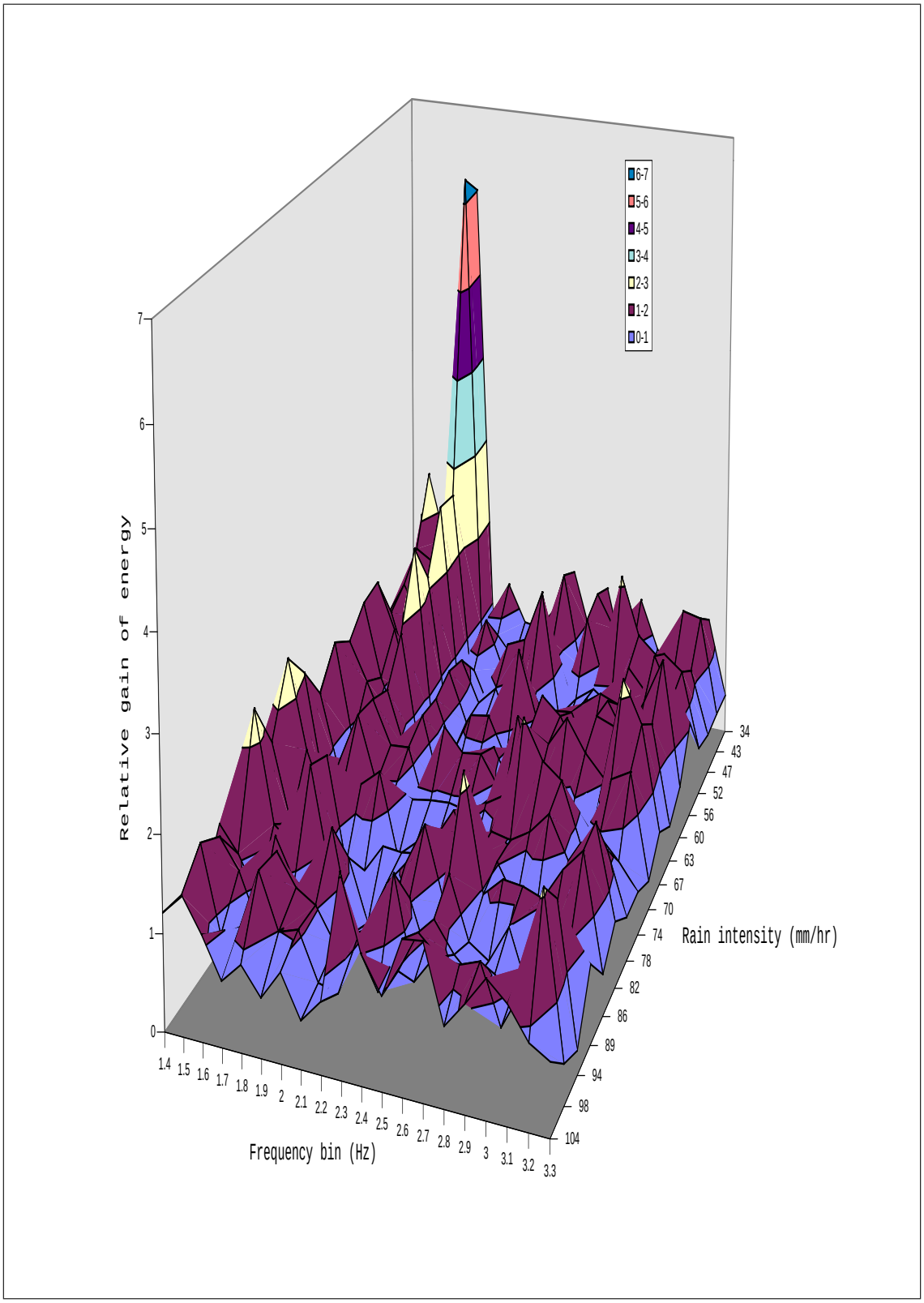

Fig 10.9 $(\mathrm{BG}_{0.1hz} \sim r)$ Relative gains of the spectral energy for frequency bins in 0.1 Hz resolution under various rain intensities. The somewhat obvious feature is the existence of a trench around 2.0 Hz, which corresponds to the significant wave frequency.

10.4 Summary

Here we basically focus on providing experimental evidences and refine numerical processes for clarifying a few ambiguities discussed in the earlier chapters. The results show: the rain-induced stress should distribute in a certain water depth rather than just on the surface; the partition of momentum flux due to rain is dependent on wind and rain conditions; the difficulties encountered from the Fourier perspective; and, energy phenomena for different scales are not universal. Overall, they indicate that the coupling system involves complex scaling problems. ❖

Chapter 11

Wavelet Coherences and the Energy Cascade of the Coupling System

11.1 Introduction

The previous chapter focuses mainly on the globally oriented characterizations of rain's effects on waves, as well as those from the Fourier spectral perspective; and it provides few insights of the interactions for the energy cascade mechanisms put forward in the earlier Chapter. With the facilitation of the identified best wavelet basis and its peculiar characteristics in coherence analyses, in this chapter we aim at providing a few evidences for the proposed mechanism of the energy cascade model and plying the manifestations on the interaction among coupling scales.

11.2 Coherence features of the coupling systems

Both wind-wave (non-stationary wave field from spectral viewpoint) and Stokes wave (stationary) cases will be used to study the coherent features in the coupling systems.

11.2.1 Wind-wave cases

In most wave tank experiments, which are invariably not only limited in modeling scales but also distorted in modeling factors, the full spectrum of a complex system of interaction

is basically hard to be realized. Nevertheless, the data acquired is used to deduce a few possibly intricate or fine tendencies concerning interaction mechanisms of wind, wave, and rain coupling system.

Figure 11.5 $(du \sim r, d)$ shows effects of rain on wave-current coherences for aqueous flows measured at several depths under 6.0 m s^{-1} wind. It is seen that, for aqueous flows measured in the near-surface region (2 and 3 cm below the mean water surface), the rain has greater influences for the high-frequency end (about $>$ 3.5 Hz) and the coherences there are significantly reduced; while for deeper depths (4 and 5 cm below the mean water surface) the coherence curves widen and their values increase at the high-frequency end. However, at a greater depth (9 cm) the coherences are overall reduced, and it is especially significant at the low- and high-frequency ends (Figure 11.6 $(du \sim r, d_9)$). The implications are:

1. Rain induces different impact patterns of wave-current coherences at different depths.

2. Near the air-water interface (2 and 3 cm), waves and aqueous flows of small scales are somewhat diversified or randomized due to the rains; therefore, the coherences for high carrier frequencies are reduced.

3. Since small scale components (waves and turbulences) do not penetrate deep and diminish rapidly, at somewhat deeper depths (4 and 5 cm) smaller scale aqueous flows are able to be tuned with corresponding scales of surface waves. This implies an energy redistribution to these smaller scales at these intermediate depths. It is also noted that, though coherence does not need to be dependent on the energy content of correlated elements, it is generally true that the higher is the energy content (in a relative sense) of a scale the higher the coherence of that scale will be.

4. With an energy redistribution to these smaller scale wave components, since they are still of scales at the high-frequency end and are associated with energy dissipation scales when compared with scales at low-frequency end, an enhancement of energy cascade to dissipation scales is anticipated at these depths.

5. With an enhanced energy dissipation due to rain at the above intermediate depths, less energy can propagate into a further depth. It is therefore quite reasonable to anticipate that the coherences for the whole scale range at deep depths are reduced. This feature is clearly shown in Figure 11.6 $(du \sim r, d_9)$.

6. Overall, one can argue that scales of main power contents that are under the action of rain do not penetrate as much as those without the action of rain. Or stated in a different perspective, rain de-tunes various scales in a deep region. Again these are consistent with illustrations of the energy cascade mechanisms.

Another set of curves similar to Figure 11.5 $(du \sim r, d)$ but under a different wind velocity of 5.1 m s^{-1} is shown in Figure 11.7 $(du \sim r, d, w_5)$. It shows basically the same tendencies.

Figure 11.8 $(du \sim r, d, w)$ shows wave-current coherences under different wind velocities of 6.1, 5.1, 4.0 m s^{-1} for depths 2 and 5 cm with and without rain. The implications are: (1) For higher wind velocity, the peak coherence increases (again, we see the above mentioned general rule) and also shifts toward a lower frequency. From these we see that wavelet coherences are able to identify the stages of development of waves — since all the signals are measured at the same cross section in the oval tank, higher wind induces a more mature stage of development. (2) The behaviors of spectral curves are extreme — the Fourier coherences are almost always equal to 1 for regions with peak energy contents, while always pouncing here and there for regions with less energy contents. Therefore it is generally impossible for spectral coherences to identify stages of development. This character will also be seen in a few additional figures to be shown later. (3) A close examination of these curves provides additional illustrations of a few above mentioned points related to Figures 11.5 $(du \sim r, d)$ and 11.7 $(du \sim r, d, w_5)$.

In the proposed energy cascade model the mechanisms center on the stratification of receiving water body. Measurements under the stratification were arranged for 4.0 and 5.1 m s^{-1} winds with aqueous flows measured at the 5 cm depth. Due to difficulty in

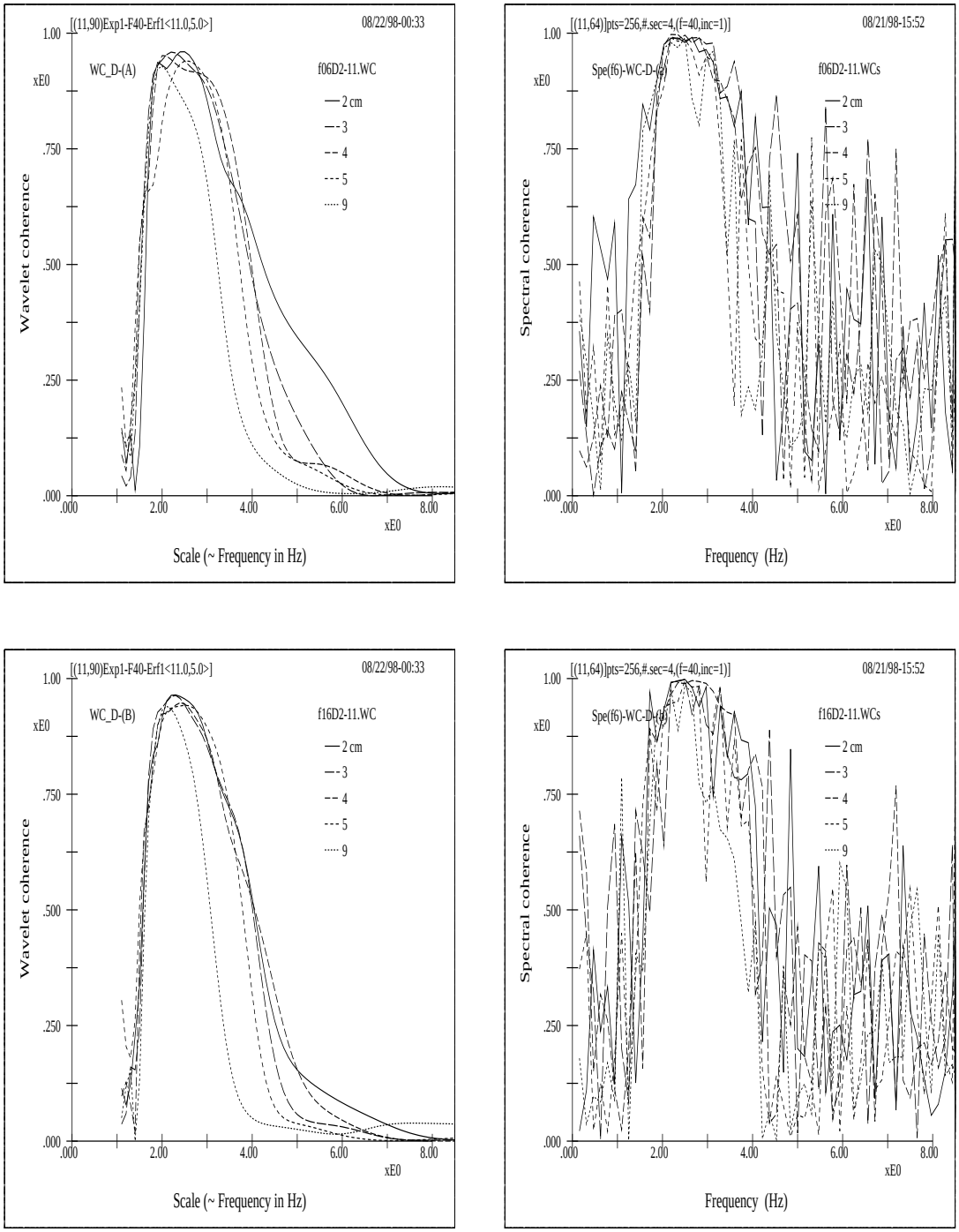

Fig 11.1 $(du \sim r, d\ (l_1\text{-B}))$ The wavelet `(left)` and spectral `(right)` coherences between waves and aqueous flows at each individual depth as indicated in the figures without `(top)` and with `(bottom)` rain (68 mm hr^{-1}) under 6.0 m s^{-1} wind. Here the length of the data segment is 1024-point. In reference to the two subsequent figures using longer data lengths the usefulness of the redundancy of CWT is most obviously seen since the wavelet coherence curves here are in extremely good proximities to those using longer data lengths.

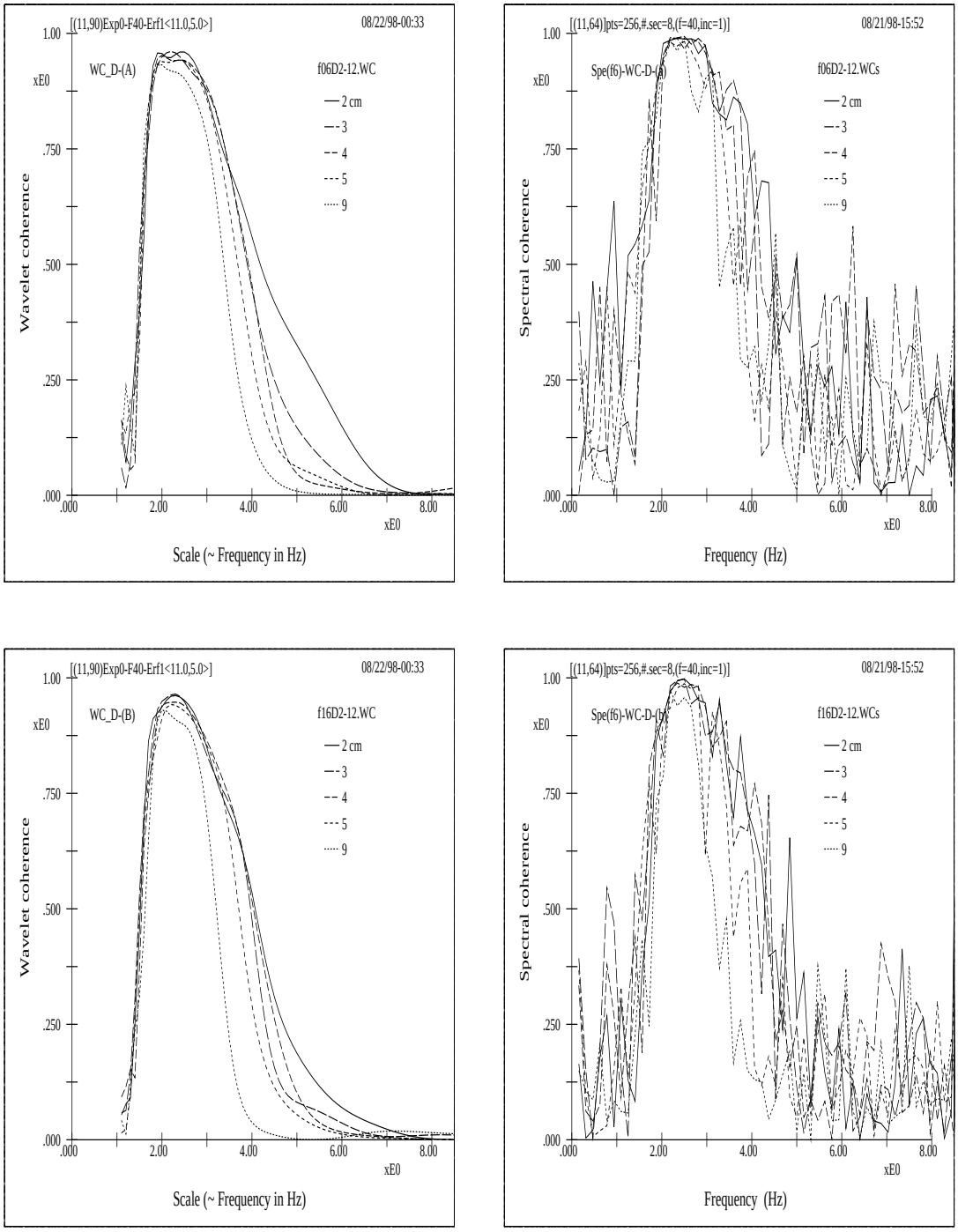

Fig 11.2 ($du \sim r, d$ (l_2-B)) The wavelet (`left`) and spectral (`right`) coherences between waves and aqueous flows at different depths without (`top`) and with (`bottom`) rain (68 mm hr^{-1}) under 6.0 m s^{-1} wind. Here the length of the data segment is 2048-point.

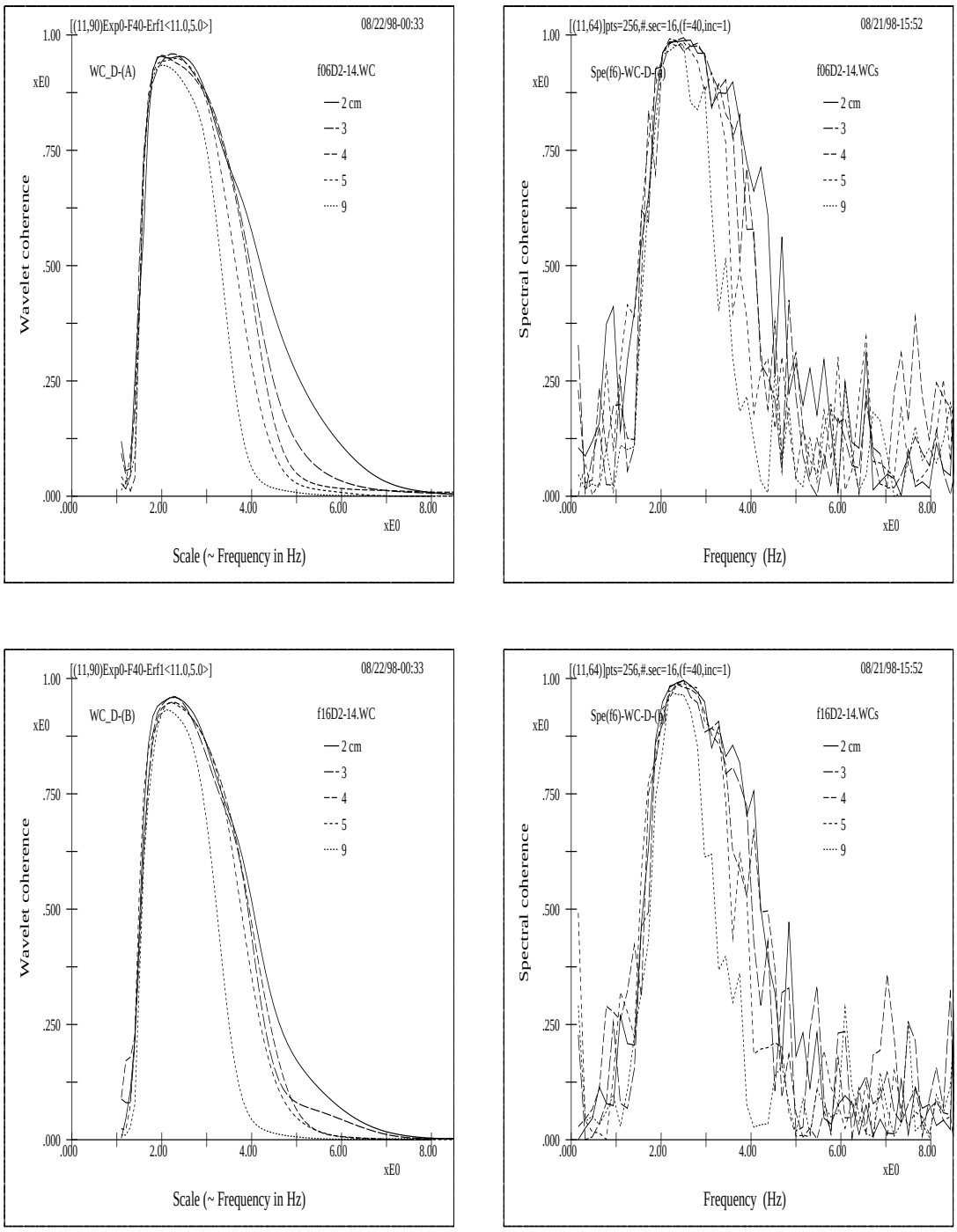

Fig 11.3 ($du \sim r, d$ (l_4-B)) The wavelet `(left)` and spectral `(right)` coherences between waves and aqueous flows at different depths without `(top)` and with `(bottom)` rain (68 mm hr^{-1}) under 6.0 m s^{-1} wind. Here the length of the data segment is 4096-point. The inferiorities of spectral coherences are reflected by the rapid fluctuations of the coherent curves as well as the extremely slow improvement when the data lengths are increased.

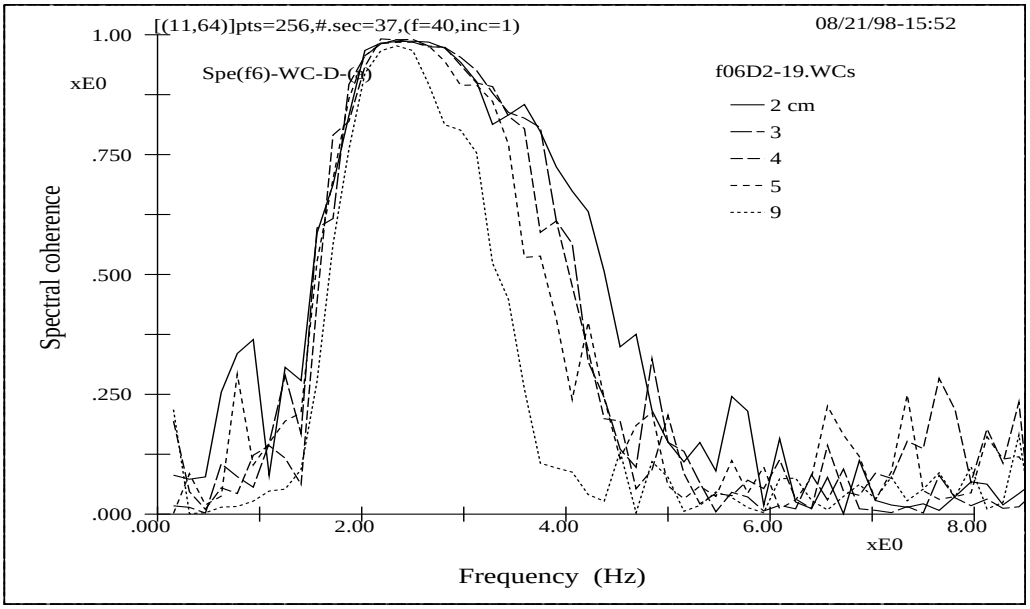

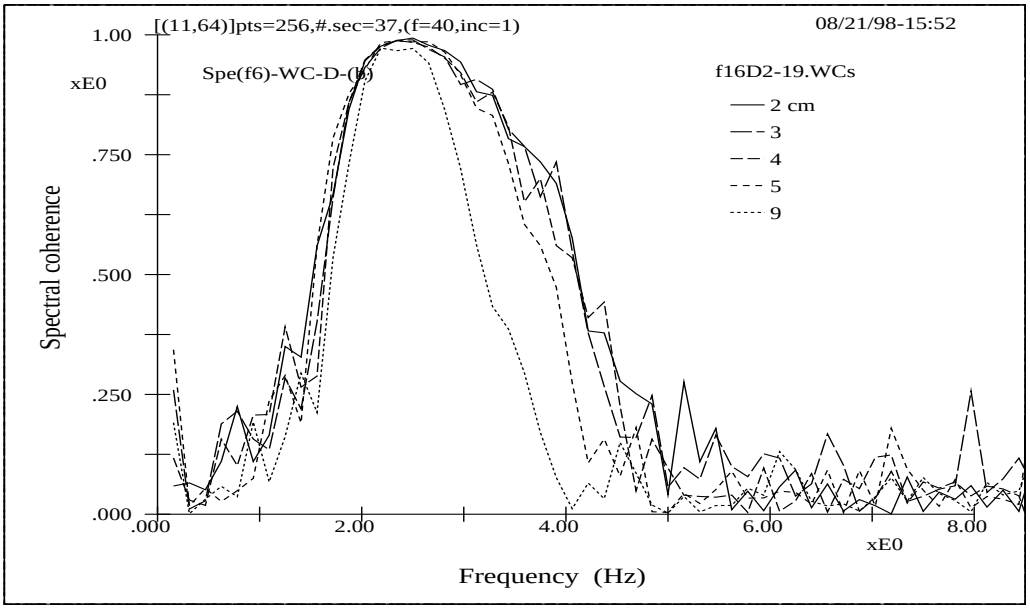

Fig 11.4 $(du \sim r, d\ (l_9\text{-F}))$ The spectral coherences between waves and aqueous flows at different depths without `(top)` and with `(bottom)` rain (68 mm hr^{-1}) under 6.0 m s^{-1} wind. Here the length of the data is 9472-point. Though the function bases of spectral and wavelet coherences are different, the spectral coherence curves are seen to approximate those of wavelet coherences for regions with more energy contents; nevertheless, serious wriggling still exists in most of the curves except near the peak coherence regions. It is therefore concluded that the spectral coherence can hardly be useful in identifying intricate phenomena or micro activities within a complicated interaction process.

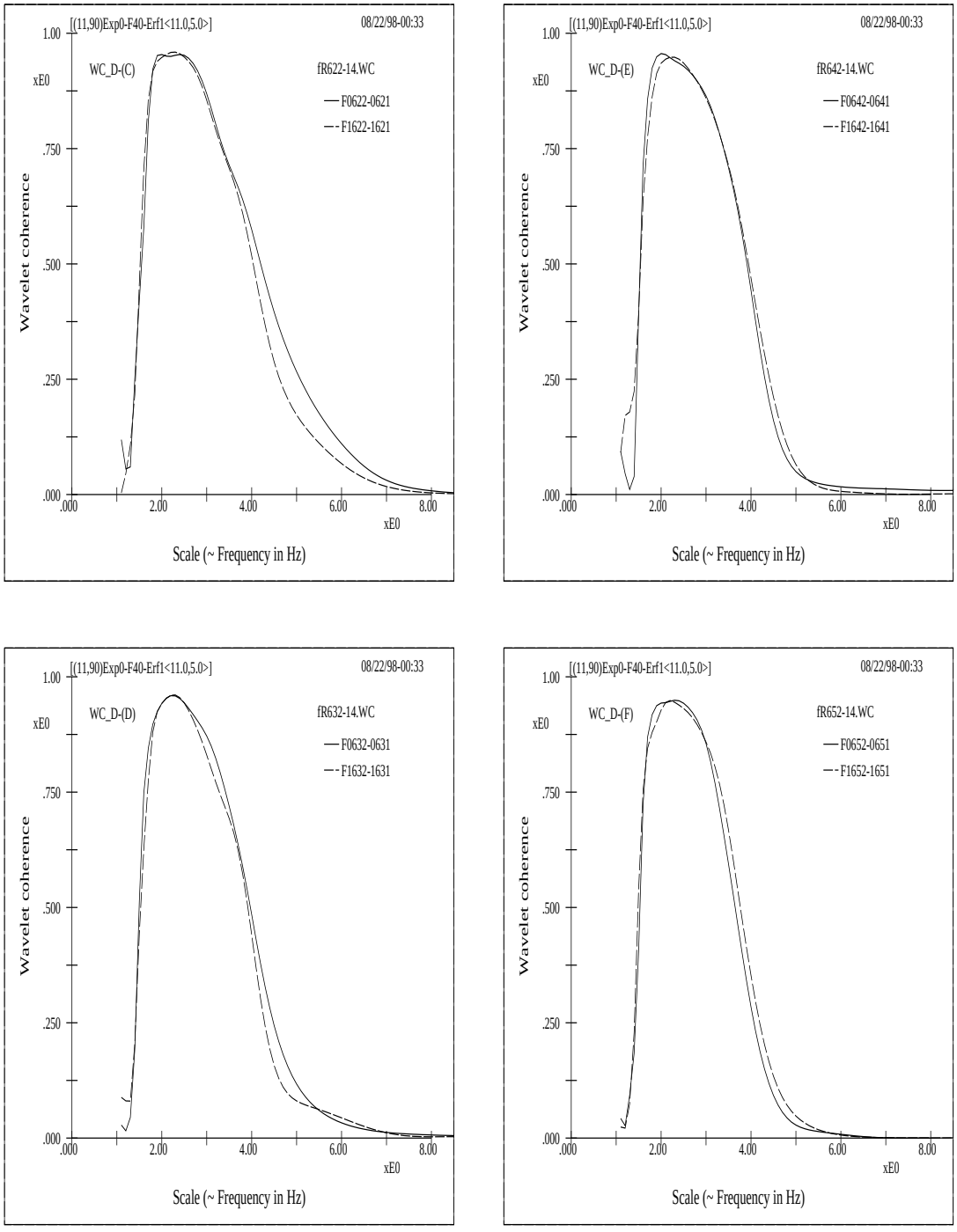

Fig 11.5 $(du \sim r, d)$ Wavelet coherences between wave and aqueous flow with (dashed lines) and without (solid lines) rain. The rain intensity is 68 mm hr^{-1}, wind velocity 6.0 m s^{-1}, and the aqueous flows are measured at 2 `(top left)`, 3 `(bottom left)`, 4 `(top right)`, and 5 `(bottom right)` cm below the mean water surface. The implied energy phenomena are explained in the text.

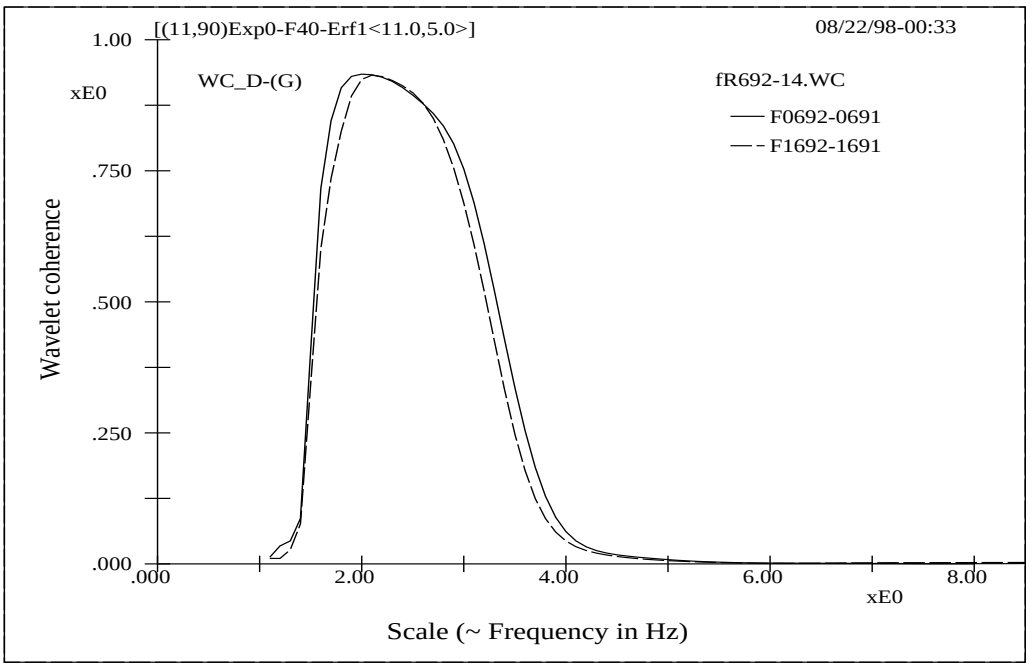

Fig 11.6 $(du \sim r, d_9)$ Rain's effects on wave-current coherence for aqueous flow measured at 9 cm below the mean water surface. Here the solid and dashed lines are without and with rain respectively (6.0 m s^{-1} wind speed and 68 mm s^{-1} rain intensity). It is seen that rain reduces the overall coherence in a deeper region.

providing the proper seeding for LDV measurements, burst rates for a few experiments are just two low to be significant. Figure 11.9 $(du_\rho \sim r, d, w)$ shows the two cases together with cases without the stratification and either with or without rain. The prominent feature induced by the stratification is associated with the enhancement of coherence at the low-frequency side. This suggests the enhanced coupling of low-frequency motions and indicates the possibility of energy transfer from surface waves to internal waves. At the high-frequency end, effects of stratification seems to depend on wind velocities. For high wind velocity, small scale waves are in a more developed state and internal breakdowns induced by the density gradient on high-frequency motions may be more significant, thus reducing the coherences between the aqueous flows and surface waves. As for cases under low wind velocity of 4.1 m s^{-1}, since energy contents of the whole system are generally only about one fourth to one third of those of high wind velocities, it is anticipated that the wave and aqueous flow fields are in a developing stage (as is also indicated by the

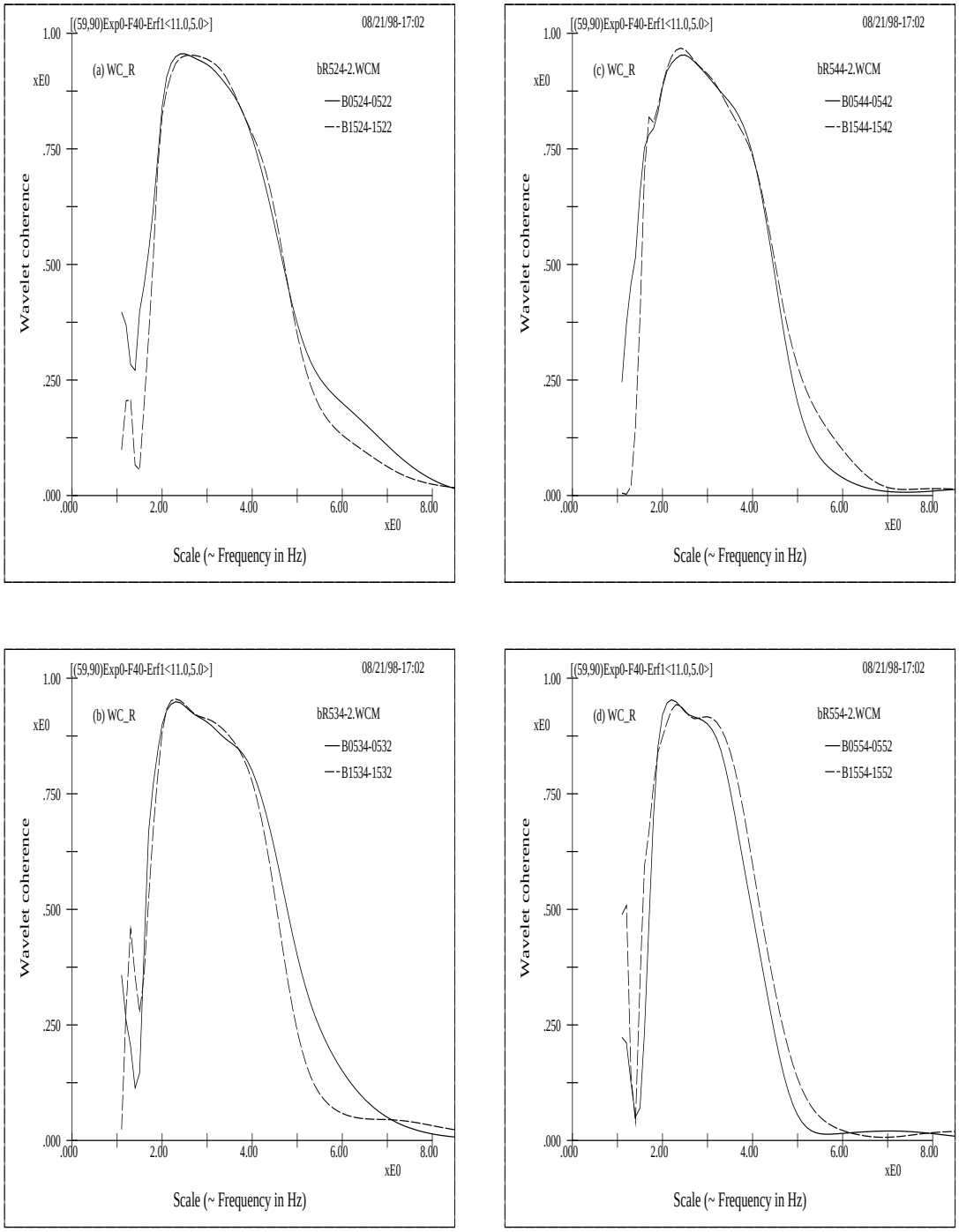

Fig 11.7 $(du \sim r, d, w_5)$ Wave-current coherences with (dashed lines) and without (solid lines) rain for various depths. The rain intensity is 68 mm hr^{-1}, wind velocity 5.1 m s^{-1}, and the aqueous flows are measured at 2 `(top left)`, 3 `(bottom left)`, 4 `(top right)`, and 5 `(bottom right)` cm below the mean water surface.

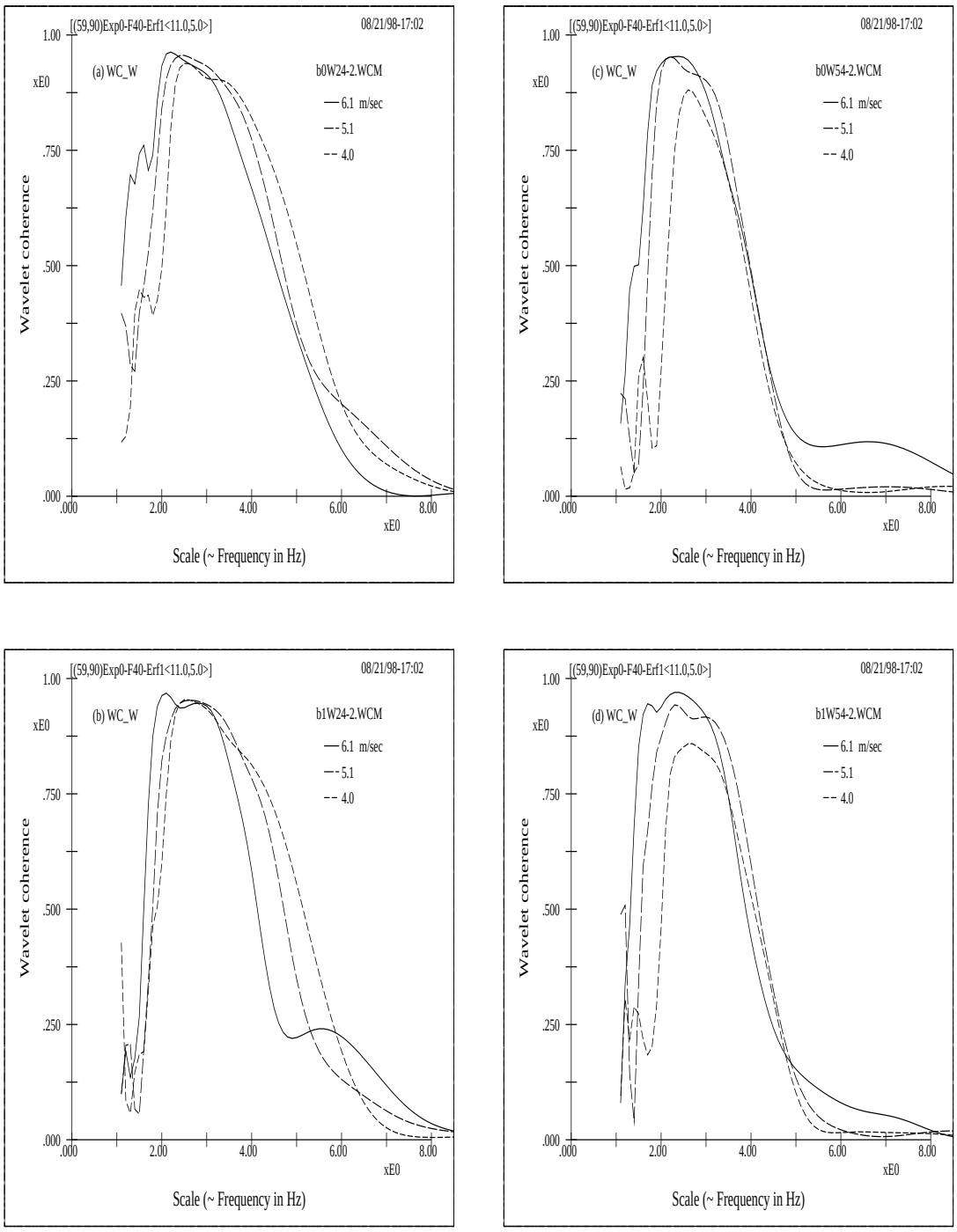

Fig 11.8 $(du \sim r, d, w)$ Wavelet coherences between waves and aqueous flows under different wind velocities without `(top)` and with `(bottom)` the rain (68 mm hr^{-1}) for aqueous flows measured at depths of 2 `(left)` and 5 `(right)` cm. Since under high wind velocities the wave and current fields are better developed or in a more mature stage, the peak coherence increases and shifts to a lower frequency.

relatively low coherence peak) and the energy phenomena between surface and internal wave interactions are not as significant as those at high wind velocities. Moreover, small scale disturbances associated with the breakdown of high-frequency internal waves are also less important due to a lack of energy input. Therefore, the surface wave mode is more significant than the internal wave mode; besides, the better stratification under low wind also imposes a stabling effects that increase the coherences of small scale motions.

11.2.2 Stokes wave cases

Coherent features of Stokes waves also provide a few interesting and informative accounts regarding the evolution of different scales within the coupling system. Figure 11.12 ($du \sim r, d$) shows the wave-current coherences under different rain intensities for Stokes waves having a fundamental harmonic at 1.4 Hz with a corresponding wave slope of 0.06. The fundamental harmonic frequency is estimated from the Fourier spectra of these Stokes waves. A typical spectrum is shown in Figure 11.10 (FS–Stokes). And the wave slope is estimated from the envelope curve of the extracted fundamental harmonic band as shown in Figure 11.11 (Wave Slope).

It is seen from the coherence curves that rain enhances and broadens wave-current coherences near the fundamental harmonic for aqueous flows measured at various depths. For the second harmonic, the coherence curves also broaden somewhat and shift to the right (except near the surface where rain-induced turbulences cause the coherence to drop). These tendencies clearly indicate that rain causes the diversification of scales for such relatively simple wave fields. And the phenomena agree with the argument that the impact of rain provides the impetus of interactions through the tuning and de-tuning of waves of different scales.

It should also be noted that, even for this quite stationary wave field, spectral coherences just do not behave any better than for the non-stationary one. Figure 11.13 ($du \sim r, d$ (F)) shows spectral coherence curves using the same data set as in Figure 11.12 ($du \sim r, d$). Once again, the identified wavelet analyzing function basis and its associated method of

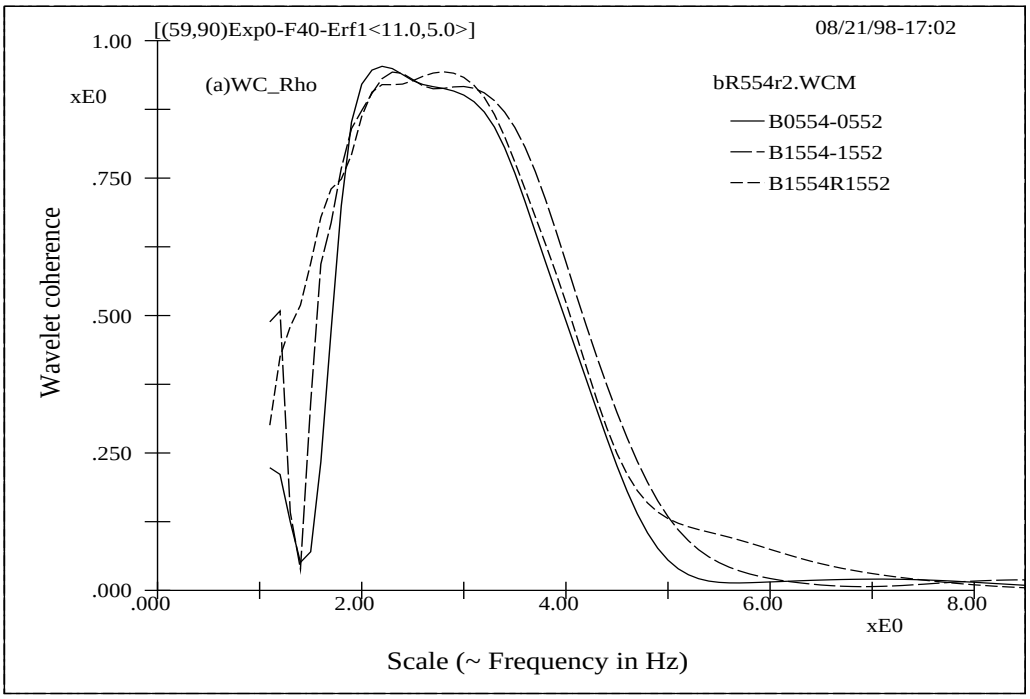

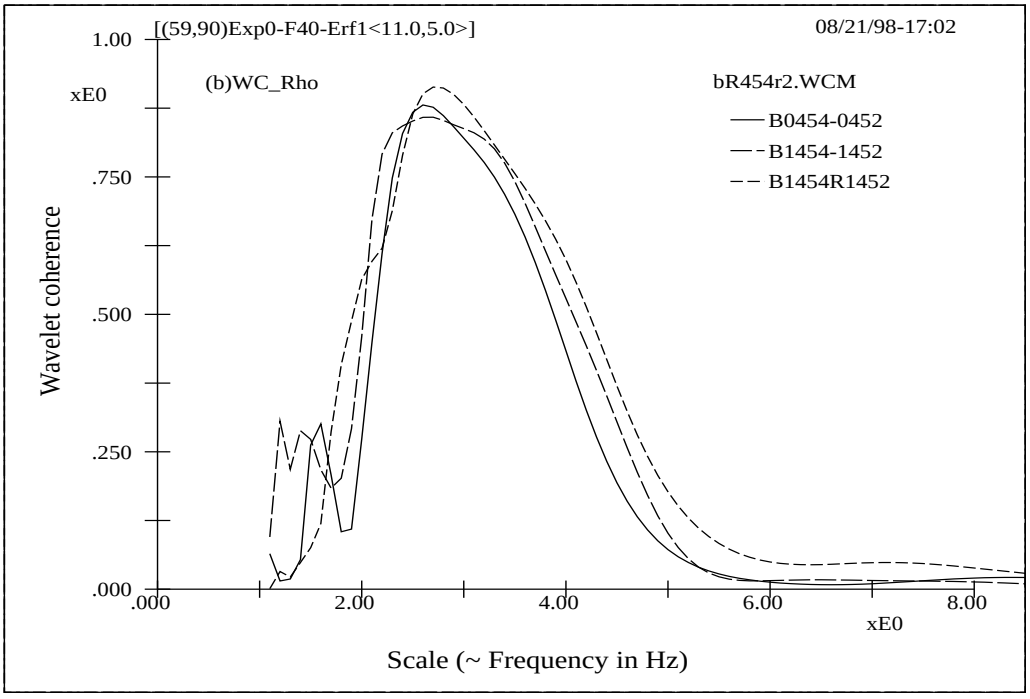

Fig 11.9 $(du_\rho \sim r, d, w)$ Effects of stratification on the wavelet coherences between waves and aqueous flows: The short dashed lines are the cases with rain and stratification; the solid and long dashed lines are the cases without stratification but, respectively, without and with rain (68 mm hr^{-1}). The top figure is for wind velocity of 5.1 m s^{-1} and the bottom for 4.0 m s^{-1}.

analysis are vindicated. And the various aforementioned factors leading to usefulness of applications are illuminated further. Most importantly, we are in a firmer position to believe that the wavelet viewpoint provides a better description of the innate physics for not only the non-stationary but also stationary signals; of course, this should formerly be attributed to the appropriateness of depicting waves as modulated wave forms that are akin to the intrinsic instability of water waves (Benjamin [12]; Benjamin and Feir [13]; Feir [21]; Whitham [73]; Yuen and Lake [77]; Lake and Yuen [30]; Lake et al. [32]; Lake and Yuen [31]; Longuet-Higgins [46, 47]; Stuart and DiPrima [65]; Su [66]; Melville [54, 53]; Hwang et al. [29]; Lee and Wu [39]).

The wave-current coherences for aqueous flows measured at different depths (2, 3, 4, and 5 cm below the mean water surface) for Stokes wave having a fundamental harmonic of 2.7 Hz with a high corresponding wave slope of 3.0 is shown in the right sub-figure of Figure 11.14 $(du \sim r, s)$ (the left shows those of the previous Stokes waves), and the top and bottom sub-figures are without and with the rain, respectively. For the right sub-figures, due to the high wave slope, the coherence for aqueous flows measured in the near-surface region is significantly lower than those measured in the deeper region. It is generally difficult to tell rain's effects on these coherence curves due to the high non-linear effects as a result of the Benjamin and Feir side-band instability (Lee and Wu [39]); the latter overshadows rain's effects. But still, two points need to be stated. First, we see again that the wavelet approach is able to discriminate the coherent levels at the frequency band of main energy content, where the values of spectral coherences are almost saturated to have the value of unity. Second, a significant feature due to rain for the high wave steepness case is the obvious increase of wave-current coherence at the low-frequency side for aqueous flow measured at the depth of 5 cm. Again, this indicates that rain causes the energy to propagate into the sub-surface region and is consistent with the previous results. Furthermore, since only internal waves have an effective mechanism to transfer energy in the vertical direction, this implies that there is a chance for the growth of internal waves in natural environments, where the stratification is almost always present; therefore, it is

anticipated that rain catalyzes the mechanisms of energy cascade.

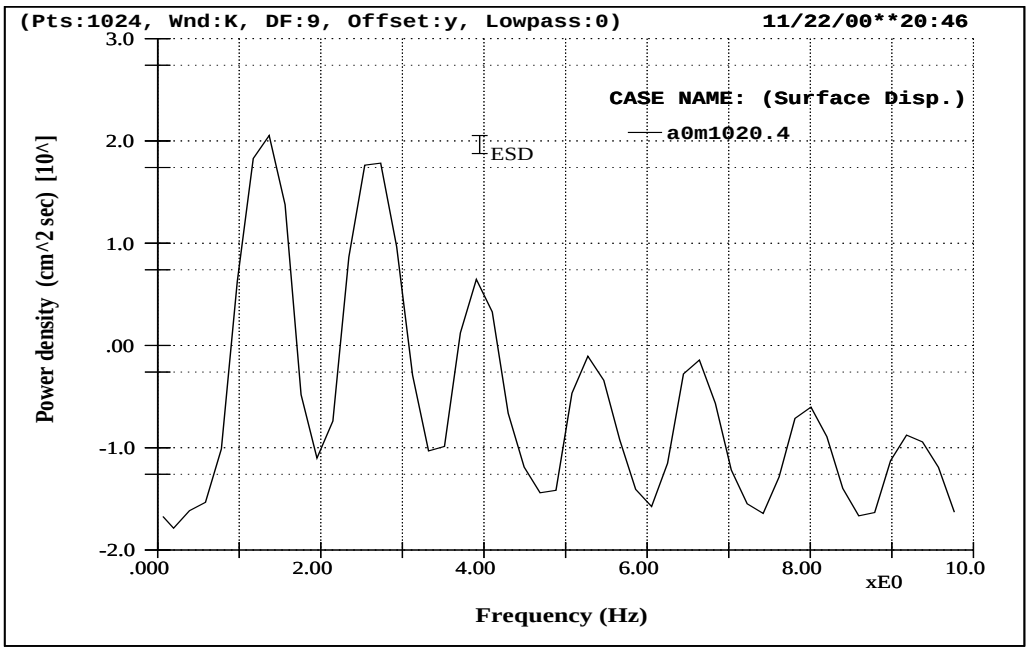

Fig 11.10 (FS–Stokes) A representative power spectrum for the Stokes waves with a fundamental harmonic at about 1.4 Hz. Its related wave-current coherences are shown in Figures 11.12 ($du \sim r, d$) and 11.13 ($du \sim r, d$ (F)).

11.2.3 Non-concurrent or displaced measurement cases

All the above figures focus on wave-current coherences; note that the wave and aqueous flows were measured simultaneously at nearly the same cross section right behind the raining segment. Let us examine coherences of a few different kinds where data are either not measured simultaneously or not at the same cross section, such as current-current coherences between different depths, or wave-wave coherences between different wave gauges, or wave-current coherences between measurements at different cross sections.

Figure 11.15 ($uu_U \sim r, d, w$) shows the wavelet coherences between aqueous flows measured at different depths with and without the rain for two different wind velocities. Here, aqueous flows are measured at a section right under the rain segment (70 cm ahead of the end of rain module). For cases without the rain the coherences are basically unimportant, and no obvious features can be told; however, with the input of rain, peculiar as well as

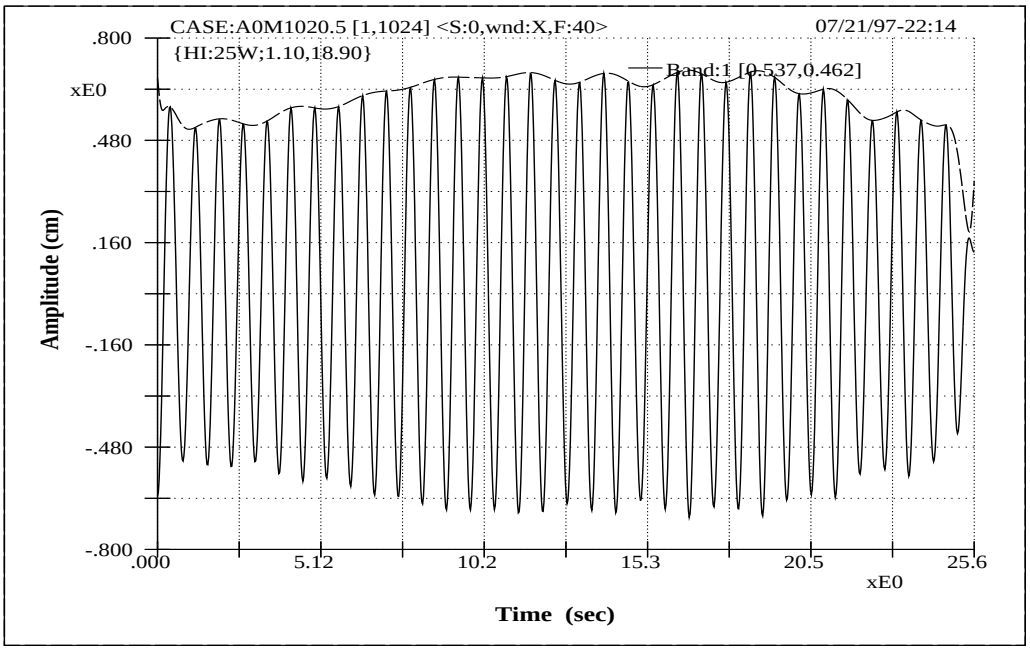

Fig 11.11 (Wave Slope) Amplitude modulation for the frequency band of fundamental harmonic of the Stokes wave shown in Figure 11.10 (FS–Stokes). Representative value of the wave slope is estimated from its envelope curve derived from the Hilbert transform method.

unambiguous features show up for both wind velocities. Two significant peaks are seen in each of the bottom sub-figures. These peaks correspond to the main frequencies of individual wind waves. There are two interesting points to note here: First, the general features of each individual curves are individually consistent for both wind velocities; second, relative tendencies of various curves follow the trends of their own wind velocities. In the figure we see that the coherences of aqueous flows at 3 and 4 cm depths are quite small; while the coherences for 4 and 5 cm and for 3 and 5 cm both have similar sharp peaks for both wind velocities. Contrasting to the above cases, let us examine the coherences for measurements taken at a cross section not directly under the raining segment (either with or without the rain). Interestingly, the features disappear, as shown in Figure 11.16 ($uu_D \sim r, d$). Overall, there are strong indications that the rain acts like a beating mechanism of tuning and de-tuning, and it therefore provides the impetuses of scale interactions and causes the development of waves of certain scales. These properties, coupled with buoyancy effects, support the arguments of surface waves and internal

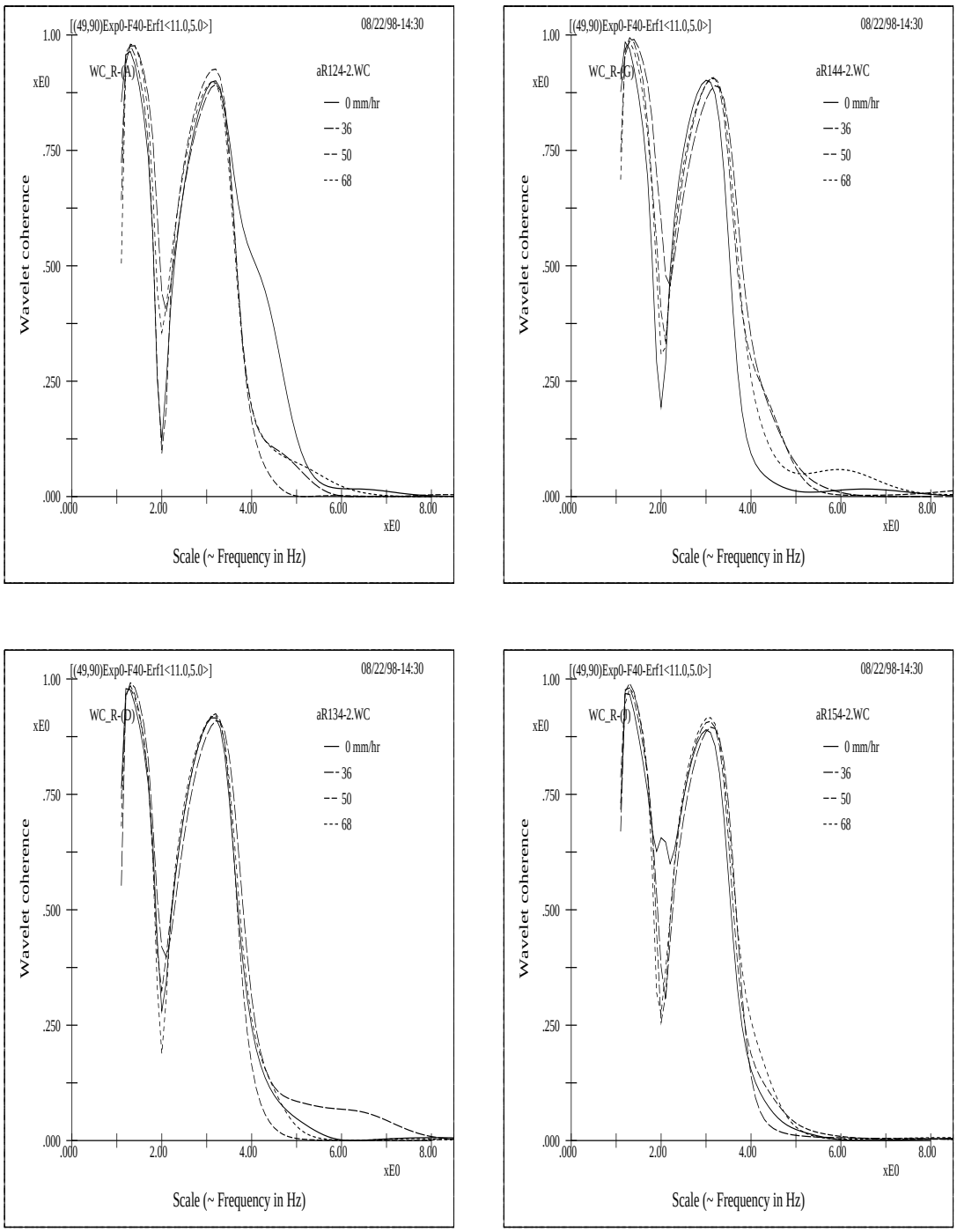

Fig 11.12 $(du \sim r, d)$ The wavelet coherences between waves and aqueous flows under different rain intensities for Stokes waves with a fundamental harmonic at 1.4 Hz and wave slope of 0.06. The aqueous flows were measured at 2 `(top left)`, 3 `(bottom left)`, 4 `(top right)`, and 5 `(bottom right)` cm below the mean water surface. A few effects due to rains are explained in the text.

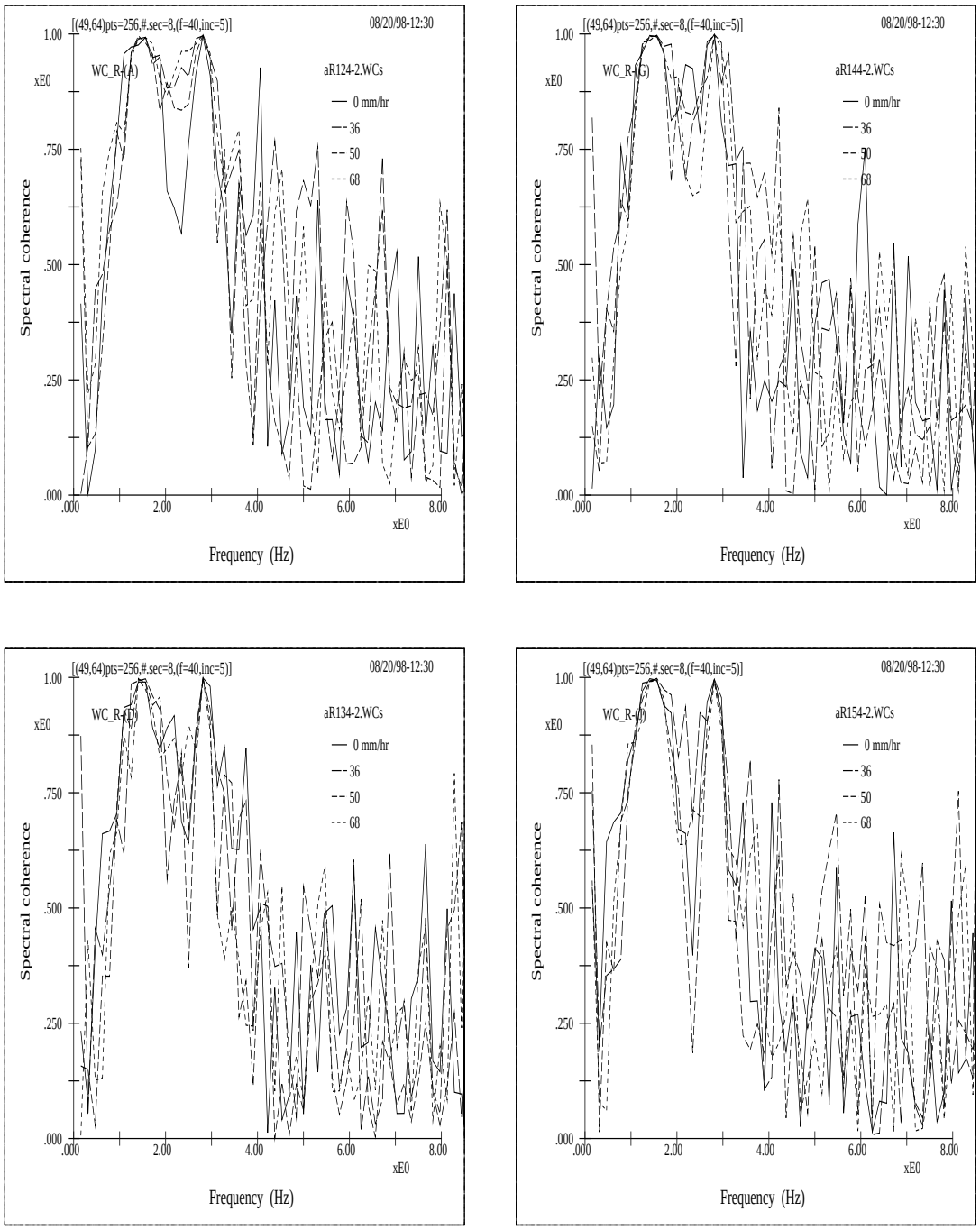

Fig 11.13 $(du \sim r, d\ (\mathrm{F}))$ Spectral coherences using the same data sets as in the previous figure. Note that even for such an extremely stationary condition the performance of spectral coherence is relatively poor. Together with the previous figure it can be concluded that a redundant system has far obvious advantages over an orthonormal one for studying the coherence statics. Most importantly, they point out that even for stationary signals the wavelet viewpoint can still provide better depictions of the intrinsic physics. This must be related to the appropriateness of the modulation descriptions of waves.

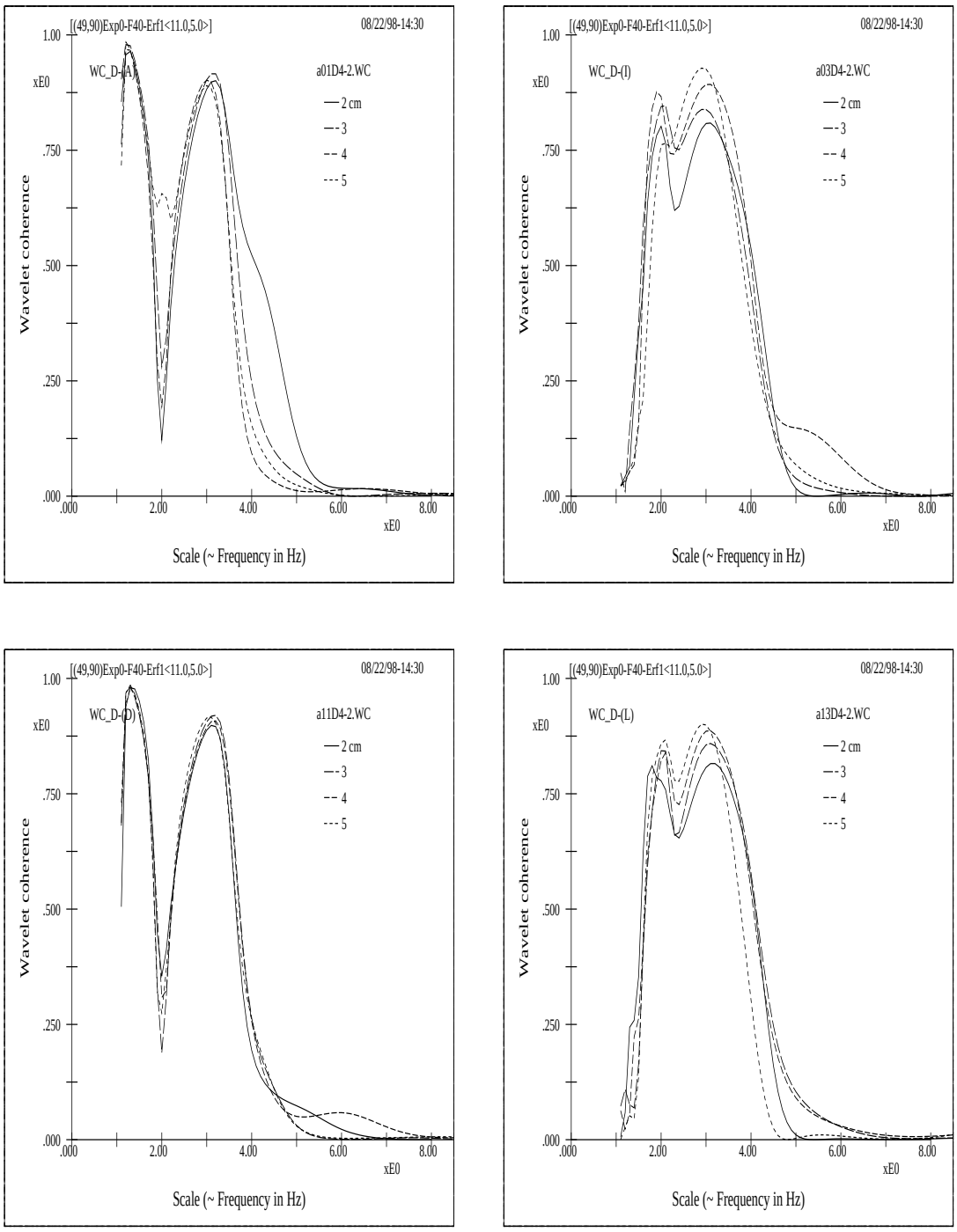

Fig 11.14 $(du \sim r, s)$ The wavelet coherences between waves and aqueous flows measured at the specified depth without (`top`) and with (`bottom`) 45 mm hr^{-1} rain for two groups of Stokes wave. Figures on the left are for Stokes waves with a 1.4 Hz fundamental harmonic (corresponding wave slope of 0.06) (`left`); figures on the right are for a 2.7 Hz fundamental harmonic (a high corresponding wave slope of 0.3) (`right`). The high wave slope significantly reduces the coherences near the surface regions.

waves interactions.

It is also noted that the coherences of these non-concurrent or displaced measurement cases are relatively very low when compared with those of simultaneous measurements. Moreover, as to coherences between displaced measurements we note that the wavelet approach is also in a much stronger position to provide various argumentive points than the Fourier approach can be. But results of displaced measurements somewhat lack a strong universal consistency, probably due to the rapid diminish of their identities as shown in figure 8.5 (ACC ~ ID).

As a final note: It seems that the high coherence peak for aqueous flows at 3 and 5 cm may be intuitively dubious since the coherences between 3 and 4 cm are low. But we argue that the endowment of such a thinking can have its ground only if the basis functions are orthogonal to each others such that they are mutually exclusive. However, the best wavelet basis functions in the continuous domain are non-orthogonal and quite redundant for all scales that exfoliate both within individual and neighboring scales. Nevertheless, we regard that such a situation implies the possible capability for the function basis to reverberate the ramifications or branching of water waves and to shed particular flow or penetration patterns due to impact of rain drops.

11.3 Summary

It is probably more than enough to provide so many figures just for showing the serviceability of the chosen function basis and its associated coherence method of analysis; nevertheless, these figures reveal many reasonable aspects of physics and justify the reasoning for the energy phenomena in the multi-scale coupling system concerning wind, wave, and rain interactions. Most profoundly, we are further convinced that waves, especially those in our wave tank, are intrinsically modulating and instability should be a common nature of water waves with even a slight nonlinearity. Therefore, the wavelet approach is a tactic with more natural perception for both non-stationary and stationary

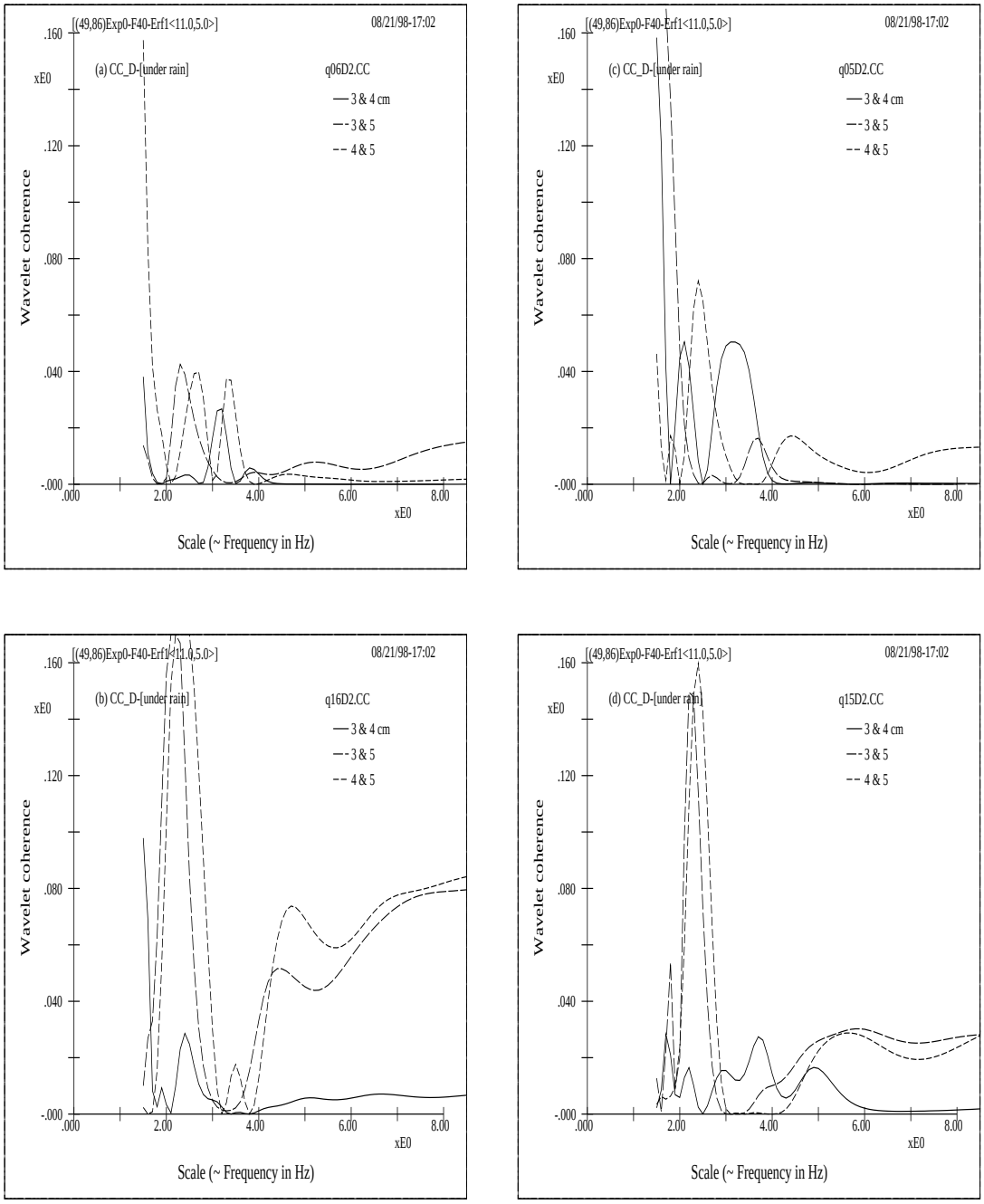

Fig 11.15 $(uu_U \sim r, d, w)$ The wavelet coherences between aqueous flows measured at different depths without (`top`) and with (`bottom`) the rain (68 mm hr^{-1}) under two different wind velocities of 6.0 (`left`) and 5.1 (`right`) m s^{-1}. Here, the measurement section is right under the raining segment. Since the aqueous flows were not measured simultaneously, the coherences are relatively low. However, the two significant peaks show unambiguous tendencies. The phenomenon here strongly indicates the tuning and detuning mechanism related to rain drop's beating effects as explained in the text. An additional point regarding the effects of the non-orthogonal wavelet constituents as opposed to the mutual exclusiveness of the orthogonal constituents is also stated in the text.

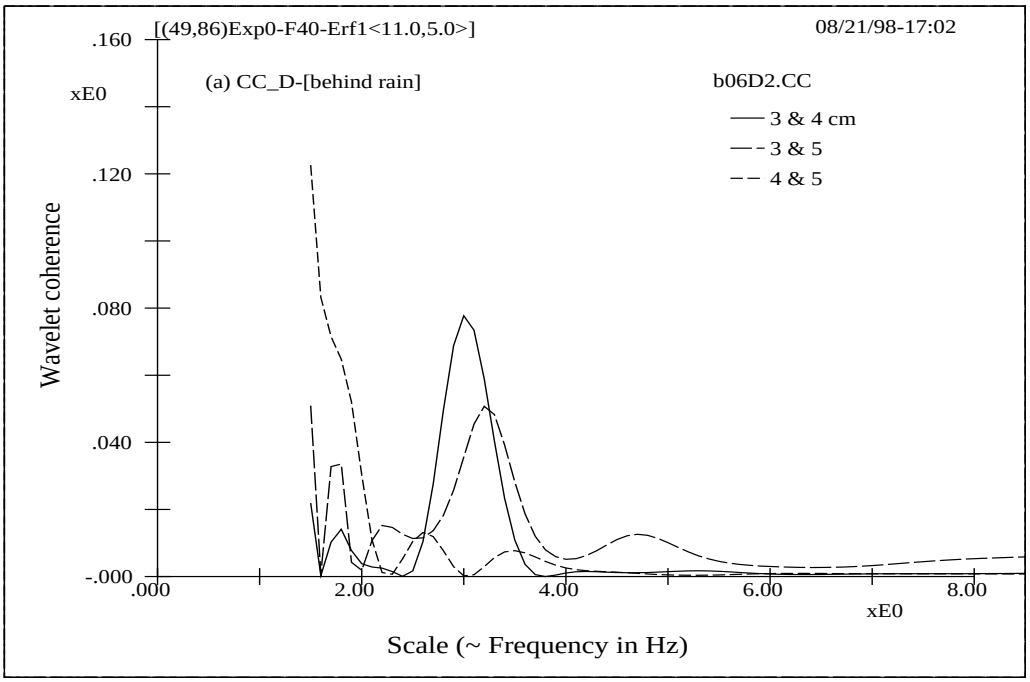

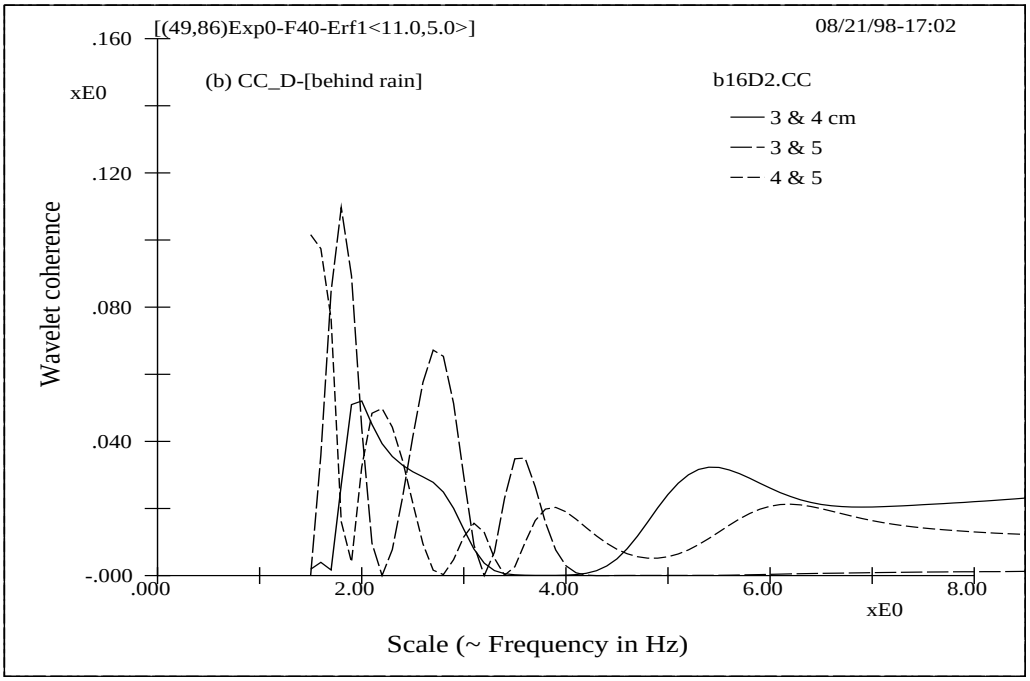

Fig 11.16 $(uu_D \sim r, d)$ The wavelet coherences between aqueous flows measured at different depths without `(top)` and with `(bottom)` the rain (68 mm hr^{-1}) under wind velocity of 6.0 m s^{-1}. Here, the measurement section is right behind the raining segment. Quite in contrast to the cases where measurements are taken right under the raining segment, the two peaks disappear and no trend is observed.

wave fields. Overall, experimental results, on the one hand, provide a practical validation for the numerical experiments regarding the optimum function basis; and, on the other hand, provide evidences of the physics concerning rain's effects on the damping of waves among the coupling scales, vis-à-vis, the energy cascade of the scale interaction among surface and internal waves. ❖

Chapter 12

A Wavelet Variant for Refined Ridge Extraction and Informative Physics

12.1 Introduction

As a spin-off of the present study on the best wavelet for water waves, a wavelet variant is proposed and characterized in this chapter. Although the wavelet variant may not be intimately related to the forms of water waves or the relevant kinetics, it has refined capability in the extraction of power ridge of signals and provides additional potentiality for the yielding of unseen physics. And these were discovered by chance due to a simple coding error that lingered initially in the program. The variant, though not strictly a wavelet as required by the admissibility condition, features the same analytical approach and numerical implementation as the continuous wavelet transform. It will be shown that the wavelet variant outperforms the Morlet wavelet in the extraction of power ridge, as well as in the provision of informative physics, both from the modulus and phase renditions of their transforms.

12.2 The wavelet variant and its modulus and phase renditions

For many wavelet analyses, the transforms concern only real basis functions. In such a sense, phase information may be of little concern in certain applications or in different fields. However, for water waves and time-frequency analyses, a complex function basis provides far more illuminating physics from either of its transform modulus or phase. Here the wavelet variant possesses the same important parameter as that of the Morlet wavelet, i.e., the carrier frequency that enables a "scale" to be a much more meaningful "frequency". And the wavelet variant has conceptually a "basis function" $\psi(t)$ defined as:

$$\psi(t) = \frac{1}{\pi^{\frac{1}{4}}} \left(\left[\mathrm{sgn}(t) \sin \omega_0 t - i \cos \omega_0 t \right] - e^{-\omega_0^2/2} \right) e^{\frac{-t^2}{2}}. \tag{12.1}$$

The function serves like a mother wavelet and seeds its function basis. In the equation, the ω_0 is the carrier frequency of the Morlet wavelet and it is also relevant to the modulation frequency of the counterpart Gabor transform (a modulated Gaussian or windowed Fourier transform); $\mathrm{sgn}(t)$ is the signum function; the time exponential stands for a Gaussian envelope; and, the constant term within the parenthesis serves for matching the counterpart constant in the Morlet wavelet representation and it is basically related to the requirement for a finitely supported signal. Figure 12.1 (BF–Variant) shows the real and imaginary parts of the quasi basis function. Here the "quasi" term is given in the sense that the basis may not be mathematically right for basis requirement. Considering both its analytical origin and the same numerical implementation, the "wavelet variant" is thus named. In fact, compared with the equation of the Morlet wavelet, the only difference is the presence of the signum function. Figure 12.2 (BF–Morlet) shows those of the Morlet wavelet.

The scaled and translated versions of the wavelet variant is:

$$\psi_{a,b}(t) = \frac{1}{\sqrt{a}\pi^{\frac{1}{4}}}\left[\operatorname{sgn}(t)\sin\frac{\omega_0\,(t-b)}{a} - i\cos\frac{\omega_0\,(t-b)}{a} - e^{-\omega_0^2/2}\right]e^{\frac{-\left(\frac{t-b}{a}\right)^2}{2}}, \quad (12.2)$$

where a is the scale parameter and b is the translation parameter. The $\frac{\omega_0}{a}$ physically means a carrier frequency and is the core target of the transform information. Note that the "frequency" or "scale" ordinate shown in all modulus and phase renditions in all the figures to be presented in this chapter represents exactly the values of this variable (i.e., scale-adjusted ω_0 or carrier frequency). Note again that many existing studies adopt the imperceivable scalar "a" in their presentations and analyses. A scalar is purely a number without a physical unit and it is both abstract and undiscerning.

For a lot of wavelet applications, the wavelet bases are real and thus yield only the modulus results (such as those listed in the earlier chapter concerning the discrete transforms related to orthogonal, bi-orthogonal, and semi-orthogonal wavelets, as well as the wavelet packets). Even for bases that are complex, different categories quite often place different or unequal weights on their modulus and phase renderings. In other words, modulus and phase renditions of a transform may provide different degrees of significance in feature identifications. And some transforms may yield trivial phase information. It will be shown that the present quasi basis function yields somewhat equally informative contents from both its modulus and phase renditions.

For the present approach our methodology may include additional unconventional thinking and we define the modulus and phase in the following ways.

Let $f(t)$ be a signal function, the modulus $\mathcal{M}$ of the transform coefficient is defined either as

$$\mathcal{M} = |\langle f(t), \mathbf{I_m}\psi(t)\rangle + i\mathcal{H}\left[\langle f(t), \mathbf{I_m}\psi(t)\rangle\right]|, \quad (12.3)$$

or

$$\mathcal{M} = |\langle f(t), \mathbf{R_e}\psi(t)\rangle + i\mathcal{H}\left[\langle f(t), \mathbf{R_e}\psi(t)\rangle\right]|, \quad (12.4)$$

where $\mathbf{R_e}$ and $\mathbf{I_m}$ represent real and imaginary part, respectively, $\langle , \rangle$ means the inner product, and $\mathcal{H}$ stands for the Hilbert transform. Note that the implementation of transform in either definition is based on only real or imaginary part alone. In this sense, the modulus may lack the mathematical formalism of a "basis", but here we first point out that the first definition gives basically the same result as Morlet wavelet's, while the second definition yields information that is especially useful in easy extraction of signal power ridges and that is also superior to what provided by the Morlet wavelet.

As to the phase $\mathcal{P}$ it is defined as

$$\mathcal{P} = \tan^{-1} \frac{\mathbf{R_e}\langle f(t), \psi(t)\rangle}{\mathbf{I_m}\langle f(t), \psi(t)\rangle} + \left(\frac{\pi}{2} \text{ or } 0\right), \tag{12.5}$$

or

$$\mathcal{P} = \tan^{-1} \frac{\mathbf{I_e}\langle f(t), \psi(t)\rangle}{\mathbf{R_m}\langle f(t), \psi(t)\rangle} + \left(\frac{\pi}{2} \text{ or } 0\right). \tag{12.6}$$

The difference of the two definitions and the presence of the optional constants will become clear when we come to show the transform planes of phase to be shown later. Basically the added constant reflects a phase rotation, and they can be used to switch the pattern of significant time-frequency features or to show easy visualizations in accord with either the power ridges of component signals or the time-frequency spreads of constituent components of a signal (or the spreads of basis functions).

Further explanations of the origins and implementations of these definitions will also be amended later. Topics of intrinsic nature related to time-frequency characterizations will also be discussed. One may also note that such details are more than practically needed — since if we are merely concerning the application of a basis, then simply the physical portrayals of modulus and phase suffice to tell all that matter. Nevertheless, one will come to realize that these additional efforts are desirable as well as forthright since we are making performance comparisons among different basis categories, in particular, the Morlet wavelet, the Gabor transform , or short-time Fourier transform, which have well established analytical exploitations. It is also hoped that by going through these

characterizations they enhance our deeper understanding of the intrinsic natures or inner workings of different types of function basis and provides prospects for further studies.

12.3 The analytics of complete oscillation and total positivity

A complex function basis provides frequency information and enables us to study amplitude and phase separately. However, there exists a deep concern about the existence of negative frequencies, as well as the interaction between amplitude and phase (or frequency) or the inter dependency between amplitude and frequency. Negative frequencies retard our perceptible realization. A common approach to get round the negative frequency is to perform an analytic procedure either on the function basis or on the signal. It is generally desirable that the basis functions should be as much analytic as possible.

Here let us point out three significant, as well as fundamental, concepts that connect "the analytic property" to "the complete oscillation and total positivity" as mentioned in an earlier chapter. First, the Fourier transform of the product of two functions (such as the product of a signal and a window function) is associated with an operation of linear convolution in the opposite paired domain; conversely, a convolution in one domain corresponds to a multiplication in the other domain. Therefore, if one can design a frequency window which localizes only in the positive frequency and then multiplies the spectral results of a signal with such a window then we might have the desired analytic signal. Second, since the frequency window must not extend to the negative frequency, its center should lie reasonably away from the zero frequency, i.e., the window distribution curve should decays properly fast toward the zero frequency. Third, for the Fourier transform pair, a shift in one domain is equivalent to an oscillation in the other domain. Combining the above three points we come to comprehend the relation between "being analytic" and "being with complete oscillation and total positivity". Overall, this can be stated as: to have a high analytic degree, the analyzing basis functions in the time domain should have

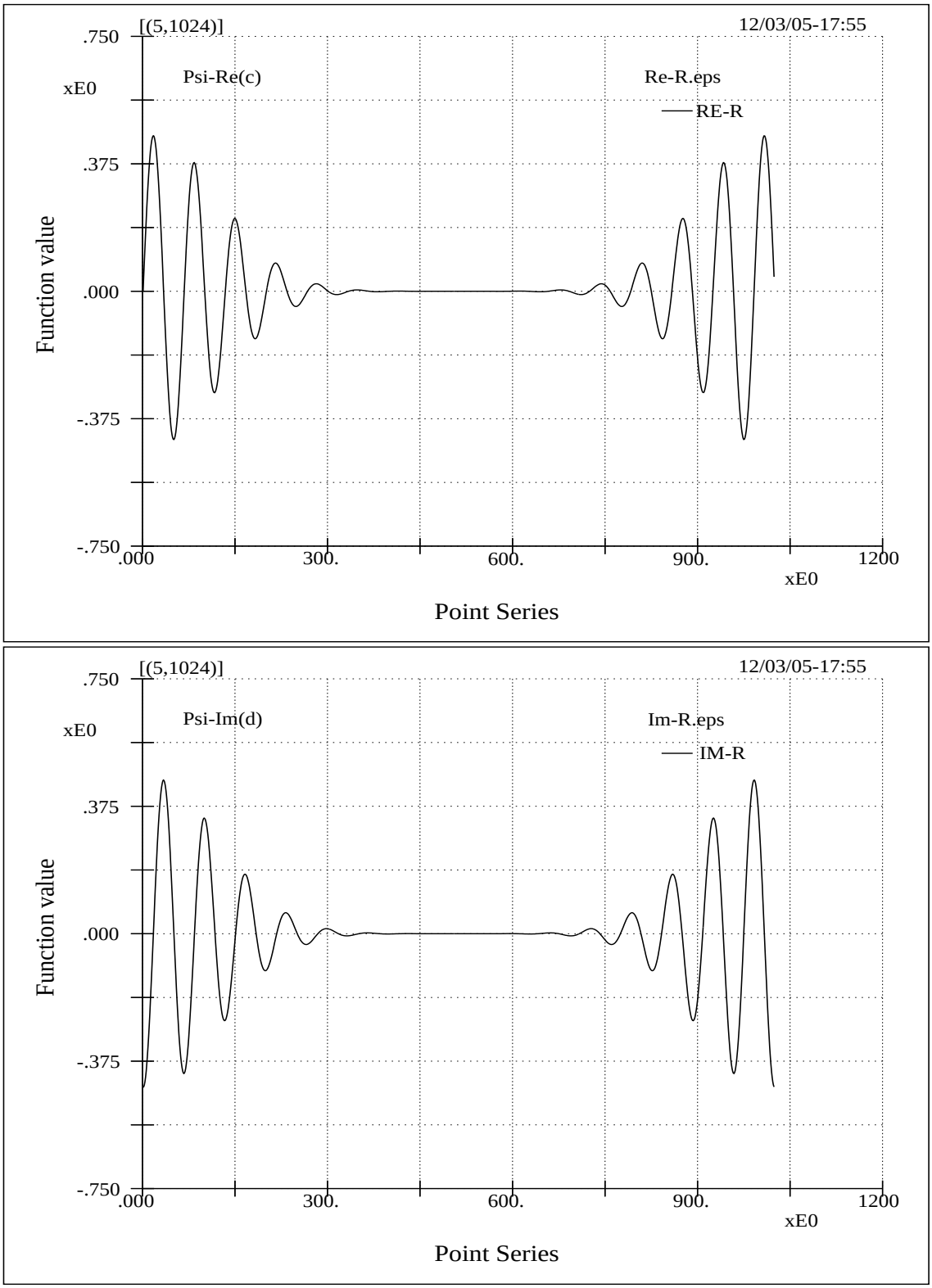

Fig 12.1 (BF–Variant) The real and imaginary parts of the wavelet variant for use in the time-frequency renditions of modulus and phase as defined by equations 12.3, 12.4, 12.5 and 12.6. Note the symmetry in both parts, as well as the utilizations of different renditions as compared to the normal form of transform associated with the Morlet wavelet.

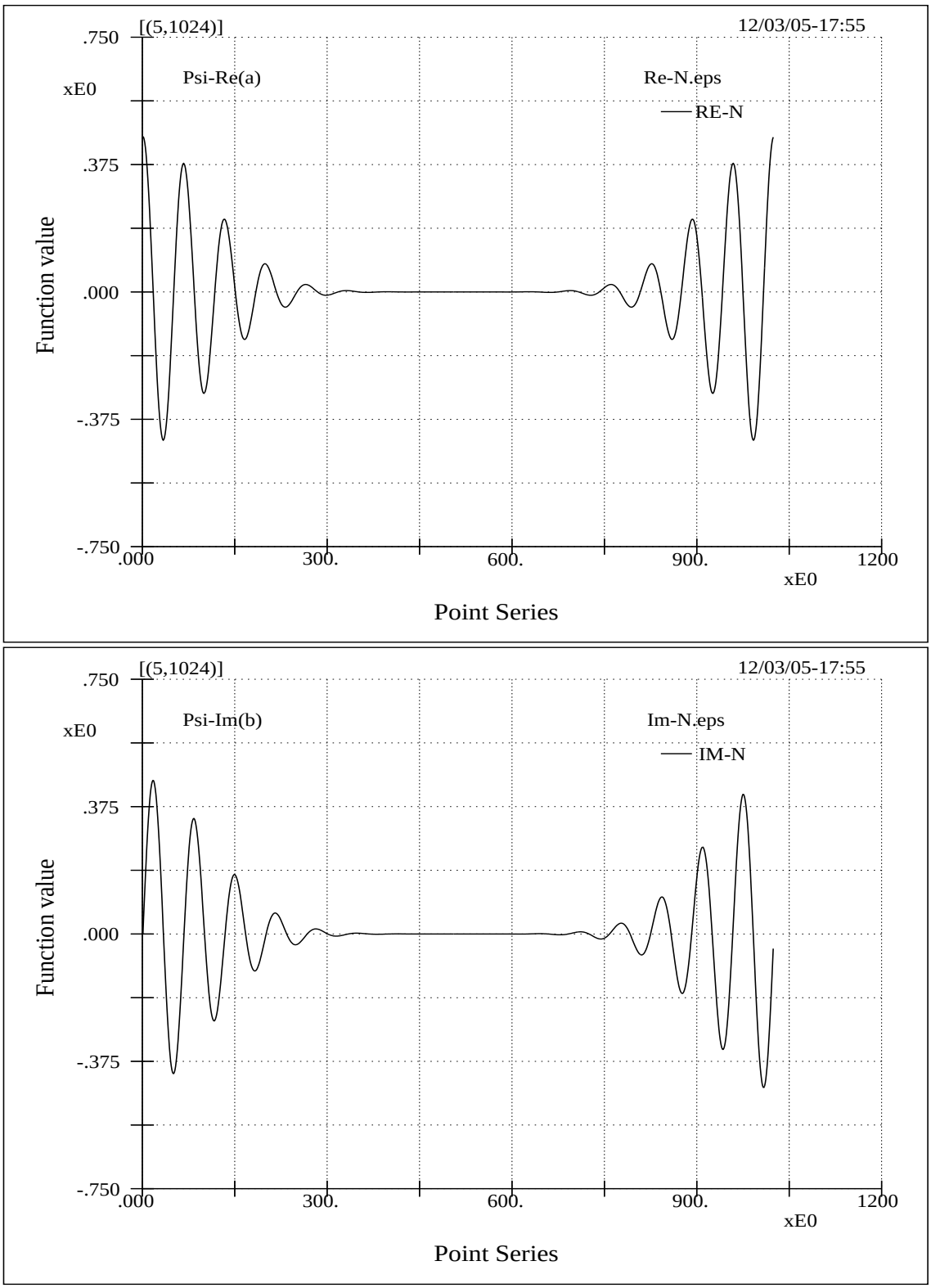

Fig 12.2 (BF–Morlet) The real and imaginary parts of the Morlet wavelet. Its modulus rendition is equivalent to the first definition of modulus (equation 12.3). The wavelet is a Gaussian style wavelet and it possesses an important parameter for intrinsic and perceptible physics, i.e., the carrier frequency, for various wave applications.

both reasonable oscillation and high regularity such that they are properly and narrowly band-limited in the frequency domain.

The above explanations lead to the basic and important understanding why the modulated Gaussian shape function, such as those of the Gabor function basis and the Morlet wavelet basis, are commonly adopted in analyses of water wave related signals — these basis have the highest possibility in revealing physically meaningful features from the conventional time-frequency viewpoint.

Talking about frequency, naturally, it is to be associated with the phase or the phase plane rendition. However, to the author's knowledge, the phase plane information of most transforms is quite often rampant and provides little physical interest. More precisely, it rarely provides easy identification of power ridges, i.e., it does not clearly show the instantaneous frequencies associated with the most significant wave components. Part of the reasons is – the phase (or frequency) should intuitively be more or less independent of amplitude, but in fact it is not – this is also the reason why a phase plane is always fully occupied no matter how insignificant the energy content of a region may be. Figure 12.3 (Deg-Ana) makes example such a feature. It should also be noted that for a lot of time-frequency analyses there is actually very sever interaction (or interference) between amplitude and frequency [17, 38]. And again, this factor brings rampant effects on the pattern of the phase plane.

Now let us state those relevant aspects for our devised basis function as depicted by equations 12.3 through 12.6.

First, concerning the modulus, though our definitions of time-frequency modulus plane involve the Hilbert transform, which is related to an analytic process, the analyzing functions are not necessary analytic. Specifically, equation 12.3 is almost analytic and yields nearly the same results as those of Morlet wavelet. In such cases, the instantaneous frequencies corresponding to the significant constituent components are associated with the ridges of the modulus distribution, i.e., the distribution of local energy peak. As to equation 12.4, it is less analytic; nevertheless, we shall show that it provides a new and

improved way for ridge extraction. Furthermore, while the instantaneous frequencies of significant constituent components as depicted by equation 12.3 are associated with the power maxima, those as depicted by equation 12.4 are associated with modulus minima, i.e., local power trough.

Second, concerning the phase, even though the time-frequency phase plane as depicted by equation 12.5 or 12.6 is completely filled with phase values, the equations yield completely different, as well as much regular and informative, patterns as compared to those yielded by other transforms. Specifically, the phase distribution based on the Morlet wavelet transform varies so extremely such that it hardly shows any features of practical significance; in sharp contrast, our phase rendition yields almost polarized phase distribution where significant features are revealed by phase interfaces where the neighboring phases are mostly out of phase by convenient separation distances (such as $\pi/2$, π, $3\pi/2$ or 2π). Furthermore, the phase interface lines may represent either the power ridges or the time and frequency spreads of non-orthonormal basis functions.

12.4 Concepts of stationary phase, instantaneous frequency, and power ridge

In this section we further study the relationships among instantaneous frequency, stationary phase, ridge, and trough concerning the proposed transform.

Let $g(t)$ be a window function in t domain, and $g(t)$ is centered around $t = 0$ and has unit norm with reasonable decay on its support, i.e., $\widehat{g}(0) = \int_{-\infty}^{\infty} g(t)dt$ is the maximum value of $\widehat{g}(\omega)$ and is of the order of 1 For the window function, the windowed Fourier atom is

$$g_{u,\xi}(t) = g(t)e^{i\theta}. \tag{12.7}$$

The Fourier atom scaled by s is

$$g_{s,u,\xi}(t) = g_s(t)e^{i\theta_s}, \tag{12.8}$$

where subscripts u and ξ stand for translation and scaling parameters, and $g_s = \frac{1}{\sqrt{s}}g(\frac{t}{s})$ has a support of $g(t)$'s scaled by size s and is also with unit norm.

The scaled windowed Fourier transform of a real function $f(t)$ is

$$\langle f, g_{s,u,\xi}\rangle = \int_{-\infty}^{\infty} f(t)g_s(t-u)e^{-i\xi t}dt. \tag{12.9}$$

Basically, this equation provides what equation 12.3 does. And it is also similar to the Morlet wavelet transform using the simplified form by neglecting its second term.

Since any $f(t)$ can always be expressed as $f = a(t)\cos\phi(t)$, one has [67, 49]

$$\langle f, g_{s,u,\xi}\rangle = \frac{\sqrt{s}}{2}a(u)e^{i(\phi(u)-\xi u)}\left(\widehat{g}\left(s[\xi-\phi^{'}(u)]\right)+\epsilon(u,\xi)\right), \tag{12.10}$$

in which the ϵ is an overall corrective term determined by the following four elements:

- The relative variation of amplitude: $\epsilon_{a,1} \leq \frac{s|a^{'}(u)|}{|a(u)|}$;
- The relative curvature of amplitude: $\epsilon_{a,2} \leq \sup\frac{s^2|a^{''}(u)|}{|a(u)|}$;
- The rate of variation of frequency : $\epsilon_{\phi,2} \leq \sup\left[s^2|\phi^{''}(t)|\right]$; and
- The effects caused by the high frequency components of the window function, i.e., the extreme of the high end part of $|\widehat{g}(\omega)|$: $\epsilon_g = \sup_{|\omega|\geq s\phi^{'}(u)|}|\widehat{g}(\omega)|$

Now let us state a few definitions. The instantaneous frequency (or, simply, the frequency) is generally defined as the time derivative of phase. And the stationary phase is for

$$\phi(u) - \xi u = 0 \tag{12.11}$$

or

$$\xi - \phi'(u) = 0 \tag{12.12}$$

It is therefore known that the stationary phase points are where the ridge locates. But one must also keep in mind that the $f(t)$ (which can be viewed as a single component or combination of components) needs to fulfill the several restrains about ϵ. In a practical sense, the $f(t)$ should be relatively smooth and regular.

Although the above $f(t)$ is the target function rather than a basis function, we should be able to extend these arguments to the case where the $f(t)$ and $g(t)$ switch their roles – judging from the fact that various time-frequency (or time-scale) transforms are simply implementing a projection mechanism. In fact the scaled Fourier atom $g_{s,u,\xi}(t) = g_s(t)e^{i\theta}$ well follows all such requirements. Overall here we clearly illustrate analytically the uses of "complete oscillation and total positivity" and its relationship with the extraction of ridge.

Now let us discuss the analytic degree as related to equation 12.3.

Here we exploit the difference between $\langle f(t), \mathcal{A}[\psi]\rangle$ and $\langle f(t), \psi\rangle$, where $\psi(t)$ is based on equation 12.3, $\mathcal{A}$ means finding the analytic counterpart, and the simulated signal $f(t)$ is an X-signal (a signal composed of two linear chirps with a cross in frequencies).

The top sub-figure of figure 12.3 (Deg-Ana) shows how analytic the basis is – there is basically no energy distribution except at the top area of high frequency.

In the above description we illustrate the relation between ridge and stationary phase points, and we know there is a strong possibility that the two might not be completely coincided. Now let us discuss the corresponding points as will be depicted by equation 12.4 to the ridge points or the stationary phase points as depicted by equation 12.3. And this is done numerically using the Mathematica programming language. It is calculated that the frequencies at the trough points is equal to $\frac{1}{0.969621}$ the values of the ridge points associated with stationary phase points. Here the ω_0 is taken as the commonly adopted value of 5, but different reasonable ω_0 yield values little different from 0.9696. It is also

noted that in all subsequent figures in comparison the values of parameter ω_0 (which may take an adapted value to better fit the physics, such as wave's decay property) are the same.

For equation 12.4, since the corresponding basis function lacks the property of complete oscillation and is poorly analytic, we take a different approach in modulus representation: first, the transform is performed only on the real part of equation 12.1, then the analytic signal procedure is applied to that transform result, and finally the envelope curve of the modulus is calculated accordingly.

In the following section we will focus on the analytic signal procedure. And this basically deals with the Hilbert transform.

As to phase plane information different designs arise different constructs. The one adopted here follows the most commonly approach. Let suppose we have a real function basis, then we have two ways to derive the phases. One way is to devise an analytic function basis with real and imaginary parts as oppose to a basis with real functions only. The other way is to first convert the real signal into an analytic counterpart signal and then apply the transform of the real function basis. It can be shown that the two approaches yield the same results (see e.g., [49]). For equation 12.3, this is what is performed. But for equation 12.4, the complex basis is directly used.

12.5 The analytic signal procedure and the Hilbert transform

Having stated the usefulness of an analytic signal or analytic function basis in power ridge extraction in association with the Gabor transform and the Morlet wavelet transform, we now work on the contents of such a procedure that aims at finding the analytic counterpart of a function. It will be clear that such a procedure inherently involves the Hilbert transform.

Another direct relevance of this section to the present study lies on the use of the

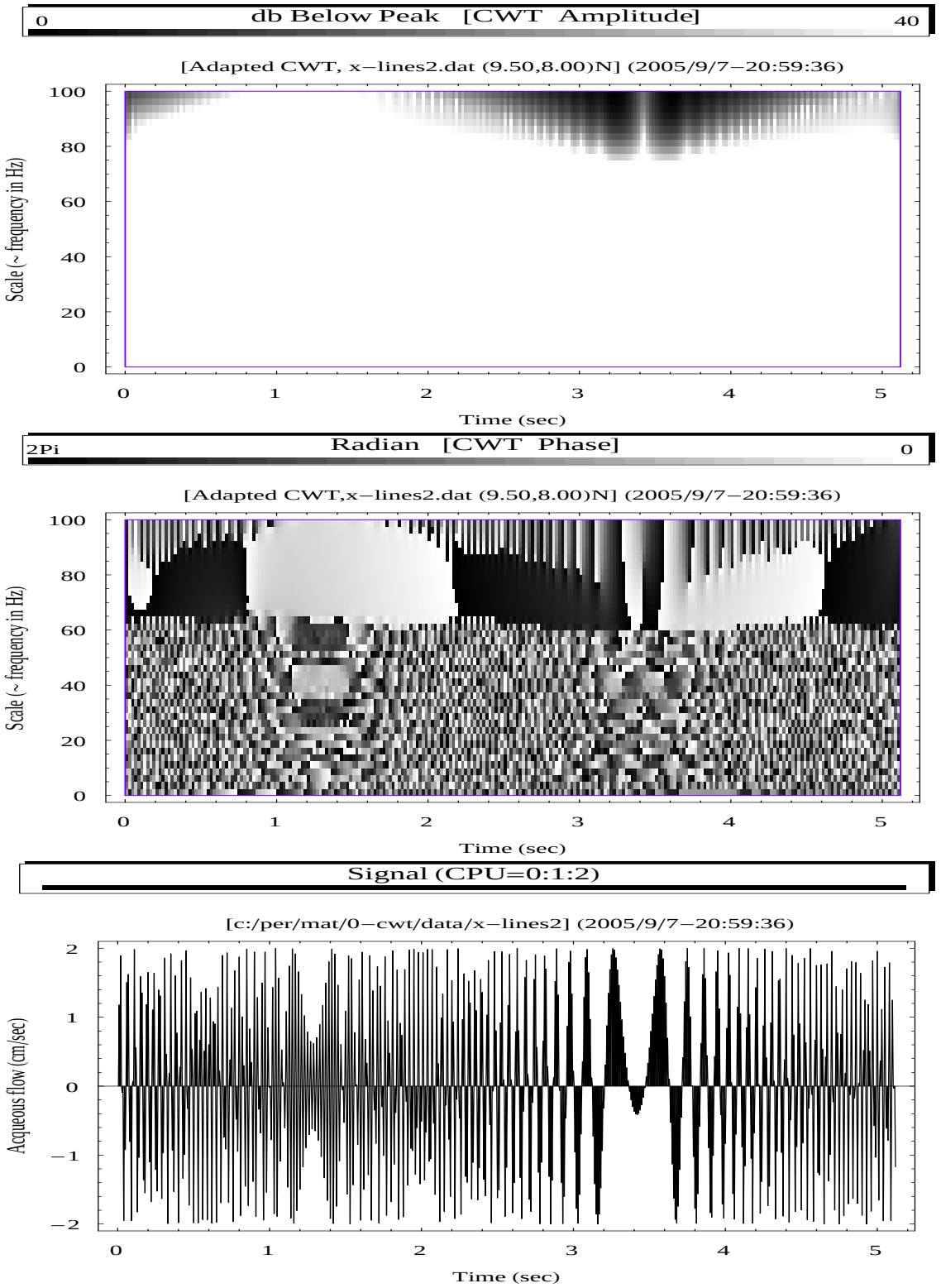

Fig 12.3 (Deg-Ana) This figure shows the analytic degree of ψ related to equation 12.3. The top sub-figure shows the power (modulus squared) of the difference between $\langle f(t), \mathcal{A}[\psi]\rangle$ and $\langle f(t), \psi\rangle$, where $\mathcal{A}$ means the analytic counterpart. The mid sub-figure shows the corresponding phase. Here $f(t)$ is an X-signal composed of two linear chirps as given in the bottom sub-figure (see also figure 12.15 (C-XS)).

Hilbert transform in equations 12.3 and 12.4, even though the perspective now is not on the relation between instantaneous frequency and the ridge point – since neither the quasi-wavelet meets the basic assumption of being a well band-limited function (as is the case for a Gaussian wavelet) nor its analytic form is provided. Therefore, it warrants for us to work through the details that lead to a very easy implementation of the Hilbert transform. This also helps to illustrate possible difficulties or uncertainties that quite often induce paradoxes due to non-conformance to the constraints listed earlier.

Let a real signal be $f_r(t)$ and its sensible imaginary counterpart be $f_i(t)$. The real and imaginary parts form a complex signal $z(t)$. A complex function allows us to define its amplitude (or modulus) function $a(t)$ and phase function $\phi(t)$ of a complex exponential. The derivative of the phase yields the natural definition of instantaneous frequency (or local wavenumber in spatial domain) $\omega_i(t)$. The simple mathematical form is

$$z(t) = f_r(t) + if_i(t) = a(t)e^{i\phi(t)}, \tag{12.13}$$

with

$$\omega_i(t) = \phi'(t). \tag{12.14}$$

The main concern here is what is the sensible imaginary part since its choice affects our exploitation of instantaneous frequency. It is appropriate to point out that in the realm of signal analysis most researchers still view the instantaneous frequency as merely a primitive concept rather than a question of mathematical definition. That is to say, the proper definition of the complex signal is still regarded as an open question [17], and the issues are, at best, whether a particular definition can match our intuitive thinking; whether its results can provide adequate explanations for the physics that might be of our own logical reasoning only; or whether the intuitive assumptions induce additional concerns which might be counterintuitive and possibly bring us to new discoveries.

Since any real signal $f_r(t)$ can be expressed as

$$f_r(t) = a(t)\cos\phi(t), \tag{12.15}$$

the most intuitive realization of the complex signal $z(t)$ should be

$$z(t) = a(t)e^{i\phi(t)}. \tag{12.16}$$

Nevertheless, there are infinitely many ways to devise such a complex form. This reflects the openness of the definition of the instantaneous frequency.

In 1946 Gabor [24] proposed a definition for the complex signal that is unique for any real signal and his method is generally referred as the analytic signal procedure.

Let $F_r(\omega)$ be the Fourier transform of $f_r(t)$, the corresponding analytic signal Gabor introduced is,

$$z(t) \;=\; 2\frac{1}{\sqrt{2\pi}}\int_0^\infty F_r(\omega)e^{i\omega t}d\omega, \tag{12.17}$$

where the factor 2 is introduced so that the real part of the complex signal is equal to the original signal. As is clear from the basic properties of Fourier transform, $z(t)$ must be complex and is the inverse Fourier transform of a single-sided spectrum, which drops the negative frequency components but keeps the same positive spectral components as those of $F_r(\omega)$. Obviously, when the Fourier transform is applied to $z(t)$ again one gets only positive frequency constituents.

Next we illustrate how such a simple complex function can be used to calculate the Hilbert transform of $f_r(t)$. And, in fact, the Hilbert transform is the imaginary part of $z(t)$.

That is to say, we should verify the following identity [17]:

$$z(t) = f_r(t) + i\frac{1}{\pi}\mathcal{P}\int_{-\infty}^{\infty}\frac{f_r(\tau)}{t-\tau}d\tau, \tag{12.18}$$

in which the Hilbert transform of the signal, $\mathcal{H}[f_r(t)]$ is

$$\mathcal{H}[f_r(t)] = \widetilde{f_r(t)} = \frac{1}{\pi}\mathcal{P}\int_{-\infty}^{\infty}\frac{f_r(\tau)}{t-\tau}d\tau. \tag{12.19}$$

In the equation the symbol $\mathcal{P}$ means that the integration is carried out based on the rule of Cauchy principal value, i.e.,

$$\mathcal{P}\int = \lim_{\epsilon_1=\epsilon_2\to 0}\left(\int_{-\infty}^{t-\epsilon_1} + \int_{t+\epsilon_2}^{\infty}\right). \tag{12.20}$$

Let

$$g(t) = \frac{1}{t}, \tag{12.21}$$

then the Hilbert transform is simply the convolution of $f_r(t)$ and $g(t)$, i.e.,

$$\widetilde{f_r(t)} = \frac{1}{\pi}(f_r \star g)(t). \tag{12.22}$$

By the Fourier duality property, the Fourier transform of the convolution is

$$\mathcal{F}[\widetilde{f_r(t)}] = \widehat{H}(\omega) = \frac{1}{\pi}F_r(\omega)G(\omega). \tag{12.23}$$

Now with $F_r(\omega)$ and $G(\omega)$ being separated the Cauchy principal value operation is related to $g(t)$ only. And the Fourier transform of g is

$$\begin{aligned}\mathcal{F}[g(t)] = G(\omega) = \mathcal{P}\int_{-\infty}^{\infty}\frac{e^{-i\omega t}}{t}dt = \\ \mathcal{P}\int_{-\infty}^{\infty}\frac{\cos(\omega t)}{t}dt - i\int_{-\infty}^{\infty}\frac{\sin(\omega t)}{t}dt.\end{aligned} \tag{12.24}$$

Since the integrant associated with the real part of this equation is antisymmetry the Cauchy principal value integration of this part is zero. As to the integration of the imaginary part, since $\frac{\sin(\omega x)}{x}$ is finite for all values of x, including $x = 0$, there is no need of the principal value sign. Of this part, the integrant is symmetrical; therefore, only half of the

integration needs to be considered, and through a change of variable one gets

$$\int_0^\infty \frac{\sin \omega x}{x} dx = \mathrm{sgn}(\omega) \int_0^\infty \frac{\sin u}{u} du. \tag{12.25}$$

Here one basically know that $G(\omega)$ does not depend on the variation of ω since the integration is independent of ω. Though this integral looks simple, its integration should not be treated as a trivial process; rather, a closed form of the integration can be derived through the use the residue theorem of integration from the complex integral calculus (see for example the well written textbook by Greenberg [26]). The final result is a simple relation which only depends on the sign of ω:

$$G(\omega) = \begin{cases} -i\pi\,\mathrm{sgn}(\omega) & \omega \neq 0 \\ 0 & \omega = 0. \end{cases} \tag{12.26}$$

Accordingly, the Fourier transform of the analytic signal $\mathcal{A}[f_r(t)]$ is

$$\mathcal{F}[\mathcal{A}[f(t)]] = F_r(\omega) + i\mathcal{F}[\mathcal{H}[f_r(t)]](\omega) = \begin{cases} 2F_r(\omega) & \omega > 0 \\ 0 & \omega \leq 0. \end{cases} \tag{12.27}$$

Here we see that this equation matches exactly with equations 12.17 and 12.18 combined. And it further yields

$$\widehat{H}(\omega) = \begin{cases} -i\,F(\omega) & \omega > 0 \\ i\,F(\omega) & \omega \leq 0. \end{cases} \tag{12.28}$$

Making use of this relation the Hilbert transform is easily implemented by a simple word (subroutine) in ASYST language as is shown in Table 12.1 (HT-Asyst).

Detail manipulation of the analytic signal approach is given here not merely for its analytical interest, but rather to disclose its intrinsic nature in association with the Fourier transform properties. An alternative approach implemented in the time domain based on Parks-McClellan minimax algorithm was given in an earlier report on characterizing the amplitude and frequency modulations of water waves measured in laboratory wave

tank experiments [36]. In which trade-offs between the two implementations were also illustrated.

As is also indicated in the program one needs to exercise cautions related to non-stationary effects since the basic tactic is related to several simple processes that only manipulate the contents of the FFT of the input signal. And, additionally, we must also acknowledge that the standard deviation of a spectrum is rather significant and its refinement is quite demanding concerning the amount of data points needed.

Overall, here we further illustrate that the ridge algorithm of a Gabor type wavelet transform is only true when the various restraints listed in section 12.4 are obeyed. In analytical term, if we regard the inner product of the transform of equation 12.10 as a linear operator $\mathcal{L}$, then $\mathcal{L}$ must be of a weak continuity, i.e., $\mathcal{L}f(t)$ is modified by a small amount if $f(t)$ is only slightly modified. Thorough numerical experiments on this using laboratory wave data fully support these arguments.

In reality, the above elaborations further manifest an important realization: Due to the fact that the operations associated with orthonormal transforms or any transform that emphasizes efficiency are not in weak form, these function bases just do not provide as much informative physics as what can be provided by the continuous wavelet transform using the Morlet wavelet – Redundancy is sometimes quite helpful [51].

Let us recap the scheme for the definition of equation 12.4. Rather than converting the signal into its analytic counterpart and then projecting it into a real wavelet basis (or rather than directly projecting the real signal into an analytic wavelet basis), the signal is first projected into the real part of the wavelet basis and then the analytic signal procedure is applied to the transform coefficients. In this way the time-frequency power density distribution is obtained as the envelop of the real part wavelet coefficients, i.e., the modulus of the complex transform coefficients.

Tab 12.1 (HT-Asyst) An ASYST word (equivalently, a subroutine in some computer languages) that performs the Hilbert transform of a signal. The word takes a one dimensional array as the input argument. As seen from the programming, the basic tactic is related to several processes that manipulate the contents of the FFT of the input signal. Owing to these manipulations, the analytical procedure endows many properties that are intrinsic to FFT.

```
\ ------------------------------------------------------------------------
\  A small program piece which finds the imaginary part of a real signal
\     based on the analytic signal procedure.
\  The computation makes use of the final results of complex calculus based
\     on Cauchy principal value integration.
\  The length of the input array will be automatically truncated to the
\     maximum allowable power of 2.
\ ------------------------------------------------------------------------
: my.hilbert
  fft   []size   n.fft.pts  :=
  dup   becomes>  t1

  dup   sub[ 1 , n.fft.pts  2  /  ]
  0     +1     z=x+iy   *
  t1    sub[ 1 , n.fft.pts  2  /  ]  :=

        sub[ n.fft.pts  2  /  1 +   ,  n.fft.pts  2 / ]
  0     -1     z=x+iy   *
  t1    sub[ n.fft.pts  2  /  1 +   ,  n.fft.pts  2 / ]  :=

  t1    ifft
  zreal
;
\ ------------------------------------------------------------------------
```

12.6 Characterizations of frequency leakages and phase ambiguities

The concept of time-frequency resolution basically manifests the principal of Heisenberg uncertainty. In plain language, this is to say that, since any function can not be finitely supported both in time and frequency domains, the signal – no matter how simple it is – must occupy a finite area in the time-frequency plane and there exists no point-distribution whatsoever. Hence there comes the term resolution. For a basis function, the time-frequency resolution measures its spreads in both time and frequency. And the spreads are generally taken as the second central moments in time and frequency of the basis function. In this sense, if the basis functions are not independent, their time-frequency resolution windows will be overlapping. And this in turn means there are frequency leakage and phase ambiguity. Again the more plain explanation is that one frequency (or one scale, or one basis function) will contaminate all its neighboring frequencies (or other scales of basis functions), and any point in the time-frequency plane really is associated with distorted energy that is coming from its surroundings. Hence come the terms of frequency leakage-out and -in.

In a practical sense, if the time or frequency distances of the constituent components of a signal are too short, there will be significant overlapping of their energy, and the power of one component might be overshadowed by others. And it is impossible to separate precisely the constituent components. It is therefore important for us to characterize the behaviors of frequency leakage and phase ambiguity of the wavelet variant and to compare them with those of other bases, in particular, those of the Morlet wavelet.

For equation 12.3 the corresponding basis function is of a modulated Gaussian which has an envelope centered and peaked at zero time, and the basis function has an exact carrier frequency. As for equation 12.4 the corresponding basis function has an envelope which can be treated as either with a singly peaked bump or with doubly peaked bumps according to one's desire whether to pin the envelope curve to the zero center point of

the oscillation curve. But here the basis function does not have a real carrier frequency, nevertheless, the oscillation does possess a frequency parameter. The practical way to characterize the smearing effects both in time and frequency is to study the projections among the basis functions at different locates and scales.

For frequency leakage-out we mean the smearing brought by a unit "scale" (or normalized scale) basis function to its neighboring scales; conversely, there is a frequency leakage-in distribution curve which is induced by neighboring individual scales. For time smearing we mean the ambiguity caused by the phase mismatch between two identical basis functions or wave packets. That is to say, the time smearing distribution curve is calculated by projecting a basis function wave packet into its own time-translated versions.

Programs written in both the Asyst and the Mathematica language are used to derive the results.

- Figure 12.4 (LeakOut–WV) shows the frequency leakage-out distribution curve for the proposed basis function. The frequency leakage-out is the projection of the unit scale basis function into its neighboring scales. For $\omega_0 = 5$, the curve has a root (i.e., zero value point) at scale 0.969621 rather than 1. The reason for this is conceptually the same as what was stated in the previous section concerning the corrective term ϵ. Here the most significant features are the location of the zero value modulus (i.e., the root) and the sharp steep slopes at both sides of the root. They make possible the easy identification through sharp contrast of modulus values.

- Figure 12.5 (LeakOut–MW) shows the frequency leakage-out distribution curve for basis corresponding to the simplified Morlet wavelet. Again the frequency leakage-out is the projection of the unit scale basis function into its neighboring scales. The curve has no root but it has a peak at scale also near to 1. The weight that centers around the zero derivative peak contributes to a relatively broader leakage of energy into its neighboring scales, and there is no sharp contrast in the modulus values.

- For the proposed basis function, the leakage-out distribution curve has two bumps at opposite sides of the root point; while the Morlet wavelet has a single solid bump. This explains why it is appropriate to investigate time and frequency leakages rather than to use time and frequency resolution windows in discriminating their capabilities in analyses.

- Figure 12.6 (LeakIn–WV) shows the frequency leakage-in distribution curve for the present basis function. The frequency leakage-in is the projection of a non-unit scale basis function into the unit scale basis function. This distribution curve shows consistent results with that of the frequency leakage-out. Here the parameter values are the same as those of the previous figures. Here the prominent features are also the zero value root point and the small influences from its surrounding proximity.

- Figure 12.7 (LeakIn–MW) shows the frequency leakage-in distribution curve for the simplified Morlet wavelet. Again it shows consistent results with corresponding frequency leakage-out.

- Figure 12.8 (PhaAmbi–WV) shows phase noise or time smearing effects associated with the proposed basis function. The phase noise is caused by the phase mismatch between two identical but translated or shifted basis functions. That is to say, it is calculated by projecting a unit scale basis function into its various time-translated versions. Once more, the prominent feature is the existence of a root at the point of zero phase shift. And again, this zero value and smallness around it provide the very significant contributions to the basis' usefulness. Here the modulus is also doubly peaked at the opposite sides of the zero phase point.

- Figure 12.9 (PhaAmbi–MW) shows phase noise or time smearing effects associated with the simplified Morlet wavelet. The phase noise is calculated by projecting a unit scale simplified wavelet function into its various time-translated versions. There is a peak rather than a root at the center. And the largeness of values around the peak

point indicates significant interference from phase. The obvious deduction is the difficulty in getting informative features from the its phase plane rendition, and this is certainly related to the afore-mentioned effects of "randomness".

- Combing all the above depictions, one comprehends the reasons why the proposed basis function is able to be helpful in time-frequency or time-scale characterizations and why it is able to be more informative than the Morlet wavelet. It also becomes clear that, regarding the ridge points, the Morlet wavelet (or the basis function corresponding to equation 12.3) is associated with power maxima; while the new basis (or equation 12.4) is associated with the minimum trough points. It is also noted that that a multiplication factor of about $\frac{1}{0.9696}$ is needed for scale adjustment such as to match the trough point to unit scale location.

- For phase plane representations using the proposed basis function, the following specific properties contribute to the possible usefulness in feature extractions. First, at the zero (or low) value trough point (i.e., root point) either the real or the imaginary part (depending on the choice of a phase datum) is of nil value. Second, the leakages, both in and out, are always in opposite signs with respect to the root point. Third, the root point is a reflection point of the leakage distribution curves. Fourth, different visual patterns might show up through the rotation of phase or by adding a phase datum. Fifth, in general, significant features occur at phase value interfaces that separate the neighboring phases at convenient separation distances.

- For the proposed basis function the closed form representation for the leakage-out is derived as

$$\begin{aligned} P(a,\omega_0) \;=\; & \frac{1}{\left(\frac{\left(\frac{1}{a}\right)^2+1}{\omega_0^2}\right)^{0.5}}\left(\frac{1}{2}\left(\sqrt{\frac{\left(1+\frac{1}{a}\right)^2\omega_0^2}{\left(\frac{1}{a}\right)^2+1}}\times\right.\right. \\ & \left.\left.{}_1F_1\left(1;\frac{3}{2};-\frac{\left(1+\frac{1}{a}\right)^2\omega_0^2}{2\left(\left(\frac{1}{a}\right)^2+1\right)}\right)\operatorname{sgn}\left(1+\frac{1}{a}\right)+\right. \end{aligned}$$

$$\sqrt{\frac{(a-1)^2\omega_0^2}{\left(\left(\frac{1}{a}\right)^2+1\right)a^2}}\times$$
$$_1F_1\left(1;\frac{3}{2};-\frac{(a-1)^2\omega_0^2}{2\left(\left(\frac{1}{a}\right)^2+1\right)a^2}\right)\operatorname{sgn}\left(1-\frac{1}{a}\right)+\Big)\Big), \quad (12.29)$$

in which a is a scale, ω_0 stands for a representative carrier frequency parameter (i.e., $a = 1$) and here it is taken as $\omega_0 = 5$, and the $_1F_1$ stands for a hypergeometric function.

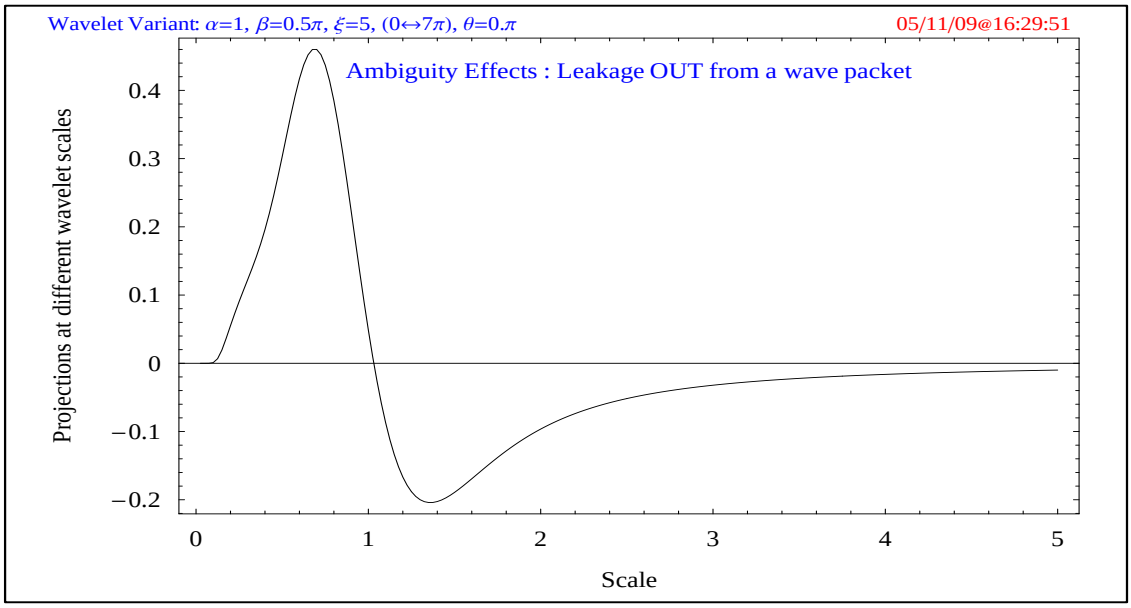

Fig 12.4 (LeakOut–WV) The frequency leakage-out distribution curve for the wavelet variant. The leakage-out is the projection of the unit scale basis function into its neighboring scales (or frequencies). For $\omega_0 = 5$ the curve has a root at scale 0.969621. This root zero near scale 1 and the sharp steep slopes at both sides of the root make possible the easy identification of energy ridges.

12.7 Tested numerical and water wave signals

Both numerically simulated and experimentally acquired signals are used to examine the performances of the wavelet variant. And their results are compared to those of the Morlet wavelet.

The numerical experimentation involves the following simulated signals:

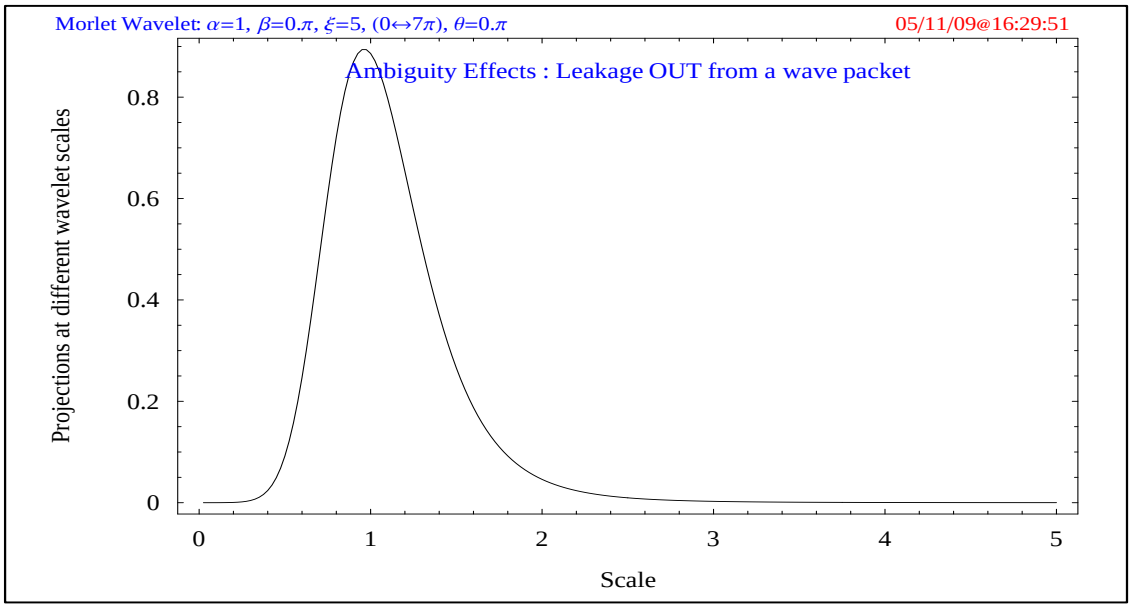

Fig 12.5 (LeakOut–MW) The frequency leakage-out distribution curve for the Morlet wavelet. The curve peaks at a scale around unity and the concentrated weight here makes difficult the identification of nearby ridges.

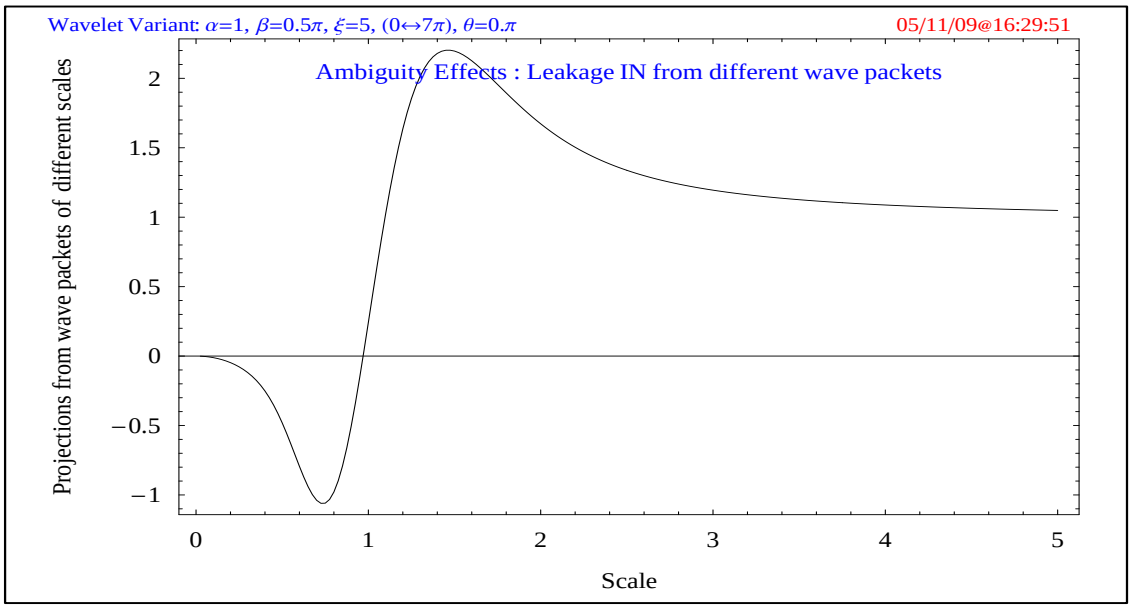

Fig 12.6 (LeakIn–WV) The frequency leakage-in distribution curve for the wavelet variant. The leakage-in is the projection of a non-unity scale basis function into the unity scale basis function. Again there is a root zero near the unity scale 1 and there are the sharp steep slopes at both sides of the root. It shows consistent results with the frequency leakage-out and make possible the easy identification of energy ridges.

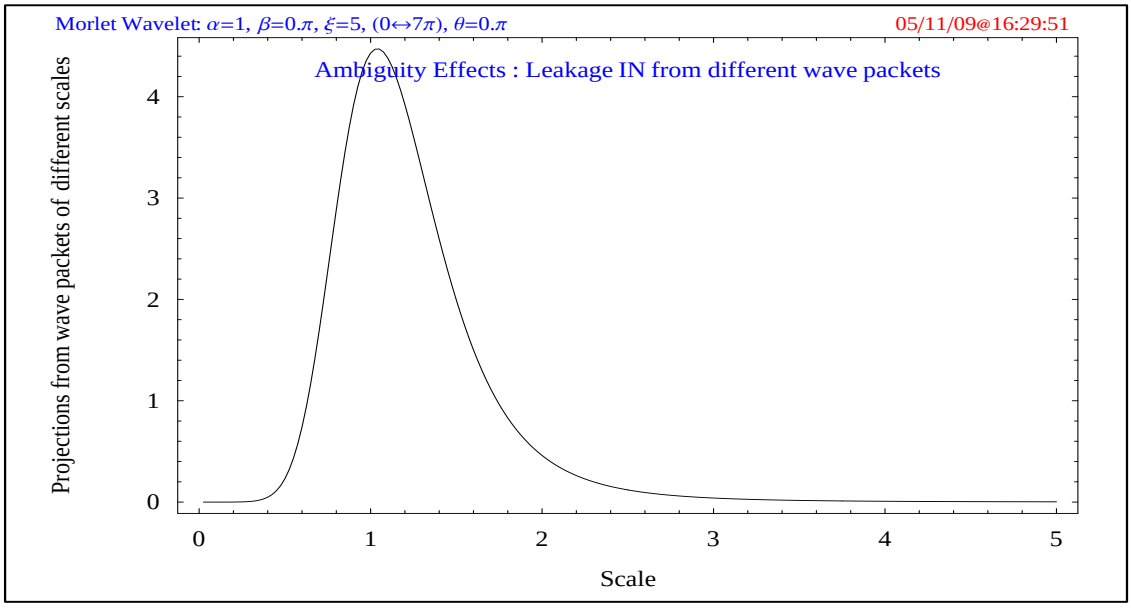

Fig 12.7 (LeakIn–MW) The frequency leakage-in distribution curve for the Morlet wavelet. The frequency leakage-in is the projection of a non-unity scale wavelet function into the unity scale. It shows almost the same pattern as the that of the frequency leakage-out.

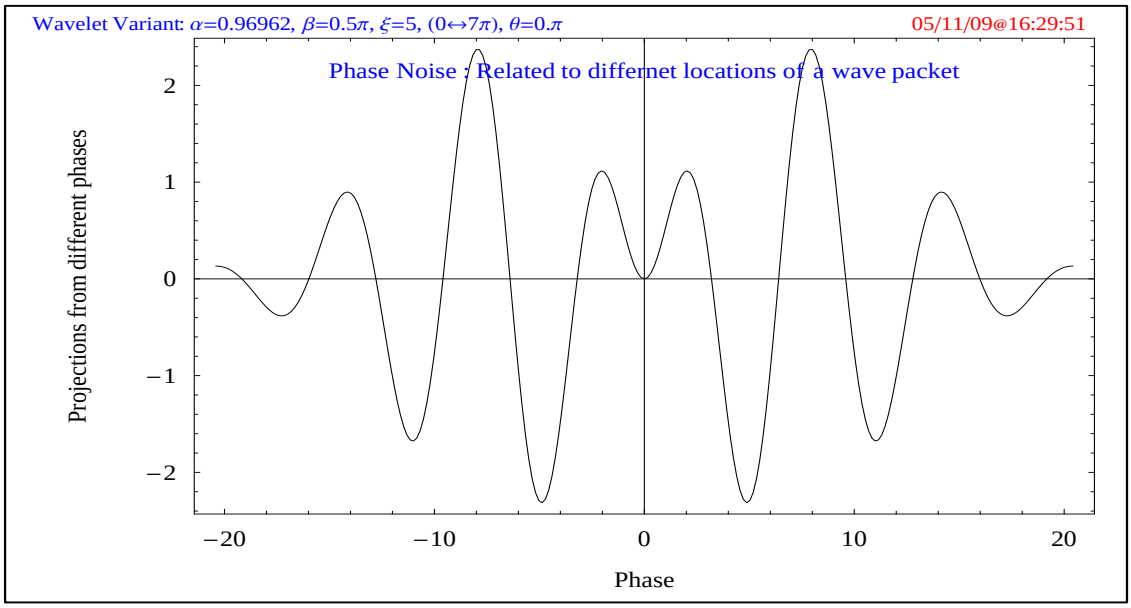

Fig 12.8 (PhaAmbi–WV) The phase noise or time smearing effects associated with the wavelet variant. The phase noise is caused by the phase mismatch between two identical but translated basis functions. That is to say, it is calculated by projecting a unity scale basis function into its various time-translated versions. Once more, there is a root at the zero phase point. And this root zero and the smallness around it provide additional reasons for the usefullness of the wavelet variant.

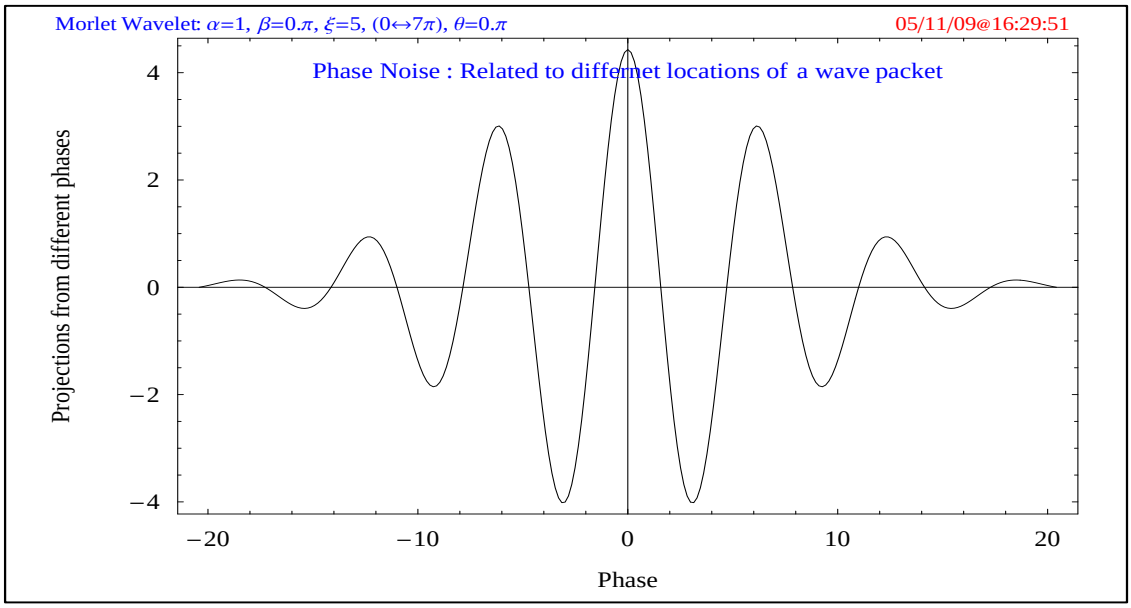

Fig 12.9 (PhaAmbi–MW) Phase noise or time smearing effects associated with the Morlet wavelet. Again there is a peak rather than a root at the center. The large values around the center point indicate that it is hard to get informative features from the phase plane information using such a basis.

- A parabolic chirp with a frequency range of zero to Nyquist rate of 100 Hz;
- A signal composed of two liner chirps with equal and constant power content (i.e., the amplitudes are the same) and crossing at a frequency point at half of its Nyquist rate. It is here denoted as an X-signal;
- An X-signal with a power ratio 0.01 between the two component signals;
- A signal composed of two liner chirps that are parallel (i.e., they are displaced versions in time) and have the same power contents;
- A signal composed of two liner chirps that are parallel but with a power ratio of 0.04.

For real world signals, water waves from experiments in laboratory tank, either generated by wind or mechanical generator, are used. They include:

- Wind waves with respective spectral peaks at about 2.0 to 2.6 Hz;

- Stokes waves with different fundamental harmonic frequencies and different wave steepness values.

12.8 Comparisons of the two transforms

Followings are the results and the feature comparisons for the two transforms using the test signals and real wave data from water tank experiments.

- Figures 12.10 (C-CS-Zm), 12.11 (C-CS-Zm-Pm-1), and 12.12 (C-CS-Zm-Pm-2) show the time-frequency zoom-ins of the modulus and phase planes of a section of a parabolic chirp with 100 Hz Nyquist rate under several setups, such as, different bases, different numerical resolutions, and different rendering parameters. The figures provide a basic and general glimpse of the difference in performance of the two transform approaches.

- The top two sub-figures in figure 12.10 (C-CS-Zm) are respectively the modulus and phase rendition, based on the Morlet wavelet (equation 12.3). Although there is a large blank area it is not quite obvious to pinpoint the power ridge for the naked eyes. The bottom two sub-figures are associated with the wavelet variant and the modulus and phase planes are rendered in accordance with equations 12.4 and 12.5, respectively. Apparently, the wavelet variant is able to provide both easier and precise identifications of the instantaneous frequency from either of its modulus or phase renditions. Contrarily, nothing physically significant can be told from the phase rendition associated with the Morlet wavelet.

- Sub-figures in Figure 12.11 (C-CS-Zm-Pm-1) shows the same zoom-in section associated with the wavelet variant but with different numerical resolutions in scale (or frequency) and different adaptations in the shape of each scale's time-frequency window. Physically, different ω_0 parameter means different decaying property of waves. And generally a larger ω_0 is for a smaller scale a (high frequency and fast

decaying); conversely, a smaller ω_0 is for a larger scale a (low frequency and slow decaying). Here even though the frequency resolution is coarser when compared to that of the previous figure, both the modulus and phase planes still provides very clear features of the instantaneous frequency. Moreover, the phase plane renditions show clear interfacial features at all the interfacial points for all the time steps; that is to say, the intermediate time translation points that do not exactly locate at the frequency points yet still provide the same sharp interfacial features. Again this feature is absent in the phase plane rendition using the Morlet wavelet.

- Figure 12.12 (C-CS-Zm-Pm-2) together with the previous figure 12.11 (C-CS-Zm-Pm-1) shows additional characterizations associated with the wavelet variant. The top and bottom sub-figures of figure 12.11 (C-CS-Zm-Pm-1) correspond to equations 12.5 and 12.6, respectively, and they indicate a manipulation of coordinate axes. Here they show the same identification. Note that the top and bottom sub-figures have a difference in phase equal to a rotation of $\frac{\pi}{2}$ (the constant added to equations 12.5 and 12.6). Here in the bottom sub-figure there are two interfacial phase lines. Though somewhat irregular they indicate the time and frequency spreads in a sense similar to leakage or ambiguity effects from the peak frequency ridge. One more thing to note is that the alternating dark-and-light vertical strips of phase suggest the cycles of the trough and peak of the signal. Overall, such renditions possess distinguishable contrasts that are visually sharp and readily diagnosable.

- Figure 12.13 (C-CS) shows the full extend of the same parabolic chirp for both the Morlet wavelet (the left sub-figures) and the wavelet variant (the right sub-figures) shown in both 2-D and 3-D. The difference in easiness of identification is obvious; moreover, the phase plane associated with the Morlet wavelet yields no practical information. Note that there is a slight up-shift of instantaneous frequency for the wavelet variant, and this up-shift factor is about $\frac{1}{0.9696}$ as derived previously, but such a deviation may not be important numerically due to the adopted resolution.

- Figure 12.14 (C-XS-Zm) shows a zoom-in section of an X-signal that is composed of two intersecting linear chirps of equal and constant power contents. The left sub-figures are for the Morlet wavelet, and the right sub-figures are for the wavelet variant. Their comparisons manifest the same characterizations or features as depicted by those of the previous parabolic chirp. Again, there is a big difference in the performances of the two approaches, especially in their phase characterizations.

- Figure 12.15 (C-XS) shows time-frequency characterizations of the full extend of the same X-signal. The left and right sub-figures are those of the Morlet wavelet and the wavelet variant, respectively. Basically they feature the same depictions as those mentioned above. There are some intricate points to note here. First, around the signal intersecting point both transforms seem to have distortion in modulus renditions; nevertheless, the wavelet variant transform is far more informative in its phase rendition. Second, the existence of the saw-tooth spikes in the 3-D modulus rendition for the wavelet variant may reflect the non-exact match between the instantaneous frequency and the step resolution. Note that, in the bottom right sub-figure, the rendering of modulus has been inverted for easy visualization, i.e., a trough in the 2-D plane (top right sub-figure) turns to a peak in the 3-D figure.

- Figure 12.16 (C-XS-Pha) illustrates the effects of phase manipulation on the same X-signal based on the wavelet variant. Again, some of the interfacial lines in the mid sub-figure serve as indicators of extend of frequency leakage and phase noise. Some numerically introduced interferences may also exist in certain regions.

- Figure 12.17 (C-PC) shows the ridge extraction of a signal composed of a pair of parallel chirps with equal power content and with top frequency at Nyquist rate. The frequency separation between the two chirps is one tenth of its Nyquist rate. It is clearly seen that the power ridges yielded by the Morlet wavelet (left sub-figures) are totally misleading. Whereas, the wavelet variant (right sub-figures) yields two clearly identifiable interfacial lines except near the Nyquist frequency.

Additionally, the comparison of the 3-D renditions provides enhanced illustration of the difference in performance between the two approaches. As to be seen of the two spike lines in the bottom right sub-figure. Undoubtedly, the patterns of leakage characters of the wavelet variant function provide the grounds of its superiority in feature identification.

- Figure 12.18 (C-PC-ED) shows the 2-D and 3-D modulus renditions of a signal composed of a pair of parallel chirps but now with difference in power contents, and the energy ratio of the two chirps is 0.04. In general, both transforms show difficulty in differentiating the two components of the signal due to a large energy difference and their proximity. What is surprising is that, for the Morlet wavelet, there still exists the same distortion pattern shown in the previous figure; as is incurred by the weak component. On the other hand, the wavelet variant seems to be able to leave out the influence coming from the low energy component. Overall these manifest the correspondence between different leakage characterization and different performances.

- Figure 12.19 (C-XS-ED) shows the time-frequency modulus planes for an X-signal that is composed of two intersecting chirp components with a significant power difference of a ratio of 0.01. Again, both seem to have difficulty in rendering significant features for the weak component. But still, the wavelet variant is seen to provide unambiguous identification of the strong signal component and to yield a bit more informative pattern that is associated with the weak component.

- Figure 12.20 (C-WW) shows time-frequency features of a water wave signal measured in the wind blowing laboratory oval-shaped tank described in the earlier chapter. The left and right sub-figures are for the Morlet wavelet and the wavelet variant, respectively. It is seen that the right outperforms the left not only in the easy and distinct identification of the energy ridge but also in the sharp and peculiar pattern of the phase feature.

- Figure 12.21 (C-WWL) shows the modulus and phase planes of the wavelet variant transform for a wind-generated water wave that is in a less-developed stage when referenced to the signal associated with the figure right before (figure 12.20 (C-WW)). Due to a small wind speed in the tank, the wave is in a developing stage with significant fetch effects. And the Fourier spectrum of the wave peaks at frequency higher than 3 Hz. The prominent features in both the renditions attest the wave modulation phenomena for the developing waves. And the observation of multiple locates of interface at individual steps along the time line is the outright manifestation. They highlight the complex interactions and depict the physics of energy cascade among waves, in particular, those concerning bifurcation, energy recurrence and water wave instability. Again, these observances are far less obvious for the Morlet wavelet.

- Figure 12.22 (C-SW) shows the performance differences between the two transforms for a mechanically generated Stokes wave in the wave tank. Note the Stokes wave has a small wave steepness value of about 0.06 at its fundamental harmonic band. Once again, the wavelet variant shows off more informative physics either from its modulus or phase rendition. First, both its modulus and plane planes depict the existence of interfacial lines correctly corresponding to its harmonic components. Second, there are rapid oscillations (or up-and-down variations) of interfacial lines at the high frequency harmonic in both its modulus and phase renditions. The phenomenon serves as another indication of the energy recurrence of water waves, as well as of wave evolutions and bifurcations.Third, from the wavelet variant phase rendition, at the fundamental harmonic, the first half part of the interfacial line remains relatively stable and its later half gets more or less undulating. Together with the second point they strongly testify the Benjamin-Feir side-band instability [12, 13, 30, 32, 31, 47, 66, 77]. Note again, these features are in general not discernable using the Morlet wavelet or from the Fourier spectral approach.

12.9 Summary

As an addendum to the present study on the best wavelet for water waves, a wavelet variant is proposed and its time-frequency renderings are devised and researched. The reasons that lead to the usefulness of the wavelet variant are characterized, as well as referenced to those of the Morlet wavelet, specifically, the frequency leakage-in, leakage-out and phase ambiguity or time smearing effects. Both numerical signals from simulation and water wave signals from tank experiments are used to test the functioning of the proposed variant and the Morlet wavelet. It is seen that the wavelet variant in most circumstances provides easy and clear identifications of time-scale features both from its modulus and phase renditions; most profoundly, the phase plane results of the proposed variant are far more informative than as can be provided by the Morlet wavelet. Additionally, the wavelet variant is capable of highlighting the power ridge, the extend of frequency leakage, the range of influence from phase noise, as well as the energy recurrence, the evolution and the instability phenomenon of water waves. Lastly, we note that the wavelet variant lacks a few stringent requirements in mathematical or analytical robustness concerning a function basis, such as the transform completeness, the wavelet admissibility condition, as well as the renderings of modulus and phase; nonetheless, the associated algorithm and the numerical approach are identical to those of the wavelet transform and the outcomes yield unique time-frequency characterizations and a few significant physics. ❖

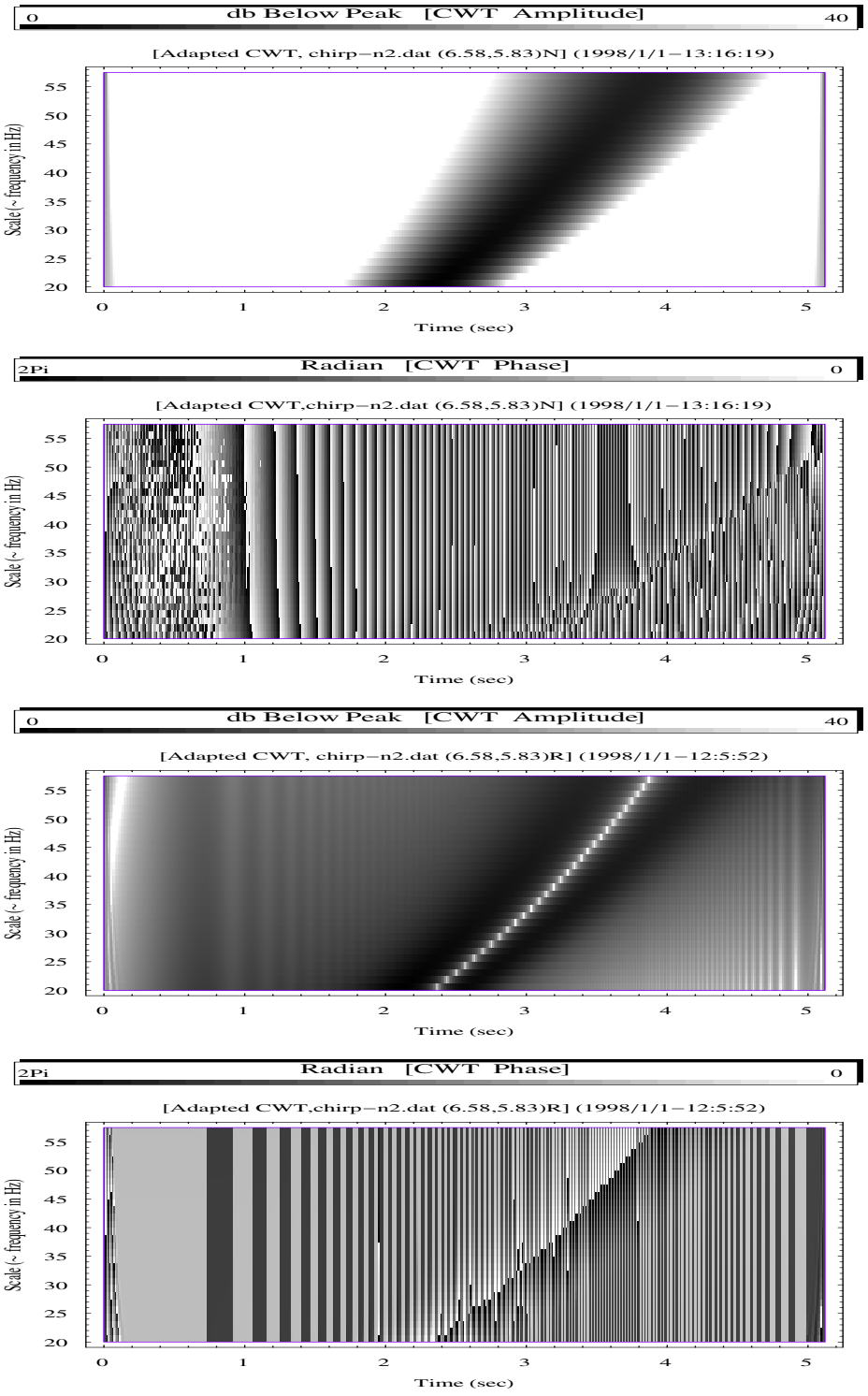

Fig 12.10 (C-CS-Zm) The time-Frequency zoom-in of a section of the parabolic chirp with the frequency range of zero to Nyquist rate of 100 Hz. The top two sub-figures are the modulus and phase renditions associated with equation 12.3, i.e., the Morlet wavelet; the bottom two sub-figures are associated with the wavelet variant in accordance with equations 12.4 and 12.5. It is obvious that the wavelet variant outperforms the Morlet wavelet in easy identification of the power ridge either from the modulus or phase rendition. Moreover, the phase associated with the Morlet wavelet does not yield anything significant.

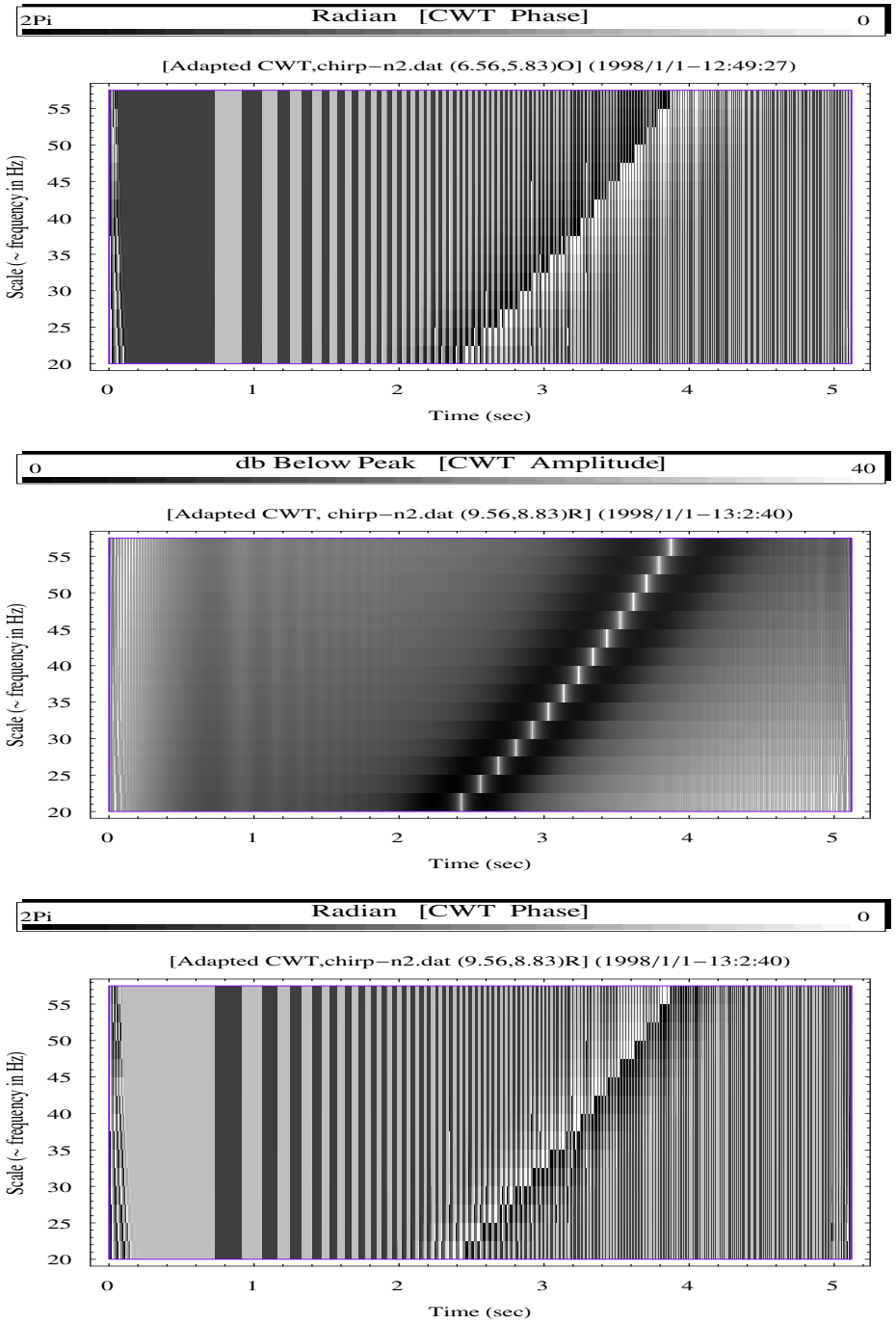

Fig 12.11 (C-CS-Zm-Pm-1) The same zoom-in section as of the previous figure but with different numerical resolutions in frequency and different adaptations in the shape of each scale's time-frequency window that are associated with the wavelet variant. Physically, different ω_0 parameter means different decaying property of waves, and a larger ω_0 is for a larger scale a or low frequency waves, conversely, a smaller ω_0 is for a smaller scale a. Even though the frequency resolution is coarser when compared to that of the previous figure, both the modulus and phase planes still provide very clear features of the instantaneous frequency. Moreover, the phase plane renditions show clear-cut interfacial pattern at all the interfacial points for all the time steps.

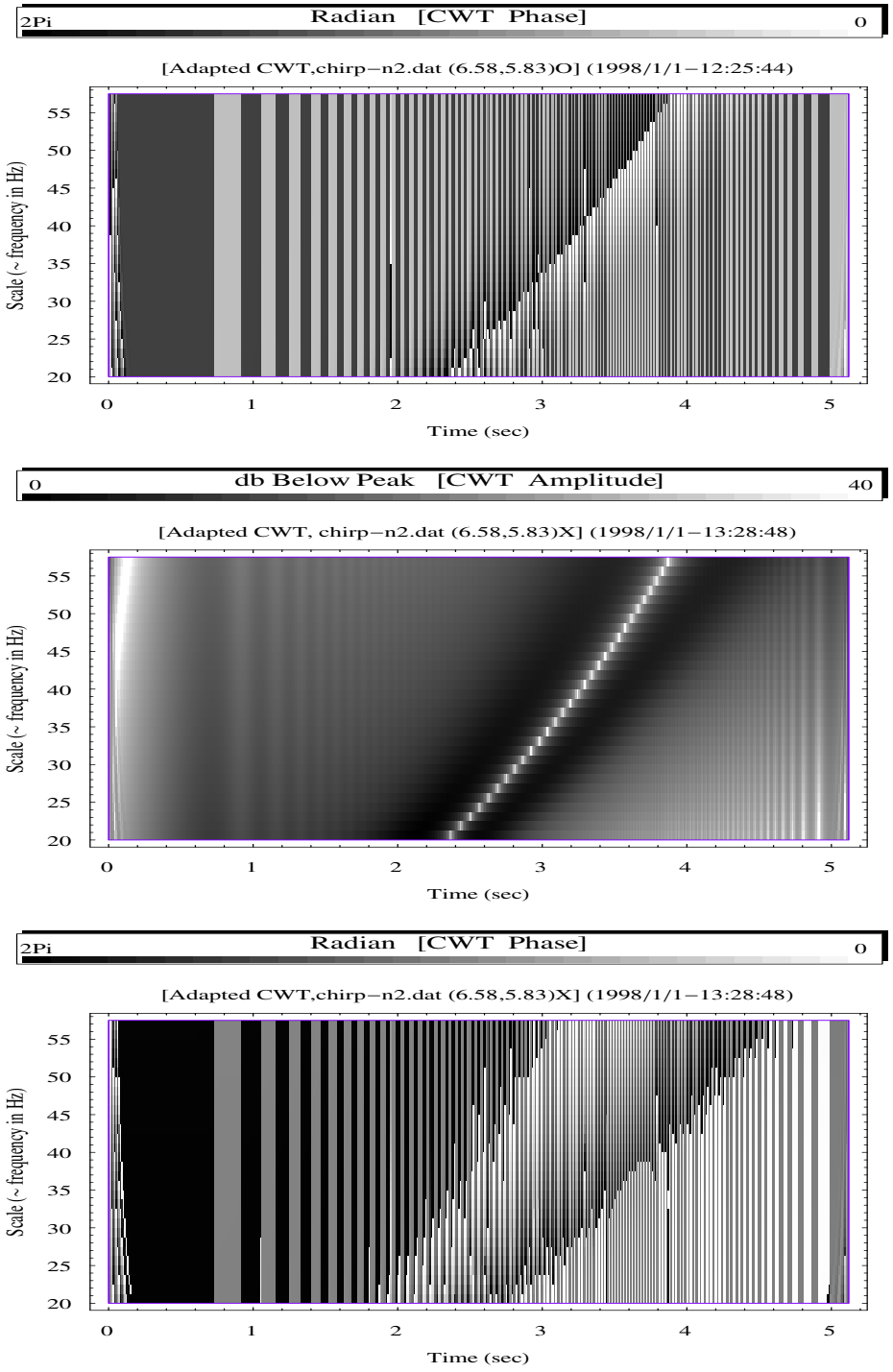

Fig 12.12 (C-CS-Zm-Pm-2) This figure together shows additional characterizations associated with the wavelet variant using different parameters and phase renderings. The top and bottom sub-figures are the results of a manipulation of coordinate axes. In the bottom sub-figure there are two interfacial phase lines. Though somewhat irregular they indicate the time and frequency spreads in a sense similar to leakage or ambiguity effects from the peak frequency ridge. Note that the alternating dark-and-light vertical strips of phase indicate the cycles of the trough and peak of the signal. Overall, these renditions possess distinct contrasts that are visually sharp and readily discernible.

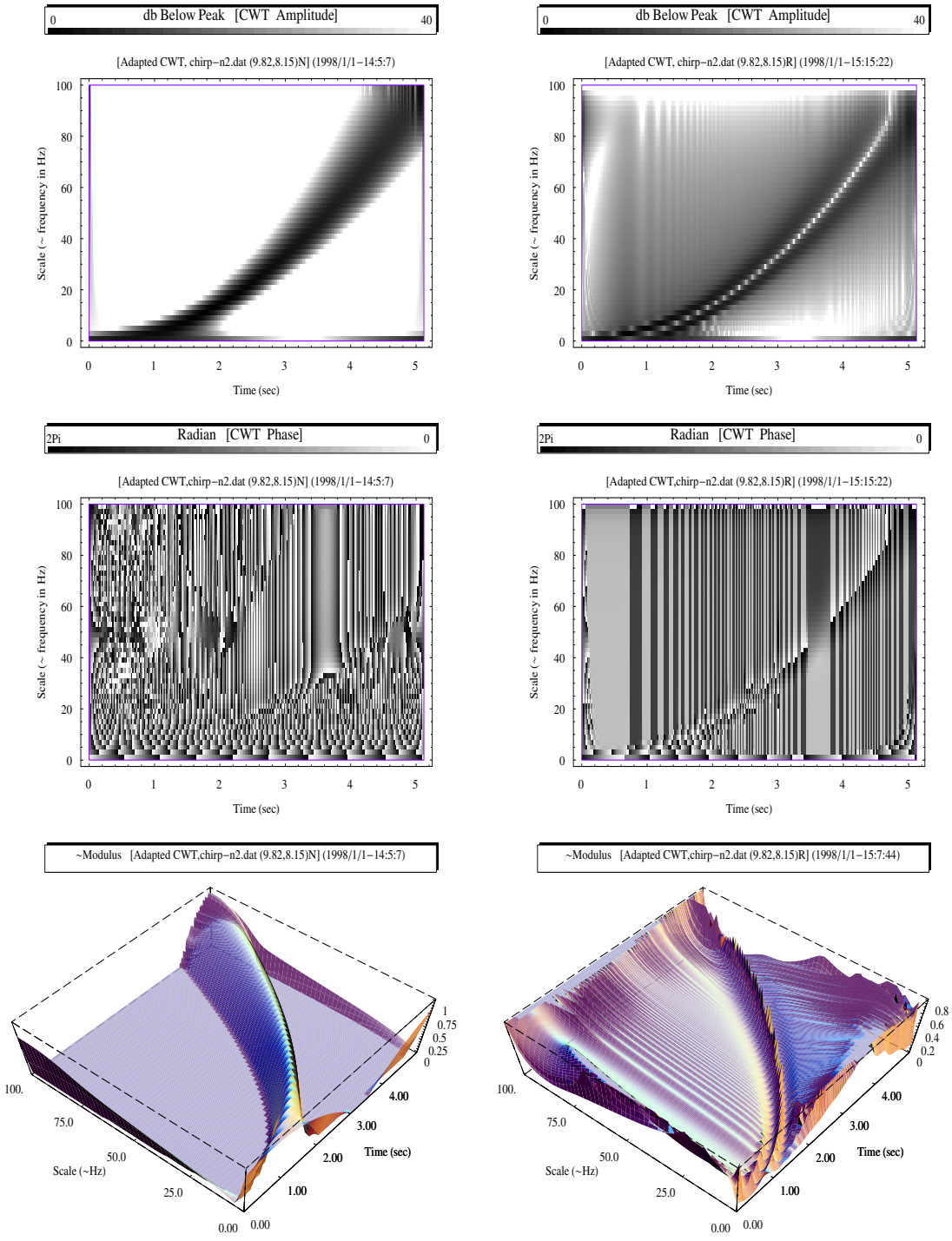

Fig 12.13 (C-CS) The full extend of the same parabolic chirp for both the Morlet wavelet (left sub-figures) and the wavelet variant (right sub-figures) shown in both 2-D and 3-D. Again, the difference in easiness of identification is self-explanatory; moreover, the phase plane associated with the Morlet wavelet yields no practical information. Note that the slight displacement of instantaneous frequency ridge (about $\frac{1}{0.9696}$) may be of little concern numerically due to the resolution adopted.

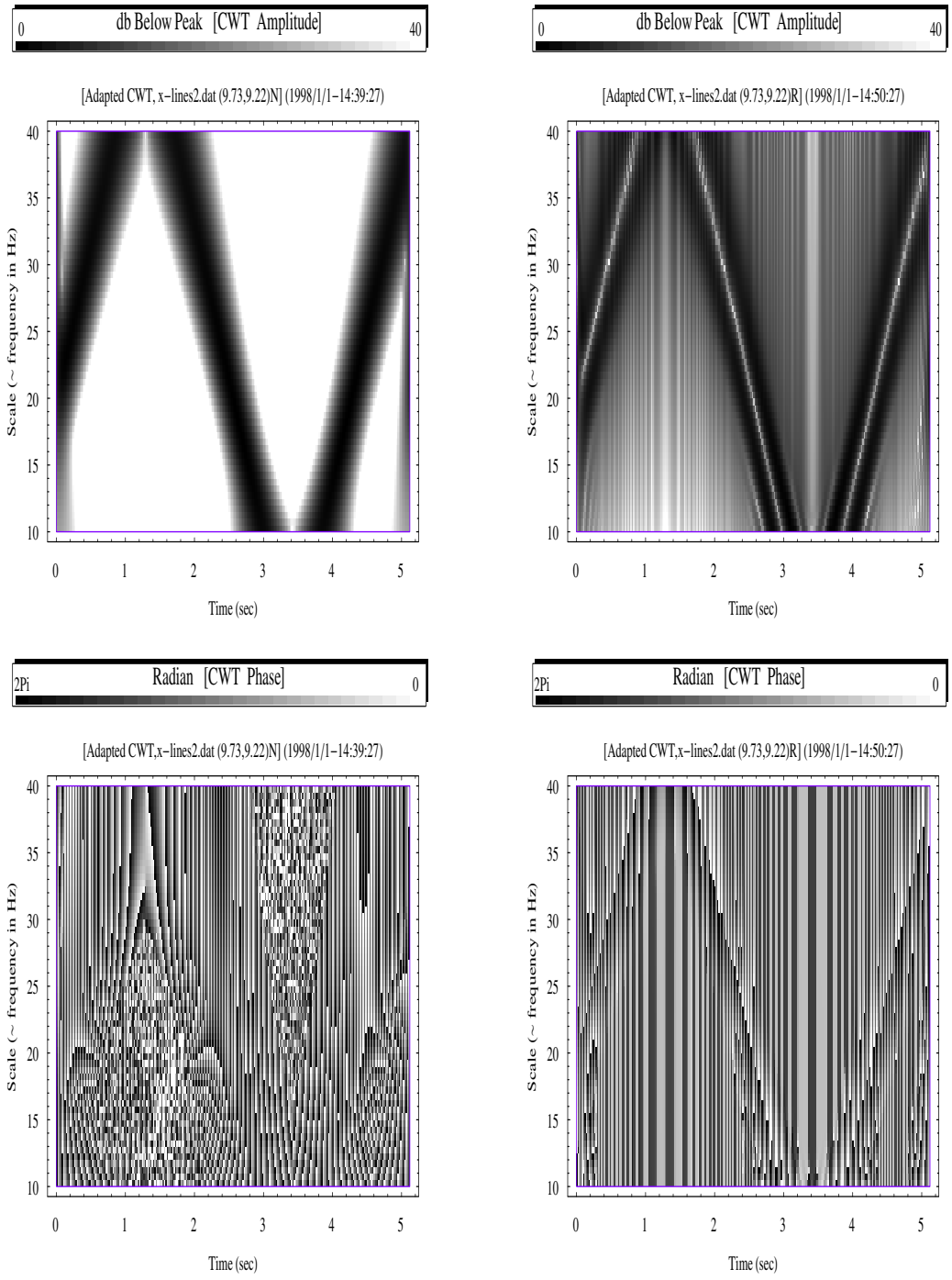

Fig 12.14 (C-XS-Zm) This figure shows a zoom-in section of an X-signal that is composed of two intersecting linear chirps of the same and constant power contents. The left sub-figures are for the Morlet wavelet, and the right sub-figures are for the wavelet variant. These comparisons manifest the same characterizations or features as depicted by those of the previous parabolic chirp. Again, there is a big difference in the performances of their phase outcomes.

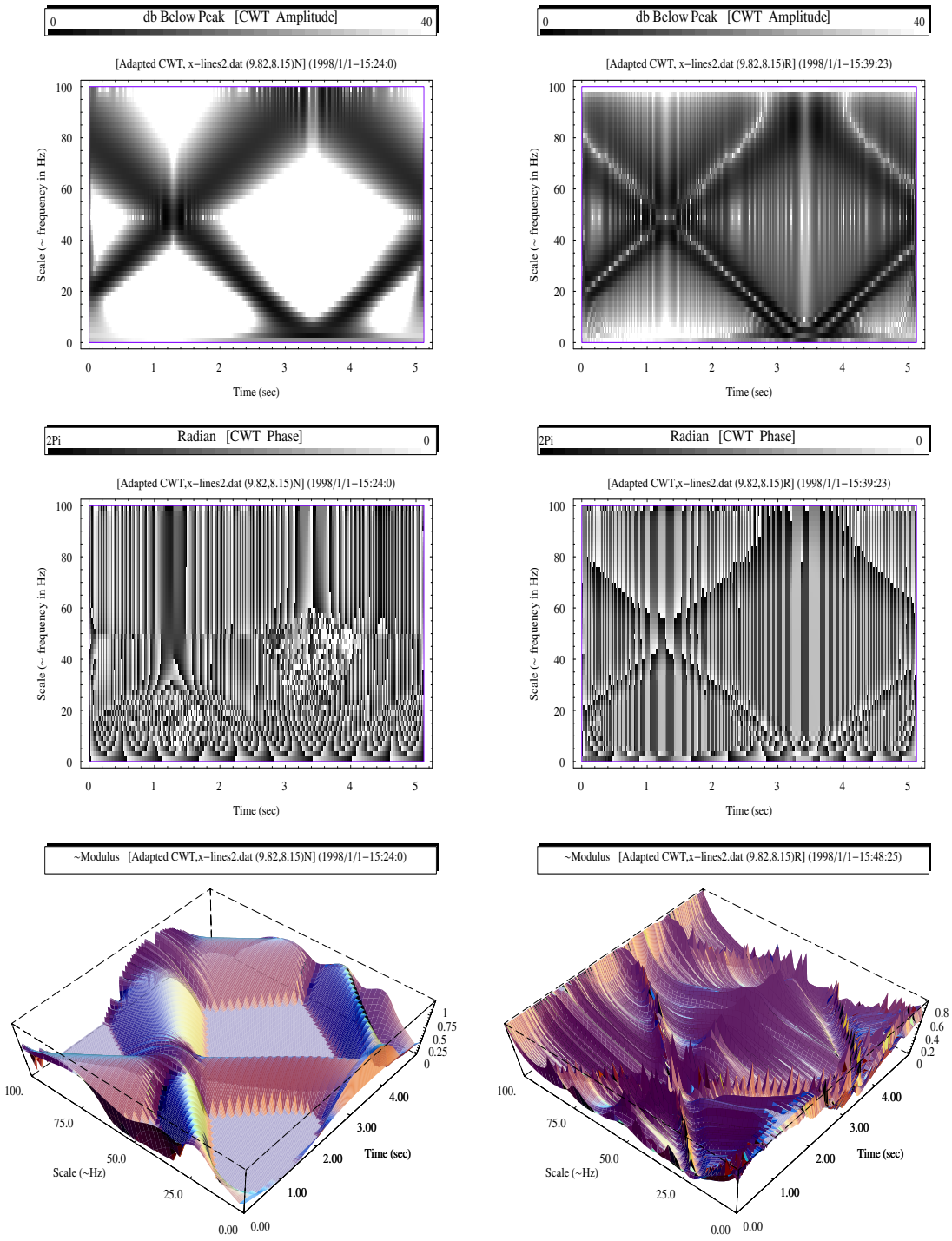

Fig 12.15 (C-XS) Time-frequency characterizations of the full extend of the same X-signal in 2-D and 3-D. Basically they feature the same depictions as those mentioned above. Some intricate points can be observed: for example, around the signal intersecting point both seem to have distortion in modulus renditions; the wavelet variant performs far much better in its phase rendition; and, the existence of the saw-tooth spikes in the 3-D modulus rendition for the wavelet variant may reflect the non-exact match between the instantaneous frequency and the step resolution. Note that, in the bottom right sub-figure, the rendering of modulus has been inverted for easy visualization.

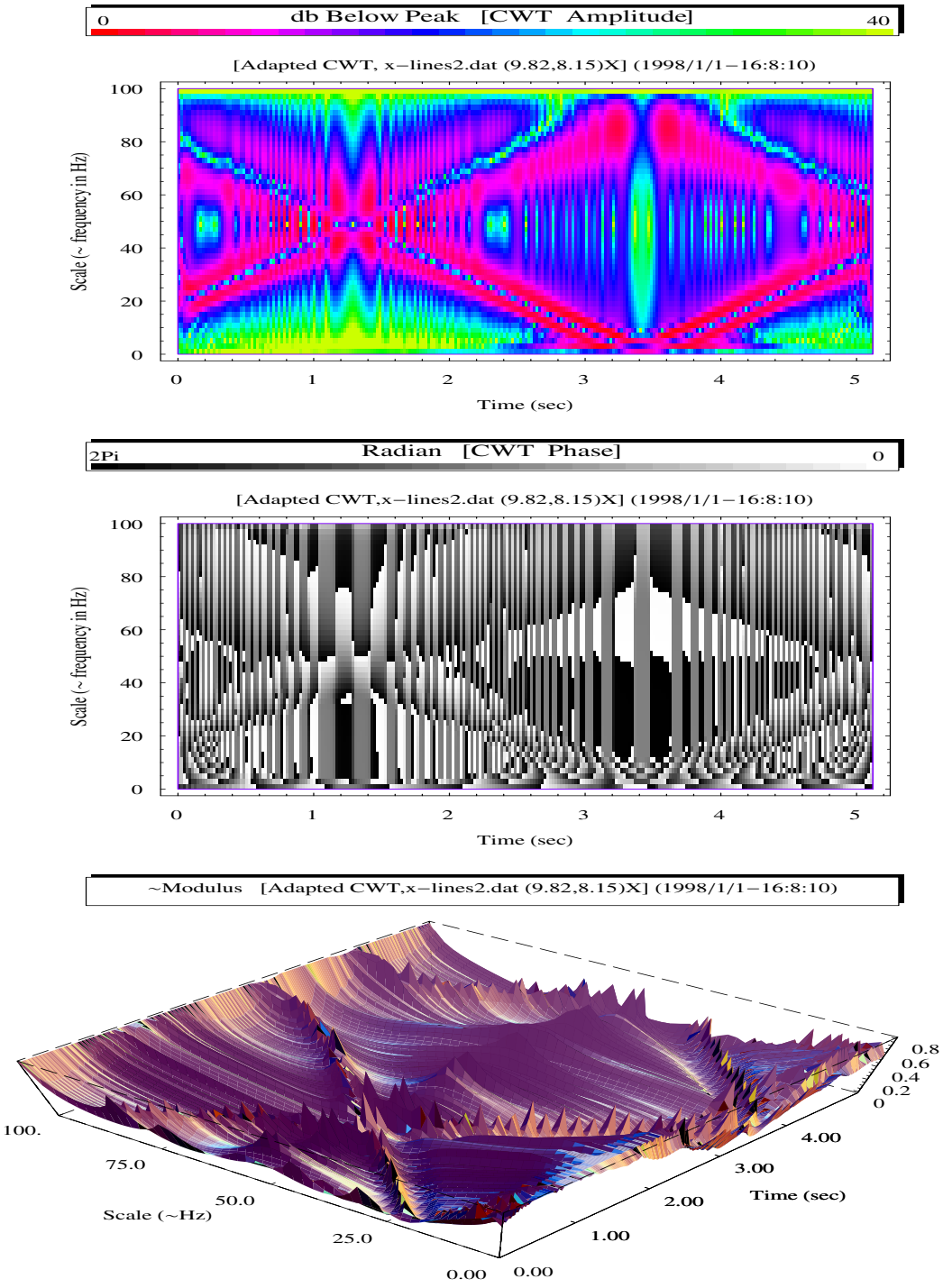

Fig 12.16 (C-XS-Pha) The effects of phase manipulation on the same X-signal based on the wavelet variant. The interfacial lines in the mid sub-figure serve as indicators of extend of frequency leakage and phase noise. Note that the spread phenomenon seems to reflect the effects of Heisenberg uncertainty. And numerically introduced interferences may also exist in certain regions.

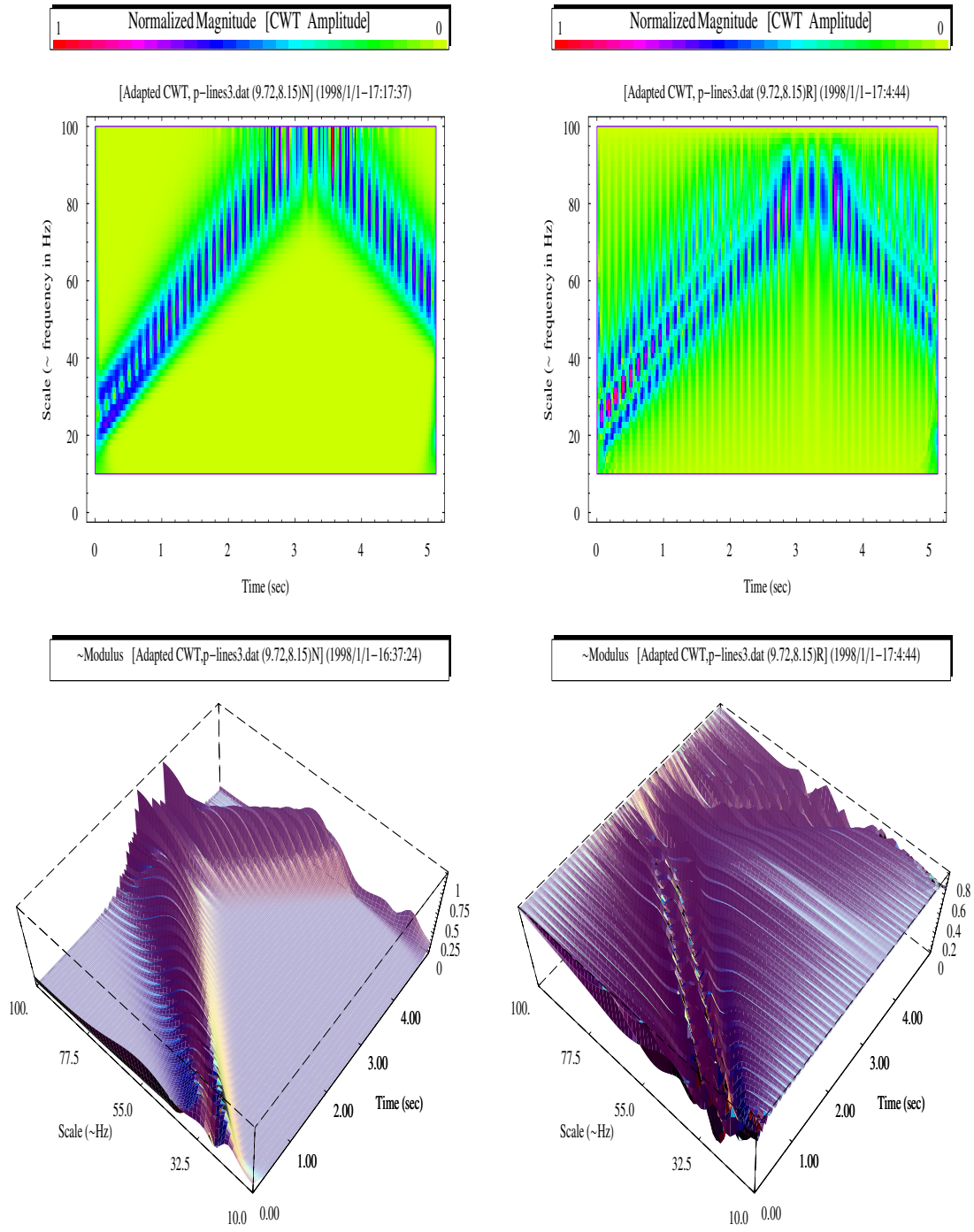

Fig 12.17 (C-PC) The ridge extraction of a signal composed of a pair of parallel chirps of equal power content and with top frequency at Nyquist rate. The frequency separation between the two chirps is one tenth of its Nyquist rate. It can be seen that the ridges yielded by the Morlet wavelet (left sub-figures) are totally misleading. Whereas, the wavelet variant (right sub-figures) shows two clearly identifiable interfacial lines. The 3-D renditions provides enhanced illustration of the difference in performance.

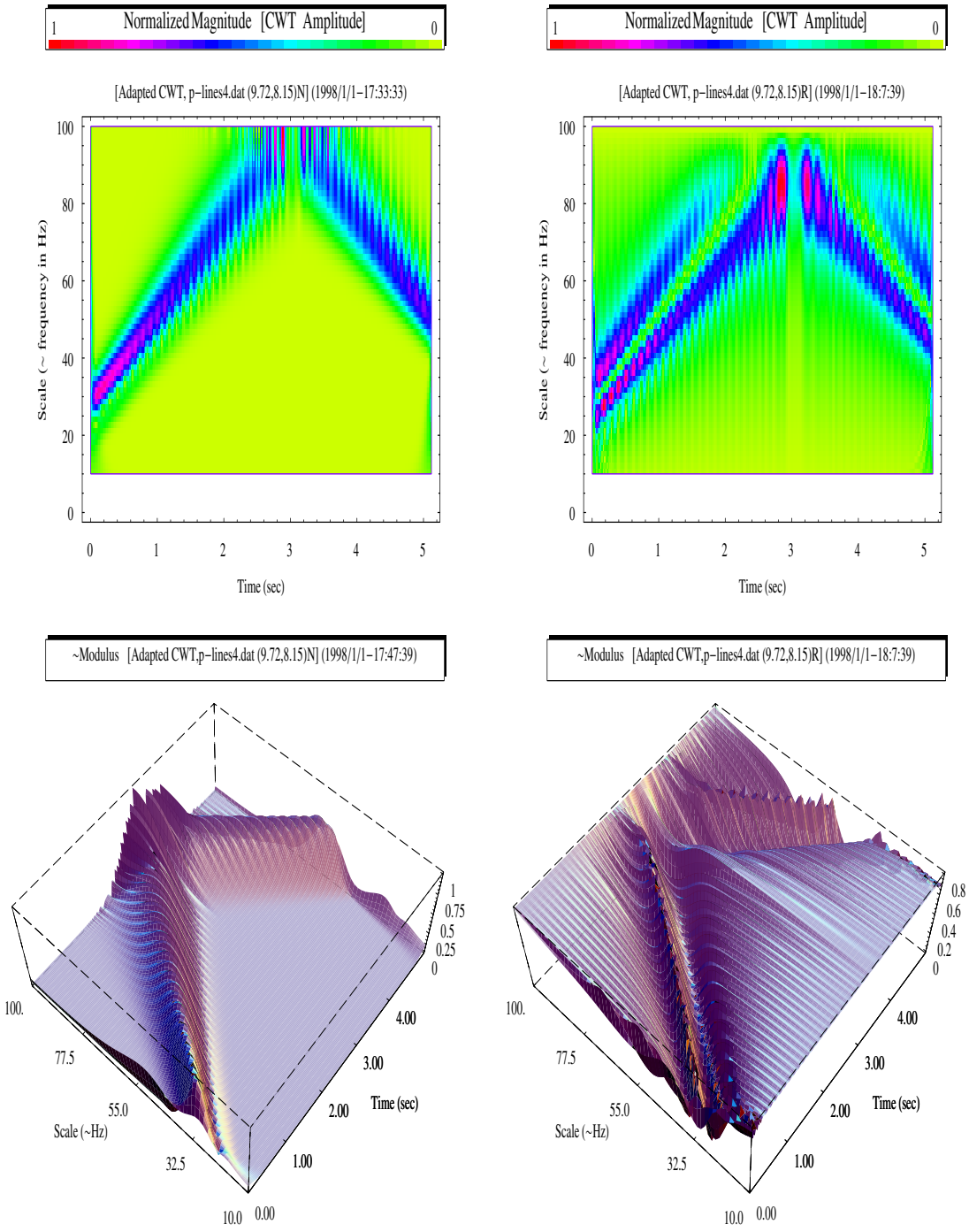

Fig 12.18 (C-PC-ED) This figure shows the 2-D and 3-D modulus of a signal also composed of a pair of parallel chirps but now with energy ratio of 0.04. The left sub-figures are for the Morlet wavelet, and the right sub-figures are for wavelet basis variant. Both transforms show difficulty in distinguishing individual components owing to the large power difference and the proximate frequency. Moreover, for the Morlet wavelet, it is surprising that the weak component still imposes the same distortion pattern shown in the previous figure.

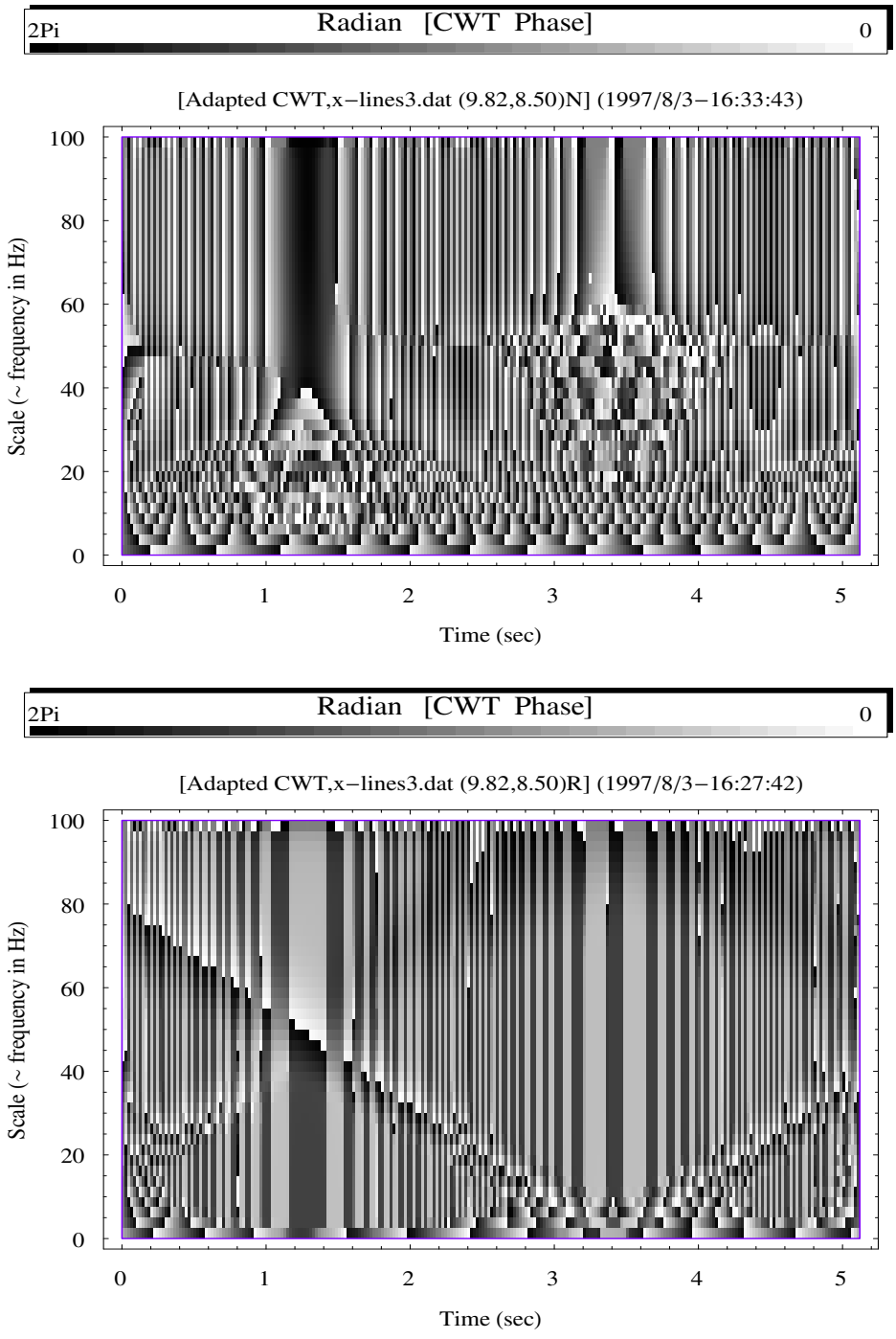

Fig 12.19 (C-XS-ED) The time-frequency phase planes for an X-signal which is composed of two intersecting component chirps with power ratio of 0.01. Here, both transforms show difficulty in rendering significant features for the weak component. But still, the wavelet variant is seen to provide unambiguous identification of the strong signal component, as well as to yield a bit more informative pattern that is associated with the weak component.

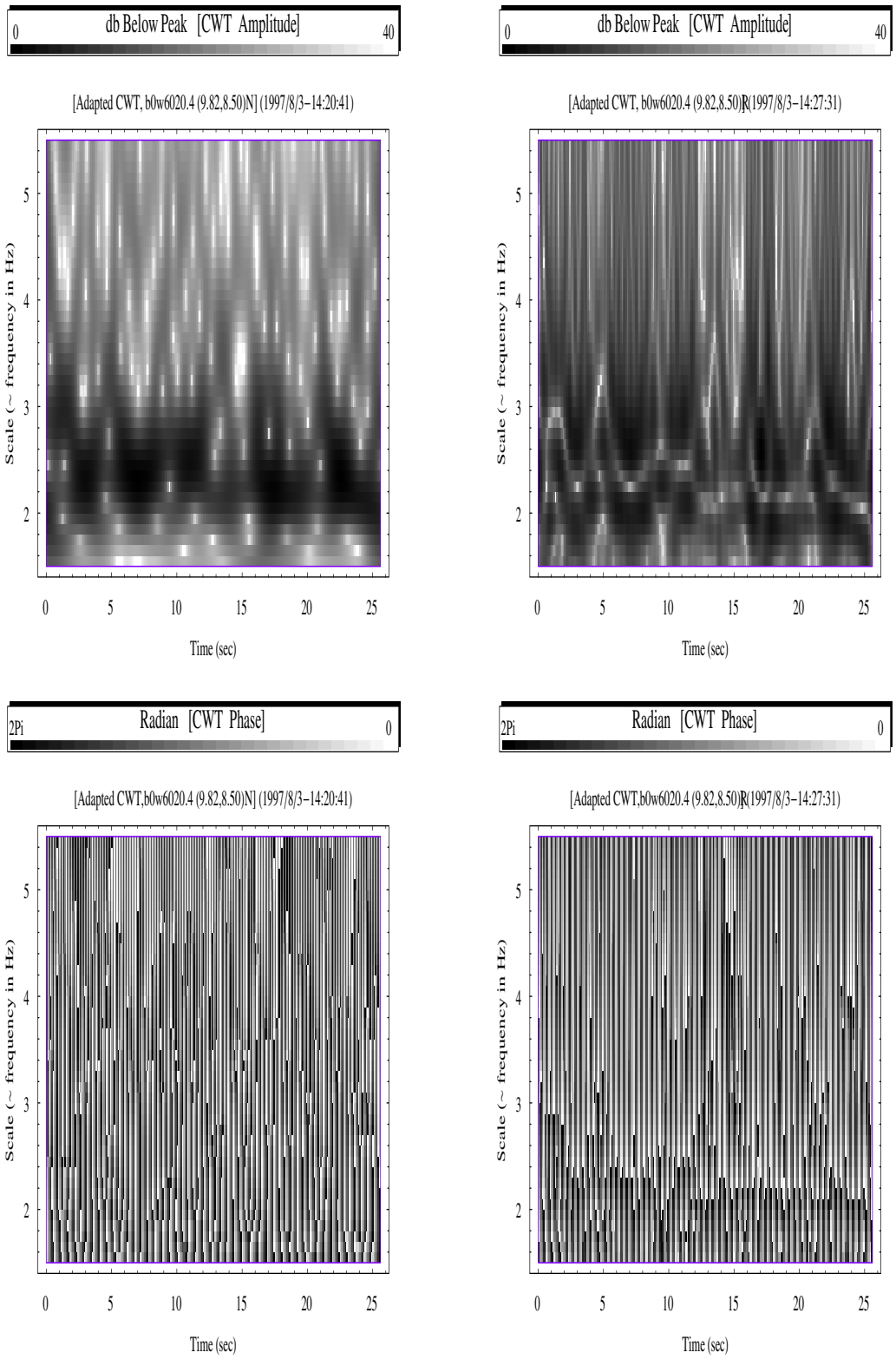

Fig 12.20 (C-WW) The modulus and phase renditions of a wind-generated water wave in the laboratory oval tank. The left and right sub-figures are, respectively, for the Morlet wavelet and the wavelet variant. The wavelet variant is seen to yield not only the easy and distinctive modulus pattern but also the sharp and peculiar phase rendering.

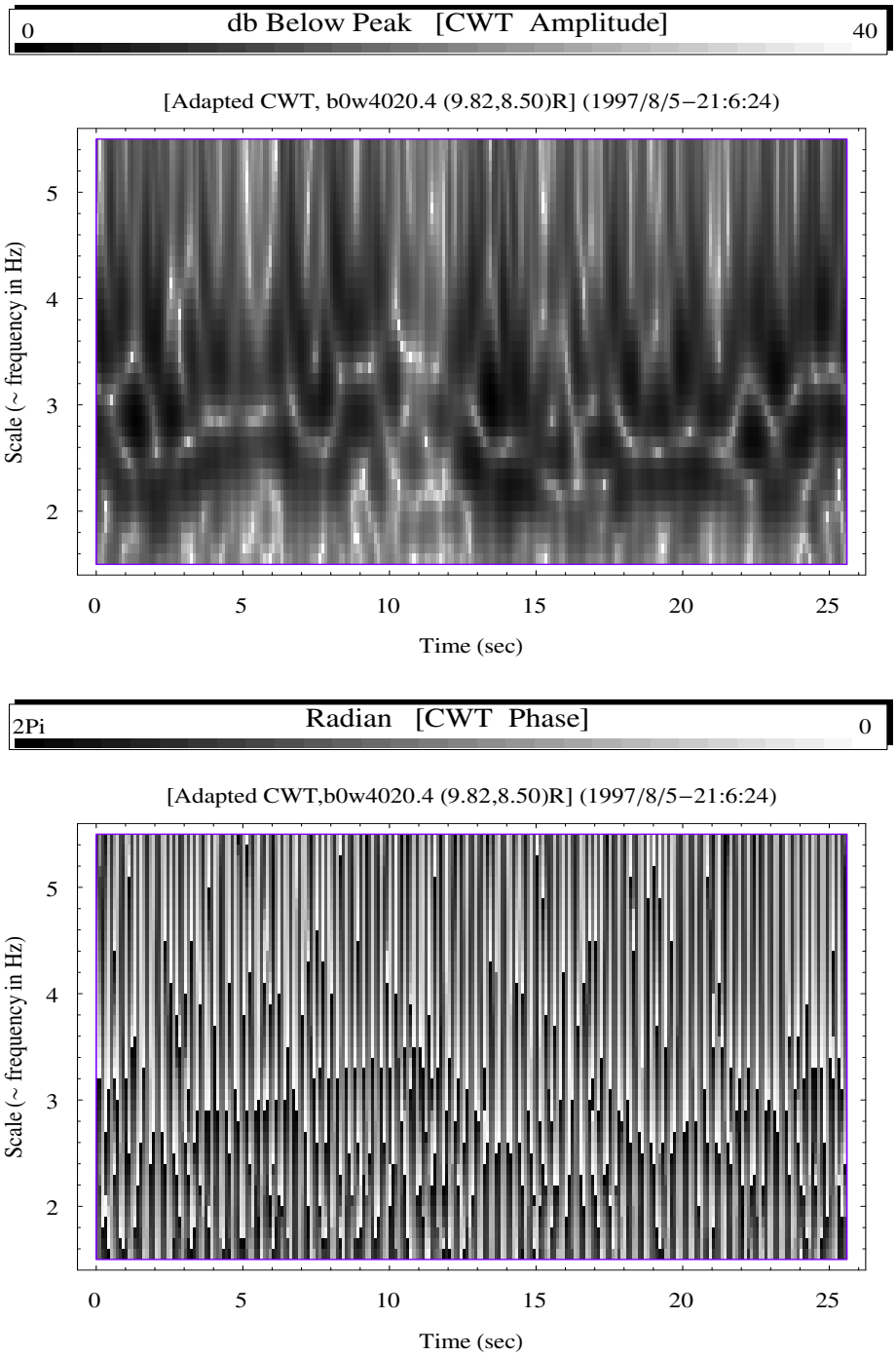

Fig 12.21 (C-WWL) The modulus and phase planes of the wavelet variant transform for a less developed wind-generated water wave (when compared to the wave used in the figure right above) due to a small wind speed in the tank. Both renditions provide quite distinguish characteristics that feature the multiple interfacing points along the time line. It reflects the existence of complex scale components and the mutual interactions among them. The physics displayed here concerns the various energy phenomena of water waves, such as evolution, modulation, bifurcation, and instability. Note that these observances are generally absent for the Morlet wavelet.

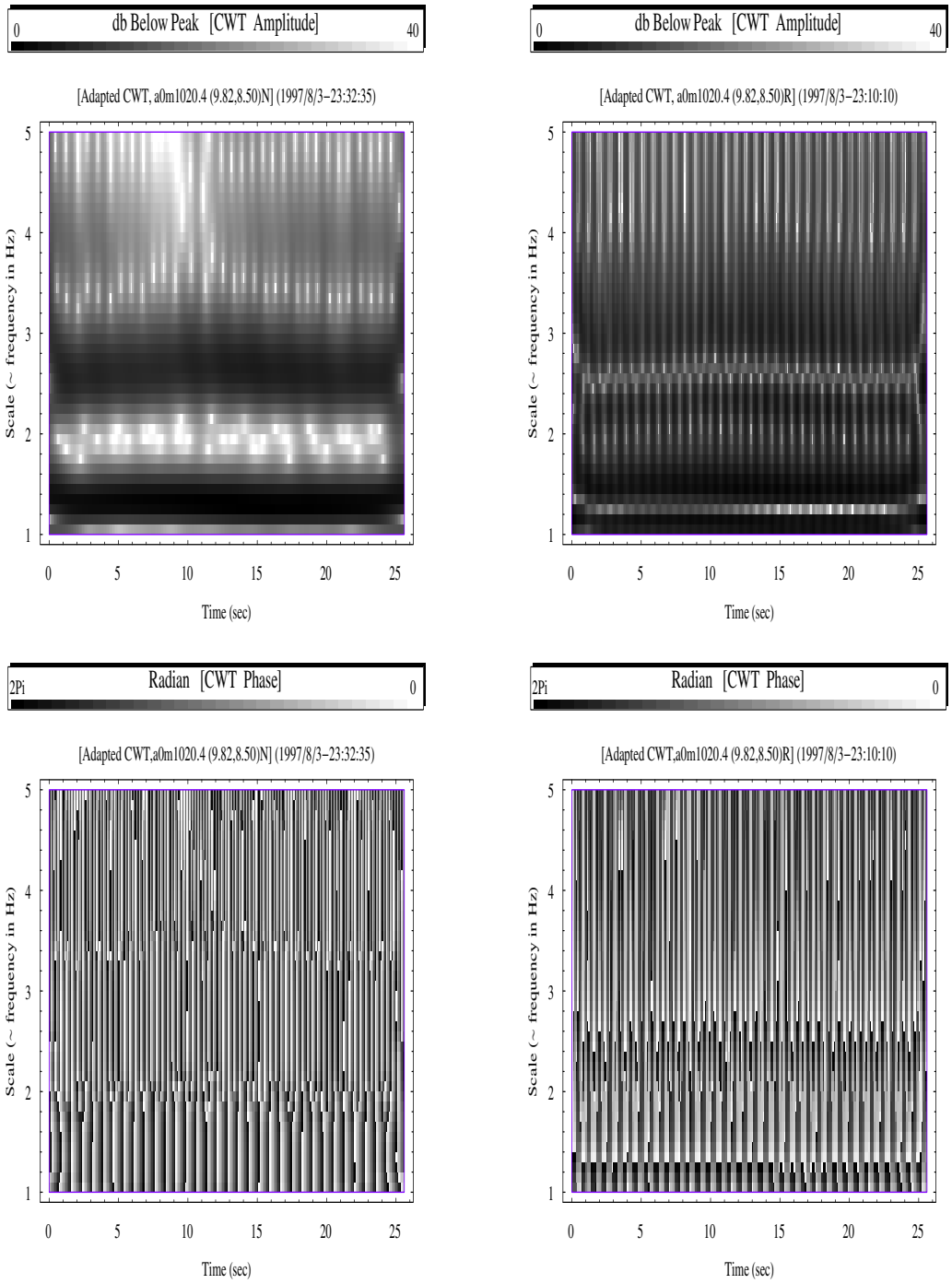

Fig 12.22 (C-SW) The modulus and phase renditions of a mechanically generated Stokes wave. Over again, the wavelet variant (right sub-figures) shows off more informative physics either from its modulus or phase rendition. Such as: (1) Both renditions depict the existence of interfacial lines correctly corresponding to its harmonic components. (2) There are rapid up-and-down oscillations of interfacial locates at the high frequency harmonic in both renditions. (3) At the fundamental harmonic, the first half of the interfacial line remains relatively stable and its later half gets a bit undulating. Overall, these provide intricate physics and serve as the indication of wave evolutions and energy recurrences, such as bifurcations and side-band instability.

Chapter 13

Conclusions

13.1 Introduction

The subject matters in this study can basically be summed up further into the following master theses. The first is the identification of the best wavelet basis for water waves. The second is the optimization of that best basis for practical modeling of water waves, as well as better physics. The third is the validation through the comparisons of coherence performances between the wavelet approach and the Fourier spectral approach using measured signals from wave and current fields. The fourth is an application that concerns the exploration of physics regarding the damping of waves due to rain in the wind, wave and rain coupling system. And herein an energy cascade model is proposed and the model elaborates on the interaction scales in the coupling system that involved both surface waves and internal waves in a natural setting. And the wavelet coherences based upon the above realizations are used to furnish the evidences. The fifth concerns a discovery that extends the design of the best wavelet bases — a wavelet variant outperforming the Morlet wavelet in many aspects both from the modulus and the phase renditions, as well as yielding some informative physics of water waves.

When the author embarked wavelet studies and ventured into their utilizations, the only idea in mind is "why use wavelet and which basis to choose?" None of the above theses were initiated systematically and their downright interconnectedness was not fore-

seen. In fact, most were stumped upon quite independently and their relevances were found mostly not by intentions but by chances or even by mistakes, nevertheless, in the end, they uphold with strength the conclusion on the issue concerning the ultimate best wavelet for water waves.

13.2 Summary

Focusing on the interest for water wave related studies and applications, comprehensive categories of discrete wavelet bases, as well as the continuous wavelet, were investigated. Extensive sets of **Asyst** programs were developed from the ground up and a comprehensive workbench was devised. The programs makes possible the illustrations of various intrinsic properties of wavelets and their relevant characterizations, as well as their possible implications in the identification of the best wavelet for water wave physics.

Employing the jurisdiction of entropy statistics and the probability distributions of transform coefficients the best wavelet basis in the discrete domain is identified. Furthermore, through the incorporation of the physics of the carrier frequency the corresponding best wavelet in the continuous domain is discerned. As follows, the best wavelet in the discrete domain is the dual semi-orthogonal cardinal spline wavelet devised by Chui [1, 2, 16], and the corresponding counterpart in the continuous domain is the Morlet wavelet.

In addition to the identification of the best wavelet we further discuss the best wavelet's deficiency in physical modeling and provide an intuitive and practical optimization catering water wave decay properties.

To serve as a vindication of the aforementioned realizations, the wavelet coherences associated with the best basis are compared to the Fourier spectral coherences for data of wave and current fields measured in a wind-wave tank.

Furthermore, to give as a credited example of their applications and recognitions, an energy cascade model concerning the interaction scales in the wind, wave and rain

coupling system is proposed and the best wavelet and its coherence approach are put into tests for laboratory experiments.

Finally, as a by-product of the present research process a wavelet variant with distinguish properties is added.

It is the author's belief that the best, as well as the ultimate, wavelet for water wave physics has thusly been named.

Below is a list of some of the main contents:

- The comprehensive discrete wavelet categories included:
  - orthonormal;
  - bi-orthogonal;
  - semi-orthogonal;
  - wavelet packet, both the best level bases and best branching bases;
  - from the most symmetrical till the least symmetrical orthonormal;
  - from the most compactly supported in the time domain till the most compactly supported in the frequency domain.
- The depictions of wavelet natures and their possible pragmatic implications:
  - mother and farther wavelets;
  - the concepts of wavelet translation and dilation;
  - time-frequency window and the difference between scale and frequency, as well as the Heisenberg uncertainty;
  - the zoom-in or blowup of any individual wavelet and the fractal nature of wavelets;
  - the phase distributions of wavelet characteristic functions — the concept of linear phase filtering versus the practical behaviors of wavelets, as well as relevant advantages or disadvantages in water wave applications.

- The identification of the best basis and the inclusion of Fourier bases — the entropy statistics, the cumulative probability distributions:
  - based on broad and inclusive criteria of entropy statistics — from energy point of view, or from displacement point of view, etc;
  - wind wave signals from a small laboratory water tank are used for the jurisdictions — thusly, for water wave signals in the nature there cannot be any wavelet that is more suitable than the optimal wavelet identified here, since the present jurisdiction is made upon the highly transient short water waves generated by wind;
  - the relevance between the phase distribution of the wavelet characteristic function and the entropy;
  - the solely and distinctly identifiable value in every entropy category points to the same best discrete wavelet basis — the dual semi-orthogonal cardinal spline wavelet;
  - entropy values for orthonormal wavelets are inferior to those of nonorthogonal ones;
  - in all criteria the best wavelet's result is undoubtedly superior to the Fourier's.
- The role of the phase distribution of the wavelet characteristic function for various basis constructions:
  - the phase distributions of the characteristic functions for all wavelet categories are provided;
  - the distribution feature of phase hints a wavelet's practical usefulness in water wave physics;
  - the entropy results are of statistics and they provide no analytical clues concerning the usefulness of a basis — the property of the constant phase filtering gives rise to the best performance concerning water wave simulations;

  - the constant phase filtering is a strong indication of the level of regularity of the shapes of water waves — a reflection of the property of "complete oscillation and total positivity" of the cardinal spline wavelet.

- The counterpart wavelet in the continuous domain to the best wavelet in discrete domain:
  - the complex Morlet wavelet is identified and the usefulness arising from the existence of its carrier frequency;
  - the manipulation of wavelet redundancy or non-orthogonality for the purpose of minimizing uncertainty or ambiguity of signal analyses;
  - the additional and specific advantages associated with the continuous domain that lead to the usefulness in practical applications;
  - the relevances among the redundancy, orthogonality, and phase distribution;
  - the implications of the wavelet properties of "complete oscillation and total positivity";
  - the limited practicality of instituting multi-voice or multi-wavelet algorithms [20];
  - the savvying of flexible constructions of wavelets time-frequency windows.

- The further optimization for water wave physics:
  - the decaying properties of water waves of different scales and their relation to the adaptation of wavelet time-frequency window;
  - the constant decay parameter of the continuous wavelet — unrealistic description, as well as an over-estimation of decay for longer waves and an under-estimation for shorter waves;
  - scales verse frequencies — mathematics versus physics — the importance of the association of a wavelet and a carrier frequency parameter;

  - an intuitively proposed complementary error function and the modeling of wave decay phenomenon — the adaptation of wavelet time-frequency window and the carrier frequency;
  - better ridge extractions for a wider range of scale — numerical simulation using chirp signals and real data from laboratory wave tank;
  - a more suitable approach for discerning micro phenomena, such as feeble features evolving under multi-factor interactions.

- The comparisons of the wavelet coherences and the Fourier spectral coherences
  - when compared to the Fourier coherence formulation, from mathematics to statistics, the wavelet coherence formulation is a natural extension with less artificial intervention;
  - the poor performance of spectral coherences is reflected by the rapid variation of the coherent curves as well as the extremely slow improvement when the data lengths are increased;
  - the wavelet coherent curves are consistently far superior to the Fourier coherent ones.

- The symptoms related to the Fourier coherence can be attributed to:
  - the unsatisfactory deconvolution mechanism of a blackbox operation;
  - the serious phase noise and ambiguity effects;
  - the uncertainties associated with Fourier numerics;
  - the rapid diminishing of autocorrelation functions;
  - critical variations due to slight changes of signal – a symptom that is associated with an orthonormal bases.

- The superior performance of wavelet coherences can be attributed to:

- the basis functions being associated with the minimum entropy basis;
- the set of continuous transform coefficients being extremely redundant;
- with intimate analytical origin;
- less interventions and fewer side effects in numerics;
- with respect to their shapes of wave form, almost all the discrete basis functions, except those of the best basis here, are too odd to serve the practical simulation of water waves;
- the physical significance of the present adaptation of time-frequency windows to the mimicking of wave decay or evolution;
- probably, the most fundamental, as well as the most primal, factor is that component waves are intrinsically modulating in nature .

- As an example of application, the best wavelet and the coherence approach are used to contemplate the physics for the rapid calming of waves in the coupling system of the wind, wave and rain.
  - an energy cascade model for the coupling system is proposed and the model concerns the interaction scales among the wind, wave, and rain;
  - problems related to existing studies, both theoretically and experimentally oriented, on rain's effects on waves are investigated; relevant experiments (apart from those of coherence-oriented) are also conducted to furnish a few evidences and explanations;
  - the energy cascade model focuses on two categories of mechanisms: one emphasizes the local mechanism within the air and aqueous boundary layers and the other emphasizes the stratification-induced mechanism governing the whole water body;
  - the local mechanism reflects the role played by a match layer due to rain of interfacial aqueous flows;

- the stratification-induced mechanism involves the following key elements: the vortical contribution to wave attenuation, the impact of rain and the catalysts of tuning and de-tuning processes, and the forming of tetra-interactions of surface waves, and the diversification of coupling scales due to triad interactions of surface and internal waves;
- the wavelet coherent features, either of wave-current or current-current, of various scales under a few different settings, either wind or Stokes waves, are used to expedite the arguments of the proposed mechanisms;
- the identified optimum wavelet basis and its associated method of coherent analysis are able to form a sensitive tool for possible identifications or explanations of the mechanisms and physics.

- A wavelet variant is provided at the end as an addendum to the present study on the best wavelet for water waves. And its time-frequency renderings are devised and researched.
  - the reasons that lead to the usefulness of the wavelet variant are characterized, specifically, the frequency leakage-in, leakage-out and phase ambiguity or time smearing effects;
  - both numerical signals from simulation and water wave signals from tank experiments are used to test the functioning of the proposed variant and the comparisons with those of the Morlet wavelet are made; It is seen that the wavelet variant outperforms in most of the circumstances, in particular its visibility and easiness in identifications of time-scale features from both its modulus and phase renditions; Most profoundly, the phase plane results of the proposed variant are far more precise and informative than as can be provided by the Morlet wavelet;
  - the wavelet variant is capable of highlighting the power ridge, the extend of frequency leakage, the range of influence from phase noise, as well as water

wave physics such as, the energy recurrence, the wave evolution or modulation and the instability phenomenon.

Lastly, a point to note again: Here we put up an optimal, as well as the ultimate, wavelet basis that is both mathematically and physically right for water waves; moreover, together with the proposed wavelet coherence methodology, their usefulness can be expected for studies involving multi-factor and multi-scale interactions in a complex coupling system. And the author firmly believes that the best basis herein identified is the last word in wavelets concerning their applications to water waves. ❖

BIBLIOGRAPHY

[1] Chui, C.K. *An Introduction to Wavelets*. Academic Press, Inc., San Diego, California, USA, 1992.

[2] Chui, C.K. On cardinal spline-wavelets. In M. B. Ruskai, G. Beylkin, R. Coifman, I. Daubechies, S. Mallat, Y. Meyer, and L. Raphael, editor, *Wavelets and Their Applications*, pages 439–452. Jones and Bartlett Publishers, Boston, New York, USA, 1992.

[3] Adrian, R.J. *Laser velocimetry*, chapter 5, pages 155–244. Hemisphere Publishing Corporation, New York, NY, USA, 1983.

[4] Akansu, A.N., W.A. Serdijn and I.W. Selesnick. Emerging applications of wavelets: A review. *Physical Communication*, 3:1–18, 2010.

[5] Atlas, D. Footprints of storms on the sea: A view from spaceborne synthetic aperture radar. *J. Geophys. Res.*, 99:7661–7969, 1994.

[6] Auscher, P. Wavelet bases for L^2(R) with rational dilation factor. In M. B. Ruskai, G. Beylkin, R. Coifman, I. Daubechies, S. Mallat, Y. Meyer, and L. Raphael, editor, *Wavelets and Their Applications*, pages 439–452. Jones and Bartlett Publishers, Boston, New York, USA, 1992.

[7] Ball, F.K. Energy transfer between external and internal gravity waves. *J. Fluid Mech.*, 19:465–478, 1964.

[8] Battle, G. Cardinal spline interpolation and the block spin construction of wavelets. In C.K. Chui, editor, *Wavelets: A tutorial in Theory and Applications*, pages 73–90. Academic Press, Inc., San Diego, California, USA, 1992.

[9] Bliven, L.F., and J.P. Giovanangeli. An experimental study of microwave scattering from rain- and wind-roughened sea. *Int. J. Remote Sens.*, 14:855–869, 1993.

[10] Bliven, L.F., H. Branger, P. Sobieski, and J.P. Giovanangeli. An analysis of scatterometer returns from a water surface agitated by artificial rain: Evidence that ring waves are the main feature. *Int. J. Remote Sens.*, 14:1315–2329, 1993.

[11] Bracewell, B. *The Fourier Transform And Its Applications*. McGraw-Hill Book Company, Singapore, second edition, 1986.

[12] Brooke Benjamin, T. Instability of periodic wave trains in nonlinear dispersive systems. *Proc. Roy. Soc. Lond.*, A299:59–75, 1967.

[13] Brooke Benjamin, T., and J.E. Feir. The disintegration of wave trains on deep water. *J. Fluid Mech.*, 27:417–430, 1967.

[14] Caldwell, D.R., and W.P. Elliott. Surface stresses produced by rainfall. *J. Phys. Oceanogr.*, 1:145–148, 1971.

[15] Caldwell, D.R., and W.P. Elliott. The effect of rainfall on the wind in the surface layer. *Boundary-Layer Meteorology*, 3:146–151, 1972.

[16] Chui, C.K. *Wavelets: A Tutorial in Theory and Applications*. Academic Press, Inc., San Diego, California, USA, 1992.

[17] Cohen, L. *Time-Frequency Analysis*. Prentice Hall PTR, Englewood Cliffs, New Jersey, USA, 1995.

[18] Coifman, R., Y. Meyer, and M.V. Wickerhauser. Size properties of wavelet packets. In M. B. Ruskai, G. Beylkin, R. Coifman, I. Daubechies, S. Mallat, Y. Meyer, and L. Raphael, editor, *Wavelets and Their Applications*, pages 453–470. Jones and Bartlett Publishers, Boston, New York, USA, 1992.

[19] Coifman, R., Y. Meyer, and M.V. Wickerhauser. Wavelet analysis and signal processing. In M. B. Ruskai, G. Beylkin, R. Coifman, I. Daubechies, S. Mallat, Y. Meyer, and L. Raphael, editor, *Wavelets and Their Applications*, pages 153–178. Jones and Bartlett Publishers, Boston, New York, USA, 1992.

[20] Daubechies, I. *Ten Lectures on Wavelets*. SIAM, Philadelphia, USA, 1992.

[21] Feir, J.E. Some results from wave pulse experiments. *Proc. Roy. Soc. Lond.*, A299:54–58, 1967.

[22] Froment, J., and S. Mallat. Second generation compact image coding with wavelets. In C.K. Chui, editor, *Wavelets: A tutorial in Theory and Applications*, pages 655–678. Academic Press, Inc., San Diego, California, USA, 1992.

[23] Goda, Y., and Y. Suzuki. Estimation of incident and reflected waves in random sea experiments. In *Proc. of the 15th Conf. on Coastal Engineering*, pages 825–845, 1974.

[24] Gabor, D. Theory of communication. *Journal of the IEE*, 93:429–457, 1946.

[25] Green, T., and D.F. Houk. The mixing of rain with near-surface water. *J. Fluid Mech.*, 90:569–588, 1979.

[26] Greenberg, M.D. *Advanced Engineering Mathematics*. Prentice Hall PTR, Englewood Cliffs, New Jersey, USA, 1988.

[27] Hasselmann, K. On the nonlinear energy transfer in a gravity wave spectrum. *J. Fluid Mech.*, 12:481–500, 1962.

[28] Houk, D.F., and T. Green. A note on surface waves due to rain. *J. Geophys. Res.*, 81:4482–4484, 1976.

[29] Hwang, P.A., D. Xu, and J. Wu. Breaking of wind generated waves: Measurements and characteristics. *J. Fluid Mech.*, 202:177–200, 1989.

[30] Lake, B.M., and H.C. Yuen. A note on some nonlinear water wave experiments and comparison of data with theory. *J. Fluid Mech.*, 83:75–81, 1977.

[31] Lake, B.M., and H.C. Yuen. A new model for nonlinear gravity waves, Part 1, Physical model and experimental evidence. *J. Fluid Mech.*, 88:33–62, 1978.

[32] Lake, B.M., H.C. Yuen, H. Rundgaldier, and W.E. Ferguson. Nonlinear deep-water waves: Theory and experiment, Part 2, Evolution of a continuous wave train. *J. Fluid Mech.*, 83:49–74, 1977.

[33] Lamb, H. *Hydrodynamics*. Cambridge University Press, Cambridge, England, sixth edition, 1932.

[34] Lee, Y.R., and J. Wu. Wavelet and wavelet packet best basis for laboratory water waves. In *Proc. 18th Conf. On Ocean Engineering in Taiwan*, pages 83–94, 1996.

[35] Lee, Y.R., and J. Wu. Continuous wavelet transform using a locally adapted time-frequency window. In *Proc. 18th Conf. On Ocean Engineering in Taiwan*, pages 95–106, 1996.

[36] Lee, Y.R. Signal analysis from wave modulation perspective – Part I: Characterizing the analytic signal procedure. Technical report, No.1997–7, Institute of Harbor and Marine Technology, Taichung, Taiwan, 1997.

[37] Lee, Y.R. *Interaction Scales in a Wind, Wave, and Rain Coupling System*. Ph.D. Dissertation, University of Delaware, Newark, Delaware, Nov. 1999.

[38] Lee, Y.R. Signal Analysis from Wave Modulation Perspective. Technical report, No.2001–09, Institute of Harbor and Marine Technology, Taichung, Taiwan, 2001.

[39] Lee, Y.R., and J. Wu. Time-frequency features and side band instability. In *Proc. 19th Conf. On Ocean Engineering in Taiwan*, pages 32–39, 1997.

[40] Lee, Y.R., and J. Wu. Fourier perspectives of rain's effects on surface waves. *Proc. 22th Conf. on Ocean Engineering in Taiwan*, pages 59–66, 2000.

[41] Lee, Y.R., and J. Wu. Wave characterizations based on Gabor's analytic signal procedure. *Proc. 23th Conf. on Ocean Engineering in Taiwan*, pages 208–215, 2001.

[42] LeMehaute, B., and T. Khangaonkar. Dynamic interaction of intense rain with water waves. *J. Phys. Oceanogr.*, 20:1805–1812, 1990.

[43] Lighthill, M.J. Physical interpretation of the mathematical theory of wave generation by wind. *J. Fluid Mech.*, 14:385–398, 1962.

[44] Liu, P. Wavelet spectrum analysis and ocean wind waves. In E.F. Georgiou, editor, *Wavelets in Geophysics*, pages 151–166. Academic Press, Inc., San Diego, California, USA, 1994.

[45] Longuet-Higgins, M.S. Action of variable stress at the surface of water waves. *Phys. Fluids*, 12:737–740, 1969.

[46] Longuet-Higgins, M.S. The instability of gravity waves of finite amplitude in deep water I, Superharmonics. *Proc. Roy. Soc. Lond.*, A360:471–488, 1978.

[47] Longuet-Higgins, M.S. The instability of gravity waves of finite amplitude in deep water II, Subharmonics. *Proc. Roy. Soc. Lond.*, A360:489–505, 1978.

[48] Mallat, S. Multiresolution approximation and wavelets. *Trans. Amer. Math. Soc.*, 315:69–88, 1989.

[49] Mallat, S. *A Wavelet Tour of Signal Processing*. Academic Press, Inc., San Diego, California, USA, 1998.

[50] Mallat, S. *A Wavelet Tour of Signal Processing*. Academic Press, Inc., San Diego, California, USA, second edition, 1999.

[51] Mallat, S., and S. Zhong. Wavelet transform maxima and multiscale edges. In M. B. Ruskai, G. Beylkin, R. Coifman, I. Daubechies, S. Mallat, Y. Meyer, and L. Raphael, editor, *Wavelets and Their Applications*, pages 67–104. Jones and Bartlett Publishers, Boston, New York, USA, 1992.

[52] Massopust, P.R. *Fractal Functions, Fractal Surfaces, and Wavelets*. Academic Press, Inc., San Diego, California, USA, 1994.

[53] Melville, W.K. Wave modulation and breakdown. *J. Fluid Mech.*, 128:489–506, 1983.

[54] Melville, W.K. The instability and breaking of deep water waves. *J. Fluid Mech.*, 115:165–185, 1982.

[55] Meyer, Y. *Wavelets and operators*. Cambridge University Press, New York, USA, 1992.

[56] Miles, J.W. On the generation of surface waves by turbulent shear flows. *J. Fluid Mech.*, 7:469–478, 1960.

[57] Moore, R.K., Y.S. Yu, A.K. Fung, D. Kaneko, G.J. Dome, and R.E. Werp. Preliminary study of rain effects on radar scattering from water surface. *IEEE J. Oceanic Eng.*, OE-4:31–32, 1979.

[58] Nystuen, J.A. A note on the attenuation of surface gravity waves by rainfall. *J. Geophys. Res.*, 95:18353–18355, 1990.

[59] Phillips, O.M. On the generation of waves by turbulent wind. *J. Fluid Mech.*, 2:417–445, 1957.

[60] Phillips, O.M. *The Dynamics of the Upper Ocean*. Cambridge University Press, New York, USA, second edition, 1977.

[61] Poon, Y.K., S. Tang, and J. Wu. Interaction between rain and wind waves. *J. Phys. Oceanogr.*, 22:977–987, 1992.

[62] Press, W.H., S.A. Teukolsky, W.T. Vetterling, and B.P. Flennery. *Numerical Recipes in Fortran*. Cambridge University Press, New York, USA, second edition, 1992.

[63] Simmons, W.F. A variational method for weak resonant wave interactions. *Proc. Roy. Soc.*, A:551–575, 1969.

[64] Soumekh, M. *Fourier Array Imaging*. Prentice Hall, Inc., Englewood Cliffs, New Jersey, USA, 1994.

[65] Stuart, J.T., and R.C. DiPrima. The Eckhaus and Benjamin-Feir resonant mechanisms. *Proc. Roy. Soc. Lond.*, A362:27–41, 1978.

[66] Su, M.Y. Evolution of groups of gravity waves with moderate to high steepness. *Phys. Fluids*, 25:2167–2174, 1982.

[67] Tchamitchian, Ph., and B. Torresani. Ridge and skeleton extraction from the wavelet transform. In M. B. Ruskai, G. Beylkin, R. Coifman, I. Daubechies, S. Mallat, Y. Meyer, and L. Raphael, editor, *Wavelets and Their Applications*, pages 123–151. Jones and Bartlett Publishers, Boston, New York, USA, 1992.

[68] Tennekes, H., and J.L. Lumley. *A First Course in Turbulence*. The MIT Press, Cambridge, Massachusetts, USA, 1972.

[69] Tsimplis, M. The effect of rain in calming the sea. *J. Phys. Oceanogr.*, 22:404–412, 1992.

[70] Tsimplis, M., and S.A. Thorpe. Wave damping by rain. *Nature*, 342:893–895, 1989.

[71] Turner, J.S. *Buoyancy Effects in Fluids*. Cambridge University Press, Cambridge, England, 1973.

[72] Van Dorn, W.G. Wind stress on an artificial pond. *J. Marine Res.*, 12:249–276, 1953.

[73] Whitham, G.B. Nonlinear dispersion of water waves. *J. Fluid Mech.*, 27:399–412, 1967.

[74] Wickerhauser, M.V. Acoustic signal compression with wavelet packets. In C.K. Chui, editor, *Wavelets: A tutorial in Theory and Applications*, pages 679–700. Academic Press, Inc., San Diego, California, USA, 1992.

[75] Wickerhauser, M.V. Comparison of picture compression methods: wavelet, wavelet packet, and local cosine. In C.K. Chui, editor, *Wavelets: Theory, Algorithms, and Applications*, pages 585–621. Academic Press, Inc., San Diego, California, USA, 1994.

[76] Wu, J. Wind-induced drift currents. *J. Fluid Mech.*, 68:49–70, 1975.

[77] Yuen, H.C., and B.M. Lake. Nonlinear deep water waves: Theory and experiment. *Phys. Fluids*, 18:956–960, 1975.

[78] Zhang, X. Wavenumber spectrum of very short wind waves: An application of two dimensional Slepian windows to spectral estimation. *J. of Atmospheric and Oceanic Technology*, 11:489–505, 1994.

[79] 李勇榮： 水波時頻分析之優化－***Asyst*** 與 ***Mathematica*** 程式集。 交通部運輸研究所港灣技術研究中心，106–037-7937，台灣台中，2016。

[80] 李勇榮： 消坡塊模型試驗之比較研究。 交通部運輸研究所港灣技術研究中心，106–224–7A56，台灣台中，2017 (1991 第一版)。